Physical Modelling of the Bowed String and Applications to Sound Synthesis

Charlotte G. M. Desvages

THE UNIVERSITY
of EDINBURGH

Thesis submitted in fulfilment of
the requirements for the degree of
Doctor of Philosophy
to the
University of Edinburgh — 2018

Declaration

I declare that this thesis has been composed solely by myself and that it has not been submitted, either in whole or in part, in any previous application for a degree. Except where otherwise acknowledged, the work presented is entirely my own.

Charlotte G. M. Desvages
June 2018

Abstract

This work outlines the design and implementation of an algorithm to simulate two-polarisation bowed string motion, for the purpose of realistic sound synthesis. The algorithm is based on a physical model of a linear string, coupled with a bow, stopping fingers, and a rigid, distributed fingerboard. In one polarisation, the normal interaction forces are based on a nonlinear impact model. In the other polarisation, the tangential forces between the string and the bow, fingers, and fingerboard are based on a force-velocity friction curve model, also nonlinear. The linear string model includes accurate time-domain reproduction of frequency-dependent decay times. The equations of motion for the full system are discretised with an energy-balanced finite difference scheme, and integrated in the discrete time domain. Control parameters are dynamically updated, allowing for the simulation of a wide range of bowed string gestures. The playability range of the proposed algorithm is explored, and example synthesised gestures are demonstrated.

Lay Summary

The sound of a musical instrument can be digitally reproduced with various methods. One can make use of libraries of pre-recorded samples, and combine them together to create new sounds. Another approach is to synthesise sound from scratch, using algorithms. An increasingly popular method to design these algorithms is based on producing simulations of the waves propagating in an instrument when it is played; audio output is then extracted directly from these simulations, by choosing a “listening spot” on the virtual instrument.

This work employs this so-called physical modelling approach to sound synthesis, and applies it to the reproduction of bowed string sounds. A detailed mathematical description of the physical system is presented, including the vibrations of the string, the friction of the bow, and the left-hand fingers of a musician pinning the string against the neck of the instrument. The vibrations of the plucked string, in isolation, are also given particular attention.

A numerical method is then employed to convert these equations into an algorithm, in order to produce simulations. This algorithm can be seen as a virtual instrument; it is driven by control parameters closely related to those employed by a musician on a real bowed string instrument (e.g. bow force, left hand finger position. . .). Simulation results for the bowed string model are presented at the end of this thesis, in order to demonstrate the potential of the proposed algorithm for realistic and flexible sound synthesis.

Acknowledgements

This thesis is the fruit of four years of research, all through which I have been lucky to benefit from the incredible support of many around me. They have consistently sustained my energy, even when it was dissipating; and unlike the numerical schemes you will read about in this manuscript, they have done so unconditionally.

First of all, I am infinitely grateful to my PhD supervisors, Dr. Stefan Bilbao and Dr. Michael Newton; I could not have wished for a better team. They have always pushed me to strive for excellence, and offered their unreserved support, even (and particularly) in the most challenging times over the past few years. Their trust in me is in great part responsible for making me a confident researcher, a better speaker, an enthusiastic teacher, and a stronger person overall.

I would like to thank my colleagues and friends from the Acoustics and Audio Group, for making this team such a joy to work with. In particular, thanks to Amaya López-Carromero for too many things to list here, including conference travel shenanigans and Christmas arts and crafts. Thanks to Dr. Brian Hamilton (the Linux/VIM guru), Dr. Alberto Torin (for the best jokes in town), Dr. Craig Webb (master of real-time and of simian nights out), and Dr. Michele Ducceschi (string modelling buddy, also official Party Guy), for their much-appreciated advice throughout the past years; thanks to Dr. Reg Harsley, for the mutual support during our PhDs (and the incredible baked goods).

Thanks to my NESS colleagues at the Edinburgh Parallel Computing Centre; in particular, thanks to James Perry for turning my messy Matlab prototypes into a real-time virtual instrument, and thanks to Kostas Kavoussanakis for always keeping me on track and pushing me to go the extra mile.

I have had the pleasure of meeting many talented researchers throughout my studies, at conferences, seminars, and other events; I am thankful for the stimulating discussions I have had with them, which have often given me much-needed insight on my work.

Thanks to the LAM team at the Université Pierre et Marie Curie in Paris, for welcoming me in their lab to perform exploratory experimental measurements; thanks, in particular, to Dr. Jean-Loïc Le Carrou, for his help and guidance.

Many thanks to the three examiners of this thesis, for providing valuable feedback and helping shape the final version of this manuscript. In particular, thanks to Dr. Murray Campbell for fruitful discussions on experimental results; many thanks to external examiners Dr. Stefania Serafin and Dr. Cyril Touzé for travelling all the way to snowy Edinburgh.

My research was funded by a PhD scholarship from the Edinburgh College of Art. Many of my research expenses were funded by the European Research Council, under grant StG-2011-279068-NESS. I have also been lucky to have twice been named Emil Torick Scholar by the Audio Engineering Society Educational Foundation, and awarded an educational grant as a result. The support of these organisations is gratefully acknowledged.

I warmly thank my friends and family for their support, without which I would not have been able to achieve this work; special thanks to Margaux for keeping me sane during the past few months. I am infinitely grateful to Chris, for being the best and most supportive partner I could have hoped for, and in particular for bearing with me throughout the messiness of the writing-up period.

Enfin, merci à mes parents, qui m'ont toujours fait confiance à cent pour cent, et m'ont poussée à poursuivre mes ambitions. À chaque étape, à chaque moment, à chaque décision, j'ai pu compter sur leur soutien sans faille ; je leur en serai toujours infiniment reconnaissante.

Contents

Declaration iii

Abstract v

Lay Summary vii

Acknowledgements ix

List of Tables xv

List of Figures xvii

1 Introduction 1
- 1.1 Physics-based synthesis of stringed instruments . . . 1
- 1.2 The bow-string interaction . . . 2
- 1.3 Thesis objectives . . . 3
- 1.4 Thesis outline . . . 4

2 The linear string: equations of motion and numerical schemes 7
- 2.1 Time-domain physical modelling of strings . . . 7
  - 2.1.1 The 1D wave equation . . . 7
  - 2.1.2 The stiff string . . . 14
- 2.2 From equations of motion to synthetic sound . . . 18
  - 2.2.1 Review of numerical methods . . . 19
  - 2.2.2 Time series and temporal FD operators . . . 23
  - 2.2.3 Spatio-temporal grid functions and finite difference operators . . . 26
  - 2.2.4 FD scheme for the 1D wave equation . . . 31
  - 2.2.5 FD scheme for the stiff string equation . . . 38

3 Time-domain modelling of frequency-dependent damping in linear strings 45
- 3.1 Introducing losses into the linear stiff string model . . . 46
- 3.2 A review of damping mechanisms in linear strings . . . 47
  - 3.2.1 Cuesta and Valette's study . . . 47
  - 3.2.2 Air viscosity . . . 49

3.2.3 Viscoelasticity . . . 52
3.2.4 Thermoelasticity . . . 54
3.2.5 Summary . . . 55
3.3 Frequency-dependent loss in the time domain: framework, principles, and past models . . . 57
3.3.1 Characteristic equation . . . 57
3.3.2 Condition for passivity . . . 58
3.3.3 Condition for realisability . . . 58
3.3.4 Existing models . . . 59
3.3.5 Approximating the impedance with Foster structures . . . 60
3.4 Optimising the approximations . . . 61
3.4.1 Fitting to the impedance Z_{th} . . . 62
3.4.2 Fitting to the decay rate σ_{th} . . . 63
3.4.3 Validity of the approximations . . . 65
3.4.4 Optimisation . . . 66
3.5 Space-time domain system . . . 69
3.5.1 The infinite string . . . 69
3.5.2 Boundary conditions . . . 70
3.6 Time-domain simulations . . . 71
3.6.1 An interleaved FD scheme . . . 71
3.6.2 Boundary conditions and matrix form . . . 71
3.6.3 Energy analysis and stability condition . . . 73
3.6.4 Scheme update . . . 74
3.7 Simulation results and analysis . . . 76
3.7.1 Reproduction of the theoretical Q-factors . . . 76
3.7.2 Discrete power balance and invariant quantity . . . 80

4 Playing the string: a two-polarisation bowed, stopped string model 83
4.1 Interacting with a string . . . 83
4.2 Model description . . . 84
4.2.1 A two-polarisation model . . . 84
4.2.2 Vertical polarisation . . . 86
4.2.3 Horizontal polarisation . . . 91
4.2.4 Energy analysis . . . 96
4.3 Finite difference scheme . . . 99
4.3.1 Localising interactions in the discrete spatial domain . . . 100
4.3.2 Vertical polarisation . . . 101
4.3.3 Horizontal polarisation . . . 103
4.3.4 Energy and stability analysis . . . 105
4.3.5 Scheme update: vertical polarisation . . . 107
4.3.6 Scheme update: horizontal polarisation . . . 108
4.4 Simulation results . . . 113

5 Control and gesture-based sound synthesis 121
5.1 Control parameter space and playability of the virtual bowed string 122
5.1.1 The concept of playability of a bowed string instrument 122
5.1.2 The force-force control parameters 124
5.1.3 Exploring the parameter space: a numerical experiment 125
5.1.4 Results 126
5.1.5 A tool for sound synthesis control 131
5.2 Gesture reproduction for sound synthesis 132
5.2.1 Summary of the control parameters 132
5.2.2 Example gestures 133

6 Conclusions and perspectives 139
6.1 Summary and contributions 139
6.2 Open questions 140
6.2.1 Frequency-dependent losses in the linear string 140
6.2.2 Impact parameters 141
6.2.3 Friction force 141
6.2.4 Aliasing 142
6.3 Perspectives and further work 142

Appendix A Maximum bow force and pitch flattening: relation with Friedlander's analysis 145

List of Tables

2.1 Tension T, inharmonicity factor B, and modal frequencies f_m for the modes of a violin A string and a cello D string, in the absence or presence of stiffness. The pitch deviation Δp (cents) is given for each mode of both strings, between the stiff string and the non-stiff string. — Parameters: see Violin A string and Cello D string on page xxix. 19

3.1 Computation times for 1 second of output ($F_s = 44.1$ kHz) in MATLAB, each averaged over 10 simulation runs, with different randomised initial conditions. Substantial speedup is achieved by employing fewer damping terms. — Parameters: see page xxix. 79

List of Figures

2.1 Small string element dx under tension. 8

2.2 Snapshots of the propagation of a pulse along an ideal string (top), a stiff string with low stiffness (middle, $E = 1 \times 10^{10}$Pa), and with high stiffness (bottom, $E = 2 \times 10^{11}$Pa). In the absence of stiffness, the pulse propagates without changing shape; however, the stiffness term introduces dispersion, and high frequency components start to lead low frequencies. — Parameters: $L = 1$ m, $T = 100$ N, $\rho = 7850$ kg/m^3, $r = 0.5$ mm. 16

2.3 Basic digital waveguide diagram. A bidirectional M-sample delay line contains sampled versions of the backward- and forward-going waves, as defined in (2.4). A filter at the string termination can be used to model frequency-dependent phenomena. 21

2.4 Action of e_{t-} and e_{t+} on the value of $u(t)$ evaluated at time step n (i.e. at $t = nk$). The dark red outline denotes the point around which the operator is centred; the orange fill denotes the points used by the operator. 24

2.5 From left to right: stencils of δ_{t-} and μ_{t-}, δ_{t+} and μ_{t+}, $\delta_{t\cdot}$ and $\mu_{t\cdot}$, and δ_{tt}, over the temporal grid, when centred on time step n. 26

2.6 From top-left to bottom-right, in reading order: stencils of δ_{x-}, δ_{x+}, δ_{xx}, and δ_{xxxx} on the spatio-temporal grid, when centred on time step n and grid point l. 27

2.7 Stencils of the operators $\delta_{t\cdot}\delta_{xx}$ (left) and $\delta_{t-}\delta_{xx}$ (right) over the space-time discrete grid, when centred on time step n and grid point l. 28

2.8 Snapshots of the simulation of the propagation of a pulse with the proposed scheme for the 1D wave equation, where the grid spacing has been set just under its minimal stable value, such that $\frac{h_{\text{min}}}{h} = 1.005$. — Parameters: $L = 1$ m, $T = 500$ N, $\rho = 7850$ kg/m^3, $r = 0.5$ mm, $F_s = 44.1$ kHz. 35

2.9 Left: numerical dispersion relation $\omega(\beta)$ for Scheme (2.61) for the 1D wave equation, in 3 different conditions: $\frac{h_{\text{min}}}{h} = 1$ (in solid dark blue; this is in fact the continuous dispersion relation), $\frac{h_{\text{min}}}{h} = 0.95$ (in dashed medium blue), and $\frac{h_{\text{min}}}{h} = 0.7$ (in dotted light blue). Note the significantly lowered cutoff frequencies when operating away from the stability limit; about half of the total bandwidth is lost for $\frac{h_{\text{min}}}{h} = 0.7$. Right: propagation of a pulse simulated with $\frac{h_{\text{min}}}{h} = 0.7$; note that high frequencies are trailing behind the main pulse. — Parameters: $L = 1$ m, $T = 400$ N, $\rho = 7850$ kg/m^3, $r = 0.5$ mm, $F_s = 44.1$ kHz. 36

2.10 Stencil of the proposed FD scheme for the 1D wave equation. The filled red circle denotes the location of the updated grid value; as its calculation only depends on values at previous time steps (i.e., there are no yellow circles on the $n + 1$ line), the scheme is explicit. 37

2.11 Top: total numerical energy $\mathrm{H}_{w,s}^n$ (in dark blue), sum of the kinetic (in light blue) and potential (in green) energy terms. Bottom: normalised energy variations of $\mathrm{H}_{w,s}^n$ relative to $\mathrm{H}_{w,s}^0$; due to floating-point rounding errors, $\mathrm{H}_{w,s}^n$ deviates by a few bits either side of $\mathrm{H}_{w,s}^0$ as the simulation progresses. The energy is therefore said to be conserved to machine accuracy. — Parameters: $L = 1$ m, $T = 100$ N, $\rho = 7850$ kg/m^3, $r = 0.5$ mm, $F_s = 44.1$ kHz. 38

2.12 Numerical dispersion relation $\omega\left(\beta\right)$ for Scheme (2.81) for the stiff string equation, in 3 different conditions: $h = h_{\text{min}}$ (in solid dark blue, at the stability limit), $\frac{h_{\text{min}}}{h} = 0.95$ (in dashed medium blue), and $\frac{h_{\text{min}}}{h} = 0.7$ (in dotted light blue). The solid black curve corresponds to the dispersion relation in the continuous case. Note that at the stability limit, even though there is no loss of bandwidth, numerical dispersion still occurs. — Parameters: $L = 1$ m, $T = 400$ N, $\rho = 7850$ kg/m^3, $r = 0.5$ mm, $E = 200$ GPa, $F_s = 44.1$ kHz. 41

2.13 Stencil of the proposed FD scheme for the stiff string equation. The calculation of the grid value at time step $n + 1$ (in red) only requires points at past time steps (in yellow); the scheme is explicit. 42

2.14 Top: total numerical energy $\mathrm{H}_{w,s}^n$ (in dark blue), sum of the kinetic energy (in light blue), potential energy due to tension (in green), and potential energy due to stiffness (in orange). Bottom: normalised energy variations of $\mathrm{H}_{w,s}^n$ relative to $\mathrm{H}_{w,s}^0$. As in the case of the ideal string, the discrete energy is conserved to machine accuracy. — Parameters: $L = 1$ m, $T = 100$ N, $\rho = 7850$ kg/m^3, $r = 0.5$ mm, $E = 200$ GPa, $F_s = 44.1$ kHz. 43

3.1 Diagram (not drawn to scale) of a cross-section of the string, oscillating along the z-axis at frequency ω, and resulting tangential air flow velocity profile $U(R, \theta, \omega)$ along the R-axis (in green). The viscous shear force F_{a} exerted by the air onto the string (in red) is proportional to the flow velocity gradient $\partial_R U$ at the string surface. Viscous phenomena may be considered to be confined to a thin boundary layer, the thickness of which depends on the frequency of the string oscillations. . 50

3.2 Stiff string element sustaining a bending strain. The compressed part (in red) heats up, the expanded part (in blue) cools down. The large red arrows represent heat conduction from warmer to cooler areas; the smaller arrows, pointing downwards, represent heat conduction from the string surface into the air. 54

3.3 Left: impedances (real part) as a function of frequency, as derived in [113], with contributions from: air viscosity (in green); viscoelasticity (in red); thermoelasticity (in orange); all three phenomena (in brown). Right: Q-factors as a function of frequency, with contributions from: air viscosity (in green); viscoelasticity (in red); both air viscosity and viscoelasticity (in orange); all three phenomena (in brown). — Parameters: see Cello D string on page xxix. The two unknown parameters were adjusted to $Q_{\mathrm{t}} = 18,000$, $\zeta_{\mathrm{v}} = 0.003$ [113]. 56

3.5 Real part of $\Gamma_q(j\omega)$ (left, in red) and $\beta^2 \Xi_{q'}(j\omega)$ (right, in blue), as a function of frequency, for a range of $a_q, b_q, a'_{q'}, b'_{q'}$ values. The dispersion relation $\beta(\omega)$ is that of a lossless string. — Parameters: see Cello D string on page xxix. The free parameters are logarithmically spaced, taking values within the following ranges: $b_q = 10^{-5}$—10^{-2}, $a_q = 50$—10^4, $b'_{q'} = 10^{-5}$—10^{-3}, and $a'_{q'} = 500$—2×10^5. For reference, each a_q-b_q pair is indicated on the left plot, by a dot on each corresponding curve; note that b_q plays the role of a gain factor, while a_q can be interpreted as a cutoff frequency. 62

3.6 Top: dispersion relation $\beta(\omega)$, as per (2.27) (in black) and (3.41) (in green), with parameters as indicated in the text. Bottom: error $\Delta\beta \triangleq \left|\frac{\beta - \beta_{\boldsymbol{\chi}}}{\beta}\right|$, in percent. The corrections brought by $Z_{\boldsymbol{\chi}}$ to the dispersion relation are minimal; the simplified relation (2.27) is a satisfactory approximation to $\beta(\omega)$. — Parameters: see Cello D string on page xxix. 65

3.7 Left: smallest decay rate associated with $Z_{\boldsymbol{\chi}}$, as a function of frequency, obtained with a root-finding algorithm on (3.36) (in solid black), and with the first-order approximation (3.37) (in dashed green). Right: relative error $\Delta\sigma$ between the root and its approximation. The true root and the first order approximation differ at most by 0.1%. — Parameters: see Cello D string on page xxix. The damping parameters were inferred from preliminary calculations; here, $M = 5$ ($a_1 = 0$), $M' = 2$. 66

3.8 Optimised $Q_{\boldsymbol{\chi}}$ and relative error ΔQ (left plot), with the corresponding $\mathrm{Re}\left(Z_{\boldsymbol{\chi}}(j\omega)\right)$ (right plot), for a violin A string (top), a cello D string (middle), and a double bass A string (bottom). Figures on the left illustrate a fit with the fewest possible terms such that $\Delta Q \leqslant 1\%$ over the frequency range. Figures on the right illustrate the best fit obtained. $Q_{\mathrm{th}}(\omega)$, $\mathrm{Re}\left(Z_{\mathrm{th}}(j\omega)\right)$ are drawn in black; $Q_{\boldsymbol{\chi}}(\omega)$, $\mathrm{Re}\left(Z_{\boldsymbol{\chi}}(j\omega)\right)$ are drawn in purple; each participating Γ_q term is drawn in red (Γ_1 in dark red, as $a_1 = 0$), and each $\Xi_{q'}$ term in blue (Ξ_1 in dark blue, as $a'_1 = 0$). — Parameters: see page xxix. 67

3.9 Top: Q-factors computed from time-domain simulations, for the violin A string (left), the cello D string (middle), and the double bass A string (right) presented in Section 3.4, superimposed with the theoretical loss profile Q_{th} (in grey). The orange crosses correspond to simulations performed with the minimal number of $\boldsymbol{\gamma}_q^{n+1/2}$, $\boldsymbol{\xi}_{q'}^{n+1/2}$ yielding an acceptable fit (see Figure 3.8, left figures). The green circles correspond to simulations performed with the best fit obtained for each string (see Figure 3.8, right figures). Bottom: error $\Delta Q \triangleq \left|\frac{Q_{\mathrm{th}}-Q_{\mathbf{x}}}{Q_{\mathrm{th}}}\right|$, in percent. — Parameters: see page xxix; $F_s = 44.1$ kHz. 77

3.10 Normalised time-domain output waveform computed for a violin A string (top), a cello D string (middle), and a double bass A string (bottom). Three time frames are presented for each string, starting respectively at initial time (left), 1 second later (middle), and 2 seconds later (right). Each plot contains two waveforms, each corresponding to fewer or more impedance terms, colour-coded as in Figure 3.9. — Parameters: see page xxix; $F_s = 44.1$ kHz. 78

3.11 Q-factors measured on simulations of a violin A string: detail. 79

3.12 Top: total energy E^n for the cello D string (in black), sum of the stored energy H_w^n (in orange) and the cumulated dissipated powers $k\sum_{p=1}^{n}\mathrm{Q}_{w,\gamma}^{p}$ (in pink) and $k\sum_{p=1}^{n}\mathrm{Q}_{w,\xi}^{p}$ (in light blue). Bottom: normalised energy variations of E^n relative to H_w^0. — Parameters: see Cello D string on page xxix; $F_s = 44.1$ kHz, $M = 4$, $M' = 3$. The corresponding loss profile can be seen in Figure 3.9, top centre plot. 80

4.1 String displacement in two polarisations. The displacement $y(x,t)$ in the horizontal polarisation is parallel to the plane formed by the bow and the string; the displacement $w(x,t)$, in the vertical polarisation, is orthogonal to this plane. 85

4.2 Visualisation of the deformation variables $\Delta_{\mathcal{F}}$ and $\Delta_{\mathcal{B}}$. Top: $\Delta_{\mathcal{F}}(t)$ represents the distance by which the fingertip deforms upon contact with the string surface. Bottom: $\Delta_{\mathcal{B}}(t)$ can be interpreted as the deformation of the flexible bow hair against the string. 89

4.3 Diagram summarising the forces applied onto the string by the finger, bow, and fingerboard, in the vertical polarisation. 91

4.4 Description of a stick-slip cycle in the Helmholtz regime. The bow (in red) is moving upwards. A solid green circle indicates that the bow is sticking to the string; a dashed circle indicates slipping in the direction of the black arrow. The green arrows indicate the travel direction of the Helmholtz corner. As indicated by the grey arrow, the figures should be read clockwise. 93

4.5 Friction curve $\varphi_{\mathcal{B}}\left(v_{\mathrm{rel},\mathcal{B}}\right)$ for the bow, from [100]. 94

4.6 Coulomb step friction curve $\varphi_{\mathcal{N},\mathcal{F}}\left(v_{\mathrm{rel},\mathcal{N},\mathcal{F}}\right)$ for the finger and fingerboard. 95

4.7 Diagram summarising the forces applied onto the string by the finger, bow, and fingerboard, in the horizontal polarisation. The tangential friction forces arise from the normal contact forces described in Section 4.2.2. 97

4.8 Magnitude of $\sigma_{\mathcal{F}}^n$ relative to that of $\sigma_{\mathcal{B}}^n$, as a function of distance between the bow and finger contact points, for a simulated cello D string. The magnitude of $\sigma_{\mathcal{F}}^n$ decays exponentially with increasing distance. The friction force exerted by a finger a few centimetres away from the bowing point is negligible in the calculation of the bow friction force. — Parameters: see Cello D string on page xxix; $F_s = 44.1$ kHz. 110
4.9 Friedlander's graphical construction to solve for the bow relative velocity. The solutions for $v_{\text{rel},\mathcal{B}}^n$ lie at the intersections of the friction curve $\varphi_{\mathcal{B}}$ (in black) and the straight line $\eta_{\mathcal{B}}$; three cases are illustrated, with a different intercept value. In case (a), in blue, the solution is given by $v_{\text{rel},\mathcal{B}}^n = 0$; the bow is sticking to the string. In case (b), in green, the solution for $v_{\text{rel},\mathcal{B}}^n$ is strictly positive; the string is slipping against the bow. Under certain conditions (case (c), in red), there are multiple solutions to Equation (4.76); this ambiguity is resolved by choosing the solution on the same branch of φ_B as the previous time step. (i) corresponds to the sticking phase; (ii) corresponds to the slipping phase; (iii) is physically unstable, and not seen in bowed string motion [75]. 111
4.10 Top row: energy balance plots for a 2-second simulation of a bowed cello D string, with a stopping finger pressing the string against the fingerboard. The vertical polarisation is shown on the left, the horizontal polarisation on the right. For each polarisation, the energy and cumulated power is shown for the string (in green), the bow (in red), the finger (in blue), and the fingerboard (in orange); the total energy and cumulated power is drawn in black (note that, for the horizontal polarisation, the black curve is masked by the blue curve). Middle row: on the same time scale, force control signals for the bow (in red) and the finger (in blue), in each polarisation. Bottom row: locations $x_{\mathcal{B}}$, $x_{\mathcal{F}}$ of the bow and finger (same for both polarisations). — Sample rate: $F_s = 44.1$ kHz. 116
4.11 Energy transfers in the vertical polarisation during a 2-second simulation (top), with visualisations of the system state (not to scale) at different timestamps. The shadow of the string displacement in the vertical polarisation is displayed in grey, at the back of the graph. 117
4.12 Energy transfers in the horizontal polarisation during a 2-second simulation (top), with visualisations of the system state (not to scale) at different timestamps. The shadow of the string displacement in the horizontal polarisation is displayed in grey, at the bottom of the graph; the fingerboard is transparent. Timestamps are the same as that shown for the vertical polarisation in Figure 4.11. 118
4.13 Variations of R_w^n (top, vertical polarisation) and R_u^n (bottom, horizontal polarisation) away from 1; small values indicate that the numerical energy is indeed balanced. 119

5.1 Schelleng diagram, reproduced from [90], showing the minimal and maximal downwards bow forces delimiting the Helmholtz playable region, as a function of the bow-bridge distance, for a given bow velocity. 123

5.2 Bow control for the present model is characterised by the magnitude $\left|\vec{f}_{\mathrm{ext}\mathcal{B}}\right|$ and angle θ of an external resultant force vector applied onto the bow. 124

5.3 An example playability-force diagram. Each marker on the left plot represents one simulation, performed with one combination of transverse and normal bow force. Each simulation was examined 1.8 s after initial application of the horizontal bow force, and categorised into one of four playing regimes (excluding constant sticking and constant slipping). Typical string displacement and associated relative velocity waveforms are shown for each of the four detected regimes. The diagonal black and blue lines on the diagram respectively mark the estimated minimum and maximum bow force angles, between which Helmholtz motion is reliably obtained in the simulation, regardless of bow force magnitude. — Parameters: see Cello D string on page xxix. — Figure reproduced from [31]. 125

5.4 Playability-force diagrams for different bowing positions. The axes have been adjusted so that zero force is at the top right of each plot, so as to reflect the diagram shown in Figure 5.2. Note that, while the bow force vector angle changes, rotation of the bow itself is not implied. — Parameters: see Cello D string on page xxix. — Figure reproduced from [31]. 128

5.5 Relative membership counts for detected playing regimes, plotted against decreasing bow-bridge distance. — Figure reproduced from [31]. 129

5.6 Estimated minimum, maximum, and implied range of bow force angles that produce reliable Helmholtz motion, as a function of bow position. — Figure reproduced from [31]. 129

5.7 Spectrogram (1st plot) of the synthetic sound produced by bowing a violin A string with varying bow position $x_{\mathcal{B}}^{n}$ (2nd plot), bow downwards force $f^{n}_{\mathrm{ext}\mathcal{B},(w)}$ (3rd plot), and bow tangential force $f^{n}_{\mathrm{ext}\mathcal{B},(w)}$ (4th plot). (i) Higher harmonics appear when increasing the bow force and bowing closer to the bridge. (ii) An increase in bow tangential force does not influence the spectral content of the sound, but globally increases its amplitude. (iii) The free string oscillations decay as soon as the bow is lifted up, at frequency-dependent rates. — Parameters: see Violin A string on page xxix. 134

5.8 Top: spectrogram of the bowed first harmonic on a violin A string. Bottom: simulation snapshot, showing the bow and finger positions. — Parameters: see Violin A string on page xxix. 135

5.9 Top: spectrogram of a synthesised gesture, showing a glissando along a cello D string followed by a vibrato; the stopped string vibrations are then left to decay. Bottom: corresponding finger position along time. — Parameters: see Cello D string on page xxix. 136

5.10 Large amplitude oscillations of a violin A string, resulting in repeated collisions and friction with the fingerboard. Top: vertical polarisation; bottom: horizontal polarisation. The grey vertical lines mark times when the string is anywhere in contact with the fingerboard; the red lines denote contact events at the readout position ($x = {}^{L}\!/_{2}$). The displacement of the string was initialised with the shape of the fundamental transverse mode, in both polarisations, to emulate a “diagonal” pluck; collision and friction both generate higher partials. — Parameters: see Violin A string on page xxix. 137

List of Symbols

Physical parameters

	Symbol	**Units**	**Description**
String	ρ	kg.m^{-3}	Mass density
	S	m^2	Cross-sectional surface area
	T	N	Tension
	E	Pa	Young's modulus
	I_0	m^4	Area moment of inertia
	b_q, $q = 1, \ldots, M$	kg.m^{-1}.s^{-1}	Damping parameters (gain)
	$b'_{q'}$, $q' = 1, \ldots, M'$	kg.m.s^{-1}	Damping parameters (gain)
	a_q, $q = 1, \ldots, M$	s^{-1}	Damping parameters (resonant freq.)
	$a'_{q'}$, $q' = 1, \ldots, M'$	s^{-1}	Damping parameters (resonant freq.)
Fingerboard	$K_{\mathcal{N}}$	—	Stiffness parameter
	$\alpha_{\mathcal{N}}$	—	Power law exponent for impact force
	$\beta_{\mathcal{N}}$	—	Nonlinear impact damping coefficient
	$\varepsilon(x)$	m	Distance between string and fingerboard; action of the instrument
	$\mu_{\mathcal{N}}$	—	Friction coefficient
Finger	$K_{\mathcal{F}}$	—	Stiffness parameter
	$\alpha_{\mathcal{F}}$	—	Power law exponent for impact force
	$\beta_{\mathcal{F}}$	—	Nonlinear impact damping coefficient
	$M_{\mathcal{F}}$	kg	Mass
	$\lambda_{\mathcal{F}}$	kg.s^{-1}	Linear damping coefficient
	$\mu_{\mathcal{F}}$	—	Friction coefficient
Bow	$K_{\mathcal{B}}$	—	Stiffness parameter
	$\alpha_{\mathcal{B}}$	—	Power law exponent for impact force
	$\beta_{\mathcal{B}}$	—	Nonlinear impact damping coefficient
	$M_{\mathcal{B}}$	kg	Mass
	$\lambda_{\mathcal{B}}$	kg.s^{-1}	Linear damping coefficient

Continuous differential operators

Symbol	Alternative notation	Description
$\partial_t^m \bullet$	$\frac{\partial^m \bullet}{\partial t^m}$	m^{th} order partial time differentiation
$\partial_x^m \bullet$	$\frac{\partial^m \bullet}{\partial x^m}$	m^{th} order partial spatial differentiation
$\dot{\bullet}$	$\frac{d\bullet}{dt}$	First order total time differentiation
$\ddot{\bullet}$	$\frac{d^2\bullet}{dt^2}$	Second order total time differentiation

Discrete operators

k is a time step (s), and h a grid spacing (m).

Temporal operator	Construction	Approximates	Accuracy
$e_{t\pm}$	Backward and forward time shift		
$\mu_{t\pm}$	$\frac{e_{t\pm}+1}{2}$	1, identity	$O(k)$
$\mu_{t\cdot}$	$\frac{e_{t+}+e_{t-}}{2}$	1, identity	$O(k^2)$
δ_{t+}	$\frac{e_{t+}-1}{k}$	$\frac{d}{dt}$, ∂_t	$O(k)$
δ_{t-}	$\frac{1-e_{t-}}{k}$	$\frac{d}{dt}$, ∂_t	$O(k)$
$\delta_{t\cdot}$	$\frac{e_{t+}-e_{t-}}{2k}$	$\frac{d}{dt}$, ∂_t	$O(k^2)$
δ_{tt}	$\delta_{t+}\delta_{t-}$	$\frac{d^2}{dt^2}$, ∂_t^2	$O(k^2)$

Spatial operator	Construction	Approximates	Accuracy
$e_{x\pm}$	Backward and forward space shift		
δ_{x+}	$\frac{e_{x+}-1}{h}$	$\frac{d}{dx}$, ∂_x	$O(h)$
δ_{x-}	$\frac{1-e_{x-}}{h}$	$\frac{d}{dx}$, ∂_x	$O(h)$
$\delta_{x\cdot}$	$\frac{e_{x+}-e_{x-}}{2h}$	$\frac{d}{dx}$, ∂_x	$O(h^2)$
δ_{xx}	$\delta_{x+}\delta_{x-}$	$\frac{d^2}{dx^2}$, ∂_x^2	$O(h^2)$
δ_{xxxx}	$\delta_{xx}\delta_{xx}$	$\frac{d^4}{dx^4}$, ∂_x^4	$O(h^2)$

Acronyms

1D	one-dimensional
2D	two-dimensional
3D	three-dimensional
ALF	anomalous low frequencies
DOF	degree of freedom
DW	digital waveguide
FD	finite difference
IBP	integration by parts
LHS	left hand side
ODE	ordinary differential equation
PDE	partial differential equation
RHS	right hand side
SBP	summation by parts

Table of physical parameters

String physical parameters

The following table contains measured physical parameters on violin, viola, cello, and double bass strings, taken from the literature. In particular, for the violin, viola, and cello strings, parameters are extracted from the work of two authors. Pickering [82] performed measurements on isolated strings; in contrast, Percival [81], estimated physical constants from measurements on strings mounted on the instrument. For the double bass strings, the data was extracted from an unpublished report by Guettler [44][1]; the strings are assumed to have a solid steel core.

L is the string speaking length, ρ_L is the linear mass density, r is the string radius, T the tension, and E Young's modulus. Parameters are given for each of the four strings of each instrument, in orchestral tuning.

Instrument	**String**	**Parameters**			
		ρ_L (g.m^{-1})	r (mm)	T (N)	E (GPa)
Violin	E5	0.41	0.165	73.0	62.5
($L = 32$ cm)	A4	0.72	0.30	57.10	19.5
	D4	1.61	0.44	56.88	4.56
	G3	2.79	0.425	43.90	4.79
Viola	A4	0.82	0.18	91.7	81.3
($L = 38$ cm)	D4	1.26	0.22	62.78	55.3
	G3	2.17	0.335	48.15	8.01
	C3	4.87	0.36	48.13	18.1
Cello	A3	1.66	0.375	153.0	25.0
($L = 69$ cm)	D3	2.50	0.44	102.6	25.0
	G2	6.16	0.605	112.67	8.6
	C2	21.2	0.72	172.74	22.4

---

[1] Accessed on `http://knutsacoustics.com/files/Typical-string-properties.pdf`.

		ρ_L (g.m^{-1})	r (mm)	T (N)	E (GPa)
Double bass	G2	6.62	0.518	285.53	200
($L = 106$ cm)	D2	12.04	0.699	291.54	200
	A1	22.16	0.95	301.35	200
	E1	40.72	1.286	310.65	200

In order to account for the stiffness of wound strings, it is assumed that only the string core contributes to bending stiffness. The radius of the core is approximated as half of the total string radius.

Finger, fingerboard, and bow parameters

This table contains the parameter values employed in simulations involving the left-hand finger, fingerboard, and bow. These values have simply conjectured from trial and error, and have not been calibrated against experimental measurements; they are given here on an indicative basis.

Object			**Parameters**		
	K	α	β	M (kg)	λ (kg.s^{-1})
Bow	10^5	2.0	20.0	0.1	20.0
Finger	10^3	2.5	50.0	0.02	30.0
Fingerboard	10^8	1.5	10.0	—	—

String damping parameters

The following table contains the optimised values (rounded to the 5th significant digit) of the damping parameters for the violin A string, cello D string, and double bass A string, as presented in Chapter 3. Two parameter sets are given for each string: one corresponds to a fit with the fewest possible terms to ensure at most 1 % error over the frequency range, the other corresponds to the best possible fit obtained within the bounds of the study (see Figure 3.8).

Violin A string		**Cello D string**		**Double bass A string**	
$M = 4, M' = 2$		$M = 4, M' = 3$		$M = 3, M' = 3$	
a_q	b_q	a_q	b_q	a_q	b_q
0	$2.0360 \cdot 10^{-4}$	0	$2.3551 \cdot 10^{-4}$	0	$4.1649 \cdot 10^{-4}$
195.16	$1.7009 \cdot 10^{-4}$	141.95	$2.0340 \cdot 10^{-4}$	149.35	$6.4399 \cdot 10^{-4}$
1256.2	$4.2716 \cdot 10^{-4}$	725.57	$4.6739 \cdot 10^{-4}$	782.44	$1.9072 \cdot 10^{-3}$
7262.9	$1.1841 \cdot 10^{-3}$	3340.6	$1.1987 \cdot 10^{-3}$		
$a'_{q'}$	$b'_{q'}$	$a'_{q'}$	$b'_{q'}$	$a'_{q'}$	$b'_{q'}$
0	$2.7807 \cdot 10^{-7}$	0	$1.1126 \cdot 10^{-6}$	0	$1.0232 \cdot 10^{-5}$
17849	$8.8931 \cdot 10^{-7}$	48832	$2.1316 \cdot 10^{-4}$	16358	$2.7228 \cdot 10^{-5}$
		193909	$5.7803 \cdot 10^{-4}$	87732	$7.6782 \cdot 10^{-5}$
$M = 8, M' = 3$		$M = 8, M' = 5$		$M = 7, M' = 8$	
a_q	b_q	a_q	b_q	a_q	b_q
0	$1.7271 \cdot 10^{-4}$	0	$1.9454 \cdot 10^{-4}$	0	$2.9291 \cdot 10^{-4}$
61.068	$6.2519 \cdot 10^{-5}$	50.078	$8.2549 \cdot 10^{-5}$	44.237	$1.9869 \cdot 10^{-4}$
184.12	$8.0223 \cdot 10^{-5}$	138.08	$9.7381 \cdot 10^{-5}$	114.99	$2.4028 \cdot 10^{-4}$
469.71	$1.2491 \cdot 10^{-4}$	314.55	$1.4336 \cdot 10^{-4}$	243.62	$3.6402 \cdot 10^{-4}$
1158.4	$2.0375 \cdot 10^{-4}$	688.42	$2.2492 \cdot 10^{-4}$	492.89	$5.9102 \cdot 10^{-4}$
2820.7	$3.4127 \cdot 10^{-4}$	1487.1	$3.6356 \cdot 10^{-4}$	982.22	$9.6259 \cdot 10^{-4}$
6807.3	$5.8041 \cdot 10^{-4}$	3186.1	$5.8998 \cdot 10^{-4}$	1939.4	$1.3557 \cdot 10^{-3}$
16259	$9.1082 \cdot 10^{-4}$	6757.5	$8.4783 \cdot 10^{-4}$		
$a'_{q'}$	$b'_{q'}$	$a'_{q'}$	$b'_{q'}$	$a'_{q'}$	$b'_{q'}$
0	$2.3745 \cdot 10^{-7}$	0	$9.8734 \cdot 10^{-7}$	0	$8.7062 \cdot 10^{-6}$
27522	$9.0451 \cdot 10^{-7}$	29025	$6.5626 \cdot 10^{-7}$	7329.0	$4.4485 \cdot 10^{-6}$
92137	$2.6571 \cdot 10^{-7}$	383106	$7.2425 \cdot 10^{-6}$	13543	$1.0756 \cdot 10^{-5}$
		56083	$1.4029 \cdot 10^{-6}$	25281	$1.4413 \cdot 10^{-5}$
		121544	$2.2910 \cdot 10^{-6}$	48776	$1.9607 \cdot 10^{-5}$
				100287	$3.1192 \cdot 10^{-5}$
				222022	$2.4261 \cdot 10^{-5}$
				342343	$9.1038 \cdot 10^{-5}$

Chapter 1

Introduction

Sound synthesis techniques for string instruments have evolved, since the mid-20th century, from abstract synthesis [61] (wavetables, FM synthesis...) towards sampling synthesis, making use of vast libraries of pre-recorded sounds, and physical models, directly emulating the behaviour of the instruments. To this day, the most faithful synthesised sound quality is achieved by sampling techniques; however, their relative inflexibility, together with the potentially very large storage requirements for sound libraries, form a convincing case for the consideration of physical models.

Beyond storage concerns, the use of a physical model allows for great flexibility of the input parameters (typically, the instrument's geometrical and material properties, together with the player's gestural controls), and of the output parameters, usually akin to "listening conditions", which can be changed freely and dynamically along a simulation. This is a clear advantage with respect to synthesis produced with statically recorded samples, particularly for continuously excited instruments, for which the control parameters are varied throughout the production of a note, significantly changing the timbre. In this context, physical modelling sound synthesis has been an active research area, with promising results.

The work presented in this thesis is in line with this physics-based approach to sound synthesis. Throughout this manuscript, a physical model of a bowed string system is presented, in two polarisations. A sound synthesis algorithm is derived from the discretisation of the equations of motion in the space-time domain, taking advantage of the flexibility of control offered by physical modelling methods. A wide array of gestures can then be simulated, with only a handful of dynamically updated control parameters. Before diving into the depths of the numerical model, this introductory section outlines the objectives and structure of the thesis.

1.1 Physics-based synthesis of stringed instruments

Physical modelling synthesis for strings debuted in the 1970s, with the use of time-stepping methods to discretise and directly solve the 1D wave equation [89, 52, 4]. However, the very limited computational power available at the time ruled out the simulation of systems at audio sample rates in any reasonable amount of time. The next generation of numerical models therefore focused on algorithmic simplification, through physically plausible assumptions. Although not designed as a physical modelling algorithm, the Karplus-Strong string synthesis method [59, 57] was the basis for later generalisation to the digital waveguide (DW) framework [101, 102]; a comprehensive review of these models for string sound synthesis can be found in [58]. The fast execution of these algorithms, together with the realism of the synthetic sound output, made them particularly well-suited for bowed string modelling, and they are still, to this day, widely used for this purpose; see, e.g., [72, 73]. In a DW approach, the forward and backward travelling wave solutions along a string are modelled using delay lines, offering a simple and efficient strategy for certain linear time invariant systems. In particular, they are well suited for systems in one dimension, the behaviour of which is well described by the wave equation. Another class of physical models relies on the time harmonic solutions of the string equation [1]. The use of these so-called modal methods has been investigated for the study of bowed strings; see, e.g., [24]. A more in-depth review of the aforementioned physical modelling methods will be presented in Section 2.2.1.

Time-stepping methods, and more specifically finite difference methods [107], have regained appeal in musical sound synthesis (see, e.g., [8]), in part thanks to the accelerating increase in available computational power throughout the last two decades. A detailed history of the use of finite difference methods in numerical analysis since the pioneering 1928 paper by Courant *et al.* [22] can be found in [109]. String simulation in one dimension has successfully been implemented with time-stepping methods; see, e.g., [18, 7]. The system of partial differential equations describing the physical behaviour of the system is taken as a starting point, dispensing with requiring any assumptions on the form of the solution. This is particularly useful when nonlinear, time-varying, distributed interactions between the string and its environment are concerned, and analytical resolution is out of the question. This thesis is concerned with numerical simulation of the bowed string system; the finite difference method is a befitting approach to this problem.

1.2 The bow-string interaction

Numerical modelling of the strongly nonlinear friction force at the contact interface between a string and the layer of rosin coating the hair of a bow is extensively discussed in this thesis. The bow-string interaction has generated a vast body of literature, starting with the observations of Helmholtz in the 19th century [115], followed by the theoretical and experimental work of Raman in 1918 [86]. The simple introducing statement of Raman's paper would still likely gather agreement amongst many cited in this manuscript, the present author included, 100 years later:

> The vibration of stretched strings excited by bowing and their practical application in musical instruments of the violin class present many important and fascinating problems to the mathematician and the physicist.

A recent review paper by Woodhouse [118] offers a comprehensive history of the published literature on bowed string mechanics (and indeed, violin acoustics in general). The friction interaction between the string and the rosin-coated bow hair, in particular, remains an open problem. Recent work [41] has evaluated the state of the art in bow friction modelling, using both experimental and simulated results; amongst existing models, further reviewed in Section 4.2.3.ii, none was found to fit all experimental observations, although qualitative agreement was found with measurements in some aspects.

A bowing gesture can be described with a handful of dynamically varying parameters. Some of the most relevant are downwards force, bow velocity, and bow-bridge distance; musicians also make use of the tilt and angle of the bow with respect to the string in order to introduce nuances in the timbre of the produced note. Such parameters must be perfectly coordinated at all times to allow for the creation and sustain of a tone. Schelleng [90], following Raman's work [86], was the first to analytically prove that, under a number of simplifying assumptions, only a relatively narrow area of the bowing parameter space defined by the downwards force, transverse velocity, and bowing position gave rise to the characteristic stable Helmholtz motion [115] (see Figure 4.4) desired by most musicians. His work was revised by Schoonderwaldt [93], who reconsidered Schelleng's assumptions to include more refined elements of bowed string motion.

The characterisation of this narrow area in the bowing parameter space is tied to the concept of *playability* [117], the evaluation of which is a common empirical method used to validate bowed string physical models [96, 40, 97, 41]. A more playable instrument, physical or virtual, is generally characterised by the ease of access to the region of the parameter space yielding a stable note. Naturally, transient quality also constitutes a major part of playability; Guettler [45] investigated the relation between downwards bow force and bow acceleration, regarding the quality of initial transients, again under simplifying assumptions; their results were validated with simulated and experimental data by Woodhouse [119].

After Schelleng's work, an experimental study by Askenfelt [2, 3] yielded measured values for bowing control parameters on a violin. They were the first to develop a measuring rig able to record all playing parameters simultaneously, in a performance situation. More recently, the dynamic variations of these parameters during many different bowed string gestures were observed and analysed in great detail [25, 26, 69]. The control signals obtained from such studies can be mathematically reconstructed [70], or directly used, to be fed as excitation signals into a physical modelling algorithm such as the one presented in this work.

1.3 Thesis objectives

This thesis is concerned with the design and implementation of a numerical model of the bowed string system, emphasising the interactions of the string with the player. The main objective is to design a sound synthesis algorithm capable of realistically reproducing a wide range of bowed string gestures, controlled by physical parameters usually accessible and familiar to a musician.

In order to preserve maximal flexibility and versatility in handling control, the physical model shall rely on the fewest possible assumptions about the kinematic behaviour of the system, and instead rely on its dynamic description. The proposed numerical schemes shall be based upon equations of motion, and provide direct computation of the numerical solution of those equations, in the time domain, given a set of initial conditions, boundary conditions, and input control parameters. The algorithm must be stable under any excitation provided through these control parameters.

The linear behaviour of the isolated string must be reproduced accurately for a particular set of geometrical and material parameters. In particular, simulation of the free oscillations of the string shall reflect the frequency dependence of the decay times of the transverse modes of vibration. Adapting this frequency-domain loss profile to the proposed time-domain model is not necessarily straightforward; the work presented here shall describe a procedure to simulate realistic decay times, in a computationally tractable manner.

Many bowed string gestures make use of the compliance of the bow hair, allowing to bounce the bow against the string to produce short, sharp transients. The model shall be able to reproduce such behaviour; realistic damped impact modelling shall be employed, relying on a nonlinear description of the contact force between bow hair and string.

Other gestures are based on the movement of the left hand fingers along the fingerboard. To the author's knowledge, modelling of such gestures (*vibrato*, for instance) has only been attempted empirically, through filtering of the output sound; see, e.g., [105]. The proposed model shall include interaction of the string with a dynamic, absorbing fingertip, as well as a distributed, rigid fingerboard, allowing to play and smoothly transition between different stopped notes.

Through modelling of the frictional interaction between bow and string, the proposed algorithm shall simulate all known bowed string vibration regimes, within the expected bowing parameter ranges. Assessment of the simulated output provided by the algorithm shall rely, in part, on the evaluation of playability over the control parameter space.

1.4 Thesis outline

This manuscript is organised into four chapters. The next chapter introduces the mathematical background and notations employed throughout the rest of this thesis. The research contributions proposed in the present work, summarised in the conclusion, are presented in Chapters 3, 4, and 5.

Chapter 2 lays the foundations of the physical, mathematical, and numerical framework employed throughout this thesis. The 1D wave equation is first considered, before introducing a bending stiffness term. The discretisation of this simple string model into an energy-conserving finite difference scheme is then described, leading to a time-stepping algorithm providing an approximate numerical solution to the equations of motion.

Chapter 3 describes the time-domain modelling of frequency-dependent damping of the transverse string vibrations. The loss profile in the frequency-domain is described in terms of the physical parameters of the string [113]. In the time domain, the string displacement is coupled to a number of additional states, resulting in a frequency-dependent impedance, function of a set of free parameters. After optimising such parameters in order to fit the string's theoretical loss profile, the system of partial differential equations is discretised into a finite difference scheme, following the procedure outlined in Chapter 2. The quality factors of the string transverse modes are finally measured on simulated results, and compared to their target value, in order to assess the validity and accuracy of the numerical model.

Chapter 4 introduces nonlinear interaction of the string with a bow, a stopping finger, and a distributed fingerboard, in a dual-polarisation setting. In one polarisation, a nonlinear penalty impact model is employed to describe the contact forces between the string and the three objects. In the other polarisation, string motion is excited by pushing the bow across the string; the normal forces exerted by the bow, finger, and fingerboard then result in tangential friction forces. The bow friction characteristic leads to self-sustained oscillations, while the friction forces exerted in conjunction by the finger and fingerboard maintain the string in place, allowing the musician to play stopped notes.

Chapter 5 illustrates the use of the algorithm developed throughout the thesis for the synthesis of bowed string sounds. The available control parameters are the bow downwards force, transverse force, and position along the string, as well as the finger downwards force and location; they can all vary over time. The bowing parameter space is explored, in order to provide an initial evaluation of the playability of the proposed algorithm; graphical representations of the parameter space are compiled, to serve as a guiding hand for sound synthesis. Representative simulation examples are finally provided, in order to illustrate the potential of the bowed string numerical model to reproduce typical gestures, through the available set of control parameters.

List of publications

The work described in this thesis appeared in the following publications, in chronological order:

- [27] C. Desvages and S. Bilbao, "Physical modelling of nonlinear player-string interactions in bowed string sound synthesis using finite difference methods," in *Proc. Int. Symp. Mus. Acoust. (ISMA)*, Le Mans, France, 2014.

- [28] C. Desvages and S. Bilbao, "Two-polarisation finite difference model of bowed strings with nonlinear contact and friction forces," in*Proc. Int. Conf. Digital Audio Effects (DAFx)*, Trondheim, Norway, 2015.

- [29] C. Desvages and S. Bilbao, "Two-polarisation physical model of bowed strings with nonlinear contact and friction forces, and application to gesture-based sound synthesis," *Appl. Sci.*, vol. 6, no. 5(135), 2016.

- [30] C. Desvages, S. Bilbao, and M. Ducceschi, "Improved frequency-dependent damping for time domain modelling of linear string vibration," in *Proc. Int. Congr. Acoust.*, Buenos Aires, Argentina, 2016.

- [31] C. Desvages and M. Newton, “Bow control and playability of a two-polarisation time domain physical model of a bowed string,” in *Proc. Int. Symp. Mus. Room Acoust.*, Buenos Aires, Argentina, 2016.
- [78] F. Pantelić, C. Desvages, J. Prezelj, and D. Šumarac Pavlović, “Influence of bow-bridge distance on string timbre,”, in *Proc, 7th Congr. Alps Adria Acoust. Assoc. (AAAA 2016)*, Ljubljana, Slovenia, 2016.

Chapter 2

The linear string: equations of motion and numerical schemes

This preliminary chapter will introduce the formalism used in this manuscript, through a case study of the physical modelling and numerical simulation of a lossless isolated linear string. A selection of physics-based sound synthesis techniques will be reviewed, before focusing in depth on time-stepping numerical methods, specifically the finite difference (FD) method [107] which forms the basis of the synthesis work presented in this thesis. The equations of motion describing the temporal evolution of the string's transverse displacement will be used as the starting point for a FD algorithm, allowing to simulate the full system.

Section 2.1 will present the 1D wave equation and the Euler-Bernoulli lossless stiff string equation; energetic aspects and frequency-domain behaviour will be discussed. Section 2.2 will introduce the FD framework and notations used throughout the rest of this manuscript, by presenting numerical schemes for these two simplified cases.

2.1 Time-domain physical modelling of strings

2.1.1 The 1D wave equation

2.1.1.i Equation and general solutions

Consider the transverse displacement $w(x,t)$ of an infinite ideal string (in m), assuming negligible gravity, defined along spatial coordinate $x \in \mathbb{R}$ and time $t \in \mathbb{R}_{\geqslant 0}$. Let ρ be the string's material density (in kg/m^3), S the cross-sectional area (in m^2), and T the string tension along its axis (in N)[1].

The temporal evolution of $w(x,t)$ can be examined by applying Newton's 2nd law, in the transverse direction, to a small element dx of the string (see Figure 2.1), with mass $\rho S dx$ and

---

[1] A table of measured physical parameters on a variety of violin, viola, cello, and double bass strings is given on page xxix.

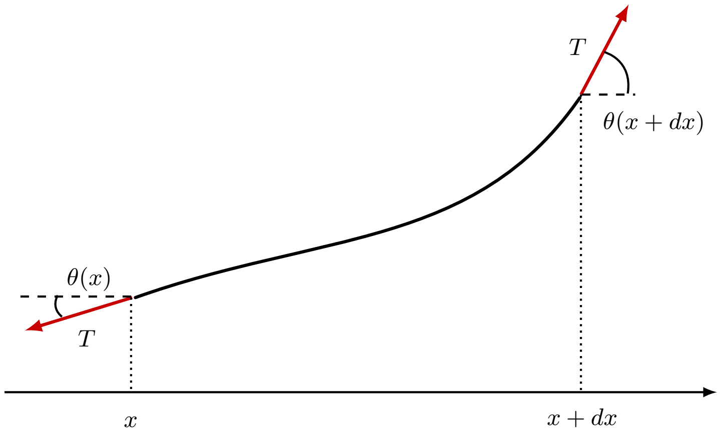

Figure 2.1: Small string element dx under tension.

acceleration a:

$$\rho S\,dx\,a = T\sin\left(\theta\left(x+dx\right)\right) - T\sin\left(\theta\left(x\right)\right) \tag{2.1}$$

where $\theta(x)$ is defined as the angle between the tension vector and the x-axis (see Figure 2.1). Under the assumption that the string displacement is small enough so that $\sin\left(\theta\left(x\right)\right) \approx \tan\left(\theta\left(x\right)\right) = \frac{\partial w}{\partial x}$, Equation (2.1) becomes:

$$\rho S a = T\frac{\partial_x w\left(x+dx\right) - \partial_x w\left(x\right)}{dx} \tag{2.2}$$

where $\partial_x^n \triangleq \frac{\partial^n}{\partial x^n}$, $\partial_t^n \triangleq \frac{\partial^n}{\partial t^n}$ will be the notation adopted for n^{th} order partial differentiation with respect to time and space in the rest of this manuscript[2][3].

Finally, in the limit $dx \to 0$ such that the string element becomes infinitesimal, the acceleration of its centre of mass can be written directly as $a = \partial_t^2 w$, and the difference on the RHS of (2.2) becomes a spatial derivative, yielding:

$$\rho S\partial_t^2 w = T\partial_x^2 w \qquad \Leftrightarrow \qquad \partial_t^2 w = c^2\partial_x^2 w\ , \quad c \triangleq \sqrt{\frac{T}{\rho S}} \tag{2.3}$$

where c is the wave propagation velocity (in m/s). Equation (2.3) is the 1D wave equation, and was first derived by Jean le Rond d'Alembert [67] in the mid-18th century, to describe the evolution of the transverse displacement of a string over time.

Let $\eta \triangleq x - ct$ and $\gamma \triangleq x + ct$. Substituting $\partial_t = -c\partial_\eta + c\partial_\gamma$, and $\partial_x = \partial_\eta + \partial_\gamma$, leads to Equation (2.3) becoming:

$$\partial_\eta\partial_\gamma w = 0 \quad \Rightarrow \quad w(x,t) = f_-(\underbrace{x-ct}_{\eta}) + f_+(\underbrace{x+ct}_{\gamma}) \tag{2.4}$$

---

[2] The symbol $\triangleq$ signifies "is defined as".

[3] The absence of exponent indicates first order partial differentiation, that is $\partial_x \triangleq \frac{\partial}{\partial x}$ and $\partial_t \triangleq \frac{\partial}{\partial t}$.

This is to say that the general solutions of (2.3) can be written as the sum of two arbitrary, twice-differentiable functions f_- and f_+, travelling in opposite directions.

Two initial conditions are required to characterise the full problem, in the form of initial displacement and velocity distributions over the infinite string. As these conditions are given in terms of w and its first time derivative at a single point in time $t = 0$, the problem is said to be an initial value problem.

2.1.1.ii Preamble: integral calculus

This short section recalls some fundamental rules and properties of integral calculus. Such properties will be extensively referred to throughout the rest of this manuscript, in the context of frequency-domain Fourier and Laplace analysis, and time-domain energy calculations. In particular, the Laplace and Fourier transforms allow transfer from space-time domain to frequency domain, and as such require integration over time and space. Likewise, the calculation of energy and power measures requires the evaluation of the respective contributions of various quantities over their entire spatial domain of definition.

It is useful to introduce the continuous spatial inner product between two arbitrary functions $u(x,t)$ and $v(x,t)$, defined over a simply connected subset of the real plane $(x,t) \in \mathcal{I}_x \times \mathcal{I}_t \triangleq [\mathrm{a}_x, \mathrm{b}_x] \times [\mathrm{a}_t, \mathrm{b}_t] \subseteq \mathbb{R}$, as:

$$\langle u, v \rangle_{\mathcal{I}_x} \triangleq \int_{\mathrm{a}_x}^{\mathrm{b}_x} u(x,t)\, v(x,t)\, \mathrm{d}x \tag{2.5}$$

Note that $\mathrm{a}_x, \mathrm{b}_x, \mathrm{a}_t, \mathrm{b}_t \in \mathbb{R} \cup \{-\infty, +\infty\}$. The spatial L_2-norm of $u(x,t)$ over $\mathcal{I}_x$ is defined as:

$$\|u\|_{\mathcal{I}_x} \triangleq \sqrt{\langle u, u \rangle_{\mathcal{I}_x}} \tag{2.6}$$

Integration by parts over $\mathcal{I}_x$ and $\mathcal{I}_t$ is defined by:

$$\int_{\mathrm{a}_x}^{\mathrm{b}_x} u\,(\partial_x v)\, \mathrm{d}x \triangleq uv\Big|_{\mathrm{a}_x}^{\mathrm{b}_x} - \int_{\mathrm{a}_x}^{\mathrm{b}_x} (\partial_x u)\, v\, \mathrm{d}x\ , \qquad uv\Big|_{\mathrm{a}_x}^{\mathrm{b}_x} \triangleq u(\mathrm{b}_x,t)v(\mathrm{b}_x,t) - u(\mathrm{a}_x,t)v(\mathrm{a}_x,t) \tag{2.7a}$$

$$\int_{\mathrm{a}_t}^{\mathrm{b}_t} u\,(\partial_t v)\, \mathrm{d}t \triangleq uv\Big|_{\mathrm{a}_t}^{\mathrm{b}_t} - \int_{\mathrm{a}_t}^{\mathrm{b}_t} (\partial_t u)\, v\, \mathrm{d}t\ , \qquad uv\Big|_{\mathrm{a}_t}^{\mathrm{b}_t} \triangleq u(x,\mathrm{b}_t)v(x,\mathrm{b}_t) - u(x,\mathrm{a}_t)v(x,\mathrm{a}_t) \tag{2.7b}$$

where the integral becomes improper and the boundary terms vanish, by convention, if $\mathrm{a}_x, \mathrm{b}_x, \mathrm{a}_t, \mathrm{b}_t = \pm\infty$.

Finally, the Leibniz integral rule allows a partial time derivative to be brought outside a spatial integral, becoming a total time derivative, if a_x and b_x are time-independent:

$$\int_{\mathrm{a}_x}^{\mathrm{b}_x} \partial_t u(x,t)\, \mathrm{d}x = \frac{d}{dt} \int_{\mathrm{a}_x}^{\mathrm{b}_x} u(x,t)\, \mathrm{d}x \tag{2.8}$$

This simply means that the integral result of $u(x,t)$ over its spatial domain has no x dependence, when the bounds of such domain do not move over time.

2.1.1.iii Dispersion relation

It is useful to examine the behaviour of the solutions of (2.3) in the frequency domain. As the system is described by a linear PDE, any general solution $w(x,t)$ can be written as a linear combination of particular solutions. The principle of Fourier analysis lies in assuming that these solutions are complex exponentials, each with a different amplitude, frequency, and phase delay. In the present case, where independent variables are time and space, each of these complex exponentials can be seen as a propagating sinusoidal wave. The 2D Fourier transform of $w(x,t)$, denoted as $\widehat{w}(\beta,\omega)$, is defined as:

$$\widehat{w}(\beta,\omega) \triangleq \frac{1}{2\pi}\int_{-\infty}^{\infty}\int_{-\infty}^{\infty} w(x,t)e^{-j(\omega t+\beta x)}\,\mathrm{d}x\,\mathrm{d}t \tag{2.9}$$

where the temporal frequency $\frac{\omega}{2\pi}$ (Hz) and wavelength $\frac{2\pi}{\beta}$ (m) are respectively related to the angular frequency ω (rad/s) and the wavenumber β (rad/m). The Fourier transform of $\partial_t w$ follows, using integration by parts:

$$\begin{aligned}\widehat{\partial_t w} &= \frac{1}{2\pi}\int_{-\infty}^{\infty}\int_{-\infty}^{\infty} \partial_t w\, e^{-j(\omega t+\beta x)}\,\mathrm{d}x\,\mathrm{d}t \\ &= \frac{j\omega}{2\pi}\int_{-\infty}^{\infty}\int_{-\infty}^{\infty} w\, e^{-j(\omega t+\beta x)}\,\mathrm{d}x\,\mathrm{d}t \\ &= j\omega\,\widehat{w}\end{aligned} \tag{2.10}$$

An analogous derivation can be made with the first order spatial derivative, yielding $\widehat{\partial_x w} = j\beta\,\widehat{w}$. Iterating this process yields the general relations between the Fourier transform of $w(x,t)$ and that of its partial derivatives:

$$\widehat{\partial_t^n w} = (j\omega)^n\,\widehat{w} \tag{2.11a}$$

$$\widehat{\partial_x^n w} = (j\beta)^n\,\widehat{w} \tag{2.11b}$$

As a result, taking the Fourier transform of the 1D wave equation (2.3) yields:

$$-\omega^2\widehat{w} = -c^2\beta^2\widehat{w} \qquad \Rightarrow \qquad \omega = \pm c\beta \tag{2.12}$$

Note that the same result can be obtained by inserting a test solution of the form $w(x,t) \triangleq e^{j(\omega t+\beta x)}$ into the wave equation (2.3); this is then equivalent to examining the behaviour of a single one of the particular wave-like solutions of (2.3). For the sake of brevity, throughout the rest of this work, this test solution, or ansatz[4], will be employed for frequency-domain analysis in lieu of a full Fourier transform.

The relation (2.12), linking the temporal and spatial frequencies of a propagating sinusoidal wave, is referred to as the dispersion relation. Dispersion occurs when the propagation velocity of a wave depends on its frequency; for instance, a wave packet comprising multiple sinusoidal components (e.g., a pulse) will spread out when travelling in a dispersive medium, and lose its initial shape. The velocity of each individual single-frequency component is referred to as the phase velocity $v_\varphi \triangleq \frac{\omega}{\beta}$, whereas the velocity of the envelope of the wave packet centred around a particular frequency is known as the group velocity $v_g \triangleq \frac{d\omega}{d\beta}$. In the case of the ideal string, they are given by:

$$v_\varphi = v_g = \pm c \tag{2.13}$$

As v_φ does not depend on frequency (and indeed $v_\varphi = v_g$), the ideal string is non-dispersive.

2.1.1.iv Energy analysis

The rate of change of the total energy $H_{w,s}$[5] of the infinite string can be obtained by computing the inner product of the wave equation (2.3) with the string velocity $\partial_t w$ over $\mathbb{R}$, yielding:

$$\dot{H}_{w,s} = 0 \ , \qquad H_{w,s}(t) \triangleq \frac{\rho S}{2} \left\| \partial_t w \right\|^2 + \frac{T}{2} \left\| \partial_x w \right\|^2 = H_{w,s}(0) \geqslant 0 \tag{2.14}$$

where the norm is taken over $\mathbb{R}$, and the dot notation implies total time differentiation. As $H_{w,s}$ is constant over time, the system is energy-conserving. The first term of $H_{w,s}$ is the kinetic energy of the string, while the second term is the potential energy due to the string tension. These respective contributions can be independently evaluated at any time, from knowledge of $w(x,t)$. This capacity, when applied to a discrete time setting, makes for a particularly useful monitoring tool to ensure that a numerical energy balance is maintained throughout a simulation, and therefore that numerical results can be trusted, to some extent, to be representative of the physical system.

It is straightforward to bound the norm of the velocity and gradient of the infinite string, at all times, in terms of its total initial energy $H_{w,s}(0)$ (determined by the initial conditions imposed on the system):

$$\left\| \partial_t w \right\| \leqslant \sqrt{\frac{2H_{w,s}(0)}{\rho S}} \tag{2.15a}$$

$$\left\| \partial_x w \right\| \leqslant \sqrt{\frac{2H_{w,s}(0)}{T}} \tag{2.15b}$$

As will be shown throughout Section 2.2, energetic manipulations in discrete time are also a reliable way to ensure that numerical schemes are stable. Indeed, establishing such bounds on the velocity and gradient of the string in the discrete domain ensures that the growth of the numerical solution is limited by a finite positive value, function of the constant numerical energy. The solution therefore remains within valid energetic bounds, and the scheme is said to be stable.

---

[4] "A mathematical statement which is assumed to be true for a given problem, for the purpose of solving or investigating that problem; esp. a hypothesized solution to a mathematical problem." OED Online. Oxford University Press, 2017.

[5] Here, the subscript s indicates "string". This will facilitate the distinction between the energy contributions of multiple components introduced later in Chapters 3 and 4.

The notation $H_{w,s}$ has been chosen for the total energy of the string; indeed, the given energetic results, derived here from Newton's 2nd law, can also be obtained from the Hamiltonian formalism (see, for example, [60, Chap. 12]). Within that framework, $H_{w,s}$ is known as the Hamiltonian of the system. Recent works in physical modelling of strings have made use of the Hamiltonian framework, through numerical time integration of the Hamilton equations describing the system [21]; the port-Hamiltonian formalism [114] also makes use of such framework, and has seen recent applications in physical modelling of acoustic and audio systems [36]. The ideal string is said to be a time-independent Hamiltonian system, as $H_{w,s}$ is constant over time.

2.1.1.v Boundary conditions

The modelling of infinite strings has little practical interest for this work. Strings used in musical instruments are finite; mathematically, their spatial domain of definition is a simply connected subset of the real line. The arising problem then requires providing a set of two boundary conditions, one at either end of the string, in addition to the pair of initial conditions. These supplementary conditions can be defined in terms of w and/or its spatial derivatives, at two separate points in the spatial domain; the problem is now said to be a boundary value problem.

Consider now the transverse displacement $w(x,t)$ of a string of length L (m), defined over $x \in \mathcal{D} \triangleq [0, L]$, and time $t \in \mathbb{R}_{\geqslant 0}$. The wave equation (2.3) still stands, and the energy balance equation becomes:

$$\dot{H}_{w,s} = T \partial_t w \partial_x w \Big|_0^L \tag{2.16}$$

where the definition (2.14) now implies that the norm is taken over $\mathcal{D}$. Restricting the problem to that of an isolated string with perfectly reflecting terminations, conditions must be imposed such that the boundary terms in (2.16) vanish, so that no energy is transmitted through the string ends, and the total string energy $H_{w,s}(t)$ stays constant over time. This can be achieved with two types of boundary conditions:

$$w(0,t) = 0 \;\; ; \quad w(L,t) = 0 \qquad \text{(Dirichlet)} \tag{2.17a}$$

or

$$\partial_x w(0,t) = 0 \;\; ; \quad \partial_x w(L,t) = 0 \qquad \text{(Neumann)} \tag{2.17b}$$

The Dirichlet conditions (2.17a) correspond to a string with fixed terminations; the Neumann conditions (2.17b) represent free terminations. Note that a combination of a Neumann condition at one end and a Dirichlet condition at the other is also valid.

Physical modelling for string sound synthesis is concerned with configurations found in stringed instruments, where the strings are normally attached to a bridge or soundboard at one end, and generally considered fixed at the other end. In order to first focus this study on the behaviour of the isolated string, Dirichlet terminations will be employed, later complemented by further conditions when stiffness is introduced in Section 2.1.2.v.

2.1.1.vi String modes and eigenfrequencies of the fixed string

Consider solutions of the 1D wave equation (2.3) of the form $w(x,t) \triangleq W(x)q(t)$, where $W(x)$ and $q(t)$ are real-valued functions of space and time, respectively. Introducing this test solution into (2.3) leads to:

$$\rho S\, W(x)\ddot{q}(t) = T\, q(t)W''(x) \quad \Rightarrow \quad \frac{\ddot{q}(t)}{q(t)} = c^2 \frac{W''(x)}{W(x)} \triangleq \gamma^2 \tag{2.18}$$

where γ^2 must be a real constant, as the LHS (dependent only on t) must equal the RHS (dependent only on x), for any x and t. The prime notation implies total spatial differentiation. Two ordinary differential equations (ODEs) are extracted from (2.18):

$$\ddot{q}(t) = \gamma^2 q(t) \qquad \Rightarrow \qquad q(t) = q_1 e^{\gamma t} + q_2 e^{-\gamma t} \tag{2.19a}$$

$$W''(x) = \frac{\gamma^2}{c^2} W(x) \qquad \Rightarrow \qquad W(x) = A_1 e^{\frac{\gamma}{c}x} + A_2 e^{-\frac{\gamma}{c}x} \tag{2.19b}$$

where q_1, q_2 and A_1, A_2 are complex constants, respectively set by the initial and boundary conditions. The case $\gamma = 0$ is trivial, and of no interest here. The Dirichlet (fixed) boundary conditions (2.17a) inserted in (2.19b) lead to, for the left boundary:

$$W(0) = 0 \quad \Rightarrow \quad W(x) = \begin{cases} 2jA_1 \sin\left(\frac{\gamma'}{c}x\right), & \text{if } \gamma = j\gamma' \in j\mathbb{R} \\ 2A_1 \sinh\left(\frac{\gamma}{c}x\right), & \text{if } \gamma \in \mathbb{R} \end{cases} \tag{2.20a}$$

and for the right boundary:

$$\begin{aligned} W(L) = 0 \quad &\Rightarrow \quad \begin{cases} \sin\left(\frac{\gamma' L}{c}\right) = 0\,, & \text{if } \gamma \in j\mathbb{R} \\ \sinh\left(\frac{\gamma L}{c}\right) = 0\,, & \text{if } \gamma \in \mathbb{R} \end{cases} \\ &\Rightarrow \quad \begin{cases} \gamma'_m = \frac{m\pi c}{L}\,,\ m \in \mathbb{N}\,, & \text{if } \gamma \in j\mathbb{R} \\ \gamma = 0\,, & \text{if } \gamma \in \mathbb{R} \end{cases} \end{aligned} \tag{2.20b}$$

Again, the trivial case $\gamma = 0$ is eliminated; hence, $\gamma \in j\mathbb{R}$. The boundary conditions imposed on the finite string therefore limit the allowed wavenumbers to a quantised set of values, corresponding to the zero-crossings of $\sin\left(\frac{\gamma' L}{c}\right)$. The set of solutions for $W(x)$ can now be written as:

$$W_m(x) = A \sin\left(\frac{\gamma'_m}{c}x\right) = A\sin\left(\beta_m x\right)\,, \qquad \beta_m \triangleq \frac{m\pi}{L}\,, \quad m \in \mathbb{N} \tag{2.21}$$

where $A \triangleq 2jA_1 \in \mathbb{R}$. Each of these solutions is referred to as an eigenmode (or normal mode) of the system, and corresponds to a temporal solution $q_m(t)$, oscillating at an angular frequency ω_m depending on the wavenumber β_m:

$$q_m(t) = q_1 e^{j\omega_m t} + q_2 e^{-j\omega_m t} \, , \qquad \omega_m \triangleq \frac{m\pi c}{L} \, , \ \ m \in \mathbb{N} \tag{2.22}$$

where $q_1, q_2 \in \mathbb{C}$ must be complex conjugates for the string displacement $w(x,t)$ to be real; their real and imaginary parts are determined by the two initial conditions imposed on the system. Note that the dispersion relation (2.12) still holds. Furthermore, the frequencies ω_m and wavenumbers β_m are linear functions of the positive integer m, and as such they are linearly spaced; this indicates that the modal frequencies of the ideal string form a harmonic series.

The general solution $w(x,t)$ can now be written as a linear combination of the individual solutions:

$$w(x,t) = \sum_{m=1}^{\infty} q_m(t) A \sin(\beta_m x) \tag{2.23}$$

The normal modes $W_m(x)$ of the ideal string form an orthogonal basis of infinite dimension, as the inner product of any two modes over the domain $\mathcal{D}$ verifies:

$$\langle W_m, W_p \rangle_{\mathcal{D}} = \begin{cases} 0 \, , & m \neq p \\ \frac{LA^2}{2} \, , & m = p \end{cases} \tag{2.24}$$

Setting $A \triangleq \sqrt{\frac{2}{L}}$ ensures the basis is orthonormal. As seen in Equation (2.23), the general solution can be interpreted as the superposition of an infinite number of modal shapes, given by the spatial solutions $W_m(x)$, for each of which every point of the string oscillates, in phase, at a single frequency ω_m; accordingly, they are referred to as time-harmonic solutions.

A class of physical modelling techniques, referred to as modal methods, makes use of this spatial frequency-domain decomposition. The displacement of a given physical system is projected onto the modal basis characterising such system, truncated to a finite dimension (corresponding to a chosen cutoff frequency), allowing to simplify solving for the temporal component. A brief review of modal methods will be given in Section 2.2.1.i.

2.1.2 The stiff string

2.1.2.i Review of existing models

A lossless linear stiff string can be described equivalently as an ideal string with a non-zero bending stiffness, or as a thin beam[6] under tension. Indeed, stiff string models have their roots in 1D beam theory. The most general thin beam model, described by Timoshenko's theory [111], includes the modelling of shear wave propagation. A simplification is obtained by neglecting rotational inertia in the Timoshenko model, to arrive at the so-called shear model.

---

[6] The thin beam approximation is considered valid for wavelengths greater than the beam thickness [87]; this typically includes all audible wavelengths relevant in stringed instruments.

Finally, an approximation of the shear model for large wavelengths yields the Euler-Bernoulli model, which will be used in the rest of this work, and described in the following subsections. A detailed review of aspects, advantages, and shortcomings of these respective models has been made in [50] in the context of transverse beam vibration[7], and, more recently, with applications to stiff strings in musical instrument modelling [33].

2.1.2.ii The Euler-Bernoulli stiff string equation

Consider the infinite string described in Section 2.1.1.i, now with a nonzero bending stiffness EI_0 where E is Young's modulus for the string material (in Pa) and I_0 is the area moment of inertia for a string of circular cross-section, given by $I_0 \triangleq \frac{\pi r^4}{4}$ where r is the string radius (in m). The PDE describing the temporal evolution of $w(x,t)$ becomes:

$$\rho S \partial_t^2 w = T \partial_x^2 w - EI_0 \partial_x^4 w \tag{2.25}$$

which can also be written more compactly, in terms of a linear partial differential operator $\mathcal{L}$:

$$\mathcal{L} w = 0 \ , \qquad \mathcal{L} \triangleq \rho S \partial_t^2 - T \partial_x^2 + EI_0 \partial_x^4 \tag{2.26}$$

Note that the travelling wave functions (2.4) are no longer solutions of this stiff string equation.

2.1.2.iii Dispersion relation

As discussed in 2.1.1.iii, inserting a single-frequency wave test solution of the form $w(x,t) = e^{j(\omega t + \beta x)}$ into Equation (2.25) leads to the following expressions for the dispersion relation, phase velocity, and group velocity:

$$\omega = \pm \beta \sqrt{c^2 + \kappa^2 \beta^2} \qquad \Rightarrow \qquad v_\varphi = \pm \sqrt{c^2 + \kappa^2 \beta^2} \ , \qquad v_g = \pm \frac{c^2 + 2\kappa^2 \beta^2}{\sqrt{c^2 + \kappa^2 \beta^2}} \tag{2.27}$$

where $\kappa^2 \triangleq \frac{EI_0}{\rho S}$ depends only on the material and geometric properties of the string. As v_φ is a function of the wavenumber β, waves of different wavelengths propagate at different velocities; this phenomenon is known as wave dispersion. This also means that $v_\varphi \neq v_g$; consequently, the shape of a wave packet comprised of multiple sinusoidal components will evolve as it propagates. Figure 2.2 shows the propagation of a pulse along an ideal string (top), and along a stiff string with low stiffness (middle) and high stiffness (bottom).

Wave dispersion is a phenomenon inherent to stiff strings, and it occurs audibly in a range of stringed instruments. Indeed, for a finite stiff string, as will be shown in Section 2.1.2.vi, dispersion leads to a stretching of the modal frequencies with respect to those of the ideal string; this feature of stiff strings is referred to as inharmonicity. Wave dispersion should be

---

[7] The authors in [50] also review the Rayleigh model, which can be derived from a Timoshenko model by neglecting shear deformation. They find that for a thin beam with a given geometry, shear effects always preponderate over rotational inertia, and therefore the shear model is a more appropriate simplification of Timoshenko's theory.

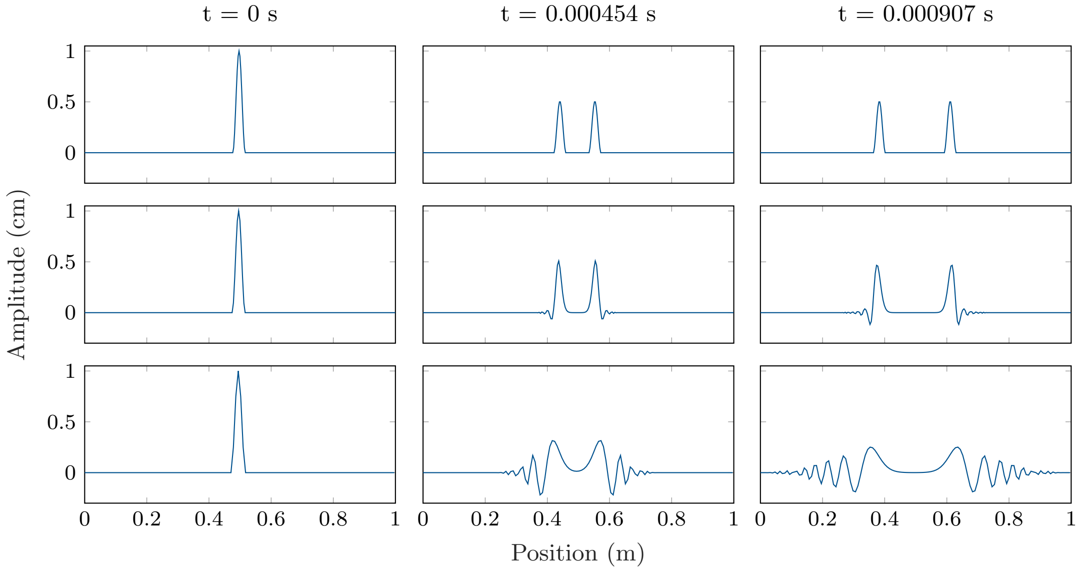

Figure 2.2: Snapshots of the propagation of a pulse along an ideal string (top), a stiff string with low stiffness (middle, $E = 1 \times 10^{10}$Pa), and with high stiffness (bottom, $E = 2 \times 10^{11}$Pa). In the absence of stiffness, the pulse propagates without changing shape; however, the stiffness term introduces dispersion, and high frequency components start to lead low frequencies. — Parameters: $L = 1$ m, $T = 100$ N, $\rho = 7850$ kg/m^3, $r = 0.5$ mm.

distinguished from numerical dispersion, brought about by discretising space and time to design numerical schemes, which will be discussed in Sections 2.2.4.vi and 2.2.5.vi.

2.1.2.iv Energy analysis

As previously applied to the ideal string, taking the inner product of $\partial_t w$ with the stiff string equation (2.25) over $\mathbb{R}$ yields the energy balance equation:

$$\dot{H}_{w,s} = 0 \, , \qquad H_{w,s}(t) \triangleq \frac{\rho S}{2} \left\|\partial_t w\right\|^2 + \frac{T}{2} \left\|\partial_x w\right\|^2 + \frac{EI_0}{2} \left\|\partial_x^2 w\right\|^2 = H_{w,s}(0) \tag{2.28}$$

where the norm is taken over $\mathbb{R}$. The third term of $H_{w,s}(t)$ represents the potential energy contribution from bending stiffness. Again, the total energy $H_{w,s}(t) = H_{w,s}(0)$ of the infinite stiff string is conserved over time. The norm of the curvature of the stiff string over the infinite domain is now bounded, in addition to those of its velocity and gradient, in terms of the string's initial energy:

$$\left\|\partial_x^2 w\right\| \leqslant \sqrt{\frac{2H_{w,s}(0)}{EI_0}} \tag{2.29}$$

2.1.2.v Boundary conditions

In order to bring this analysis to a relevant physical setting, let $w(x,t)$ henceforth be defined over the finite interval $x \in \mathcal{D}$, defined in 2.1.1.v, and over time $t \in \mathbb{R}_{\geqslant 0}$. Boundary terms now appear in the energy balance equation:

$$\dot{H}_{w,s} = T\partial_t w \partial_x w \Big|_0^L - EI_0 \left(\partial_t w \partial_x^3 w \Big|_0^L - \partial_t \partial_x w \partial_x^2 w \Big|_0^L \right) \tag{2.30}$$

where $H_{w,s}$ is defined by (2.28), with the norm taken over $\mathcal{D}$. Two types of fixed boundary conditions lead to the boundary terms on the RHS of Equation (2.30) vanishing, thus allowing $H_{w,s}$ to be conserved over time:

$$w(0,t) = \partial_x^2 w(0,t) = 0 \quad ; \quad w(L,t) = \partial_x^2 w(L,t) = 0 \tag{2.31a}$$

or

$$w(0,t) = \partial_x w(0,t) = 0 \quad ; \quad w(L,t) = \partial_x w(L,t) = 0 \tag{2.31b}$$

Another type of perfectly reflecting boundary condition for the isolated stiff string is the free condition; it is however not generally found in stringed instruments[8].

The boundary condition described by (2.31a) is known as simply supported (sometimes referred to as pivoting or hinged), while that in (2.31b) is used to represent a clamped stiff string. Again, a combination of a simply supported termination at one end and a clamped termination at the other is also valid. For most stringed instruments, as the effect of the bending stiffness term is small compared to that of the string tension, the choice of fixed boundary conditions does not bear a strong influence on the resulting string vibrations; in the rest of this work, the simply supported conditions (2.31a) are employed at both ends.

2.1.2.vi Stiff string modes and eigenfrequencies under pivoting conditions

Fletcher [37] first derived the modal shapes and eigenfrequencies of the stiff piano string, simply supported at both ends, modelled with Equation (2.25). As seen in 2.1.1.vi for the ideal string, this is achieved by examining time-harmonic solutions of the stiff string equation. Modal analysis assumes steady-state behaviour; the initial conditions determine the amplitude of the string motion, and bear no influence on the mode shapes and frequencies. Time-harmonic analysis can therefore be simplified by using a single oscillatory term for the time component, yielding:

$$w(x,t) \triangleq e^{j\omega t} W(x) \qquad \Rightarrow \qquad \omega^2 W + c^2 \frac{d^2 W}{dx^2} - \kappa^2 \frac{d^4 W}{dx^4} = 0 \tag{2.32}$$

Assuming solutions to (2.32) of the form $W(x) = Ae^{j\beta x}$, where $\beta \in \mathbb{C}$, and solving for β, leads to:

$$\omega^2 - c^2\beta^2 - \kappa^2\beta^4 = 0 \qquad \Rightarrow \qquad \beta = \pm\sqrt{\frac{\mp\sqrt{c^4 + 4\omega^2\kappa^2} - c^2}{2\kappa^2}} \tag{2.33}$$

---

[8] Free terminations do play a role in some percussion instruments, and are indeed characteristic of idiophones.

Four solutions therefore arise for β, two real and two imaginary:

$$\beta = \pm\beta_1 \,, \qquad \beta_1 \triangleq \sqrt{\frac{\sqrt{c^4 + 4\omega^2\kappa^2} - c^2}{2\kappa^2}} \in \mathbb{R} \tag{2.34a}$$

$$\beta = \pm j\beta_2 \,, \qquad \beta_2 \triangleq \sqrt{\frac{\sqrt{c^4 + 4\omega^2\kappa^2} + c^2}{2\kappa^2}} \in \mathbb{R} \tag{2.34b}$$

The general solution for the modal shapes of the stiff string can therefore be written as a linear combination of the four wavenumber solutions:

$$W(x) = A_1 e^{j\beta_1 x} + A_2 e^{-j\beta_1 x} + A_3 e^{\beta_2 x} + A_4 e^{-\beta_2 x} \tag{2.35}$$

where $A_{1,2,3,4} \in \mathbb{C}$ are constants. Simply supported boundary conditions at both ends yield, first at $x = 0$, $A_2 = -A_1 \in j\mathbb{R}$ and $A_4 = -A_3 \in \mathbb{R}$; then, at $x = L$, $A_3 = A_4 = 0$. The shape of the mth mode of the simply supported stiff string is therefore given by:

$$W_m(x) = A\sin(\beta_m x) \tag{2.36}$$

where $A \triangleq 2jA_1 \in \mathbb{R}$ is the corresponding modal amplitude; as for the ideal string, the mode shapes are normalised if $A \triangleq \sqrt{\frac{2}{L}}$. The allowed wavenumbers $\beta_m \triangleq \frac{m\pi}{L}$ follow from the boundary condition at $x = L$. The eigenfrequencies $f_m \triangleq \frac{\omega_m}{2\pi}$ are derived from $\beta_m \triangleq \beta_1(\omega_m)$:

$$f_m = \frac{mc}{2L}\sqrt{1 + \left(\frac{\kappa\pi}{cL}\right)^2 m^2} = \frac{m}{2L}\sqrt{\frac{T}{\rho S} + \frac{EI_0\pi^2}{\rho S L^2}m^2} \;, \quad m \in \mathbb{N} \tag{2.37}$$

The eigenfrequencies of the stiff string are not equally spaced, leading to inharmonicity. In the literature, a quantity $B \triangleq \left(\frac{\kappa\pi}{cL}\right)^2 = \frac{EI_0\pi^2}{TL^2}$ is often referred to as the dimensionless inharmonicity factor. The tension T required to tune the fundamental frequency of a stiff string must be adjusted with respect to that required for an ideal string of identical length, radius, and mass. Table 2.1 gives the required tension values to tune a theoretical violin A string ($L = 32$ cm) to 440 Hz and a cello D string ($L = 69$ cm) to 146.8 Hz, in the presence or absence of stiffness, as well as the theoretical frequencies and deviation from harmonicity of the first 10 modes, using the physical parameters given on page xxix.

2.2 From equations of motion to synthetic sound

Now that the physical system has been fully described, a range of numerical methods are available to generate synthetic sound, each with different advantages and drawbacks. Broadly speaking, a distinction can be made between physical modelling techniques based on approximating the PDEs describing the system, and those based on approximating their solutions.

	Violin A string			**Cello D string**		
	Non-stiff	Stiff	Δp (cents)	Non-stiff	Stiff	Δp (cents)
$B(\times 10^{-4})$		2.095			1.181	
T (N)	57.095	57.083		147.745	147.728	
f_1 (Hz)	440	440	0	146.8	146.8	0
f_2 (Hz)	880	880.27	0.54	293.6	293.65	0.31
f_3 (Hz)	1320	1321.11	1.45	440.4	440.61	0.82
f_4 (Hz)	1760	1762.76	2.71	587.2	587.72	1.53
f_5 (Hz)	2200	2205.52	4.34	734	735.04	2.45
f_6 (Hz)	2640	2649.66	6.32	880.8	882.62	3.57
f_7 (Hz)	3080	3095.44	8.66	1027.6	1030.51	4.89
f_8 (Hz)	3520	3543.14	11.35	1174.4	1178.76	6.42
f_9 (Hz)	3960	3993.03	14.38	1321.2	1327.43	8.14
f_{10} (Hz)	4400	4445.38	17.76	1468	1476.56	10.06

Table 2.1: Tension T, inharmonicity factor B, and modal frequencies f_m for the modes of a violin A string and a cello D string, in the absence or presence of stiffness. The pitch deviation Δp (cents) is given for each mode of both strings, between the stiff string and the non-stiff string. — Parameters: see Violin A string and Cello D string on page xxix.

2.2.1 Review of numerical methods

This section will provide an overview of physical modelling techniques for sound synthesis of strings, with a focus on three prominent methods. In the spatial frequency domain, modal decomposition methods [1] make use of the projection of time-dependent variables on the orthonormal modal basis of the string. In the space-time domain, travelling-wave-based methods will be reviewed, with particular attention to the digital waveguide framework [101], popular for computationally efficient sound synthesis. Finally, and still in the space-time domain, local time-stepping methods applied directly to the PDE system will be outlined; in particular, the finite difference (FD) method [107] will be introduced as the approach taken in the remainder of this work.

2.2.1.i Modal decomposition

The modal decomposition method consists of projecting the string displacement $w(x,t)$ onto the modal basis characterising the system; it is therefore clearly well-suited for linear systems. The following modal expansion of the string displacement is assumed:

$$w(x,t) = \sum_{m=1}^{\infty} q_m(t) W_m(x) \tag{2.38}$$

where $W_m(x)$ is the normalised shape of the mth mode of the stiff string, defined by Equation (2.36). Inserting (2.38) into the stiff string equation (2.25), and using the orthogonality of the modal basis, an independent ODE is obtained for the time-dependent term $q_m(t)$ of each modal component:

$$\ddot{q}_m + \left(c^2\beta_m^2 + \kappa^2\beta_m^4\right) q_m = 0 \tag{2.39}$$

which describes a simple harmonic oscillator, with natural frequency $\omega_m^2 = c^2\beta_m^2 + \kappa^2\beta_m^4$; this echoes the time-harmonic analysis of Section 2.1.2.vi. Whilst the analytical solution for the modal shapes is known in the simple case shown here, this may not be the case for more complex systems. Equation (2.39) can now be solved numerically, for instance with a time-stepping method, for the desired number of modes, and the string displacement can be computed from (2.38).

Several advantages of the modal decomposition method arise. Firstly, in the unforced case, the system of temporal ODEs can be discretised in a way which leads to an exact numerical solution. This is advantageous with respect to locally defined time-stepping methods, which may exhibit problems such as numerical dispersion; this will be further discussed in Sections 2.2.4.vi and 2.2.5.vi. Secondly, it is straightforward to introduce fine-tuned frequency-dependent damping, calibrated against, for instance, experimental decay time measurements, by introducing a loss term with a different weighting in each of the ODEs (2.39). Direct frequency-dependent loss modelling in the time domain is a much less straightforward matter, and will be the subject of Chapter 3.

A computational drawback of the modal decomposition method is that it requires storing all modal shapes of the system in memory, up to the desired synthesis frequency. It is easy to see that this may become an issue when dealing with larger systems, or systems with more than one spatial dimension, for which the modal density can become much larger than that of a string. Another drawback, perhaps more relevant to this work, with respect to locally defined methods, arises when dealing with coupled or forced systems. Any external or coupling force term, applied at a point or over a finite domain, must be projected onto the entirety of the modal basis, resulting in drastically increased computational costs in the case of nonlinear, distributed, or time-varying excitations.

2.2.1.ii Travelling-wave-based methods

Travelling-wave synthesis methods are based on the discretisation of backward- and forward-going solutions of the ideal string equation (recall Equation (2.4)), and make use of digital filters to model more complex phenomena. Specifically, these methods have been employed, through a musical acoustics prism, for experimental validation of clarinet, bowed string, and flute behaviour [74]. They have also been formalised for computationally efficient sound synthesis applications, into the so-called digital waveguide (DW) framework [103, 104][9].

A digital waveguide consists of a bi-directional digital delay line, each direction respectively containing the sampled backward- and forward-going wave (see Figure 2.3). Force or velocity

---

[9] A passage of [74] appears to foretell the widespread success of DWs for real-time musical applications, and indeed the rise of physical modelling sound synthesis: “[. . .] a fast minicomputer could produce results at a cycle rate in the audible range. The result would perhaps have some novelty: an electronical musical instrument based on a mathematical model of an acoustic instrument.”

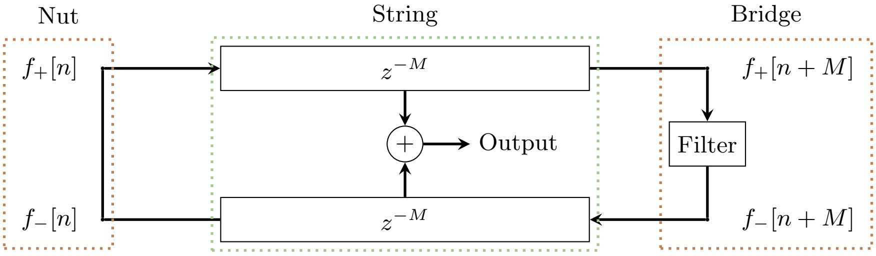

Figure 2.3: Basic digital waveguide diagram. A bidirectional M-sample delay line contains sampled versions of the backward- and forward-going waves, as defined in (2.4). A filter at the string termination can be used to model frequency-dependent phenomena.

waves are typically used, instead of displacement waves. Appropriate lumped digital filters are used to model wave dispersion, losses, and nonlinear phenomena or interactions. Several waveguides can be connected into a network, or mesh, through junctions with frequency-dependent impedance, to model more complex coupled linear systems, or 2D/3D systems. The computational efficiency of these algorithms allows for real-time applications; the Yamaha VL1 became, as early as 1994, the first commercially available real-time physical modelling synthesiser, using digital waveguides.

At its core, a digital waveguide model of a plucked string can be seen as a physical interpretation of the earlier Karplus-Strong wavetable algorithm [59, 57], where a short burst of filtered white noise is looped over the duration of a note, and filtered at each loop iteration to emulate frequency-dependent decay. The frequency content of this initial wavetable corresponds to the frequency content of the initial excitation (the pluck). Each sample of the wavetable can be seen, in waveguide terms, as a spatial component of the string displacement which travels back and forth along the string.

2.2.1.iii Locally defined time-stepping methods

Early attempts at physical modelling of strings made use of another type of time-domain method [89, 4, 12, 18], the finite difference method [107]. The PDE(s) describing the system are directly discretised in time and space, and the partial differential operators are approximated with finite differences, operating on discrete approximations of the dependent string variables, over a spatial grid and a number of time steps. The state of the system at one point in space and time only depends on its state at immediately neighbouring points; the FD method is local. Other local time-stepping methods have been used for string modelling, notably finite element methods for the simulation of piano strings [16, 17].

The computational costs associated with using the finite difference method at audio sample rates have impeded attempts at sound synthesis in or near real-time. However, the last decade has seen a resurgence of these direct methods, as high-performance consumer CPUs have become widely available. This expansion in computational power has facilitated the development of simulations for increasingly complex physical systems and phenomena.

Direct numerical integration of the equations of motion requires minimal assumptions on the form of the solution. This is a major advantage with respect to the previously discussed modal and travelling-wave methods; strongly nonlinear systems can be solved, assuming they can be described with a system of PDEs. This includes geometric nonlinearities, but also distributed, dynamic nonlinear interactions between coupled systems, permitting the simulation of a wide variety of excitations and gestures.

Furthermore, local interactions (e.g., lumped excitations, or couplings over a small area) are treated truly locally, as they only directly affect one or a few points of the whole system. The associated computational costs are therefore only minimally increased with respect to those of the isolated system, a significant advantage compared to, e.g., modal methods (see comment on page 19).

Beyond the computational costs involved with these direct methods, another issue is that of numerical dispersion. Indeed, the choice of discretisation for the problem can lead to numerical artefacts with respect to the propagation speed of different frequencies, unrelated to natural wave dispersion phenomena seen, for instance, in Section 2.1.2.iii. The manifestation of numerical dispersion in synthetic sound signals can be perceptible; however, one can make used of alternative, optimised finite difference schemes, in order to minimise these effects. Numerical dispersion will be further discussed in this work, starting with its first appearance in Section 2.2.4.vi.

A range of numerical schemes is available to approximate a given set of ODEs or PDEs, to varying degrees of accuracy. However, within this range, most options will exhibit unstable behaviour if precautions are not taken. While one can design schemes to be unconditionally stable, they tend to come with significantly higher computation times. All other schemes must be accompanied by a stability condition, usually relating time step and grid spacing (for space-time problems). As will be seen in this Section with the case studies of the ideal string and stiff string schemes, stability analysis can be performed with frequency-domain analysis (for linear systems), or directly in the time domain, with numerical energy analysis.

In the presence of strongly nonlinear phenomena in the physical system, energy can be transferred to high-frequency components. For instance, the collision of a string with a lumped, stiff object, as will be seen in Chapter 4, can trigger the propagation of a sharp deformation along the string. An exact representation of this sharp deformation, in the frequency domain, requires very high frequency components (with short wavelengths), which can lie beyond the upper frequency limit imposed by the particular discretisation of the string state[10]. Numerical artefacts therefore appear in the form of aliasing; components at frequencies larger than this limit appear to be reflected at the higher end of the spectrum, introducing undesired components to the synthesised sound. Although aliasing is a known effect in nonlinear numerical problems, to the knowledge of the present author, no research has been done related to the modelling of physical systems. However, when acoustics is concerned, damping is generally large at high frequencies, and accurate modelling of losses should reflect this behaviour, effectively attenuating potentially aliased high-frequency components, and significantly reducing perceptual artefacts.

---

[10] In the finite difference framework, this upper frequency limit is generally more restrictive than the Nyquist frequency given by the chosen audio sample rate; this issue will be explored when treating frequency-domain behaviour of particular FD schemes, starting in Section 2.2.4.vi.

Before proceeding to the examination of numerical schemes used to solve the stiff string equation, and later more complex systems, it is necessary to introduce the framework behind the finite difference method. To this end, the FD operators will be defined in terms of their effect on discrete approximations in time and/or space of continuous functions. The terms “time series” and “grid function” will be used to refer to a discrete function of time and space, respectively. For reference, a comprehensive list of all the FD operators used in this manuscript is presented on page xxvi.

2.2.2 Time series and temporal FD operators

Let $u(t)$ be an arbitrary, continuous function of time $t \in \mathbb{R}_{\geqslant 0}$. Let k be a short time interval, in s; when audio applications are concerned, k is chosen in relation to the desired audio sampling rate ($k = \frac{1}{F_s}$). A sampled (or discrete-time) version of u is defined by evaluating $u(t) \approx u(nk)$, where $n \in \mathbb{N}_0$ is a time step index. Temporal FD operators approximate continuous time differentiation around time $t = nk$ using local evaluations of u, one or several time steps away from t.

2.2.2.i Time shifting operators

All temporal FD operators can be constructed from the time shifting operators (2.40), the effects of which are, on $u(t)$[11]:

$$e_{t-}u(t) = u(t-k) \qquad (2.40\text{a}) \qquad\qquad e_{t+}u(t) = u(t+k) \qquad (2.40\text{b})$$

Figure 2.4 illustrates the action of $e_{t\pm}$ over the value of $u(nk)$. Note that e_{t-} is not defined for the function’s initial value $u(0)$, which must be treated separately by setting initial conditions.

2.2.2.ii Derivation of the finite difference operators

The FD operators are used to approximate the continuous partial differential operators. They can be derived by truncating the Taylor series expansion of a continuous function, about points one or more time steps away from $t = nk$ (for temporal FD operators).

This derivation also gives access to an estimate of the accuracy of the individual operators, in terms of powers of the chosen time step. When dealing with full FD schemes involving multiple operators, accuracy must be computed for the complete scheme, and will depend on the relation between operators, and between time and grid spacings.

Let $u(t)$ be infinitely differentiable over $\mathbb{R}_{\geqslant 0}$. The Taylor series expansion of u about

---

[11] Note that although the following is derived in continuous time, t will ultimately be limited to take values that are integer multiples of the time step k.

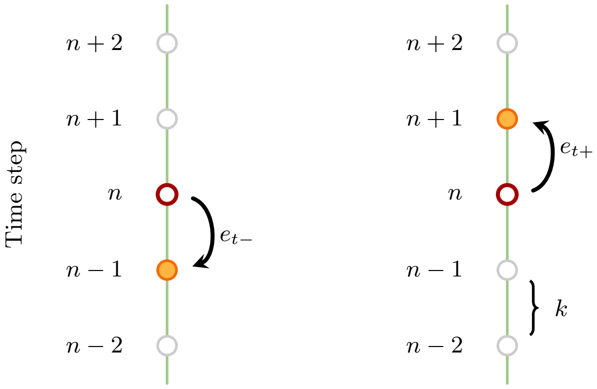

Figure 2.4: Action of e_{t-} and e_{t+} on the value of $u(t)$ evaluated at time step n (i.e. at $t = nk$). The dark red outline denotes the point around which the operator is centred; the orange fill denotes the points used by the operator.

$t \pm k = (n \pm 1)\,k$ is:

$$u(t \pm k) = u(t) \pm k\dot{u}(t) + \frac{k^2}{2}\ddot{u}(t) + O(k^3) \tag{2.41}$$

where $O(k^m)$ is a function containing the Taylor series terms of order $\geqslant m$[12]. Truncating beyond the first order derivative term of (2.41) leads directly to the first order forward and backward temporal finite difference operators:

$$\dot{u}(t) = \frac{u(t+k) - u(t)}{k} + O(k) \quad \Rightarrow \quad \delta_{t+} \triangleq \frac{e_{t+} - 1}{k} = \frac{d}{dt} + O(k) \tag{2.42a}$$

$$\dot{u}(t) = \frac{u(t) - u(t-k)}{k} + O(k) \quad \Rightarrow \quad \delta_{t-} \triangleq \frac{1 - e_{t-}}{k} = \frac{d}{dt} + O(k) \tag{2.42b}$$

Both δ_{t+} and δ_{t-} are first-order accurate (in time) when centred around t. It is however possible to show that they are second-order accurate when centred around the half time step $t \pm \frac{k}{2}$[13].

Another first order difference operator can be derived, centred around t, by subtracting $u(t-k)$ from $u(t+k)$:

$$\dot{u}(t) = \frac{u(t+k) - u(t-k)}{2k} + O(k^2) \quad \Rightarrow \quad \delta_{t\cdot} \triangleq \frac{e_{t+} - e_{t-}}{2k} = \frac{d}{dt} + O(k^2) \tag{2.43}$$

The terms containing even-order derivatives cancel out, and the remaining terms are factors of k^2, giving rise to second-order accuracy in time for the difference operator $\delta_{t\cdot}$, centred around t.

---

[12] When operating at audio sample rates, the time step k is small; the terms in the Taylor series that are factors of higher powers of k rapidly become small with increasing m, and hence can be neglected in order to define the finite difference operators. Naturally, however, for high-frequency oscillations, the truncated high-order Taylor series terms become larger, since the high-order temporal derivatives of $u(t)$ take larger values. This is a potential source of inaccuracy, at frequencies closer to the Nyquist limit, in simulation results.

[13] An mth order accurate operator in time is defined as yielding an approximation to the continuous time derivative of $u(t)$ to within a factor of the mth power of the time step k. Note that this is to be distinguished from the order of differentiation approximated by the operator; for instance, as seen here, FD operators approximating first order differentiation may be derived to a higher order of accuracy.

It is sometimes useful, for accuracy and/or stability reasons, to employ averaging operators to approximate identity. Forward and backward temporal averaging operators are derived by truncating the first order and above terms of (2.41), and adding $u(t)$ to both sides of the resulting equation:

$$u(t) = \frac{u(t+k)+u(t)}{2} + O(k) \qquad \Rightarrow \qquad \mu_{t+} \triangleq \frac{e_{t+}+1}{2} = 1 + O(k) \tag{2.44a}$$

$$u(t) = \frac{u(t-k)+u(t)}{2} + O(k) \qquad \Rightarrow \qquad \mu_{t-} \triangleq \frac{e_{t-}+1}{2} = 1 + O(k) \tag{2.44b}$$

μ_{t+} and μ_{t-} are first-order accurate when centred around t. Adding $u(t+k)$ to $u(t-k)$, now truncated from the second order terms onwards, yields the second-order accurate averaging operator, centred around t:

$$u(t) = \frac{u(t+k)+u(t-k)}{2} + O(k^2) \quad \Rightarrow \quad \mu_{t\cdot} = \frac{e_{t+}+e_{t-}}{2} \triangleq 1 + O(k^2) \tag{2.45}$$

Note that $\delta_{t\cdot}$ can now be written in terms of $\delta_{t\pm}$ and $\mu_{t\pm}$:

$$\delta_{t\cdot} \triangleq \delta_{t\pm}\mu_{t\mp} \tag{2.46}$$

Higher order FD operators can also be derived, with the same methods, from combinations of Taylor expansions truncated at higher orders. For the sake of brevity, it is noted that second-order accurate operators for approximating higher order derivatives can be written in terms of the first order operators presented here. The second order temporal partial differential operator is approximated by the second order temporal FD operator, second-order accurate, centred around t:

$$\delta_{tt} \triangleq \delta_{t\pm}\delta_{t\mp} = \frac{d^2}{dt^2} + O(k^2) \tag{2.47}$$

Temporal FD operators can be used to approximate both total and partial temporal derivatives. The previous derivations can be straightforwardly extended to spatial operators, which will therefore only be briefly described in the next section.

2.2.2.iii Stencil size

Moving towards a fully discrete setting, the notation u^n is adopted to designate a time series defined over a discrete temporal grid, evaluated at time step $n \in \mathbb{N}_0$, such that $u^n \triangleq u(nk)$. The operators derived in 2.2.2.ii are directly applied to the time series u^n; for instance, $\mu_{t+}u^n \triangleq \frac{1}{2}\left(u^{n+1}+u^n\right)$.

A temporal FD operator applied on a time series at a given time step will involve a number of neighbouring points; the span of the operator over the time grid is referred to as the stencil of the operator. Figure 2.5 illustrates the respective stencils of $\mu_{t\pm}$, $\delta_{t\pm}$, $\mu_{t\cdot}$, $\delta_{t\cdot}$, and δ_{tt}, centred on time step n.

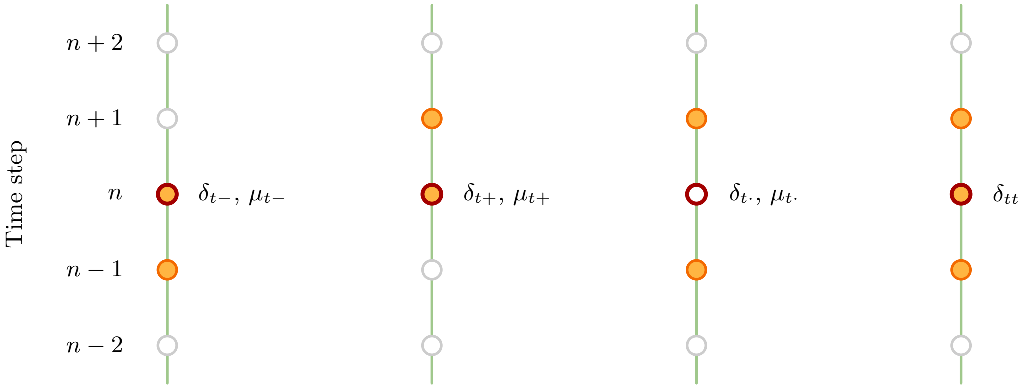
Time step
$n+2$
$n+1$
n
$n-1$
$n-2$
δ_{t-}, μ_{t-}
δ_{t+}, μ_{t+}
$\delta_{t\cdot}$, $\mu_{t\cdot}$
δ_{tt}

Figure 2.5: From left to right: stencils of δ_{t-} and μ_{t-}, δ_{t+} and μ_{t+}, $\delta_{t\cdot}$ and $\mu_{t\cdot}$, and δ_{tt}, over the temporal grid, when centred on time step n.

2.2.3 Spatio-temporal grid functions and finite difference operators

Consider now a function of both time and space, $u(x,t)$, defined over $x \in \mathbb{R}$ and $t \in \mathbb{R}_{\geqslant 0}$. Let h be a small distance, in m, spatial counterpart of the time interval k defined in 2.2.2. The function u is now sampled in both time and space, such that $u(x,t) \approx u(lh, nk)$, where $l \in \mathbb{Z}$ is a grid point index.

2.2.3.i Spatial shifting and finite difference operators

Similarly to the temporal operators, the spatial FD operators are constructed from the fundamental shifting operators e_{x-} and e_{x+}, the effect of which is, on $u(x,t)$:

$$e_{x-}u(x,t) = u(x-h,t) \qquad (2.48a) \qquad\qquad e_{x+}u(x,t) = u(x+h,t) \qquad (2.48b)$$

The spatial first order (total or partial) derivative can be approximated by:

$$\delta_{x-} \triangleq \frac{1-e_{x-}}{h} = \frac{d}{dx} + O(h) \qquad (2.49a) \qquad\qquad \delta_{x+} \triangleq \frac{e_{x+}-1}{h} = \frac{d}{dx} + O(h) \qquad (2.49b)$$

$$\delta_{x\cdot} \triangleq \frac{e_{x+}-e_{x-}}{2h} = \frac{d}{dx} + O(h^2) \qquad (2.49c)$$

Finally, when the stiff string is concerned, second and fourth order spatial operators are needed, defined by:

$$\delta_{xx} \triangleq \delta_{x\pm}\delta_{x\mp} \qquad (2.50a) \qquad\qquad \delta_{xxxx} \triangleq \delta_{xx}\delta_{xx} \qquad (2.50b)$$

The notation u_l^n is adopted to designate a grid function defined over a discrete spatio-temporal grid, evaluated at time step $n \in \mathbb{N}_0$ and grid point $l \in \mathbb{Z}$, such that $u_l^n \triangleq u(lh, nk)$.

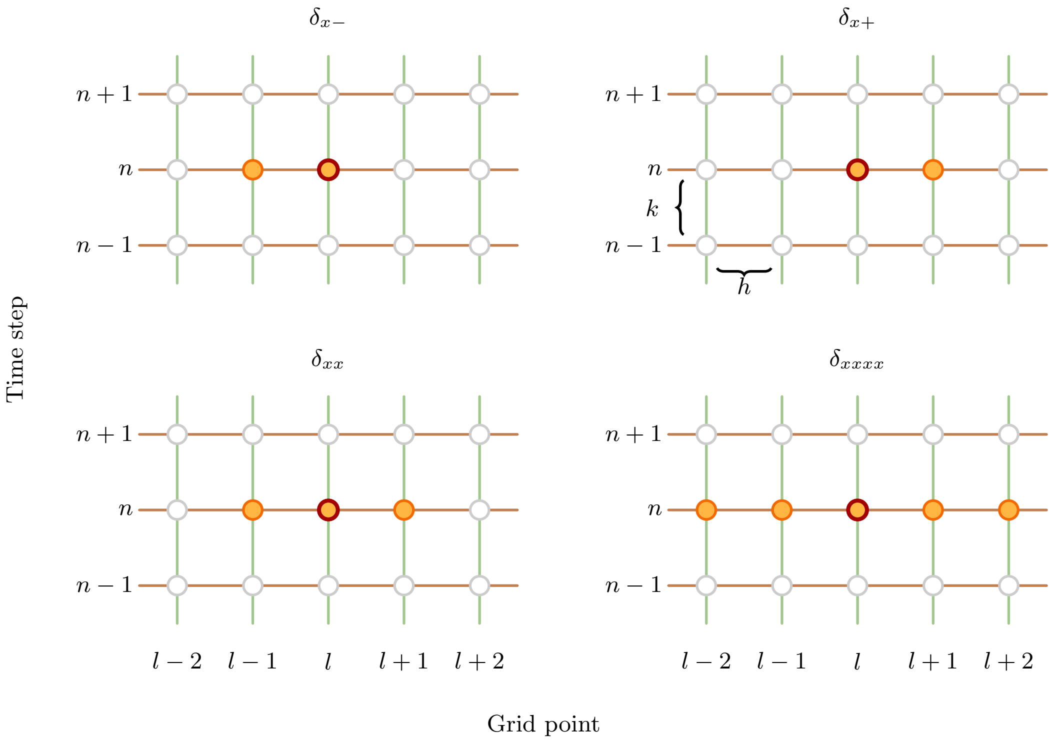

Figure 2.6: From top-left to bottom-right, in reading order: stencils of δ_{x-}, δ_{x+}, δ_{xx}, and δ_{xxxx} on the spatio-temporal grid, when centred on time step n and grid point l.

Accuracy analysis and issues related to partial and total differentiation are analogous to those evoked in Section 2.2.2.ii for temporal operators. Note that, when dealing with finite spatial domains, the spatial difference operators may call to grid values outside the domain of definition; as will be clarified in Sections 2.2.4.ii and 2.2.5.ii, the points located at the edge of the spatial grid must be treated separately, and in concordance with the system's boundary conditions. Figure 2.6 illustrates the spatio-temporal grid upon which 1D schemes are defined, and shows the stencils of all spatial FD operators used in this work.

2.2.3.ii Mixed time and space derivatives

As temporal and spatial FD operators can each approximate both total and partial differentiation, they can all operate on time-dependent grid functions; it is also straightforward to extend their use to the approximation of cross-term partial derivatives. For instance, partial differentiation with respect to time (first order) and space (second order) can be approximated by:

$$\delta_{t-}\delta_{xx} = \partial_t \partial_x^2 + O(h^2) + O(k) \tag{2.51a}$$

$$\delta_{t\cdot}\delta_{xx} = \partial_t \partial_x^2 + O(h^2) + O(k^2) \tag{2.51b}$$

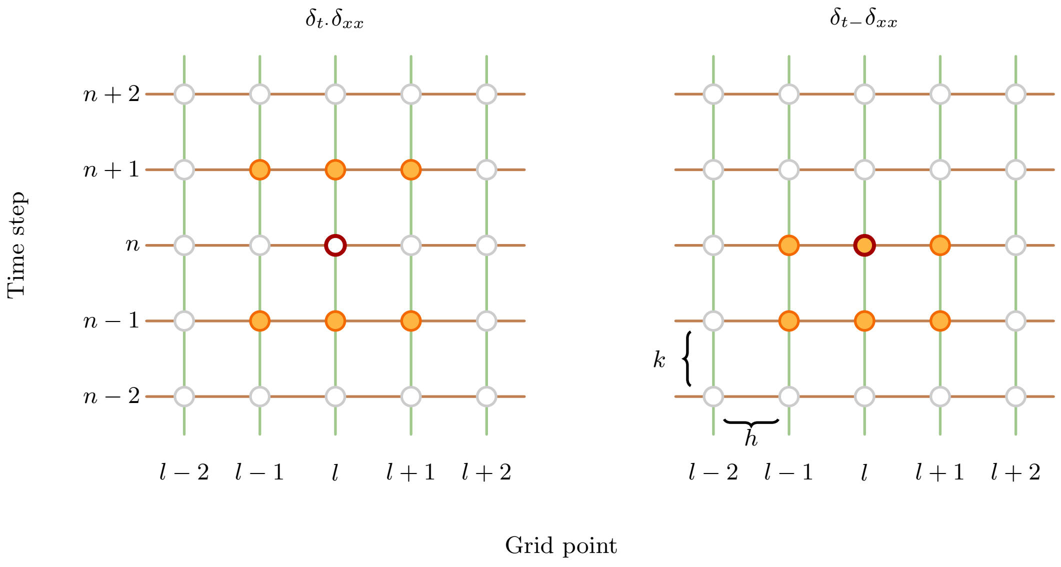

Figure 2.7: Stencils of the operators $\delta_{t\cdot}\delta_{xx}$ (left) and $\delta_{t-}\delta_{xx}$ (right) over the space-time discrete grid, when centred on time step n and grid point l.

The stencils of $\delta_{t\cdot}\delta_{xx}$ and $\delta_{t-}\delta_{xx}$ are shown on Figure 2.7. Stencils can also be drawn for full FD schemes, involving multiple operators; examples will be given later on, when presenting the schemes for the ideal and stiff string equations (see Sections 2.2.4.vii and 2.2.5.vii).

2.2.3.iii Matrix notation

Solving a PDE system with FD methods requires the rearrangement of proposed schemes into temporal recursion relations, which allow the state of the system at a future time step to be computed from past states. A distinction must then be made between explicit schemes, which allow the future state to be computed independently for each grid point, and implicit schemes, for which the future state of a particular grid point is coupled to that of its neighbours, requiring the solution of a linear system to update the grid values at each time step. Implicit schemes are therefore generally more computationally expensive than their explicit counterparts; however, as will be demonstrated throughout the rest of this study, they can exhibit accuracy and stability advantages (see, for instance, Section 3.5), and are invaluable when treating nonlinear problems (see Chapter 4).

It is therefore helpful to introduce matrix notations for the spatial FD operators, allowing them to operate on state vectors, the elements of which are the values of the grid function at each grid point within the discrete spatial domain. For a grid function u_l^n defined over $l \in \mathbb{Z}$, and $n \in \mathbb{N}_0$, the state vector $\mathbf{u}^n$ at time step n is defined as:

$$\mathbf{u}^n \triangleq \left[\ldots, u_{l-1}^n, u_l^n, u_{l+1}^n, \ldots\right]^{\mathsf{T}} \tag{2.52}$$

where ^{T} indicates transposition. Note that the temporal FD operators can be applied directly to the state vector $\mathbf{u}^n$, e.g.:

$$\delta_{t-}\mathbf{u}^n = \frac{1}{k}\left(\mathbf{u}^n - \mathbf{u}^{n-1}\right) \tag{2.53a}$$

$$\mu_{t\cdot}\mathbf{u}^n = \frac{1}{2}\left(\mathbf{u}^{n+1} + \mathbf{u}^{n-1}\right) \tag{2.53b}$$

Let the bold notation $\boldsymbol{\delta}$, applicable to all spatial FD operators, indicate that they operate element-wise over entire state vectors $\mathbf{u}^n$ instead of individual grid values u_l^n. For example, let the effect on $\mathbf{u}^n$ of the vector equivalents $\boldsymbol{\delta}_{x-}$ and $\boldsymbol{\delta}_{xx}$ of the respective local operators δ_{x-} and δ_{xx} be:

$$\boldsymbol{\delta}_{x-}\mathbf{u}^n \triangleq \left[\ldots, \delta_{x-}u_{l-1}^n, \delta_{x-}u_l^n, \delta_{x-}u_{l+1}^n, \ldots\right]^{\mathsf{T}} \tag{2.54a}$$

$$\boldsymbol{\delta}_{xx}\mathbf{u}^n \triangleq \left[\ldots, \delta_{xx}u_{l-1}^n, \delta_{xx}u_l^n, \delta_{xx}u_{l+1}^n, \ldots\right]^{\mathsf{T}} \tag{2.54b}$$

The action of spatial operators on the grid function u_l^n can now be computed as a matrix-vector multiplication, with the appropriate general matrix representations:

$$\mathbf{D}_{x-} \triangleq \frac{1}{h}\begin{bmatrix} \ddots & & & & 0 \\ \ddots & 1 & & & \\ & -1 & 1 & & \\ & & -1 & 1 & \\ 0 & & & \ddots & \ddots \end{bmatrix} \tag{2.55a}$$

$$\mathbf{D}_{x+} \triangleq -\mathbf{D}_{x-}^{\mathsf{T}} \tag{2.55b}$$

$$\mathbf{D}_{xx} \triangleq \mathbf{D}_{x+}\mathbf{D}_{x-} \tag{2.55c}$$

$$\mathbf{D}_{xxxx} \triangleq \mathbf{D}_{xx}\mathbf{D}_{xx} \tag{2.55d}$$

These matrix and state vector notations must be adapted when dealing with finite domains and the description of boundary conditions, as is the case in the rest of this work; this will be further discussed in Section 2.2.4.ii.

2.2.3.iv Key identities and manipulations

As in the continuous case, it is useful to examine the energy exchanges between internal components and external contributions of the system. To this end, discrete operations and manipulations equivalent to those used in the continuous case (see Section 2.1.1.ii) must be established for grid function.

Consider two arbitrary grid functions $\mathbf{u}^n$ and $\mathbf{v}^n$ (in vector representation), defined for time steps $n \in \mathbb{N}_0$, and over a discrete spatial domain $\mathfrak{D}$, containing an arbitrary (finite or infinite) number of points separated by a fixed grid spacing h. The discrete inner product over $\mathfrak{D}$ between $\mathbf{u}^n$ and $\mathbf{v}^n$ is given by:

$$\langle \mathbf{u}^n, \mathbf{v}^n \rangle_{\mathfrak{D}} \triangleq \sum_{l \in \mathfrak{D}} h u_l^n v_l^n = h {\mathbf{u}^n}^{\mathsf{T}} \mathbf{v}^n \tag{2.56}$$

The discrete L_2-norm of $\mathbf{u}^n$ over $\mathfrak{D}$ can be written in terms of the magnitude of $\mathbf{u}^n$:

$$\left\|\mathbf{u}^n\right\|_{\mathfrak{D}} \triangleq \sqrt{\langle \mathbf{u}^n, \mathbf{u}^n \rangle_{\mathfrak{D}}} = \sqrt{h}\left|\mathbf{u}^n\right| \ , \qquad \left|\mathbf{u}^n\right| \triangleq \sqrt{\mathbf{u}^{n\mathsf{T}}\mathbf{u}^n} \tag{2.57}$$

Familiar results, which emerge from application of the chain rule in the continuous domain, can be derived in the discrete domain by expanding temporal FD operators:

$$\left(\delta_{t\cdot}\mathbf{u}^n\right)^{\mathsf{T}}\mathbf{u}^n = \frac{1}{2}\delta_{t\pm}\left(\mathbf{u}^{n\mathsf{T}}\mathbf{u}^{n\mp1}\right) \tag{2.58a}$$

$$\left(\mu_{t\pm,\cdot}\mathbf{u}^n\right)^{\mathsf{T}}\left(\delta_{t\pm,\cdot}\mathbf{u}^n\right) = \frac{1}{2}\delta_{t\pm,\cdot}\left|\mathbf{u}^n\right|^2 \tag{2.58b}$$

It is useful to introduce the following bounds:

$$\begin{aligned}
\mathbf{u}^{n\mathsf{T}}\mathbf{u}^{n\pm1} &= \left|\mu_{t\pm}\mathbf{u}^n\right|^2 - \frac{k^2}{4}\left|\delta_{t\pm}\mathbf{u}^n\right|^2 \\
&\geqslant -\frac{k^2}{4}\left|\delta_{t\pm}\mathbf{u}^n\right|^2 && (2.58c) \\
\left|\mathbf{u}^n + \mathbf{v}^n\right| &\leqslant \left|\mathbf{u}^n\right| + \left|\mathbf{v}^n\right| && (2.58d) \\
\left|\boldsymbol{\delta}_{x\pm}\mathbf{u}^n\right| &\leqslant \frac{2}{h}\left|\mathbf{u}^n\right| && (2.58e) \\
\left|\boldsymbol{\delta}_{xx}\mathbf{u}^n\right| &\leqslant \frac{2}{h}\left|\boldsymbol{\delta}_{x\pm}\mathbf{u}^n\right| \\
&\leqslant \frac{4}{h^2}\left|\mathbf{u}^n\right| && (2.58f)
\end{aligned}$$

Consider now a finite discrete spatial domain $\mathfrak{D} \triangleq [0, \ldots, N_{\mathfrak{D}}]$, analogous to the continuous domain $\mathcal{D}$, containing $N_{\mathfrak{D}} + 1$ grid points, spaced by $h = \frac{L}{N_{\mathfrak{D}}}$. Let $\mathbf{u}^n$, $\mathbf{v}^n$ be defined over this finite domain $\mathfrak{D}$. The discrete operation analogous to integration by parts is summation by parts (SBP), and can be defined straightforwardly in terms of vector representations of the spatial operators. At a given time step, omitting the superscript n for clarity, SBP is defined as:

$$\begin{aligned}
h\,\mathbf{u}^{\mathsf{T}}\left(\boldsymbol{\delta}_{x-}\mathbf{v}\right) &= -h\left(\boldsymbol{\delta}_{x+}\mathbf{u}\right)^{\mathsf{T}}\mathbf{v} - u_0 v_{-1} + u_{N_{\mathfrak{D}}+1}v_{N_{\mathfrak{D}}} && (2.59a) \\
&= -h\left(\boldsymbol{\delta}_{x+}\underline{\mathbf{u}}\right)^{\mathsf{T}}\underline{\mathbf{v}} - u_0 v_{-1} + u_{N_{\mathfrak{D}}}v_{N_{\mathfrak{D}}} && (2.59b) \\
h\,\mathbf{u}^{\mathsf{T}}\left(\boldsymbol{\delta}_{x+}\mathbf{v}\right) &= -h\left(\boldsymbol{\delta}_{x-}\mathbf{u}\right)^{\mathsf{T}}\mathbf{v} - u_{-1}v_0 + u_{N_{\mathfrak{D}}}v_{N_{\mathfrak{D}}+1} && (2.59c) \\
&= -h\left(\boldsymbol{\delta}_{x-}\overline{\mathbf{u}}\right)^{\mathsf{T}}\overline{\mathbf{v}} - u_0 v_0 + u_{N_{\mathfrak{D}}}v_{N_{\mathfrak{D}}+1} && (2.59d)
\end{aligned}$$

Using these identities in combination yields:

$$\begin{aligned}
h\,\mathbf{u}^{\mathsf{T}}\left(\boldsymbol{\delta}_{xx}\mathbf{v}\right) &= h\left(\boldsymbol{\delta}_{xx}\mathbf{u}\right)^{\mathsf{T}}\mathbf{v} - u_0\delta_{x-}v_0 + v_0\delta_{x-}u_0 + u_{N_{\mathfrak{D}}}\delta_{x+}v_{N_{\mathfrak{D}}} - v_{N_{\mathfrak{D}}}\delta_{x+}u_{N_{\mathfrak{D}}} && (2.59e) \\
&= h\left(\boldsymbol{\delta}_{xx}\overline{\underline{\mathbf{u}}}\right)^{\mathsf{T}}\overline{\underline{\mathbf{v}}} - u_0\delta_{x-}v_0 + v_0\delta_{x+}u_0 + u_{N_{\mathfrak{D}}}\delta_{x+}v_{N_{\mathfrak{D}}} - v_{N_{\mathfrak{D}}}\delta_{x-}u_{N_{\mathfrak{D}}} && (2.59f)
\end{aligned}$$

where the notations $\overline{\mathbf{u}}$ and $\underline{\mathbf{u}}$ designate the state vector $\mathbf{u}$ truncated of its first and last element, respectively:

$$\overline{\mathbf{u}} \triangleq \left[u_1, \ldots, u_{N_{\mathfrak{D}}}\right]^{\mathsf{T}} \tag{2.60a}$$

$$\underline{\mathbf{u}} \triangleq \left[u_0, \ldots, u_{N_{\mathfrak{D}}-1}\right]^{\mathsf{T}} \tag{2.60b}$$

The boundary terms found in the continuous integration by parts also arise in the discrete case. However, the discrete boundary terms shown above make use of grid points outside the domain of definition; care must be taken in the practical implementation of discrete boundary conditions in order to deal with this issue.

2.2.4 FD scheme for the 1D wave equation

2.2.4.i Finite difference scheme

Consider the finite ideal string, fixed at both ends, characterised in Section 2.1.1. The dependent variable $w(x,t)$ is approximated by a discrete grid function w_l^n where $l \in \mathfrak{D}$ and $n \in \mathbb{N}_0$, as discussed in Sections 2.2.2 and 2.2.3.

A straightforward finite difference scheme for the 1D wave equation (2.3) can be derived from substitution of the continuous partial differential operators in (2.3) with the FD operators (2.47) and (2.50a), leading to:

$$\rho S \delta_{tt} w_l^n = T \delta_{xx} w_l^n \tag{2.61}$$

or, in vector notation:

$$\rho S \delta_{tt} \mathbf{w}^n = T \boldsymbol{\delta}_{xx} \mathbf{w}^n \tag{2.62}$$

where the state vector $\mathbf{w}^n$ is a finite vector containing $N_{\mathfrak{D}} + 1$ elements:

$$\mathbf{w}^n \triangleq \left[w_0^n, \ldots, w_l^n, \ldots, w_{N_{\mathfrak{D}}}^n\right]^{\mathsf{T}} \tag{2.63}$$

2.2.4.ii Energy analysis and boundary conditions

Taking the discrete inner product of $\delta_{t\cdot} w_l^n$ with Equation (2.61) over $\mathfrak{D}$, or, equivalently, multiplying (2.62) by $h\left(\delta_{t\cdot}\mathbf{w}^n\right)^{\mathsf{T}}$, yields the numerical energy balance:

$$\delta_{t-} \mathrm{H}_{w,s}^n = -T\left[\left(\delta_{t\cdot} w_0^n\right)\left(\delta_{x-} w_0^n\right) - \left(\delta_{t\cdot} w_{N_{\mathfrak{D}}}^n\right)\left(\delta_{x+} w_{N_{\mathfrak{D}}}^n\right)\right] \tag{2.64a}$$

$$\mathrm{H}_{w,s}^n \triangleq \frac{\rho S h}{2}\left|\delta_{t+}\mathbf{w}^n\right|^2 + \frac{Th}{2}\left(\boldsymbol{\delta}_{x-}\overline{\mathbf{w}}^n\right)^{\mathsf{T}} \boldsymbol{\delta}_{x-}\overline{\mathbf{w}}^{n+1} \tag{2.64b}$$

where the numerical energy $\mathrm{H}_{w,s}^n$ corresponds to a discrete approximation of the continuous Hamiltonian (2.14). Numerical boundary conditions arise immediately, for a string fixed at both ends, analogous to (2.17a) in the continuous case:

$$w_0^n = w_{N_{\mathfrak{D}}}^n = 0 \tag{2.65}$$

Under these conditions, $\delta_{t\cdot} w_0^n = \delta_{t\cdot} w_{N_{\mathfrak{D}}}^n = 0$, meaning that the numerical boundary terms vanish. Indeed, while the summation by parts (see Equation 2.59d) calls for the use of points outside the domain $\mathfrak{D}$, the affected expressions are each multiplied by a term that is zero-valued at every time step; grid values outside the domain of definition therefore have no influence on the energy balance. Under these particular boundary conditions, the numerical energy is conserved:

$$\delta_{t-} \mathrm{H}_{w,s}^n = 0 \tag{2.66}$$

Note that in the discrete domain, $\mathrm{H}_{w,s}^n$ is not necessarily non-negative; while the kinetic energy term is always positive, the potential energy term may become negative. This is central to stability analysis of FD schemes, as will be discussed in Section 2.2.4.iv.

2.2.4.iii Matrix forms

Matrix forms of spatial FD operators can now be defined with the appropriate size, taking the boundary conditions into account. Seeing as $\boldsymbol{\delta}_{x-}\overline{\mathbf{w}}^n$ and $\boldsymbol{\delta}_{xx}\mathbf{w}^n$ are respectively needed for the energy calculation and scheme update, a first definition of the backwards difference matrix might be written as:

$$\mathbf{D}_{x-}^{(1)} \triangleq \frac{1}{h} \left.\underbrace{\begin{bmatrix} -1 & 1 & & & & 0 \\ & -1 & 1 & & & \\ & & \ddots & \ddots & & \\ & & & -1 & 1 & \\ 0 & & & & -1 & 1 \end{bmatrix}}_{N_{\mathfrak{D}}+1}\right\} N_{\mathfrak{D}} \quad \Rightarrow \quad \boldsymbol{\delta}_{x-}\overline{\mathbf{w}}^n = \mathbf{D}_{x-}^{(1)}\mathbf{w}^n \tag{2.67}$$

Now, by the boundary conditions (2.65), the first and last elements of $\mathbf{w}^n$ will be null at all times. The first and last columns of $\mathbf{D}_{x-}^{(1)}$ will always multiply zero, and so a modified matrix can be defined as such:

$$\mathbf{D}_{x-}^{(2)} \triangleq \frac{1}{h} \left[\begin{array}{c|c|c} 0 & \underbrace{\begin{matrix} 1 & & & 0 \\ -1 & 1 & & \\ & \ddots & \ddots & \\ & & -1 & 1 \\ 0 & & & -1 \end{matrix}}_{N_{\mathfrak{D}}-1} & 0 \\ \vdots & & \vdots \\ 0 & & 0 \end{array}\right] \triangleq \frac{1}{h} \left.\left[\begin{array}{c|c|c} 0 & & 0 \\ \vdots & \underbrace{\quad \mathbf{D}_{x-}^{(3)} \quad}_{N_{\mathfrak{D}}-1} & \vdots \\ 0 & & 0 \end{array}\right]\right\} N_{\mathfrak{D}} \tag{2.68}$$

$$\Rightarrow \quad \mathbf{D}_{x-}^{(1)}\mathbf{w}^n = \mathbf{D}_{x-}^{(2)}\mathbf{w}^n = \mathbf{D}_{x-}^{(3)}\underline{\mathbf{w}}^n$$

For the sake of computational efficiency, it is worth redefining the state vector $\mathbf{w}^n$ as its interior $\underline{\mathbf{w}}^n$, as both its first and last values are known to be zero at all time steps:

$$\mathbf{w}^n \triangleq [w_1^n, \ldots, w_{N_{\mathfrak{D}}-1}]^{\mathsf{T}} \tag{2.69}$$

Similarly, $\mathbf{D}_{x-}$ is redefined as its $N_{\mathfrak{D}} \times (N_{\mathfrak{D}} - 1)$ interior:

$$\mathbf{D}_{x-} \triangleq \mathbf{D}^{(3)}_{x-} = \frac{1}{h} \underbrace{\left.\begin{bmatrix} 1 & & & 0 \\ -1 & 1 & & \\ & \ddots & \ddots & \\ & & -1 & 1 \\ 0 & & & -1 \end{bmatrix}\right\}}_{N_{\mathfrak{D}}-1} N_{\mathfrak{D}} \tag{2.70}$$

For this particular set of boundary conditions, the definitions of $\mathbf{D}_{x+}$ and $\mathbf{D}_{xx}$ given in (2.55) still hold, yielding a $(N_{\mathfrak{D}} - 1) \times (N_{\mathfrak{D}} - 1)$ Laplacian matrix:

$$\mathbf{D}_{x+} \triangleq -\mathbf{D}^{\mathsf{T}}_{x-} = \frac{1}{h} \underbrace{\left.\begin{bmatrix} -1 & 1 & & & 0 \\ & -1 & \ddots & & \\ & & \ddots & 1 & \\ 0 & & & -1 & 1 \end{bmatrix}\right\}}_{N_{\mathfrak{D}}} N_{\mathfrak{D}} - 1 \tag{2.71a}$$

$$\mathbf{D}_{xx} \triangleq \mathbf{D}_{x+}\mathbf{D}_{x-} = \frac{1}{h^2} \underbrace{\left.\begin{bmatrix} -2 & 1 & & 0 \\ 1 & -2 & \ddots & \\ & \ddots & \ddots & 1 \\ 0 & & 1 & -2 \end{bmatrix}\right\}}_{N_{\mathfrak{D}}-1} N_{\mathfrak{D}} - 1 \tag{2.71b}$$

Note that $\mathbf{D}_{xx}$ can directly multiply the truncated state vector $\mathbf{w}^n$ defined in (2.69).

For any type of fixed boundary conditions, where the first and last elements of the discrete state vectors are 0 at all times, the truncated vector may be used. In order to simplify notation, it is useful to define $N \triangleq N_{\mathfrak{D}} - 1$ as the number of elements in such truncated vector, such that:

$$h = \frac{L}{N_{\mathfrak{D}}} = \frac{L}{N+1} \tag{2.72}$$

Note that the size of $\mathbf{D}_{xx}$ is consistent with the fixed boundary conditions of Scheme (2.61). Taking, for example, the boundary point at $l = 0$:

$$w_0^n = 0 \quad \Rightarrow \quad \delta_{tt} w_0^n = 0 = \frac{T}{\rho S} \delta_{xx} w_0^n \tag{2.73}$$

The operator δ_{xx} yields a zero value when applied to the boundary points; the first and last rows of $\mathbf{D}_{xx}$ should therefore be zero.

Note that as $\mathbf{D}_{xx} = -\mathbf{D}^{\mathsf{T}}_{x-}\mathbf{D}_{x-}$, computation of the potential energy term in Equation (2.64b) can be simplified using the property $(\mathbf{AB})^{\mathsf{T}} = \mathbf{B}^{\mathsf{T}}\mathbf{A}^{\mathsf{T}}$ for arbitrary matrices $\mathbf{A}$ and $\mathbf{B}$, eliminating the need for explicit computation of the summation by parts:

$$h \left(\delta_{t\cdot} \mathbf{w}^n\right)^{\mathsf{T}} \mathbf{D}_{xx} \mathbf{w}^n = -h \left(\delta_{t\cdot} \mathbf{w}^n\right)^{\mathsf{T}} \mathbf{D}^{\mathsf{T}}_{x-} \mathbf{D}_{x-} \mathbf{w}^n$$

$$= -h \left(\delta_{t\cdot} \mathbf{D}_{x-} \mathbf{w}^n\right)^\mathsf{T} \mathbf{D}_{x-} \mathbf{w}^n$$

Identity (2.58a) then allows to obtain the energy balance (2.64a).

2.2.4.iv Stability

As discussed in Section 2.2.4.ii, the discrete potential energy may become negative. An intuitive example of this possibility calls back to the analysis of the continuous string, the main difference here being that the potential energy term is evaluated as the inner product of two different states, at two consecutive time steps, rather than the inner product of $\partial_x w(x,t)$ with itself, at one given time.

The non-negativity of the energy function is at the core of energy-based stability analysis for finite difference schemes. Lyapunov [68] states that the solutions of a system are stable if there exists a function of the state, referred to as Lyapunov function, that is:

- zero if and only if the state is zero (stable equilibrium),
- positive definite if and only if the state is non-zero,
- and decreasing[14] over time.

In the continuous case, setting the state variables to $\|\partial_t w\|$ and $\|\partial_x w\|$ lets the energy function (2.14) fulfil all three criteria to be a candidate Lyapunov function. As the bounds (2.15b) on the growth of the state variables demonstrate, the solutions to the continuous system are stable.

This is not necessarily true for the discrete solutions. The numerical energy $\mathrm{H}^n_{w,s}$ is not a positive definite function of the discrete state variables, hence violating the second Lyapunov criterion; therefore, there exist conditions under which the numerical solutions of Scheme (2.61) are unstable. Finding these conditions, and ensuring that they are never met, such that $\mathrm{H}^n_{w,s} \geqslant 0$ for all possible states, allows the design of a guaranteed stable scheme.

Identity (2.58c) and inequality (2.58e) allow (2.64b) to be rewritten as:

$$\begin{aligned}
\mathrm{H}^n_{w,s} &= \frac{\rho S h}{2} \left|\delta_{t+} \mathbf{w}^n\right|^2 + \frac{Th}{2} \left|\mu_{t+} \mathbf{D}_{x-} \mathbf{w}^n\right|^2 - \frac{Thk^2}{8} \left|\delta_{t+} \mathbf{D}_{x-} \mathbf{w}^n\right|^2 \\
&\geqslant h \left(\frac{\rho S}{2} - \frac{Tk^2}{2h^2}\right) \left|\delta_{t+} \mathbf{w}^n\right|^2 \\
&\geqslant 0 \quad \text{iff} \quad h^2 \geqslant h^2_{\mathrm{min}} \triangleq \frac{Tk^2}{\rho S} = c^2 k^2
\end{aligned} \tag{2.74}$$

Inequality (2.74) is the stability condition for Scheme (2.61). It sets a lower bound h_{min} for the grid spacing h, in terms of the time step k and the physical parameters of the string, below which solutions with frequency components close to the Nyquist limit suffer exponential growth.

---

[14] In the non-strict sense; constant or strictly decreasing.

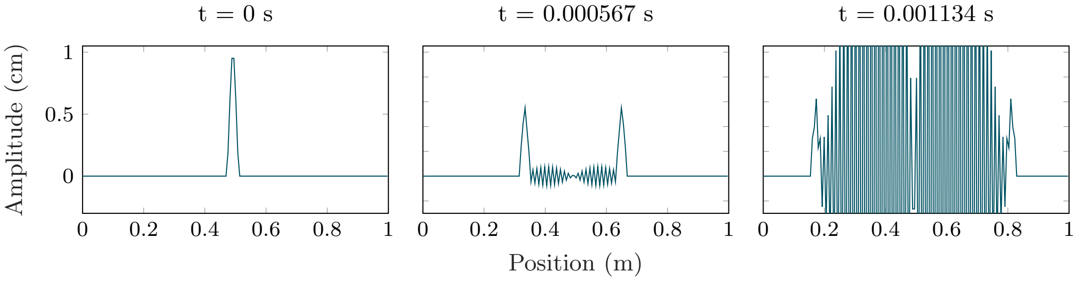

Figure 2.8: Snapshots of the simulation of the propagation of a pulse with the proposed scheme for the 1D wave equation, where the grid spacing has been set just under its minimal stable value, such that $\frac{h_{\text{min}}}{h} = 1.005$. — Parameters: $L = 1$ m, $T = 500$ N, $\rho = 7850$ kg/m^3, $r = 0.5$ mm, $F_s = 44.1$ kHz.

The stability condition can be rewritten in terms of the ratio $\frac{h_{\text{min}}}{h}$, as:

$$h \geqslant ck \qquad \Leftrightarrow \qquad \frac{h_{\text{min}}}{h} = \frac{ck}{h} \leqslant 1 \tag{2.75}$$

In practice, the time step $k = \frac{1}{F_s}$ is fixed by the sample rate; h is then adjusted to ensure stability. Note that either L or h must be slightly adjusted so that the string is divided into an integer number of segments. Throughout the rest of this work, L is adjusted for plots illustrating the effects of different values of h, while h is adjusted and L kept constant for final simulation results, so as to preserve input parameters; in both cases, the adjustments are in the order of a percent. Figure 2.8 illustrates a simulation of the propagation of a pulse with Scheme (2.61), where the stability condition is not respected ($h < h_{\text{min}}$).

2.2.4.v Accuracy

The accuracy of a given FD scheme depends on the respective accuracy of the FD operators involved, as well as the relation between grid spacing and time step imposed by the stability condition. In the case of Scheme (2.61), the definitions of FD operators δ_{tt} and δ_{xx} given in Section 2.2.2.ii lead to:

$$\rho S\delta_{tt} - T\delta_{xx} = \rho S\partial_t^2 - T\partial_x^2 + O(k^2) + O(h^2) \tag{2.76}$$

The scheme is second-order accurate in space and time.

For ideal string simulations, a fixed grid spacing is used, as close to the stability limit $h = h_{\text{min}}$ as possible, so as to limit loss of bandwidth (the next section details the relation between available bandwidth and the value of $\frac{h_{\text{min}}}{h}$). For a given choice of $\frac{h_{\text{min}}}{h}$, the grid spacing h and time step k are related by $\frac{h_{\text{min}}}{h} = \frac{ck}{h}$, and the scheme accuracy can be expressed in terms of h or k only. It can be shown that for $\frac{h_{\text{min}}}{h} = 1$, meaning that $h = ck$, Scheme (2.61) is exact, and its numerical integration yields exact solutions to the 1D wave equation (to machine accuracy), as will be seen in the next section.

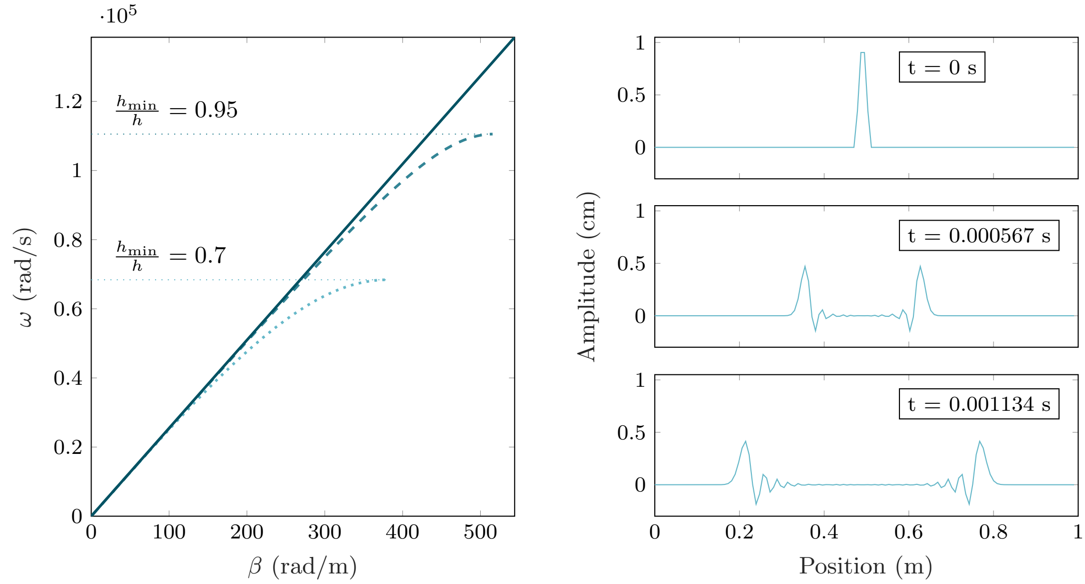

Figure 2.9: Left: numerical dispersion relation $\omega(\beta)$ for Scheme (2.61) for the 1D wave equation, in 3 different conditions: $\frac{h_{\min}}{h} = 1$ (in solid dark blue; this is in fact the continuous dispersion relation), $\frac{h_{\min}}{h} = 0.95$ (in dashed medium blue), and $\frac{h_{\min}}{h} = 0.7$ (in dotted light blue). Note the significantly lowered cutoff frequencies when operating away from the stability limit; about half of the total bandwidth is lost for $\frac{h_{\min}}{h} = 0.7$. Right: propagation of a pulse simulated with $\frac{h_{\min}}{h} = 0.7$; note that high frequencies are trailing behind the main pulse. — Parameters: $L = 1$ m, $T = 400$ N, $\rho = 7850$ kg/m^3, $r = 0.5$ mm, $F_s = 44.1$ kHz.

2.2.4.vi Numerical dispersion

The continuous 1D wave equation is non-dispersive, as seen in Section 2.1.1.ii. A similar analysis can be performed for the FD scheme. Assume, for the scope of this paragraph, an infinite ideal string, implying that the grid function w_l^n is defined for $l \in \mathbb{Z}$.

It was shown in Section 2.1.1.iii that frequency-domain analysis in the continuous domain could be simplified by inserting an ansatz of the form $w(x,t) \triangleq e^{j(\omega t + \beta x)}$ into the PDE. In the discrete domain, the ansatz naturally takes the form $w_l^n = e^{j(\omega n k + \beta l h)}$; insertion into Scheme (2.61) leads to the discrete dispersion relation:

$$\sin\left(\frac{\omega k}{2}\right) = \pm \frac{h_{\min}}{h} \sin\left(\frac{\beta h}{2}\right) \quad \Rightarrow \quad \omega = \pm \frac{2}{k} \sin^{-1}\left(\frac{h_{\min}}{h} \sin\left(\frac{\beta h}{2}\right)\right) \tag{2.77}$$

Immediately, the stability condition found in (2.75) is confirmed to be not only sufficient, but necessary. Indeed, $h < h_{\min}$ produces arguments beyond the domain of definition of $\sin^{-1}$ near the extrema of $\sin\left(\frac{\beta h}{2}\right)$.

At the stability limit, that is when $h = h_{\min}$, (2.77) reduces to the same relation (2.12) as in the continuous case, resulting in constant and equal phase and group velocities, and a non-dispersive scheme; this is consistent with the exact nature of the scheme for $h = h_{\min}$.

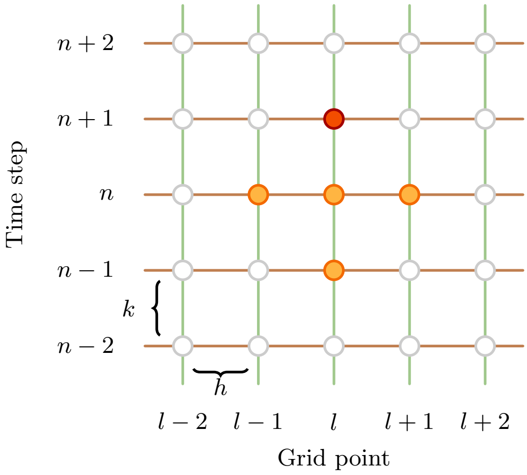

Figure 2.10: Stencil of the proposed FD scheme for the 1D wave equation. The filled red circle denotes the location of the updated grid value; as its calculation only depends on values at previous time steps (i.e., there are no yellow circles on the $n+1$ line), the scheme is explicit.

However, in the general case where $h > h_{\text{min}}$, ω no longer depends linearly on β, and numerical dispersion arises. Furthermore, the maximum representable frequency progressively decreases below the Nyquist limit $f_{\text{Ny}} \triangleq \frac{F_s}{2} = \frac{1}{2k}$, gradually restricting the available bandwidth:

$$\left|\sin\left(\frac{\omega k}{2}\right)\right| < 1 \qquad \Rightarrow \qquad \frac{\omega k}{2} < \frac{\pi}{2} \qquad \Rightarrow \qquad f = \frac{\omega}{2\pi} < f_{\text{Ny}} \tag{2.78}$$

Figure 2.9 illustrates the numerical dispersion relation for Scheme (2.61), at the stability limit as well as for $\frac{h_{\text{min}}}{h} < 1$, where the loss of bandwidth rapidly becomes problematic.

2.2.4.vii Scheme update

A recurrence vector equation is derived from (2.62) by expanding δ_{tt}, yielding:

$$\mathbf{w}^{n+1} = \left(\frac{Tk^2}{\rho S}\mathbf{D}_{xx} + 2\mathbf{I}\right)\mathbf{w}^n - \mathbf{w}^{n-1} \tag{2.79}$$

where $\mathbf{I}$ is the $N \times N$ identity matrix. The value of the string displacement at time step $n+1$ depends on its value at the two immediately preceding time steps n and $n-1$; the recurrence relation therefore requires two initial conditions, $\mathbf{w}^0$ and $\mathbf{w}^1$.

The scheme is explicit, as all grid values can be directly and independently computed from the known previous states. The stencil corresponding to Scheme (2.61) is illustrated in Figure 2.10.

The numerical energy $\mathrm{H}^n_{w,s}$ associated with Scheme (2.61) should be conserved over time, by virtue of (2.66). Figure 2.11 shows the numerical energy exchanges as computed throughout a simulation run, and the conservation of $\mathrm{H}^n_{w,s}$ to machine accuracy. The grid point values along the string were initialised with low-pass filtered white noise, so as to emulate a smooth randomised initial displacement, with zero initial velocity.

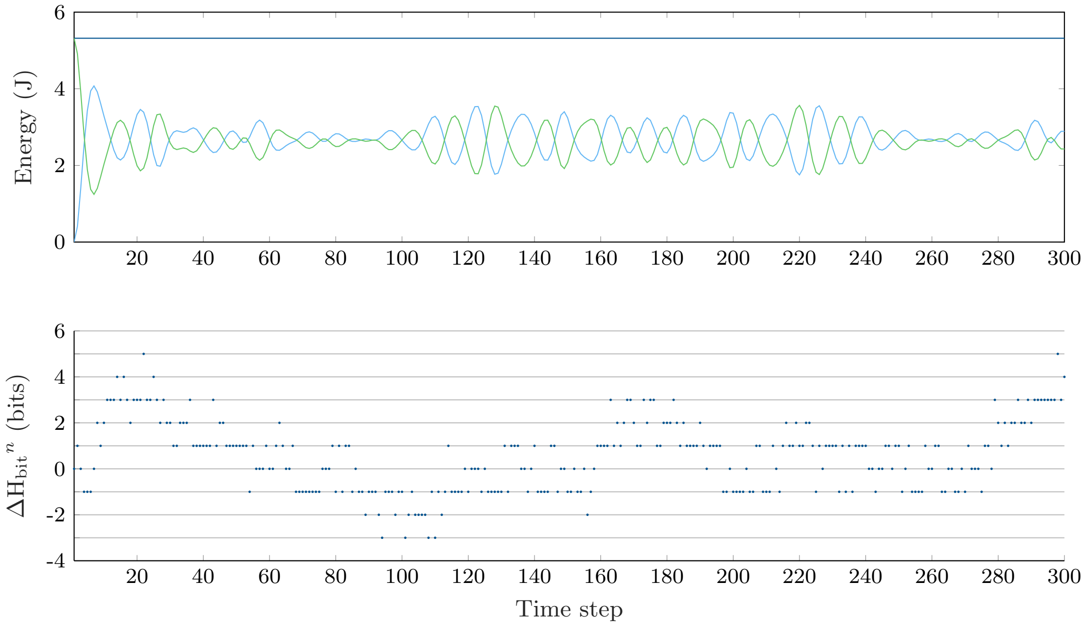

Figure 2.11: Top: total numerical energy $\mathrm{H}^n_{w,s}$ (in dark blue), sum of the kinetic (in light blue) and potential (in green) energy terms. Bottom: normalised energy variations of $\mathrm{H}^n_{w,s}$ relative to $\mathrm{H}^0_{w,s}$; due to floating-point rounding errors, $\mathrm{H}^n_{w,s}$ deviates by a few bits either side of $\mathrm{H}^0_{w,s}$ as the simulation progresses. The energy is therefore said to be conserved to machine accuracy. — Parameters: $L = 1$ m, $T = 100$ N, $\rho = 7850$ kg/m^3, $r = 0.5$ mm, $F_s = 44.1$ kHz.

The normalised energy variations in bits are calculated as follows:

$$\Delta \mathrm{H}^n_{\mathrm{bit}} \triangleq \frac{\mathrm{H}^n_{w,s} - \mathrm{H}^0_{w,s}}{\varepsilon^n_{\mathrm{H}}} \tag{2.80}$$

where $\varepsilon^n_{\mathrm{H}}$ is the floating point resolution of $\mathrm{H}^n_{w,s}$ (in joules per bit), that is the distance between $\mathrm{H}^n_{w,s}$ and the next largest number (in magnitude) describable in floating point representation.

2.2.5 FD scheme for the stiff string equation

2.2.5.i Finite difference scheme

Consider once more the transverse displacement $w(x,t)$ of a finite stiff string, discretised into a grid function w^n_l. A straightforward FD scheme for the stiff string equation (2.25) is given by:

$$\rho S \delta_{tt} w^n_l = T \delta_{xx} w^n_l - E I_0 \delta_{xxxx} w^n_l \tag{2.81}$$

As systems start to incorporate more elements, a more compact expression may be sought, in terms of a single linear operator L, the FD counterpart to $\mathcal{L}$ defined in (2.26):

$$\mathsf{L} w^n_l = 0 \,, \qquad \mathsf{L} = \rho S \delta_{tt} - T \delta_{xx} + E I_0 \delta_{xxxx} \tag{2.82}$$

Scheme (2.81) can also be written in vector form, with $\mathbf{w}^n$ the full state vector (including boundary points) defined in (2.63):

$$\rho S \delta_{tt} \mathbf{w}^n = T \boldsymbol{\delta}_{xx} \mathbf{w}^n - EI_0 \boldsymbol{\delta}_{xxxx} \mathbf{w}^n \tag{2.83}$$

2.2.5.ii Energy analysis and boundary conditions

As applied to the ideal string scheme, multiplying (2.83) by $h \left(\delta_{t\cdot} \mathbf{w}^n\right)^\mathsf{T}$ yields the numerical energy balance:

$$\begin{aligned}\delta_{t-} \mathrm{H}^n_{w,s} = {} & -T \left[\left(\delta_{t\cdot} w_0^n\right) \left(\delta_{x-} w_0^n\right) - \left(\delta_{t\cdot} w_{N_\mathfrak{D}}^n\right) \left(\delta_{x+} w_{N_\mathfrak{D}}^n\right) \right] \\ & - EI_0 \left[\left(\delta_{xx} w_0^n\right) \left(\delta_{x-} \delta_{t\cdot} w_0^n\right) - \left(\delta_{xx} w_{N_\mathfrak{D}}^n\right) \left(\delta_{x+} \delta_{t\cdot} w_{N_\mathfrak{D}}^n\right) \right. \\ & \left. - \left(\delta_{t\cdot} w_0^n\right) \left(\delta_{x-} \delta_{xx} w_0^n\right) + \left(\delta_{t\cdot} w_{N_\mathfrak{D}}^n\right) \left(\delta_{x+} \delta_{xx} w_{N_\mathfrak{D}}^n\right) \right]\end{aligned} \tag{2.84a}$$

$$\mathrm{H}^n_{w,s} \triangleq \frac{\rho S h}{2} \left| \delta_{t+} \mathbf{w}^n \right|^2 + \frac{Th}{2} \left(\boldsymbol{\delta}_{x-} \overline{\mathbf{w}}^n \right)^\mathsf{T} \boldsymbol{\delta}_{x-} \overline{\mathbf{w}}^{n+1} + \frac{EI_0 h}{2} \left(\boldsymbol{\delta}_{xx} \underline{\overline{\mathbf{w}}}^n \right)^\mathsf{T} \boldsymbol{\delta}_{xx} \underline{\overline{\mathbf{w}}}^{n+1} \tag{2.84b}$$

Note that as previously (see (2.64b)), the sign of $\mathrm{H}^n_{w,s}$ is undetermined. Boundary terms vanish under simply supported conditions, given by:

$$w_0^n = w_{N_\mathfrak{D}}^n = 0\,, \quad \delta_{xx} w_0^n = \delta_{xx} w_{N_\mathfrak{D}}^n = 0 \tag{2.85}$$

The energy balance equation is now:

$$\delta_{t-} \mathrm{H}^n_{w,s} = 0 \tag{2.86}$$

The numerical energy is conserved over time.

2.2.5.iii Matrix forms

While $\delta_{xx} w_0^n = \delta_{xx} w_{N_\mathfrak{D}}^n = 0$ was implied by the definition of the fixed ideal string scheme (see Equation (2.73)), it is explicitly specified for the simply supported stiff string. The resulting forms of the matrix operators are not affected; the modified matrix operators given in 2.2.4.iii can therefore be used for the simply supported stiff string scheme.

The state vector $\mathbf{w}^n$ is again redefined as its interior $\underline{\overline{\mathbf{w}}}^n$, containing $N \triangleq N_\mathfrak{D} - 1$ elements, as per (2.69):

$$\mathbf{w}^n \triangleq \left[w_1^n, \ldots, w_N \right]^\mathsf{T} \tag{2.69}$$

The truncated matrices are defined by (2.55a) and (2.71). The scheme update now requires another matrix, $\mathbf{D}_{xxxx}$, defined as:

$$\mathbf{D}_{xxxx} \triangleq \mathbf{D}_{xx}\mathbf{D}_{xx} = \frac{1}{h^4} \left.\underbrace{\begin{bmatrix} 5 & -4 & 1 & & & 0 \\ -4 & 6 & -4 & 1 & & \\ 1 & -4 & 6 & \ddots & \ddots & \\ & 1 & \ddots & \ddots & & 1 \\ & & \ddots & & 6 & -4 \\ 0 & & & 1 & -4 & 5 \end{bmatrix}}_{N}\right\} N \tag{2.87}$$

As with $\mathbf{D}_{xx}$ in the ideal string scheme, the size of $\mathbf{D}_{xxxx}$ is consistent with the scheme definition and boundary conditions. For instance, at the left boundary, Scheme (2.81) and boundary conditions (2.85) yield:

$$\rho S \underbrace{\delta_{tt} w_0^n}_{=0} = \underbrace{T\delta_{xx} w_0^n}_{=0} - EI_0 \delta_{xxxx} w_0^n \quad \Rightarrow \quad \delta_{xxxx} w_0^n = 0 \tag{2.88}$$

The operator δ_{xxxx} yields zero at the boundary points, meaning that the first and last rows of $\mathbf{D}_{xxxx}$ should be zero; this is reflected in the size of the modified matrix in (2.87).

As $\mathbf{D}_{xx}$ is symmetric, $\mathbf{D}_{xxxx}$ can equivalently be defined as $\mathbf{D}_{xxxx} = \mathbf{D}_{xx}^{\mathsf{T}}\mathbf{D}_{xx}$. The stiffness potential energy term in Equation (2.84b) can now be directly computed as:

$$\begin{aligned} h\left(\delta_{t\cdot}\mathbf{w}^n\right)^{\mathsf{T}} \mathbf{D}_{xxxx}\mathbf{w}^n &= h\left(\delta_{t\cdot}\mathbf{w}^n\right)^{\mathsf{T}} \mathbf{D}_{xx}^{\mathsf{T}}\mathbf{D}_{xx}\mathbf{w}^n \\ &= h\left(\delta_{t\cdot}\mathbf{D}_{xx}\mathbf{w}^n\right)^{\mathsf{T}} \mathbf{D}_{xx}\mathbf{w}^n \end{aligned} \tag{2.89}$$

As for the tension potential energy term, identity (2.58a) then allows derivation of the full energy balance (2.84a).

2.2.5.iv Stability

The stability of Scheme (2.81) relies on the non-negativity of the numerical energy $\mathrm{H}_{w,s}^n$, defined in (2.84b). As for the ideal string scheme, (2.58) can be used to rewrite $\mathrm{H}_{w,s}^n$ as:

$$\begin{aligned} \mathrm{H}_{w,s}^n = & \frac{\rho S h}{2}\left|\delta_{t+}\mathbf{w}_n\right|^2 + \frac{Th}{2}\left|\mu_{t+}\mathbf{D}_{x-}\mathbf{w}^n\right|^2 - \frac{Thk^2}{8}\left|\delta_{t+}\mathbf{D}_{x-}\mathbf{w}^n\right|^2 \\ & + \frac{EI_0 h}{2}\left|\mu_{t+}\mathbf{D}_{xx}\mathbf{w}^n\right|^2 - \frac{EI_0 hk^2}{8}\left|\delta_{t+}\mathbf{D}_{xx}\mathbf{w}^n\right|^2 \\ \geqslant & \, h\left(\frac{\rho S}{2} - \frac{Tk^2}{2h^2} - \frac{2EI_0k^2}{h^4}\right)\left|\delta_{t+}\mathbf{w}^n\right|^2 \\ \geqslant & \, 0 \quad \text{iff} \quad \frac{\rho S}{2} - \frac{Tk^2}{2h^2} - \frac{2EI_0k^2}{h^4} \geqslant 0 \end{aligned} \tag{2.90}$$

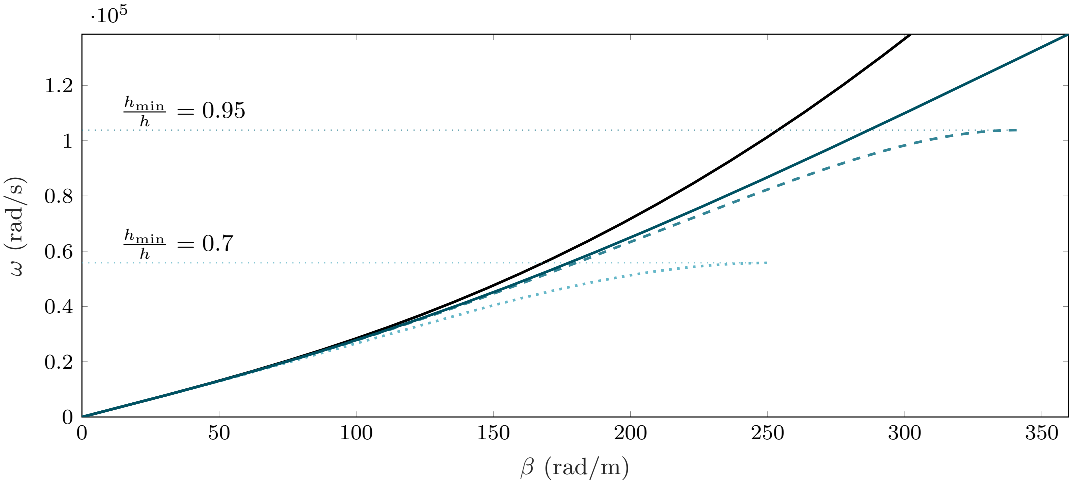

Figure 2.12: Numerical dispersion relation $\omega(\beta)$ for Scheme (2.81) for the stiff string equation, in 3 different conditions: $h = h_{\text{min}}$ (in solid dark blue, at the stability limit), $\frac{h_{\text{min}}}{h} = 0.95$ (in dashed medium blue), and $\frac{h_{\text{min}}}{h} = 0.7$ (in dotted light blue). The solid black curve corresponds to the dispersion relation in the continuous case. Note that at the stability limit, even though there is no loss of bandwidth, numerical dispersion still occurs. — Parameters: $L = 1$ m, $T = 400$ N, $\rho = 7850$ kg/m^3, $r = 0.5$ mm, $E = 200$ GPa, $F_s = 44.1$ kHz.

Rewriting (2.90) as a fourth order polynomial in h, in terms of c and κ, leads to:

$$h^4 - c^2k^2h^2 - 4\kappa^2k^2 \geqslant 0 \qquad \Rightarrow \qquad h \geqslant h_{\text{min}} \triangleq \sqrt{\frac{c^2k^2 + \sqrt{c^4k^4 + 16\kappa^2k^2}}{2}} \tag{2.91}$$

which is the stability condition for Scheme (2.81).

2.2.5.v Accuracy

The accuracy of Scheme (2.81) is that of the operator L, defined in (2.82):

$$\mathsf{L} = \mathcal{L} + O(k^2) + O(h^2) \tag{2.92}$$

The scheme is, again, second-order accurate in space and time. As for the ideal string scheme, the accuracy can be given in terms of k or h alone, if h is defined in terms of k (as per (2.91)).

2.2.5.vi Numerical dispersion

Section 2.1.2.iii showed that the continuous stiff string equation was inherently dispersive. The analysis of numerical dispersion for the stiff string scheme follows the same process as that used for the ideal string scheme (see Section 2.2.4.vi). For this analysis only, assume an infinite stiff string ($l \in \mathbb{Z}$), and a discrete test solution of the form $w_l^n = e^{j(\omega nk + \beta lh)}$. Substituting this test

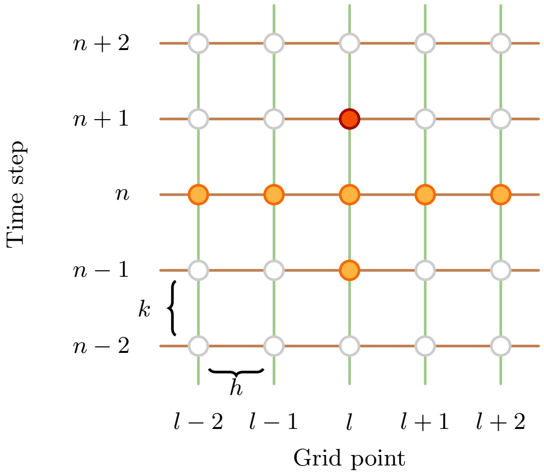

Figure 2.13: Stencil of the proposed FD scheme for the stiff string equation. The calculation of the grid value at time step $n+1$ (in red) only requires points at past time steps (in yellow); the scheme is explicit.

solution into (2.81) leads to:

$$\sin\left(\frac{\omega k}{2}\right) = \pm\sqrt{\frac{c^2k^2}{h^2} + \frac{4\kappa^2k^2}{h^4}\sin^2\left(\frac{\beta h}{2}\right)}\,\sin\left(\frac{\beta h}{2}\right)$$
$$\Rightarrow \quad \omega = \pm\frac{2}{k}\sin^{-1}\left(\sqrt{\frac{c^2k^2}{h^2} + \frac{4\kappa^2k^2}{h^4}\sin^2\left(\frac{\beta h}{2}\right)}\,\sin\left(\frac{\beta h}{2}\right)\right) \tag{2.93}$$

Here, as opposed to the ideal string scheme, numerical dispersion occurs even at the stability limit, when $h = h_{\mathrm{min}}$. Figure 2.12 compares the dispersion relations for the continuous model and the numerical scheme, at the stability limit and below.

2.2.5.vii Scheme update

A two-step recurrence vector equation can be derived from (2.81):

$$\mathbf{w}^{n+1} = \left(\frac{Tk^2}{\rho S}\mathbf{D}_{xx} - \frac{EI_0k^2}{\rho S}\mathbf{D}_{xxxx} + 2\mathbf{I}\right)\mathbf{w}^n - \mathbf{w}^{n-1} \tag{2.94}$$

where $\mathbf{I}$ is the $N \times N$ identity matrix. Again, this two-step recursion requires two initial conditions, $\mathbf{w}^0$ and $\mathbf{w}^1$, and the scheme is explicit. The stencil corresponding to the stiff string FD scheme (2.81) is shown in Figure 2.13.

Figure 2.14 shows the numerical energy exchanges throughout the simulation of a stiff string with the proposed scheme, as well as the normalised bit variations of the total energy $\Delta\mathrm{H}^n_{\mathrm{bit}}$, computed as per (2.80).

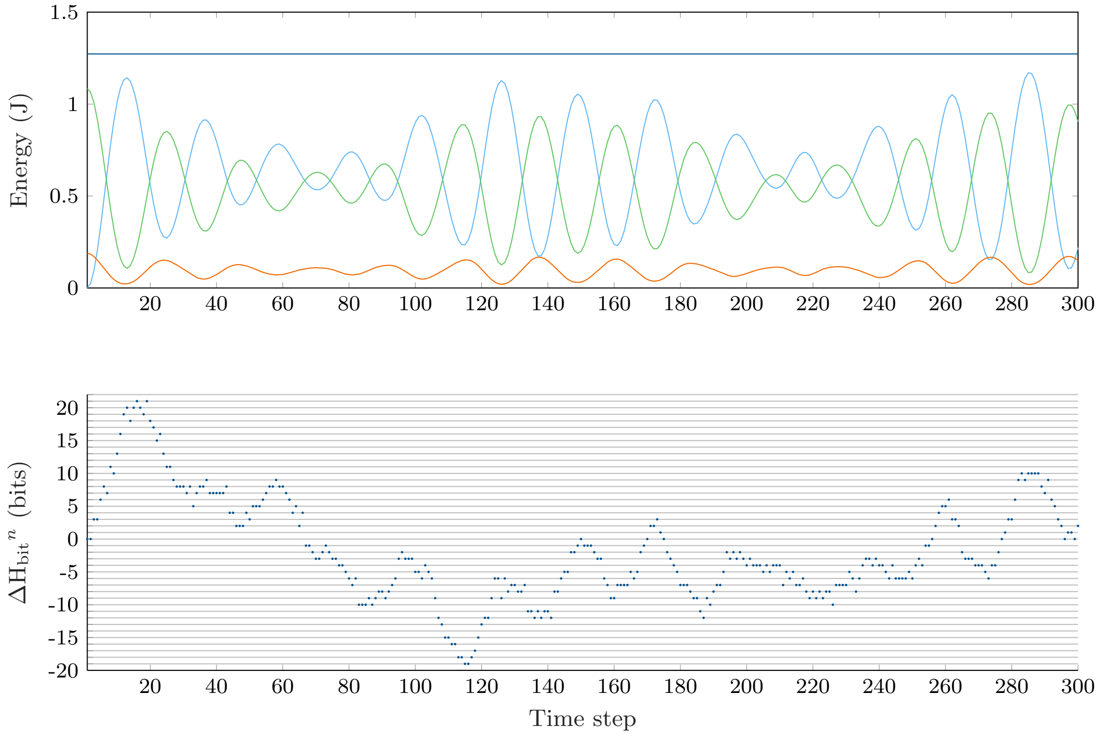

Figure 2.14: Top: total numerical energy $\mathrm{H}^n_{w,s}$ (in dark blue), sum of the kinetic energy (in light blue), potential energy due to tension (in green), and potential energy due to stiffness (in orange). Bottom: normalised energy variations of $\mathrm{H}^n_{w,s}$ relative to $\mathrm{H}^0_{w,s}$. As in the case of the ideal string, the discrete energy is conserved to machine accuracy. — Parameters: $L = 1$ m, $T = 100$ N, $\rho = 7850$ kg/m^3, $r = 0.5$ mm, $E = 200$ GPa, $F_s = 44.1$ kHz.

Concluding remarks

A physical and numerical framework has now been established, through a detailed case study of the ideal string and the stiff string systems. These systems are extremely simplified, and there indeed exist exact analytical solutions to the equations of motion describing their behaviour, rendering local time-stepping methods somewhat redundant. However, the same numerical framework can be used to simulate more complex phenomena, as long as they are describable by a system of PDEs. The next Chapter will focus on establishing such a time-domain description for the modelling of frequency-dependent damping in linear strings, thus adding a perceptually important component to the linear stiff string model presented here.

Chapter 3

Time-domain modelling of frequency-dependent damping in linear strings

The purpose of this chapter is to propose a time-domain representation of existing models for the physical phenomena causing energy dissipation in linear strings, and which lie at the origin of the particular frequency-dependent decay profile observable experimentally. A method will be proposed to obtain frequency-dependent expressions for Q-factors and decay rates with a passive time-domain system, involving a number of free parameters. An optimisation routine will be used to fit such parameters so that the resulting loss profile closely matches the theoretical damping ratios. The quality of the fit will be evaluated at various orders of approximation, in order to determine the best compromise between computational efficiency and accurate modelling.

The fitted parameters will then be used as input for time-domain simulations, computed with a FD scheme discretising the passive system. Quality factors will finally be measured for the simulated transverse modes, in order to verify that the resulting loss profile indeed matches the theoretical model.

Section 3.1 is a brief introduction to the principles of frequency-domain analysis in the context of transient regimes. In Section 3.2, models for damping processes in linear strings are reviewed, as found in the literature, and used to derive a general complex impedance as a function of string parameters. A frequency-domain framework is introduced in Section 3.3, useful to approximate the theoretical loss model, based on the principles of network synthesis. Section 3.4 describes the process of fitting the approximated loss profile to the theoretical model; representative optimisation results are discussed. Section 3.5 features the description of a FD scheme used to produce time-domain simulations of the optimised system. Finally, results from these simulations are presented in Section 3.6, assessed on a number of accuracy and efficiency criteria.

Some aspects of the work presented in this chapter were described in [30].

3.1 Introducing losses into the linear stiff string model

The isolated stiff string model described in Chapter 2.1.2 serves as a starting point for this study. It is perfectly energy-conserving, as no damping mechanisms are taken into account; it is thus obviously not applicable to the modelling of real strings, with decay times typically on the order of a few seconds. Careful reproduction of the frequency-dependent loss profile of the string's transverse modes is crucial when targeting high-quality sound synthesis.

Several attempts at modelling arbitrary frequency-dependent dynamic behaviour have been made in the space-time domain. Of particular interest to musical acoustics is the work by Chaigne, Lambourg, and Matignon [20, 65] on damped impacted plates, employing a frequency-domain description similar to that presented in this work. Time-domain modelling of viscothermal losses in acoustic pipes has also been the subject of a number of studies [49, 51, 110, 9]. Most closely related to the current problem, is a recent publication by Parret-Fréaud *et al.* [79], establishing a method to reproduce the behaviour of a given material, directly in the discrete time domain; results are presented for longitudinal wave propagation along a cantilever beam. Their proposed approach relies on approximating the frequency-dependent dynamic modulus[1] of the material, measured experimentally, as the transfer function of a digital filter, itself constructed as a passive network of one-pole filters. Although presented in the context and framework of linear viscoelasticity theory, the work described in [79] thus shares similar goals (and indeed, a similar modelling process) to those discussed in this Chapter — the main difference would be the optimisation of filter coefficients in the discrete time domain, as opposed to the continuous domain fitting presented here (see Sections 3.3 and 3.4).

When the more specific problem of stiff string damping is concerned, two particular approaches stand out, both making use of FD schemes similar to those employed in this work. The first was developed by Ruiz in his 1970 Masters thesis [89], published a year later as a pair of journal articles [52, 53], and was seen again in the work of Chaigne and Askenfelt [18]. The second approach was more recently proposed by Bensa *et al.* [7], and has been employed for sound synthesis of piano strings [16, 17]. The suitability of these two simplified approaches will be reviewed in more detail in Section 3.3.4, showing that more refined modelling of damping processes is necessary.

Preamble: the Laplace transform

In Chapter 2, the analysis of single-frequency wave solutions of the lossless stiff string equation led to the derivation of dispersion relations, linking the temporal and spatial frequencies of such waves as they propagate along the string. When damping or forcing is introduced, however, a crucial point of interest then becomes the transient response of the system, and its dependence on frequency.

---

[1] The dynamic modulus of a viscoelastic material is the complex ratio of measured stress to an applied oscillatory strain; it is a function of frequency.

To this end, and throughout the rest of this work, test solutions of the form $e^{st+j\beta x}$ will be employed, where $s = \sigma + j\omega$ is a complex temporal frequency, and $\beta \in \mathbb{R}$ is a real wavenumber[2]. When $\sigma < 0$, this is simply an exponentially damped wave, with decay rate $-\sigma$ (s^{-1}). The steady-state, periodic wave test solution is to the Fourier transform what the new test solution, being a function of a complex frequency s, is to the Laplace transform. This test solution will be inserted into the PDE system under the assumption that the string is infinite in space and time, leading to a characteristic polynomial in s and β; this yields not only a dispersion relation, but also the frequency dependence of the decay rate σ.

For example, inserting the test solution $w(x,t) = e^{st+j\beta x}$ into the lossless stiff string equation (2.25), and separating the real and imaginary parts of the resulting polynomial, yields:

$$\begin{aligned} s^2 + c^2\beta^2 + \kappa^2\beta^4 = 0 \qquad &\Rightarrow \begin{cases} \sigma^2 - \omega^2 + c^2\beta^2 + \kappa^2\beta^4 = 0 \\ 2\sigma\omega = 0 \end{cases} \\ &\Rightarrow \begin{cases} \omega^2 = c^2\beta^2 + \kappa^2\beta^4 \\ \sigma = 0 \end{cases} \end{aligned} \tag{3.1}$$

The dispersion relation (2.27) is found again, and $\sigma = 0$ indicates no damping. It is easy to see that adding terms to the lossless stiff string PDE (2.25) may result in a non-zero value of σ, possibly depending on the frequency ω. In particular, and as will be seen later on in this chapter, terms introducing a dependency on time history of the state variables, in the form of odd-order temporal derivatives, give rise to a non-zero imaginary part to the dispersion relation (3.1).

As will be demonstrated throughout the rest of this Chapter, loss will be assumed small enough that it does not significantly affect the modal frequencies, meaning that the dispersion relation (3.1) remains approximately valid after the introduction of damping.

3.2 A review of damping mechanisms in linear strings

The basis of this work is the model derived by Cuesta and Valette [23, 113]. They performed experimental measurements on plucked strings, and found that their results could be well explained by taking three damping mechanisms into account. The next subsections will recall the components of their linear string loss model.

3.2.1 Cuesta and Valette's study

Cuesta and Valette plucked a range of harpsichord strings, and assumed that the oscillations of each mode decayed exponentially at a frequency-dependent rate $-\sigma(\omega)$. They measured the 10 dB decay times T_{10} (s) of the transverse modes of the strings, each fixed at both ends on a highly rigid bench, so as to impede interaction with any of the string modes. They then obtained, for each string, the value of the quality factor Q for each of these modes, as a function of frequency, given by:

---

[2] On an infinite string, solutions for which β is not real are not of interest for this analysis.

$$Q \triangleq -\frac{\pi f}{\sigma} = -\frac{\omega}{2\sigma} \tag{3.2}$$

where f is the frequency (Hz) and $\sigma \triangleq -\frac{\log(10)}{T_{10}}$ is the frequency-dependent decay rate (s^{-1}); σ and $\omega \triangleq 2\pi f$ are the real and imaginary parts of the complex frequency s, respectively, as introduced in Section 3.1.

They proceeded to examine different possible damping mechanisms, the combination of which would explain the particular shape of the frequency-domain loss profile observed experimentally. In particular, they found that accounting for the contributions of three phenomena, in the frequency domain, was sufficient to offer a good fit between theory and experimental data. Sections 3.2.2 to 3.2.4 briefly review these contributions; a much more detailed account can be found in Valette and Cuesta's textbook [113].

The authors of [113] derived a frequency-dependent mechanical resistance per unit length $R(\omega) \in \mathbb{R}$ associated with each damping mechanism, under the assumption that string motion was purely periodic, i.e. that the string was forced to oscillate at a fixed frequency ω. The resulting expression was then assumed to hold true when considering free, lightly damped oscillations.

The formalism described in [113] introduces real, frequency-dependent quantities in time-domain equations, perhaps having in mind the modal solutions of the string PDE. It is, however, worth clarifying the separation between time and frequency domains, and presenting the notion of frequency-dependent mechanical resistance in terms of a more general frequency-domain complex impedance.

In a damped system, in the frequency domain, force and velocity are linearly related at the input by a complex impedance. Thus, introducing damping processes characterised by an impedance $Z(s) \in \mathbb{C}$ per unit length into the stiff string model yields the Laplace-domain equation:

$$\rho S s^2 + T\beta^2 + EI_0\beta^4 + sZ(s) = 0 \tag{3.3}$$

where the term $sZ(s)$ therefore has dimensions of force per unit area. Note that the expression for $Z(s)$ may include terms that are a function of the wavenumber $\beta(s)$.

Here, as $Z(s)$ characterises loss, it must be predominantly resistive, meaning that its imaginary part (reactance) must be small with respect to its real part (resistance), or at least small with respect to the reactance of the lossless system. Furthermore, as mentioned above, the derivation in [113] relies on the assumption that the expression for Z derived for purely periodic string motion holds true for lightly damped oscillations, that is $Z(s) \approx Z(j\omega)$. Examining the imaginary part of (3.3) then yields:

$$2\rho S\sigma\omega + \operatorname{Im}\left(sZ\left(j\omega\right)\right) = 0 \tag{3.4}$$

The modelling of strings for musical instruments (as lightly damped systems) is concerned with solutions on the s-plane that are very near the imaginary axis (as $\sigma = \mathrm{Re}(s)$ is small). The imaginary part of the loss term $sZ(j\omega)$ can therefore be approximated as:

$$\mathrm{Im}\left(sZ\left(j\omega\right)\right) = \omega\mathrm{Re}\left(Z\left(j\omega\right)\right) + \underbrace{\sigma\mathrm{Im}\left(Z\left(j\omega\right)\right)}_{\substack{\text{small near the}\\ \text{imaginary axis}}} \approx \omega\mathrm{Re}\left(Z\left(j\omega\right)\right) \tag{3.5}$$

The mechanical resistance defined by Valette and Cuesta is therefore simply the real part of the complex impedance Z, evaluated along the imaginary axis (i.e. for $s = j\omega$). The Q-factor is then extracted from (3.4), as per (3.2):

$$\frac{1}{Q} = \frac{-2\sigma}{\omega} \approx \frac{\mathrm{Re}\left(Z(j\omega)\right)}{\rho S\omega} \tag{3.6}$$

where, as before, σ may be a function of ω. Note that $Q(\omega)$ and $\mathrm{Re}\left(Z(j\omega)\right)$ have a reciprocal relationship. As will be seen in Section 3.2.5, assuming that the loss mechanisms add linearly, the inverse of the total Q-factor resulting from different damping processes can be computed as the sum of the inverses of the respective Q-factors characterising such processes.

3.2.2 Air viscosity

The first source of damping arises from the viscous drag exerted by the air onto the vibrating string. This problem was first described by Stokes [106], in the form of an infinite cylindrical pendulum oscillating through a viscous fluid. He equated the transverse motion of a cylinder through a stationary fluid to the flow of a fluid around a fixed cylinder.

Figure 3.1 shows a cross-section of the string, and illustrates the air viscosity phenomenon. As the string vibrates in one polarisation, it drags along air particles, giving rise to a flow velocity gradient in the direction orthogonal to the string surface. The air then exerts a viscous shear force onto the string, resisting its motion; as per Newton's law of friction, its magnitude is proportional to the gradient $\partial_R U$ of the tangential flow velocity $U(R, \theta, \omega)$ at the string surface, as well as to the affected surface area on the string.

The force exerted on a string surface element with surface area $\mathrm{d}A = r\mathrm{d}\theta\mathrm{d}x$ is local, as it does not depend on the position x along the string[3]. The force per unit length $\mathrm{d}F_\mathrm{a}$ (in N/m) due to air viscosity, acting at a point $(r\cos\theta, r\sin\theta)$ of the cross-section of the string (see Figure 3.1), can therefore be defined directly as:

$$\mathrm{d}F_\mathrm{a} = \mu_\mathrm{a}\, r\mathrm{d}\theta\, \partial_R U \tag{3.7}$$

where μ_a is the dynamic viscosity of air (in Pa.s).

Examination of the flow velocity profile when a string vibrates through the air at a velocity

---

[3] Considering that the string diameter is very small with respect to its length, boundary effects of air viscosity can be neglected, and the treatment presented here can assume an infinite string. As mentioned in the first paragraph of this subsection, this is an assumption also made by Stokes in his original study [106].

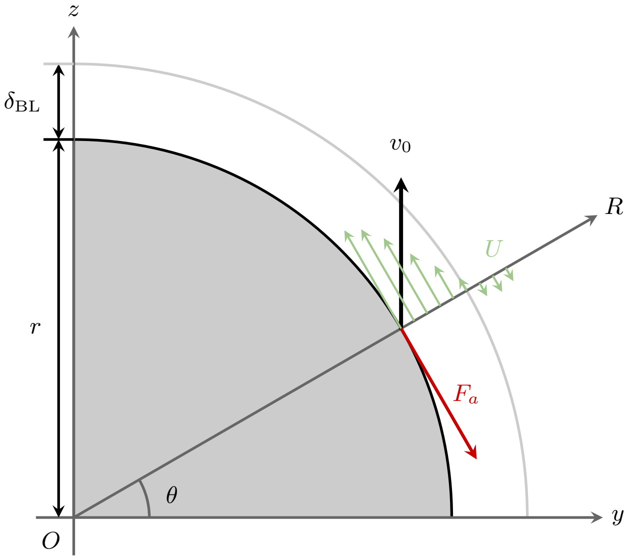

Figure 3.1: Diagram (not drawn to scale) of a cross-section of the string, oscillating along the z-axis at frequency ω, and resulting tangential air flow velocity profile $U(R, \theta, \omega)$ along the R-axis (in green). The viscous shear force F_{a} exerted by the air onto the string (in red) is proportional to the flow velocity gradient $\partial_R U$ at the string surface. Viscous phenomena may be considered to be confined to a thin boundary layer, the thickness of which depends on the frequency of the string oscillations.

v_0 (assuming periodic oscillations, i.e. $s \triangleq j\omega$) leads to rapidly decaying oscillatory solutions. Indeed, after a short distance δ_{BL} from the string surface, in the order of the characteristic length of such solutions, the flow velocity gradient becomes virtually zero. This means that viscous phenomena may be considered as confined to a thin layer of air, referred to as the viscous boundary layer [5, p. 303], the thickness of which can be derived from the solutions for the flow velocity. For this particular problem, it is a function of ω, and is defined by [113]:

$$\delta_{\mathrm{BL}} \triangleq \sqrt{\frac{\mu_{\mathrm{a}}}{2\omega\rho_{\mathrm{a}}}} \tag{3.8}$$

where ρ_{a} is the density of air (kg/m^3). In the case of lightly damped oscillations, for which $\sigma \neq 0$ and $\sigma \ll \omega$, the substitution $\omega \to -js$ yields a complex boundary layer thickness:

$$\begin{aligned} \omega \to -js \qquad \Rightarrow \qquad \delta_{\mathrm{BL}} &\triangleq \sqrt{\frac{j\mu_{\mathrm{a}}}{2\rho_{\mathrm{a}} s}} \\ &= \sqrt{\frac{\mu_{\mathrm{a}}}{2\rho_{\mathrm{a}} \left|s\right|^2}} \sqrt{j\sigma + \omega}\,, \qquad \left|s\right|^2 = \sigma^2 + \omega^2 \approx \omega^2 \\ &\approx \sqrt{\frac{\mu_{\mathrm{a}}}{2\rho_{\mathrm{a}}\omega}} \sqrt{1 + j\frac{\sigma}{\omega}} \\ &\approx \sqrt{\frac{\mu_{\mathrm{a}}}{2\rho_{\mathrm{a}}\omega}} \left(1 + j\frac{\sigma}{2\omega}\right) \end{aligned} \tag{3.9}$$

The imaginary part of δ_{BL} can be neglected for lightly damped oscillations, as $\frac{\sigma}{2\omega} \ll 1$; the expression given in (3.8) for periodic motion is assumed to hold true.

In the mid-audio range, for $f = 1\mathrm{kHz}$, $\delta_{\mathrm{BL}} = 0.034\mathrm{mm}$; for most strings used in musical instruments, the viscous boundary layer thickness is typically small with respect to the string diameter. In this case, the flow velocity gradient at any point $(r\cos\theta, r\sin\theta)$ of the surface of the string is approximately:

$$\partial_R U\,(r,\theta,\omega) \approx \frac{U(r,\theta,\omega)}{\delta_{\mathrm{BL}}} = \frac{2v_0\cos\theta}{\delta_{\mathrm{BL}}} \tag{3.10}$$

where the tangential flow velocity $U \triangleq 2v_0\cos\theta$ at the string surface depends on the string velocity v_0[4] [5, p. 357]. The total force per unit length exerted on the string, in the z-direction, can now be obtained by integrating $\mathrm{d}F_{\mathrm{a},z} = \mathrm{d}F_{\mathrm{a}}\cos\theta$ around the circular cross-section of the string[5]:

$$F_{\mathrm{a},z} = \mu_{\mathrm{a}} \int_{\theta=0}^{2\pi} \frac{2v_0\cos\theta}{\delta_{\mathrm{BL}}}\cos\theta\, r\mathrm{d}\theta = \frac{2\mu_{\mathrm{a}} r\pi}{\delta_{\mathrm{BL}}} v_0 \tag{3.11}$$

This expression for $F_{\mathrm{a},z}$ suggests a viscous force tending towards zero at low frequencies. To address this issue, and rejoin Stokes' conclusions [106], one can argue that, at low enough frequencies, the viscous force approaches its steady-flow value, given by (3.11) where the boundary layer thickness is equal to the string radius, that is $\delta_{\mathrm{BL}} = r$. The final expression for $F_{\mathrm{a},z}$ is given by the sum of the low- and high-frequency forms:

$$F_{\mathrm{a},z} = \underbrace{2\mu_{\mathrm{a}}\pi\left(1 + \frac{r}{\delta_{\mathrm{BL}}}\right)}_{\triangleq Z_{\mathrm{a}}} v_0 \tag{3.12}$$

where Z_{a} is a mechanical impedance per unit length; it follows from (3.9) that $\mathrm{Re}\,(Z_{\mathrm{a}}) \approx Z_{\mathrm{a}}$. The expression for the Q-factor related to air viscosity damping is finally obtained from (3.6), combining the expressions given in (3.12) and (3.8):

$$\begin{aligned}\frac{1}{Q_{\mathrm{a}}} &= \frac{\mathrm{Re}\,(Z_{\mathrm{a}}(j\omega))}{\rho S\omega} \\ &= \frac{2\mu_{\mathrm{a}}\pi}{\rho S\omega}\left(1 + \frac{r}{\delta_{\mathrm{BL}}}\right) \\ &= \frac{2}{\rho}\left(\frac{\mu_{\mathrm{a}}}{\omega r^2} + \sqrt{\frac{2\mu_{\mathrm{a}}\rho_{\mathrm{a}}}{\omega r^2}}\right) \qquad (3.13)\end{aligned}$$

The Q-factor Q_{a} increases with ω; the losses due to air viscosity are therefore predominant at low frequencies. The dependency in $\sqrt{\omega}$ means that air viscosity damping cannot be well represented with integer order partial derivative terms in the time domain. This is a well-known problem in time-domain modelling of viscothermal losses associated with wave propagation in tubes [49]; different approaches have been explored to tackle this issue [51, 110, 9], some of which can be adapted to the present problem, as will be described in Section 3.3.

---

[4] Recall that all quantities here, including the string velocity v_0, are defined in the frequency domain, and are in general complex-valued.

[5] It is straightforward to show, with the same method, that the total force per unit length $F_{\mathrm{a},y}$ exerted on the string element in the y-direction is zero.

The behaviour of the air surrounding the string can be fully described by a system of linear PDEs; indeed, the results above can be directly derived from the Navier-Stokes equations for incompressible flows. One could, therefore, do away with time-domain approximations of frequency-domain solutions, and tackle the full coupled problem with time-stepping simulations. However, doing so would go against the ambition of this work to design numerical schemes with efficient enough implementations so as to be usable in the context of audio synthesis. As will be seen in Section 3.7.2, accurate results can be obtained with relatively simple approximations, making the approach presented here particularly attractive for realistic, efficient sound synthesis.

3.2.3 Viscoelasticity

The second source of energy dissipation in linear string vibration is linked to the viscoelasticity of the string material. In the lossless stiff string equation (2.25), the bending stiffness term comes from evaluating the stress withstood by a string element with length dx subjected to a bending strain, assuming that the string material obeys Hooke's elasticity law (that is, stress is directly proportional to strain).

In reality, however, strings exhibit viscoelastic behaviour; when the material is subjected to a time-varying strain (such as a deformation due to the propagation of a wave), energy is dissipated by internal friction at the atomic or molecular level. Linear viscoelasticity theory generally describes behaviour at macroscopic level, at much larger scales, with constitutive laws relating stress, strain, and their respective time histories. Different classes of models arise from the choice of constitutive laws; the reader is referred to [64] for a review of such models, which are not the focus of this manuscript. It is, however, worth giving a brief overview of the microscopic phenomenon believed to be the principal cause of viscoelastic damping in metal strings[6] [113].

Internal friction damping in metallic strings arises mainly from the motion of dislocations. These one-dimensional faults in the crystal structure of the metal are distributed along the string, more or less densely. Instrument makers can increase the number of dislocations by hammering the string, or reduce it by heating up the string, thereby slightly melting the metal.

The dislocations are set into forced vibration when the string oscillates. Koehler [54], as well as Granato and Lücke [43], have conjectured that the motion of each dislocation line can be described with an elastic 1D wave equation, with viscous damping:

- a continuous "row of atoms" is detached from its neighbouring row, between two fixed anchor points;

---

[6] The following discussion concerns strings made of a material with a crystalline structure; a nylon or gut string, for instance, will not suffer dislocations.

- this dislocation line has an effective length, linear mass density, and tension;
- when set into motion, viscous friction between the vibrating dislocation and its surroundings causes energy dissipation.

Simpson and Sosin [98] later proposed to incorporate defect dragging along the dislocation line. Indeed, the Koehler-Granato-Lücke (KGL) theory considers that a newly introduced point-wise fault along a dislocation simply becomes a new, fixed anchor point, splitting the dislocation line in two. Simpson and Sosin (SS), however, considered that this defect may not be strong enough to pin the dislocation line in place, but instead it is dragged along when the dislocation is set into vibration, causing significantly more damping. Their proposed theory was experimentally validated [99] by measuring the evolution of the logarithmic decrement ζ_v on a thin copper rod, with an increasing number of defects, introduced by electron irradiation. The logarithmic decrement for underdamped systems is defined as:

$$\zeta_\mathrm{v} \triangleq \frac{\pi}{Q_\mathrm{v}} = -\frac{2\pi\sigma}{\omega} \tag{3.14}$$

For a fixed density of dislocations and defects, however, experimental measurements of ζ_v on unconstrained rods as a function of the excitation frequency show that, for relatively low forcing frequencies (i.e., in the quasi-static regime), ζ_v does not depend on frequency. Considering the scale of the problem, the quasi-static approximation is valid for frequencies below a cutoff in the order of 10 kHz; this result can therefore be reliably used for simulations of strings for musical instruments, sampled at audio frequencies.

In the frequency domain, the characteristic polynomial for the lossless unconstrained bar is obtained by setting $T = 0$ in Equation (3.1):

$$s^2 + \kappa^2\beta^4 = 0 \qquad \Rightarrow \qquad s = j\kappa\beta^2 \in j\mathbb{R}\ , \quad \kappa \triangleq \sqrt{\frac{EI_0}{\rho S}} \tag{3.15}$$

Valette and Cuesta [113] then seek to introduce a negative real part in s, to incorporate losses. They do so by introducing a small imaginary part in Young's modulus E, possibly frequency-dependent, such that $E \to (1 + j\eta)\, E$ where $\eta > 0$ is small. This approach takes its roots in viscoelasticity theory [64, Chap. 3]; the strain experienced by a linear viscoelastic material subjected to a periodic stress exhibits a short phase lag, leading to the ratio of periodic stress to strain (equal to Young's modulus for linear elastic materials) becoming complex. The resulting complex frequency s leads to the corresponding viscoelastic quality factor $Q_\mathrm{v,bar}$ for the unconstrained bar, as per (3.2):

$$s = j\kappa\sqrt{1 + j\eta}\,\beta^2 \approx j\kappa\left(1 + \frac{j\eta}{2}\right)\beta^2 \tag{3.16a}$$

$$\Rightarrow \quad \omega \approx \kappa\beta^2\ , \qquad \sigma \approx -\frac{\eta\kappa\beta^2}{2} \tag{3.16b}$$

$$\Rightarrow \quad \frac{1}{Q_\mathrm{v,bar}} = \eta = \frac{\zeta_\mathrm{v}}{\pi} = \text{constant} \tag{3.16c}$$

A frequency-independent logarithmic decrement ζ_v therefore yields a constant value for η. The same process can now be employed for the pre-stressed rod, starting with the known dispersion relation for the lossless stiff string, and noting that for strings used in musical instruments, the effects of tension largely dominate those of bending stiffness:

$$s = j\sqrt{c^2\beta^2 + \kappa^2\beta^4} = jc\beta\sqrt{1 + \frac{EI_0}{T}\beta^2} \tag{3.17a}$$

$$\begin{aligned} E \to (1 + j\eta)\, E \quad \Rightarrow \quad s &= jc\beta\sqrt{1 + (1 + j\eta)\,\frac{EI_0}{T}\beta^2} \\ &\approx jc\beta\left(1 + (1 + j\eta)\,\frac{EI_0}{2T}\beta^2\right) \end{aligned} \tag{3.17b}$$

The decay rate $\sigma(\omega) = \mathrm{Re}(s)$ and Q-factor Q_v follow as:

$$\sigma \approx -\eta c\frac{EI_0}{2T}\beta^3 \qquad \Rightarrow \qquad \frac{1}{Q_\mathrm{v}} \approx \eta c\frac{EI_0\beta^3}{T\omega} \tag{3.18}$$

The frequency dependence of Q_v can be recovered from the dispersion relation $\beta(\omega)$, given by the imaginary part of (3.17b). The real part of the corresponding mechanical impedance per unit length is given by (3.6):

$$\mathrm{Re}\left(Z_\mathrm{v}(j\omega)\right) \approx \frac{\eta EI_0}{c}\left(\beta\left(\omega\right)\right)^3 \tag{3.19}$$

In [113], it is assumed that the tension is large enough that the dispersion relation is that of the ideal string ($\omega = c\beta$), leading to $Q_\mathrm{v}^{-1} \propto \omega^2$ and $Z_\mathrm{v} \propto \omega^3$. The value of the dimensionless parameter η is undetermined; it depends on the string material, and fitting Q_v to experimental data yields values in the order of 10^{-3} [98].

3.2.4 Thermoelasticity

The third source of energy dissipation in linear strings is linked to the thermoelasticity of the string material. The bending strain to which a string element is subjected causes compression and/or expansion of the string material, leading to temperature variations across the cross-section, as per the piezocaloric effect [64, pp. 290-291]. Over time, as seen in Figure 3.2, heat

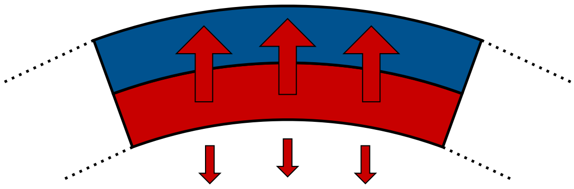

Figure 3.2: Stiff string element sustaining a bending strain. The compressed part (in red) heats up, the expanded part (in blue) cools down. The large red arrows represent heat conduction from warmer to cooler areas; the smaller arrows, pointing downwards, represent heat conduction from the string surface into the air.

is conducted from the hotter (compressed) part of the string element to the cooler (expanded) part; mechanical energy from the string motion is converted to heat, which is then irreversibly diffused within the string material, and eventually into the air. The analysis of thermoelastic damping in linear strings relies on comparing the rate at which heat is generated (i.e., the frequency of the string vibrations) with the rate at which it is conducted across the string diameter.

On the one hand, low frequency (i.e., large wavelength) string vibrations do not involve sharp deformations of the string. The compression and expansion of the string material therefore generate very little heat. This small amount of heat is conducted over distances smaller than the string diameter. The thermal diffusivity of the string material is large, allowing heat to quickly transfer from compressed to expanded areas. Since the vibration frequency is low, this transfer is fast enough that a string element has time to reach thermal equilibrium again before it is bent in the opposite direction. The process can be considered isothermal, and only minimal mechanical energy is converted to internal energy of the string material (and therefore dissipated).

On the other hand, high frequency (i.e., small wavelength) oscillations involve greater compression and expansion, and therefore larger amounts of generated heat. Since the string material sustains strains changing at much faster rates, the conduction process is too slow to be able to transfer heat from compressed to expanded areas before the local strains are reversed. The heat generated by compression is quickly dissipated when the string material is expanded again, without diffusion having taken place; the process can be considered adiabatic. Again, only a marginal amount of energy is dissipated.

Thermoelastic damping is therefore critical when heat conduction across the string's cross-section happens at similar time scales as the mechanical oscillations. Around such frequencies, the process is neither isothermal nor adiabatic, meaning that significant amounts of energy are dissipated through thermal processes. The string cannot reach thermal equilibrium before more heat is generated by compression of part of the string element, and heat builds up inside the string. The surplus heat is conducted towards the surface of the string, and dissipated into the air, assuming a constant room temperature is maintained.

Since thermoelasticity introduces a small correction over a limited frequency range, Valette and Cuesta chose to approximate the corresponding Q-factor Q_t as a constant, to be determined by fitting measurement data [113]. As will be discussed in the next subsection, this choice leads to a correction in the mid-frequency range, where neither air viscosity nor viscoelasticity dominate. The real part of the corresponding mechanical impedance per unit length $Z_\mathrm{t}(j\omega)$ is given by (3.6):

$$\mathrm{Re}\left(Z_\mathrm{t}\left(j\omega\right)\right) = \frac{\rho S \omega}{Q_\mathrm{t}} \propto \omega \tag{3.20}$$

3.2.5 Summary

Three damping mechanisms have been considered, each dissipating energy differently across the range of vibration frequencies important for musical use: air viscosity, as well as viscoelasticity

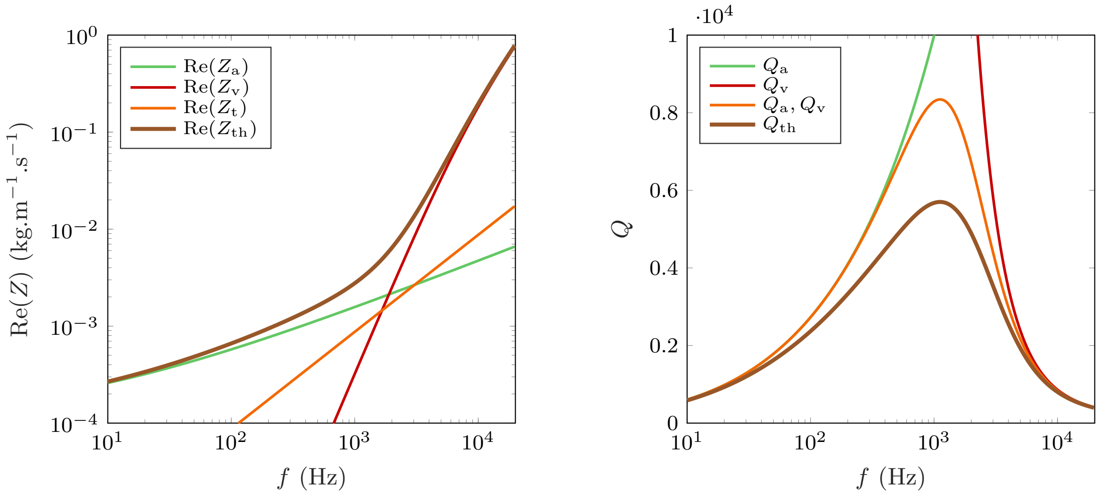

Figure 3.3: Left: impedances (real part) as a function of frequency, as derived in [113], with contributions from: air viscosity (in green); viscoelasticity (in red); thermoelasticity (in orange); all three phenomena (in brown). Right: Q-factors as a function of frequency, with contributions from: air viscosity (in green); viscoelasticity (in red); both air viscosity and viscoelasticity (in orange); all three phenomena (in brown). — Parameters: see Cello D string on page xxix. The two unknown parameters were adjusted to $Q_\mathrm{t} = 18,000$, $\zeta_\mathrm{v} = 0.003$ [113].

and thermoelasticity of the string material. Expressions for the real parts of the mechanical impedances associated with each phenomenon can be derived (or conjectured) as a function of frequency. Each process brings about a different force, all acting together to oppose the string velocity; the total equivalent mechanical impedance is the sum of those associated with each mechanism. This corresponds to a connection of impedances in series, or conversely, a structure of admittances in parallel. The real part of the total theoretical mechanical impedance per unit length $Z_\mathrm{th}(j\omega)$, and the overall Q-factor Q_th, are given by:

$$\mathrm{Re}\left(Z_\mathrm{th}\right) = \mathrm{Re}\left(Z_\mathrm{a}\right) + \mathrm{Re}\left(Z_\mathrm{v}\right) + \mathrm{Re}\left(Z_\mathrm{t}\right) \tag{3.21a}$$

$$\frac{1}{Q_\mathrm{th}} = \frac{1}{Q_\mathrm{a}} + \frac{1}{Q_\mathrm{v}} + \frac{1}{Q_\mathrm{t}} \tag{3.21b}$$

Figure 3.3 shows the Q-factor and real part of the impedance per unit length associated with each mechanism, as derived in [113], as well as the total $\mathrm{Re}\left(Z_\mathrm{th}(j\omega)\right)$ and Q_th, as a function of frequency.

It may be worth clarifying how a constant Q_t for thermoelasticity can bring about a correction on the total Q_th only when neither of the two other terms dominate. The profile of Q_th where Q_t is or isn't taken into account is illustrated on the right hand side of Figure 3.3, respectively by the brown and orange curves. The corresponding expressions are respectively given by:

$$Q_\mathrm{th}^{(\mathrm{a,v})} \triangleq \frac{Q_\mathrm{a} Q_\mathrm{v}}{Q_\mathrm{a} + Q_\mathrm{v}} \tag{3.22a}$$

$$\begin{aligned}
Q_{\mathrm{th}}^{(\mathrm{a,v,t})} &\triangleq \frac{Q_{\mathrm{a}}Q_{\mathrm{v}}Q_{\mathrm{t}}}{Q_{\mathrm{a}}Q_{\mathrm{v}}+Q_{\mathrm{a}}Q_{\mathrm{t}}+Q_{\mathrm{v}}Q_{\mathrm{t}}}\\
&= \frac{Q_{\mathrm{a}}Q_{\mathrm{v}}}{\frac{Q_{\mathrm{a}}Q_{\mathrm{v}}}{Q_{\mathrm{t}}}+Q_{\mathrm{a}}+Q_{\mathrm{v}}}\\
&\approx Q_{\mathrm{th}}^{(\mathrm{a,v})} \quad \text{iff} \quad \frac{Q_{\mathrm{a}}Q_{\mathrm{v}}}{Q_{\mathrm{t}}} \ll 1 \quad \Rightarrow \quad Q_{\mathrm{a}}Q_{\mathrm{v}} \ll Q_{\mathrm{t}}
\end{aligned} \tag{3.22b}$$

When either Q_{a} or Q_{v} is small, i.e. when losses through air viscosity or viscoelasticity are large, the total Q-factor is approximately unchanged whether or not Q_{t} is taken into account. Introducing a large, constant Q_{t} therefore brings about significant changes in the total Q_{th} in the mid-frequency range, where other damping processes do not have much effect. This is evident in Figure 3.3, where the brown and orange curves merge on the lower and higher end of the frequency spectrum.

Various approaches can now be sought to transfer the established frequency-domain loss profile into the time domain, in order to realise time-stepping simulations. The following Section 3.3 outlines the methodology and conditions that enable such transfer.

3.3 Frequency-dependent loss in the time domain: framework, principles, and past models

3.3.1 Characteristic equation

Suppose one seeks to introduce energy dissipation into the time-domain stiff string model presented in Section 2.1.2. In the Laplace domain, this is equivalent to introducing a non-zero real part to the complex frequency s. This is the starting point for the design of a FD algorithm; a system of PDEs in time and space is obtained by transferring a proposed characteristic equation in terms of s and β, designed to introduce frequency-dependent damping, back into the time domain.

To this end, consider the following characteristic equation, obtained by adding a term to that of the lossless stiff string (3.1):

$$\rho S s^2 + T\beta^2 + EI_0\beta^4 + sZ_{\boldsymbol{\chi}}(s) = 0 \tag{3.23}$$

where $Z_{\boldsymbol{\chi}}(s)$ can be interpreted as a complex impedance, function of the complex temporal frequency s, and of a set of scalar parameters as elements of a vector $\boldsymbol{\chi}$[7],. This Laplace-domain formulation originates from passive network synthesis theory [62], which seeks to design an electrical network of passive elements from a given frequency-domain transfer function. Here, $Z_{\boldsymbol{\chi}}(s)$ represents the driving-point impedance (or input impedance) of such networks [62, p. 15].

This approach is particularly relevant when considering the mechanical-electrical analogies. The dynamics of a mechanical system, as well as those of an electrical network, can be described with an effort variable (force, voltage) and a flow variable (velocity, current). Each passive electrical element (resistor, capacitor, inductor) has a lumped mechanical equivalent (damper, spring, mass). In the system described by (3.23), a passive, one-port mass-spring-damper network is driven by the force and velocity of each string element; as such, energy is drawn from the string motion and dissipated into the network, characterised by a given frequency-dependent input impedance.

---

[7] Note that, as mentioned in Section 3.2.1, the expression for $Z_{\boldsymbol{\chi}}(s)$ may involve the frequency-dependent wavenumber $\beta(s)$.

It is not guaranteed that an arbitrary form for $Z_{\boldsymbol{\chi}}$ will not only yield a definite passive (or dissipative) system, but also one that is realisable with a finite number of lumped elements (electrical or mechanical). Network synthesis pioneers [38, 15, 14] have established a set of conditions on the form of a driving-point impedance, such that the corresponding network is passive and realisable; Sections 3.3.2 and 3.3.3 review these conditions, to narrow down candidate functions for $Z_{\boldsymbol{\chi}}(s)$.

3.3.2 Condition for passivity

The proposed system must be passive, or dissipative; all solutions for the transverse displacement of the string must decay over time, in the absence of forcing terms. This is to say that all solutions of Equation (3.23) must satisfy $\mathrm{Re}(s) = \sigma \leqslant 0$, for all frequencies $\omega \in \mathbb{R}_{\geqslant 0}$ and wavenumbers $\beta \in \mathbb{R}_{\geqslant 0}$.

A condition on $Z_{\boldsymbol{\chi}}$ such that this is verified is that of positive-realness, first established by Cauer [15]. An arbitrary impedance $Z(s)$ is positive-real if and only if:

$$\begin{cases} \mathrm{Re}(s) > 0 & \Rightarrow \quad \mathrm{Re}\left(Z(s)\right) \geqslant 0\,, \quad \text{and} \\ \mathrm{Im}(s) = 0 & \Rightarrow \quad \mathrm{Im}\left(Z(s)\right) = 0 \end{cases} \tag{3.24}$$

It is straightforward to show that this condition is sufficient to ensure that all solutions of (3.23) are decaying, by showing that no solutions exist where $\sigma > 0$. Dividing (3.23) by s and examining the real part of the resulting equation yields:

$$\underbrace{\sigma\left(\rho S + \frac{T\beta^2 + EI_0\beta^4}{\sigma^2 + \omega^2}\right)}_{>0} + \underbrace{\mathrm{Re}\left(Z_{\boldsymbol{\chi}}(s)\right)}_{\substack{\geqslant 0 \text{ when } \sigma > 0, \\ \text{by (3.24)}}} = 0 \tag{3.25}$$

Equation (3.25) has no solutions when $\sigma > 0$; the system is therefore passive when $Z_{\boldsymbol{\chi}}$ is positive-real.

3.3.3 Condition for realisability

Brune [14] restricted the definition of positive-real functions to rational functions of s. He showed that this new condition is both necessary and sufficient to ensure that the proposed driving-point impedance is realisable with a one-port network of a finite number of ideal elements, and therefore describable with a system of ordinary differential equations. Indeed, such a positive-real function of s (as defined by Brune, i.e. the ratio of two polynomials each verifying (3.24)) can be written as a continued or partial fraction expansion, allowing to realise a simplified equivalent circuit[8].

Clearly, the input impedance proposed to model stiff string damping does not fit Brune's definition of positive-realness, as it is not rational (hence not realisable). For instance, as seen in Section 3.2.2, the impedance Z_a linked to air viscosity depends on $\sqrt{\omega}$; a direct transfer to the time domain of the corresponding characteristic equation (3.3) would require fractional order differentiation in time.

This irrational representation is also encountered in the modelling of viscothermal wave propagation in tubes, and can be dealt with in various ways; see, for example, [49, 51, 110, 9]. In particular, the approach used in [110, 9] is to propose an expression for the impedance as a continued or partial fraction expansion, corresponding to a canonical ladder structure of the Cauer or Foster types [15, 38], and to optimise the characteristics of each network component to yield the best fit to the theoretical impedance profile. This strategy has yielded accurate results for the particular problem of lossy wave propagation in brass instrument modelling, with minimal computational cost; the rest of this Chapter will demonstrate that this method can be successfully adapted for the string problem.

3.3.4 Existing models

Two earlier models were described in Section 3.1. The first, introduced by Ruiz [89], defines the system as:

$$Z_{\boldsymbol{\chi}}(s) = b_1 - b_3 s^2\,, \quad b_1, b_3 \geqslant 0 \tag{3.26a}$$

$$\Rightarrow\ \rho S s^2 + T\beta^2 + EI_0\beta^4 + b_1 s - b_3 s^3 = 0 \tag{3.26b}$$

$$\Rightarrow\ \rho S \partial_t^2 w = T\partial_x^2 w - EI_0\partial_x^4 w - b_1\partial_t w + b_3\partial_t^3 w \tag{3.26c}$$

In this case, $Z_{\boldsymbol{\chi}}(s)$ is not a positive-real function of s; and indeed, expanding $s = \sigma + j\omega$ in (3.26b) and examining the imaginary part of the result yields a quadratic in σ, one of the roots of which is strictly positive for all frequencies. This means that there exist exponentially growing solutions for $w(x,t)$; the proposed system is not guaranteed passive.

The second approach, described by Bensa *et al.* [7], yields the following system:

$$Z_{\boldsymbol{\chi}}(s) = b_0 + \beta^2(s) b_0'\,, \quad b_0, b_0' \geqslant 0 \tag{3.27a}$$

$$\Rightarrow\ \rho S s^2 + T\beta^2 + EI_0\beta^4 + b_0 s + b_0' s\beta^2 = 0 \tag{3.27b}$$

$$\Rightarrow\ \rho S \partial_t^2 w = T\partial_x^2 w - EI_0\partial_x^4 w - b_0\partial_t w + b_0'\partial_t\partial_x^2 w \tag{3.27c}$$

where $Z_{\boldsymbol{\chi}}(s)$ is now positive-real. The imaginary part of (3.27b) yields a single, negative solution

---

[8] The reader is referred to [48] for a detailed review of network synthesis methods developed in the first half of the 20th century.

$\sigma = \frac{-Z_{\chi}}{2\rho S}$, where the expression for β^2 can be recovered from the real part of (3.27b):

$$\rho S \left(\sigma^2 - \omega^2\right) + b_0\sigma + \left(T + b_0'\sigma\right)\beta^2 + EI_0\beta^4 = 0 \tag{3.28}$$

Assuming losses are small, the dispersion relation reduces to that derived for the lossless stiff string (3.1):

$$\begin{aligned} &\sigma^2 \ll 1\,, \quad b_0\sigma \ll 1\,, \quad b_0'\sigma \ll 1 \\ \Rightarrow\; & -\rho S\omega^2 + T\beta^2 + EI_0\beta^4 \approx 0 \\ \Rightarrow\; & \beta\left(\omega\right) \approx \sqrt{\frac{\sqrt{c^4 + 4\kappa^2\omega^2} - c^2}{2\kappa^2}} \end{aligned} \tag{3.29}$$

This is simply to say that losses are considered small enough that they do not introduce any further inharmonicity. Since all solutions for $w(x,t)$ are decaying, this model is guaranteed passive.

Although this model does yield frequency-dependent decay times, it is clearly not sufficient for accurate modelling, since the dependency of Z_{χ} on s (through β) does not correspond to that of Z_{th}.

3.3.5 Approximating the impedance with Foster structures

Consider the following form for $Z_{\chi}(s)$, extrapolated from the Bensa model [7] presented in Section 3.3.4:

$$Z_{\chi}(s) \triangleq \Gamma(s) + \beta^2\Xi(s) \tag{3.30}$$

where $\Gamma(s)$ and $\Xi(s)$ are defined as corresponding to the driving-point impedance[9] of a canonical Foster structure of the second type [38], as illustrated in Figure 3.4:

$$\Gamma(s) \triangleq \sum_{q=1}^{M} \frac{b_q s}{s + a_q} \triangleq \sum_{q=1}^{M} \Gamma_q(s)\,, \qquad \Xi(s) \triangleq \sum_{q'=1}^{M'} \frac{b'_{q'} s}{s + a'_{q'}} \triangleq \sum_{q'=1}^{M'} \Xi_{q'}(s)\,, \qquad b_q,\, a_q,\, b'_{q'},\, a'_{q'} > 0 \tag{3.31}$$

where the notation Γ_q is set to designate the qth term of the sum in Γ, likewise for $\Xi_{q'}$. The coefficients a_1, a'_1 can be made zero to introduce a frequency-independent term. The forms given in (3.31) lead to the following characteristic Laplace polynomial:

$$\rho S s^2 + T\beta^2 + EI_0\beta^4 + s\sum_{q=1}^{M} \frac{b_q s}{s + a_q} + s\beta^2 \sum_{q'=1}^{M'} \frac{b'_{q'} s}{s + a'_{q'}} = 0 \tag{3.32}$$

The corresponding time-domain system of PDEs is given by:

---

[9] Note that, because of the factor β^2, $\Xi(s)$ has dimensions of impedance per unit area.

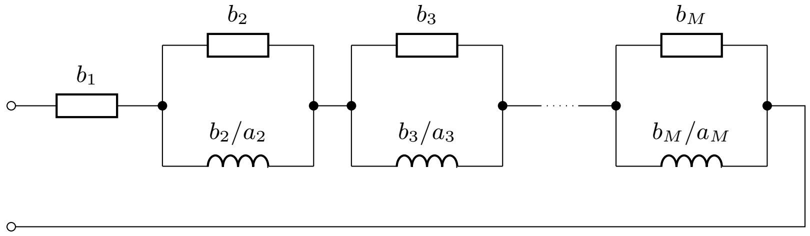

Figure 3.4: One-port Foster structure of the second type, corresponding to the driving point impedance $\Gamma(s)$ given in (3.31), with $a_1 = 0$. The symbol ▭ represents a resistance, while ⏜⏜⏜ is an inductance.

$$\mathcal{L}w = -\sum_{q=1}^{M} b_q \partial_t \gamma_q + \sum_{q'=1}^{M'} b'_q \partial_t \partial_x^2 \xi_q \tag{3.33a}$$

$$\partial_t \gamma_q = \partial_t w - a_q \gamma_q \ , \qquad q = 1, \ldots, M \tag{3.33b}$$

$$\partial_t \xi_{q'} = \partial_t w - a'_{q'} \xi_{q'} \ , \qquad q' = 1, \ldots, M' \tag{3.33c}$$

where the linear differential operator $\mathcal{L}$ is defined in (2.26), and each $\gamma_q(x,t)$ and $\xi_{q'}(x,t)$ is defined over the same spatio-temporal domain as $w(x,t)$.

As it stands, this model seeks to approximate the total losses with Γ and Ξ, by optimising the set of free parameters $b_q, a_q, b'_{q'}, a'_{q'}$ to best fit the reference loss profile. The free parameters are the elements of the vector $\boldsymbol{\chi}$, defined as:

$$\boldsymbol{\chi} \triangleq [b_1, \ldots, b_M, a_1, \ldots, a_M, b'_1, \ldots, b'_{M'}, a'_1, \ldots, a'_{M'}]^{\mathsf{T}} \tag{3.34}$$

Figure 3.5 displays the real part of an arbitrary term $\Gamma_q(j\omega)$ (left) and $\beta^2 \Xi_{q'}(j\omega)$ (right), taken along the imaginary axis. Neither of their profiles can correspond, in isolation, to that of the real part of $Z_{\text{th}}(j\omega)$, shown in Figure 3.3; a close fit to the theoretical model will hence require employing a number of these terms, in smaller or larger quantity, depending on the required fit quality.

3.4 Optimising the approximations

An expression for an approximated impedance $Z_{\boldsymbol{\chi}}(s)$ was proposed in Section 3.3.5 (see (3.30)), as a function of the collection of free parameters given by the elements of $\boldsymbol{\chi}$, defined in (3.34).

There are (at least) two equivalent ways to approach the optimisation problem. The real part of the impedance $Z_{\boldsymbol{\chi}}$ can be fitted directly to that of the theoretical impedance Z_{th}, along the imaginary axis ($s = j\omega$). Indeed, $\text{Re}\left(Z_{\boldsymbol{\chi}}(j\omega)\right)$ has a closed-form expression, given by a sum of functions of the free parameters, mostly uncoupled from each other.

Another approach arises from the fact that, as previously discussed, the modelling of strings

---

[10] See comment at the end of Section 3.1; the validity of using the lossless dispersion relation will be demonstrated in Section 3.4.2.iii.

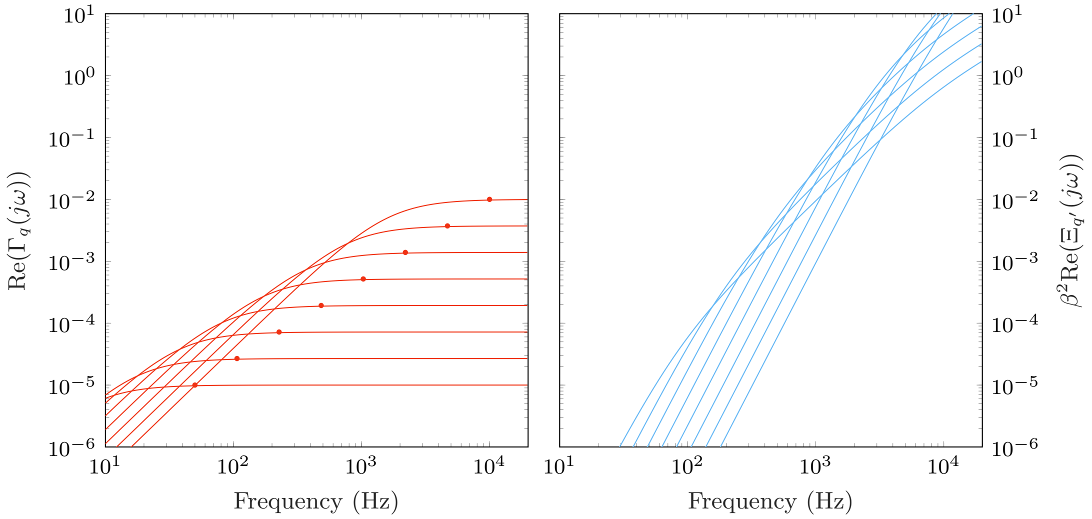

Figure 3.5: Real part of $\Gamma_q(j\omega)$ (left, in red) and $\beta^2\Xi_{q'}(j\omega)$ (right, in blue), as a function of frequency, for a range of $a_q, b_q, a'_{q'}, b'_{q'}$ values. The dispersion relation $\beta(\omega)$ is that of a lossless string[10]. — Parameters: see Cello D string on page xxix. The free parameters are logarithmically spaced, taking values within the following ranges: $b_q = 10^{-5}$—10^{-2}, $a_q = 50$—10^{4}, $b'_{q'} = 10^{-5}$—10^{-3}, and $a'_{q'} = 500$—2×10^{5}. For reference, each a_q-b_q pair is indicated on the left plot, by a dot on each corresponding curve; note that b_q plays the role of a gain factor, while a_q can be interpreted as a cutoff frequency.

for musical instruments is concerned with solutions on the s-plane that are very near the imaginary axis (as $\sigma = \mathrm{Re}(s)$ is small). The characteristic equation (3.32) is a $(M + M' + 2)^{\text{th}}$ degree polynomial in s, and, as per (3.25), all its roots are on the left half-plane. Only one of them is of interest, for which the real part $\sigma \ll 1$; as will be seen in Section 3.4.2, this assumption allows to neglect high-order terms in σ, and to find a closed-form solution for the decay rate. This solution can finally be used to fit $Q_{\boldsymbol{\chi}}$ to the theoretical decay profile Q_{th}.

As will be seen in the next paragraph, both approaches lead to the same optimisation problem.

3.4.1 Fitting to the impedance Z_{th}

The real part of the approximated impedance $Z_{\boldsymbol{\chi}}$ is taken along the imaginary axis, by substituting $s = j\omega$ into (3.30):

$$\begin{aligned} Z_{\boldsymbol{\chi}}(j\omega) &= \sum_{q=1}^{M} \frac{j\omega b_q(a_q - j\omega)}{a_q^2 + \omega^2} + \beta^2 \sum_{q'=1}^{M'} \frac{j\omega b'_{q'}(a'_{q'} - j\omega)}{{a'_{q'}}^2 + \omega^2} \\ \Rightarrow \quad \mathrm{Re}\left(Z_{\boldsymbol{\chi}}(j\omega)\right) &= \omega^2 \sum_{q=1}^{M} \frac{b_q}{a_q^2 + \omega^2} + \omega^2\beta^2 \sum_{q'=1}^{M'} \frac{b'_{q'}}{{a'_{q'}}^2 + \omega^2} \end{aligned} \tag{3.35}$$

where $\beta(\omega)$ can be derived from the real part of the characteristic polynomial (3.32); assuming losses are small, as will be shown in Section 3.4.2.iii, the expression for the dispersion relation

$\beta(\omega)$ reduces to that of the lossless stiff string, meaning that losses do not affect the modal frequencies and wavenumbers.

Expression (3.35) can be fit against the theoretical profile given by (3.21a), and illustrated in Figure 3.3.

3.4.2 Fitting to the decay rate σ_{th}

3.4.2.i General expression for $\sigma(\omega)$

The imaginary part of the characteristic polynomial (3.32) is given by:

$$2\rho S\sigma + \sum_{q=1}^{M} \frac{b_q\left(\sigma^2 + \sigma a_q + \omega^2\right)}{\left(\sigma + a_q\right)^2 + \omega^2} + \beta^2 \sum_{q'=1}^{M'} \frac{b'_{q'}\left(\sigma^2 + \sigma a'_{q'} + \omega^2\right)}{(\sigma + a'_{q'})^2 + \omega^2} = 0 \tag{3.36}$$

where (3.5) was used. This is a $(M+M'+1)^{\text{th}}$ degree polynomial in σ, with as many roots in the complex plane. A root finding algorithm can be used to directly obtain all the roots of (3.36), in terms of ω; however, the lack of a closed-form solution leads to a difficult optimisation problem with regards to a fit of $\sigma(\omega)$ to the theoretical loss profile $\sigma_{\text{th}}(\omega)$. A closed-form approximation to $\sigma(\omega)$ can still be derived, guided by previous assumptions.

3.4.2.ii Approximation of $\sigma(\omega)$ for lightly damped strings

As touched upon in the introduction of this Section 3.4, a number of assumptions are made in the context of lightly damped strings, all related to the relative magnitude of σ and ω. As previously discussed, the positive-real impedance $Z_{\boldsymbol{\chi}}(s)$ leads to solutions for s lying on the left half-s-plane; in particular, those that lie near the real axis will be of interest, for which $\text{Re}(s) \ll \text{Im}(s)$. This is to say that the quality factors $Q = \frac{-\omega}{2\sigma}$ of the string transverse modes are large.

Additionally, the positive coefficients a_q, $q = 1, \dots, M$ and $a'_{q'}$, $q' = 1, \dots, M'$ correspond to the pole locations for Γ and Ξ; they have dimensions of frequency. The following first-order approximations can therefore be made, leading to a simple closed-form solution for the small negative root of (3.36):

$$-\frac{\sigma}{a_q} \ll 1 \quad \Rightarrow \quad \begin{cases} \left(\sigma + a_q\right)^2 = a_q^2\left(\frac{\sigma}{a_q} + 1\right)^2 \approx a_q^2 \\ \sigma^2 + \sigma a_q + \omega^2 = a_q^2\left(\frac{\sigma^2}{a_q^2} + \frac{\omega^2}{a_q^2} + \frac{\sigma}{a_q}\right) \approx \omega^2 \end{cases} \qquad q = 1, \dots, M$$

$$-\frac{\sigma}{a'_{q'}} \ll 1 \quad \Rightarrow \quad \begin{cases} \left(\sigma + a'_{q'}\right)^2 = {a'_{q'}}^2\left(\frac{\sigma}{a'_{q'}} + 1\right)^2 \approx {a'_{q'}}^2 \\ \sigma^2 + \sigma a'_{q'} + \omega^2 = {a'_{q'}}^2\left(\frac{\sigma^2}{{a'_{q'}}^2} + \frac{\omega^2}{{a'_{q'}}^2} + \frac{\sigma}{a'_{q'}}\right) \approx \omega^2 \end{cases} \qquad q' = 1, \dots, M'$$

$$\Rightarrow \quad \sigma(\omega) \approx -\frac{1}{2\rho S}\left(\omega^2 \sum_{q=1}^{M} \frac{b_q}{a_q^2 + \omega^2} + \beta^2\omega^2 \sum_{q'=1}^{M'} \frac{b'_{q'}}{{a'_{q'}}^2 + \omega^2}\right) \tag{3.37}$$

The expression inside the brackets is indeed exactly $\text{Re}\left(Z_{\boldsymbol{\chi}}(j\omega)\right)$.

3.4.2.iii Dispersion relation

The approximations made in Section 3.4.2.ii are of use for determining the dispersion relation between the wavenumber β and the frequency ω, for the proposed system. The real part of the characteristic polynomial (3.32) yields:

$$\rho S\left(\sigma^2-\omega^2\right)+T\beta^2+EI_0\beta^4+\mathrm{Re}\left(sZ_{\boldsymbol{\chi}}(s)\right)=0 \tag{3.38}$$

where the real part of the impedance term $sZ_{\boldsymbol{\chi}}(s)$ is given by:

$$\mathrm{Re}\left(sZ_{\boldsymbol{\chi}}(s)\right)=\underbrace{\sum_{q=1}^{M} b_q\frac{a_q\left(\sigma^2-\omega^2\right)+\sigma\left(\sigma^2+\omega^2\right)}{\left(\sigma+a_q\right)^2+\omega^2}}_{\mathrm{Re}(s\Gamma(s))}+\beta^2\underbrace{\sum_{q'=1}^{M'} b'_{q'}\frac{a'_{q'}\left(\sigma^2-\omega^2\right)+\sigma\left(\sigma^2+\omega^2\right)}{\left(\sigma+a'_{q'}\right)^2+\omega^2}}_{\mathrm{Re}(s\Xi(s))} \tag{3.39}$$

The approximations derived above for small losses allow to simplify (3.39) to:

$$\mathrm{Re}\left(sZ_{\boldsymbol{\chi}}(s)\right)\approx\sum_{q=1}^{M} b_q\left(\sigma-a_q\right)\underbrace{\frac{\omega^2}{a_q^2+\omega^2}}_{\in[0,1]}+\beta^2\sum_{q'=1}^{M'} b'_{q'}\left(\sigma-a'_{q'}\right)\underbrace{\frac{\omega^2}{a'^2_{q'}+\omega^2}}_{\in[0,1]} \tag{3.40}$$

Each term inside the sum therefore has, at most, a magnitude in the order of $b_q a_q$ (or $b'_{q'}a'_{q'}$).

As discussed in 3.4.2.ii[11], $a_q, a'_{q'}$ are distributed across the frequency spectrum, with values hence ranging in the order of 10^2—10^5. The parameters $b_q, b'_{q'}$ can be interpreted as gain factors; in the case where losses are small, their values range in the order of 10^{-5}—10^{-2}. The products $b_q a_q$ and $b'_{q'}a'_{q'}$ therefore take values typically in the order of unity.

An expression for the wavenumber $\beta_{\boldsymbol{\chi}}(\omega)$ is derived, as in the lossless case, by solving (3.38) as a quadratic in β^2, neglecting the σ terms of degree 2 and above:

$$\beta^2_{\boldsymbol{\chi}}(\omega)\approx\frac{\sqrt{\left(T+\mathrm{Re}\left(s\Xi\left(s\right)\right)\right)^2+4EI_0\left(\rho S\omega^2-\mathrm{Re}\left(s\Gamma\left(s\right)\right)\right)}-\left(T+\mathrm{Re}\left(s\Xi\left(s\right)\right)\right)}{2EI_0} \tag{3.41}$$

For strings used in musical instruments, the tension T takes values in the order of 10^2; this means that the $\mathrm{Re}\left(s\Xi\left(s\right)\right)$ term, in the order of 1 (as discussed above), only brings about a relatively small correction to the tension term in the dispersion relation.

The bending stiffness term, on the other hand, may become dominated by $\mathrm{Re}\left(s\Gamma\left(s\right)\right)$ at low frequencies, when $\rho S\omega^2$ is small. However, fortunately, the inharmonicity brought about by this stiffness term only manifests itself significantly on the high end of the frequency spectrum; as seen in the study of the lossless stiff string (see Section 2.1.2.iii), the tension term dominates at low frequencies.

The expression for $\beta_{\boldsymbol{\chi}}(\omega)$ for the lossy system is therefore only slightly different from $\beta(\omega)$ in the lossless case. To better illustrate this point, Figure 3.6 shows the dispersion relations given

---

[11] This is easily verified with preliminary computations.

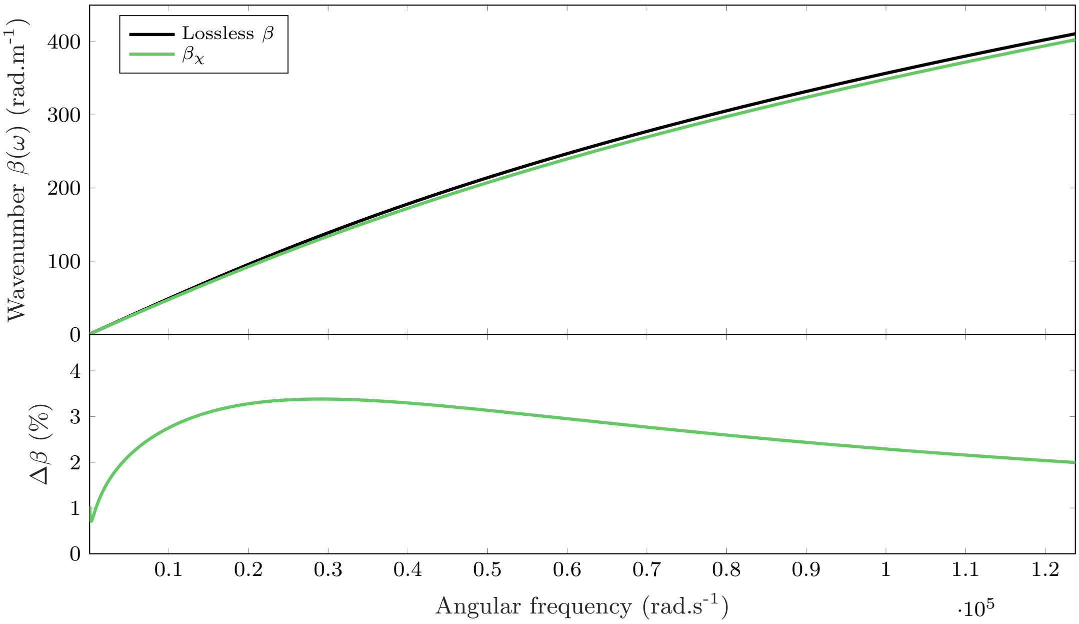

Figure 3.6: Top: dispersion relation $\beta(\omega)$, as per (2.27) (in black) and (3.41) (in green), with parameters as indicated in the text. Bottom: error $\Delta\beta \triangleq \left|\frac{\beta - \beta_{\boldsymbol{\chi}}}{\beta}\right|$, in percent. The corrections brought by $Z_{\boldsymbol{\chi}}$ to the dispersion relation are minimal; the simplified relation (2.27) is a satisfactory approximation to $\beta(\omega)$. — Parameters: see Cello D string on page xxix.

respectively by (3.41) (for $\sigma = 0$) and (2.27), plotted on the same (ω, β)-plane. The values of the parameters $\boldsymbol{\chi}$ are chosen conservatively, in order to illustrate a worst case scenario. There are $M = 8$ terms in $\Gamma(s)$, $M' = 8$ terms in $\Xi(s)$; each $a_q, a'_{q'}$ takes exponentially spaced values from 10^2—10^5; and finally, each $b_q a_q$ and $b'_{q'} a'_{q'}$ product takes values exponentially ranging from 0.5 to 5. As expected, for this conservative estimate, the error $\Delta\beta \triangleq \left|\frac{\beta - \beta_{\boldsymbol{\chi}}}{\beta}\right|$ does not exceed a few percent; the lossless dispersion relation (2.27) may be used.

3.4.3 Validity of the approximations

The validity of the approximated expression (3.37) can be verified by comparing it to the actual root σ_{root} of (3.36), obtained with a root finding algorithm, for typical string parameters, with a set of parameters $\boldsymbol{\chi}$ inferred from preliminary computations. Figure 3.7 shows the superimposed plots of the true root and its approximation, as a function of frequency, for a cello D string. The relative error between the two values is given by:

$$\Delta\sigma \triangleq \left|\frac{\sigma_{\text{root}} - \sigma}{\sigma_{\text{root}}}\right| \tag{3.42}$$

Figure 3.7 shows that the root and the first order approximation are extremely close to one another over the frequency range of interest, differing at most by 0.1% at low frequencies. The closed form (3.37) is therefore considered a very reliable approximation, and can safely be used

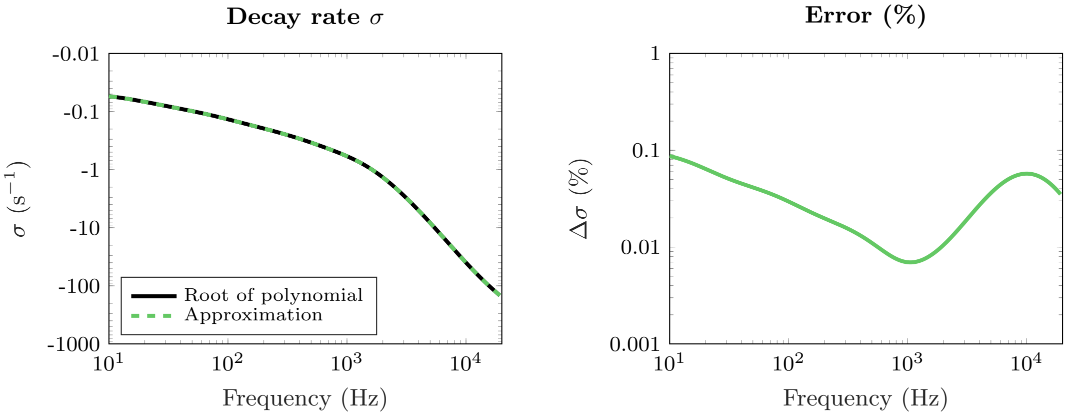

Figure 3.7: Left: smallest decay rate associated with $Z_{\boldsymbol{\chi}}$, as a function of frequency, obtained with a root-finding algorithm on (3.36) (in solid black), and with the first-order approximation (3.37) (in dashed green). Right: relative error $\Delta\sigma$ between the root and its approximation. The true root and the first order approximation differ at most by 0.1%. — Parameters: see Cello D string on page xxix. The damping parameters were inferred from preliminary calculations; here, $M = 5$ ($a_1 = 0$), $M' = 2$.

for optimisation. As a sum of relatively simple and mostly decoupled terms, (3.37) is well-suited to gradient-based optimisation methods.

3.4.4 Optimisation

The set of parameters $\boldsymbol{\chi}$ is optimised so that $Q_{\boldsymbol{\chi}}(\omega, \boldsymbol{\chi})$ best fits the theoretical Q-factor profile $Q_{\text{th}}(\omega)$, over N_ω exponentially spaced frequency bins, ranging from $f_{\min} = 10$Hz to $f_{\max} = 20$kHz; for the results presented here, $N_\omega = 500$. An optimisation routine seeks to minimise the least-squares cost function $E(\boldsymbol{\chi})$, defined as:

$$\mathrm{E}(\boldsymbol{\chi}) \triangleq \sum_{i=1}^{N_\omega} \left(\frac{Q_{\boldsymbol{\chi}}(\omega_i, \boldsymbol{\chi}) - Q_{\text{th}}(\omega_i)}{Q_{\text{th}}(\omega_i)} \right)^2 \tag{3.43}$$

A combination of gradient descent and Newton's method is employed for optimal convergence, in the form of the Levenberg-Marquardt algorithm. Initial guesses are randomised around 10^{-4}—10^{-2} for each b_q, $b'_{q'}$, and across the frequency range for each a_q, $a'_{q'}$ (see Figure 3.5).

For a given string, $Z_{\boldsymbol{\chi}}(s)$ is defined with M and M' ranging from 1 to 8, and $a_1, a'_1 = 0$. The resulting cost function, given by (3.43), is minimised, for each possible combination of Γ and Ξ terms. Evidently, in general, increasing the number of terms in either Γ or Ξ yields a closer fit; but every additional term will require the simulation of a supplementary state in the time domain, and therefore lead to an incremental increase in computational cost and memory requirements. The aim here, which will be further addressed in Section 3.6, is therefore to get the best possible fit, with the fewest possible terms in $Z_{\boldsymbol{\chi}}$.

It is of interest to present optimisation results for three strings exhibiting different loss profiles: a violin A string, a cello D string, and a double bass A string. Figure 3.8 presents two versions of the fitted $Q_{\boldsymbol{\chi}}(\omega)$ and $\mathrm{Re}\left(Z_{\boldsymbol{\chi}}(j\omega)\right)$ for each string, with the corresponding relative

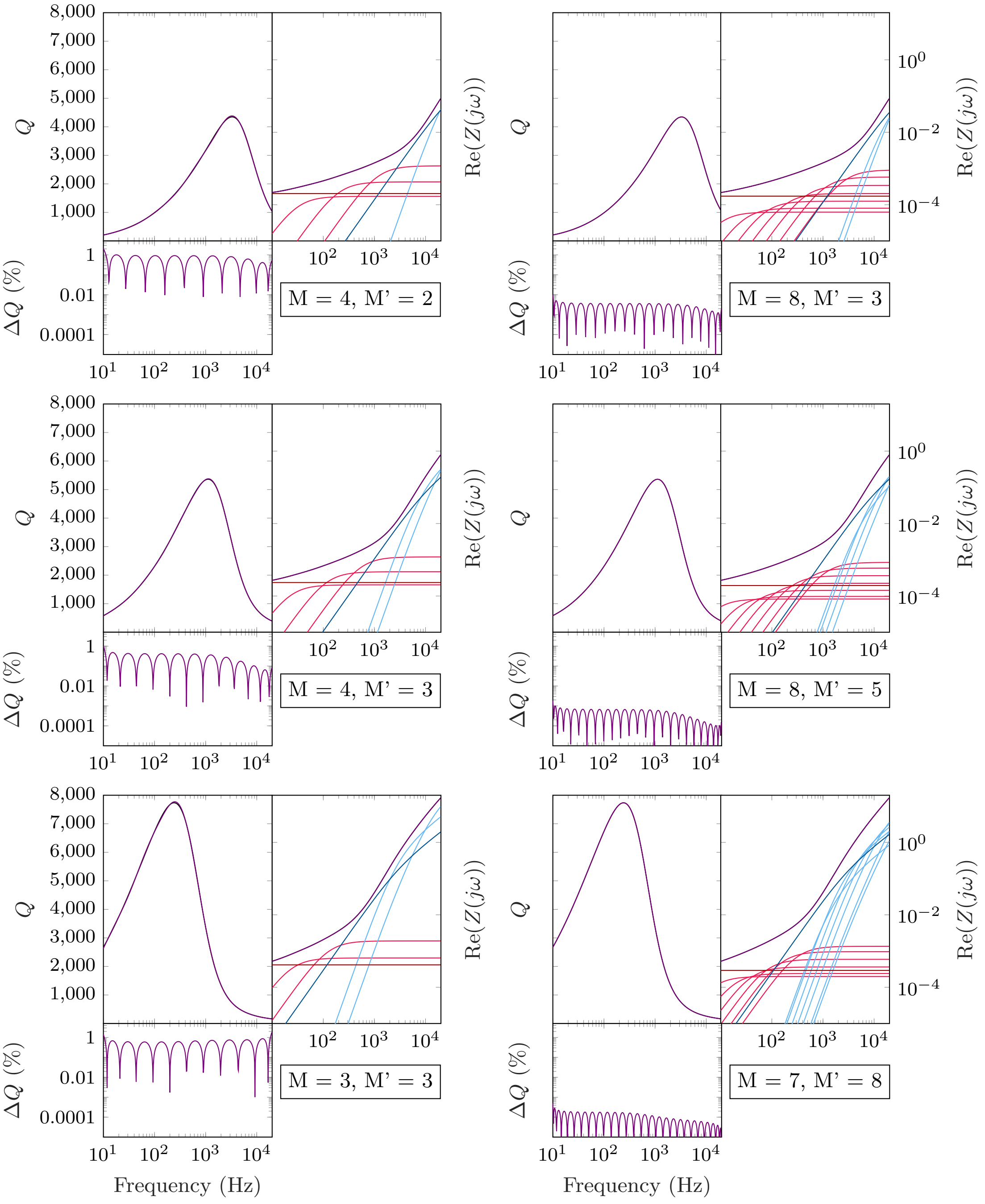

Figure 3.8: Optimised $Q_{\boldsymbol{\chi}}$ and relative error ΔQ (left plot), with the corresponding $\mathrm{Re}\left(Z_{\boldsymbol{\chi}}(j\omega)\right)$ (right plot), for a violin A string (top), a cello D string (middle), and a double bass A string (bottom). Figures on the left illustrate a fit with the fewest possible terms such that $\Delta Q \leqslant 1\%$ over the frequency range. Figures on the right illustrate the best fit obtained. $Q_{\mathrm{th}}(\omega)$, $\mathrm{Re}\left(Z_{\mathrm{th}}(j\omega)\right)$ are drawn in black; $Q_{\boldsymbol{\chi}}(\omega)$, $\mathrm{Re}\left(Z_{\boldsymbol{\chi}}(j\omega)\right)$ are drawn in purple; each participating Γ_q term is drawn in red (Γ_1 in dark red, as $a_1 = 0$), and each $\Xi_{q'}$ term in blue (Ξ_1 in dark blue, as $a'_1 = 0$). — Parameters: see page xxix.

error ΔQ, defined as:

$$\Delta Q \triangleq \left| \frac{Q_{\boldsymbol{\chi}} - Q_{\text{th}}}{Q_{\text{th}}} \right| \tag{3.44}$$

The impedance plot, on the RHS of each subfigure, also includes each individual Γ_q and $\beta^2 \Xi_{q'}$ term in the expression for $\mathrm{Re}\left(Z_{\boldsymbol{\chi}}(j\omega)\right)$. For each string, two optimisation results are shown next to one another:

- The first case shows $Z_{\boldsymbol{\chi}}$ chosen with the least number of terms yielding a fit deemed acceptable. The arbitrary criterion for acceptability is set such that the relative error ΔQ does not exceed 1% over the whole frequency range.
- The second case shows the closest fit obtained for $Z_{\boldsymbol{\chi}}$, over all the possible combinations of Γ and Ξ terms.

The first thing to note is that, beyond a certain number of terms, the optimisation algorithm seems to find a better minimum for $E\left(\boldsymbol{\chi}\right)$ by discarding surplus terms. This is why the best fit obtained in this test (RHS figure for each string) does not correspond to that obtained with $M = 8$ and $M' = 8$. Beyond a certain number of terms, the solver likely gets trapped in a good local minimum; perhaps more optimal initial guesses would result in a more accurate fit. However, each additional branch of $Z_{\boldsymbol{\chi}}$ resulting in increased computational cost, it is not deemed necessary to seek a fit with error smaller than 0.01%. Section 3.6 will provide an analysis of the time-domain simulated results as a function of the fit quality.

The violin string has a maximum Q-factor around 4 kHz; that of the double bass A string peaks around 250 Hz. One can expect that the best fit may be achieved with a different proportion of Γ and Ξ terms for the two different strings; and indeed, this is confirmed by observing the fitting results. The violin string requires all 8 addends of $\Gamma(s)$[12], but only 3 terms for $\Xi(s)$, while the double bass string requires all 8 terms of Ξ but only 7 terms for Γ. This is simply due to the two-part nature of the impedance curve; it is straightforward to see that the relative proportion of Γ and Ξ terms required to obtain the best possible fit is directly related to the location of the inflexion point of the impedance curve within the frequency range.

These qualitative observations help to inform the choice of parameter space and initial guesses for the optimisation algorithm, for a given string with known loss profile. Once the set of free parameters $\boldsymbol{\chi}$ has been determined, the time-domain system of PDEs can be solved with the help of carefully designed FD schemes, as will be presented in the next Section 3.5.

---

[12] The fit could likely have improved further by adding more terms to Γ; the limit of 8 terms was chosen arbitrarily, in order to somewhat balance the quality of the fit with the eventual computational cost.

3.5 Space-time domain system

3.5.1 The infinite string

Recall the time-domain system of PDEs describing the linear stiff string with damping, given in Section 3.3.5:

$$\mathcal{L}w = -\sum_{q=1}^{M} b_q \partial_t \gamma_q + \sum_{q'=1}^{M'} b'_{q'} \partial_t \partial_x^2 \xi_{q'} \tag{3.33a}$$

$$\partial_t \gamma_q = \partial_t w - a_q \gamma_q \ , \qquad q = 1, \dots, M \tag{3.33b}$$

$$\partial_t \xi_{q'} = \partial_t w - a'_{q'} \xi_{q'} \ , \qquad q' = 1, \dots, M' \tag{3.33c}$$

For the sake of compactness, System (3.33) can be written in matrix-vector form, as follows:

$$\boldsymbol{L}\boldsymbol{u} = \boldsymbol{0} \tag{3.46}$$

where $\boldsymbol{u}$ is a column vector, with $1 + M + M'$ elements, defined by:

$$\boldsymbol{u} \triangleq \left[\begin{array}{c|ccc|ccc} w & \gamma_1 & \cdots & \gamma_M & \xi_1 & \cdots & \xi_{M'} \end{array}\right]^{\mathsf{T}} \tag{3.47}$$

The elements of the matrix $\boldsymbol{L}$ are partial linear differential operators:

$$\boldsymbol{L} \triangleq \left[\begin{array}{c|ccc|ccc}
\mathcal{L} & \cdots & b_q \partial_t & \cdots & \cdots & -b'_{q'} \partial_t \partial_x^2 & \cdots \\
\hline
\vdots & \ddots & & 0 & & & \\
b_q \partial_t & & -b_q \left(\partial_t + a_q\right) & & & \boldsymbol{0}_{M \times M'} & \\
\vdots & 0 & & \ddots & & & \\
\hline
\vdots & & & & \ddots & & 0 \\
-b'_{q'} \partial_t \partial_x^2 & & \boldsymbol{0}_{M' \times M} & & & b'_{q'} \partial_x^2 \left(\partial_t + a_q\right) & \\
\vdots & & & & 0 & & \ddots
\end{array}\right]
\begin{array}{l}
\}\ 1 \\
\\
\Big\}\ M \\
\\
\\
\Big\}\ M' \\
\\
\end{array} \tag{3.48}$$

where $\mathcal{L}$ is defined in (2.26). Note that this symmetrical form is obtained after differentiating Equation (3.33c) twice with respect to x and inverting its sign; the benefit of doing this is apparent when computing the energy balance equation for the system.

For now, let the string be unbounded, defined over $x \in \mathbb{R}$ and $t \in \mathbb{R}_{\geqslant 0}$. The energy balance is retrieved by left-multiplying (3.46) by $(\partial_t \boldsymbol{u})^\mathsf{T}$ and integrating over $x \in \mathbb{R}$, leading to:

$$\int_{\mathbb{R}} (\partial_t \boldsymbol{u})^\mathsf{T} \boldsymbol{L}\boldsymbol{u} \, \mathrm{d}x = 0$$

$$\Rightarrow \quad \dot{H}_w = -Q_w \tag{3.49}$$

$$H_w \triangleq H_{w,s} + H_{w,\gamma} + H_{w,\xi} \qquad\qquad Q_w \triangleq Q_{w,\gamma} + Q_{w,\xi}$$

where $H_{w,s}$ is defined by (2.28), and two new energy terms appear, in terms of all the $\gamma_q(x,t)$ and $\xi_{q'}(x,t)$:

$$H_{w,\gamma}(t) \triangleq \frac{1}{2} \sum_{q=1}^{M} b_q a_q \left\|\gamma_q\right\|^2 \geqslant 0 \tag{3.50a}$$

$$H_{w,\xi}(t) \triangleq \frac{1}{2} \sum_{q'=1}^{M'} b'_{q'} a'_{q'} \left\|\partial_x \xi_{q'}\right\|^2 \geqslant 0 \tag{3.50b}$$

where the norm is defined over the real line, that is $\|\cdot\| = \|\cdot\|_{\mathbb{R}}$. The RHS of the energy balance equation (3.49) accounts for the power dissipated by the damping processes:

$$Q_{w,\gamma}(t) \triangleq \sum_{q=1}^{M} b_q \left\|\partial_t \gamma_q\right\|^2 \geqslant 0 \tag{3.51a}$$

$$Q_{w,\xi}(t) \triangleq \sum_{q'=1}^{M'} b'_{q'} \left\|\partial_t \partial_x \xi'_{q'}\right\|^2 \geqslant 0 \tag{3.51b}$$

All the power terms are positive, hence $-Q_w(t)$ is negative; by (3.49), the total energy $H_w(t)$ is decreasing over time.

3.5.2 Boundary conditions

Bounding the string to a finite spatial domain such that $x \in \mathcal{D} = [0, L]$ (as defined in Section 2.1.1.v) introduces boundary terms in the energy balance. As for the lossless string, the expressions for energy and power terms are mostly unchanged, save for the redefinition of the norm over $\mathcal{D}$ from that over $\mathbb{R}$, that is $\|\cdot\| = \|\cdot\|_{\mathcal{D}}$ (see Section 2.1.1.v). The energy balance becomes:

$$\dot{H}_w = -Q_w + B_w \tag{3.52}$$

where the boundary terms $B_w(t)$ are given by:

$$B_w \triangleq T \, \partial_t w \, \partial_x w \Big|_0^L - EI_0 \left(\partial_t w \, \partial_x^3 w \Big|_0^L - \partial_t \partial_x w \, \partial_x^2 w \Big|_0^L \right) + \sum_{q'=1}^{M'} b'_{q'} \partial_t w \, \partial_t \partial_x \xi_{q'} \Big|_0^L \tag{3.53}$$

The simply supported boundary conditions (2.31a) still allow all the boundary terms to vanish, yielding $B_w(t) = 0$; no further boundary conditions are required on any of the states γ_q and $\xi_{q'}$.

3.6 Time-domain simulations

3.6.1 An interleaved FD scheme

The dependent variables $w(x,t)$, $\gamma_q(x,t)$, and $\xi_{q'}(x,t)$ are all discretised into grid functions, with a fixed time step k and grid spacing h; each of the new states $\gamma_q(x,t)$ and $\xi_{q'}(x,t)$ is discretised onto the same spatial grid as $w(x,t)$ (see Section 2.2), over a given finite or infinite spatial domain. Moreover, let the new discrete states be defined at time step $n - 1/2, n \in \mathbb{N}$, that is half a time step away from $\mathbf{w}^n$. This half-step shift between the temporal grids of both discrete state variables characterises the proposed FD scheme as time-interleaved.

Consider the following implicit finite difference scheme, in term of the state vectors $\mathbf{w}^n$, $\boldsymbol{\gamma}_q^{n-1/2}$, $\boldsymbol{\xi}_{q'}^{n-1/2}$ thus defined (with arbitrary dimension):

$$\rho S \delta_{tt}\mathbf{w}^n = T\boldsymbol{\delta}_{xx}\mathbf{w}^n - EI_0\boldsymbol{\delta}_{xxxx}\mathbf{w}^n - \sum_{q=1}^{M} b_q \delta_{t+}\boldsymbol{\gamma}_q^{n-1/2} + \sum_{q'=1}^{M'} b'_{q'}\delta_{t+}\boldsymbol{\delta}_{xx}\boldsymbol{\xi}_{q'}^{n-1/2} \tag{3.54a}$$

$$\delta_{t+}\boldsymbol{\gamma}_q^{n-1/2} = \delta_{t\cdot}\mathbf{w}^n - a_q\mu_{t+}\boldsymbol{\gamma}_q^{n-1/2}\,, \qquad q = 1, \dots, M \tag{3.54b}$$

$$\delta_{t+}\boldsymbol{\xi}_{q'}^{n-1/2} = \delta_{t\cdot}\mathbf{w}^n - a'_{q'}\mu_{t+}\boldsymbol{\xi}_{q'}^{n-1/2}\,, \qquad q' = 1, \dots, M' \tag{3.54c}$$

The time averaging operator μ_{t+} in (3.54b) and (3.54c) is used to approximate identity, in order to ensure the stability of the scheme, as will be demonstrated in Section 3.6.3.

3.6.2 Boundary conditions and matrix form

When restricting the problem to a finite spatial domain $\mathcal{D}$, it was shown in Section 3.5.2 that in the continuous case, there is no requirement to impose further boundary conditions on any state γ_q or $\xi_{q'}$ to obtain the final energy balance equation. Indeed, all the new boundary terms arising for the lossy string can be written as the product of two terms evaluated at the boundaries, one of which is already made to vanish by the conditions imposed on $w(x,t)$.

In the case of a discrete finite domain $\mathfrak{D}$, with $N_{\mathfrak{D}}+1$ grid points, it is immediately apparent, by inspection of (3.54), that the boundary terms brought about by the summation by parts required to obtain a numerical energy balance will vanish with the discrete boundary conditions given by (2.85).

Furthermore, by (3.54b) and (3.54c), under simply supported conditions, the value of each state $\gamma_{q,l}^{n-1/2}$ and $\xi_{q',l}^{n-1/2}$ at boundary points $l = 0$ and $l = N_{\mathfrak{D}}$ will decay monotonically over time from its initial value. Indeed, for instance, expanding the operators in (3.54b) at the left boundary point $l = 0$ yields, for any state $\gamma_{q,l}^{n-1/2}$:

$$\delta_{t+}\gamma_{q,0}^{n-1/2} = -a_q \mu_{t+}\gamma_{q,0}^{n-1/2} \qquad \Rightarrow \qquad \gamma_{q,0}^{n+1/2} = \frac{2-a_q k}{2+a_q k}\gamma_{q,0}^{n-1/2} \qquad \Rightarrow \qquad \left|\gamma_{q,0}^{n+1/2}\right| < \left|\gamma_{q,0}^{n-1/2}\right| \tag{3.55}$$

Initialising boundary grid values to zero for all states is enough to ensure that the first and last elements of each $\boldsymbol{\gamma}_q^{n-1/2}$ and $\boldsymbol{\xi}_{q'}^{n-1/2}$ remain zero at all times.

The FD scheme (3.54) can therefore be written directly in matrix-vector form, in terms of a discrete state vector $\mathbf{u}^n$, with $(1+M+M')N$ elements[13], accounting for the full state of the system at the current time step. This vector is the discrete counterpart of $\boldsymbol{u}$, and contains the truncated state vector $\mathbf{w}^n$, defined by (2.69), as well as the truncated $\boldsymbol{\gamma}_q^{n-1/2}$ and $\boldsymbol{\xi}_{q'}^{n-1/2}$[14], defined as:

$$\boldsymbol{\gamma}_q^{n-1/2} \triangleq \left[\gamma_{q,1}^{n-1/2}, \gamma_{q,2}^{n-1/2}, \ldots, \gamma_{q,N}^{n-1/2}\right]^{\mathsf{T}}, \qquad q = 1, \ldots, M \tag{3.56a}$$

$$\boldsymbol{\xi}_{q'}^{n-1/2} \triangleq \left[\xi_{q',1}^{n-1/2}, \xi_{q',2}^{n-1/2}, \ldots, \xi_{q',N}^{n-1/2}\right]^{\mathsf{T}}, \qquad q' = 1, \ldots, M' \tag{3.56b}$$

The vector $\mathbf{u}^n$ is thus defined following the structure of the continuous vector $\boldsymbol{u}$, given by (3.47):

$$\mathbf{u}^n \triangleq \left[\begin{array}{c|ccc|ccc} \mathbf{w}^{n\mathsf{T}} & \boldsymbol{\gamma}_1^{n-1/2\,\mathsf{T}} & \cdots & \boldsymbol{\gamma}_M^{n-1/2\,\mathsf{T}} & \boldsymbol{\xi}_1^{n-1/2\,\mathsf{T}} & \cdots & \boldsymbol{\xi}_{M'}^{n-1/2\,\mathsf{T}} \end{array}\right]^{\mathsf{T}} \tag{3.57}$$

A finite difference scheme for System (3.46) may thus take the form:

$$\mathbf{L}\mathbf{u}^n = \mathbf{0} \tag{3.58}$$

where the $(1+M+M')N \times (1+M+M')N$ square matrix $\mathbf{L}$ is a discretisation of the continuous $\boldsymbol{L}$

---

[13] Recall, from Section 2.2.4.iii, that $N \triangleq N_{\mathfrak{D}} - 1$ is defined as the number of elements in the state vector $\mathbf{w}^n$ truncated from its first and last elements.

[14] The temporal FD operators employed on the $\boldsymbol{\gamma}_q^{n-1/2}$ and $\boldsymbol{\xi}_{q'}^{n-1/2}$ grid functions only span two time steps. The unknown system state at a future time step is defined as $\mathbf{u}^{n+1}$, and is comprised of $\mathbf{w}^{n+1}$, $\boldsymbol{\gamma}_q^{n+1/2}$, and $\boldsymbol{\xi}_{q'}^{n+1/2}$, all computed simultaneously.

defined in (3.48), where the partial derivatives are substituted for appropriate FD operators[15]:

$$\mathbf{L} \triangleq \left[\begin{array}{c|ccc|ccc} \mathsf{L} & \cdots & b_q\mathbf{I}\delta_{t+} & \cdots & \cdots & -b'_{q'}\mathbf{D}_{xx}\delta_{t+} & \cdots \\ \hline \vdots & \ddots & & 0 & & & \\ b_q\mathbf{I}\delta_{t\cdot} & & -b_q\mathbf{I}\left(\delta_{t+}+a_q\mu_{t+}\right) & & & \mathbf{0}_{MN\times M'N} & \\ \vdots & 0 & & \ddots & & & \\ \hline \vdots & & & & \ddots & & 0 \\ -b'_{q'}\mathbf{D}_{xx}\delta_{t\cdot} & & \mathbf{0}_{M'N\times MN} & & & b'_{q'}\mathbf{D}_{xx}\left(\delta_{t+}+a'_{q'}\mu_{t+}\right) & \\ \vdots & & & & 0 & & \ddots \end{array}\right] \begin{array}{l} \left.\vphantom{\mathsf{L}}\right\} N \\ \left.\vphantom{\begin{array}{c}\vdots\\ b_q\\ \vdots\end{array}}\right\} MN \\ \left.\vphantom{\begin{array}{c}\vdots\\ b_q\\ \vdots\end{array}}\right\} M'N \end{array} \tag{3.59}$$

where L is that defined by (2.82), where the spatial operators are written in matrix form:

$$\mathsf{L} \triangleq \rho S\mathbf{I}\delta_{tt} - T\mathbf{D}_{xx} + EI_0\mathbf{D}_{xxxx} \tag{3.60}$$

and, as before, $\mathbf{I}$ is the $N \times N$ identity matrix.

3.6.3 Energy analysis and stability condition

Let a discrete velocity vector $\mathbf{v}^n$ be defined as:

$$\mathbf{v}^n \triangleq \left[\begin{array}{c|ccc|ccc} \delta_{t\cdot}\mathbf{w}^{n\,\mathsf{T}} & \delta_{t+}\boldsymbol{\gamma}_1^{n-1/2\,\mathsf{T}} & \cdots & \delta_{t+}\boldsymbol{\gamma}_M^{n-1/2\,\mathsf{T}} & \delta_{t+}\boldsymbol{\xi}_1^{n-1/2\,\mathsf{T}} & \cdots & \delta_{t+}\boldsymbol{\xi}_{M'}^{n-1/2\,\mathsf{T}} \end{array}\right]^{\mathsf{T}} \tag{3.61}$$

Pre-multiplying Equation (3.58) by $(h\mathbf{v}^n)^{\mathsf{T}}$ yields the following discrete power balance[16]:

$$\delta_{t-}\mathrm{H}_w^n = -\mathrm{Q}_w^n \tag{3.62}$$

$$\mathrm{H}_w^n \triangleq \mathrm{H}_{w,s}^n + \mathrm{H}_{w,\gamma}^n + \mathrm{H}_{w,\xi}^n \qquad \mathrm{Q}_w^n \triangleq \mathrm{Q}_{w,\gamma}^n + \mathrm{Q}_{w,\xi}^n$$

where $\mathrm{H}_{w,s}^n$ is the energy function characterising the lossless stiff string, defined by (2.84b). The remaining terms are defined as:

$$\mathrm{H}_{w,\gamma}^n \triangleq \frac{h}{2}\sum_{q=1}^{M} b_q a_q \left|\boldsymbol{\gamma}_q^{n+1/2}\right|^2 \geqslant 0 \tag{3.63a}$$

---

[15] Spatial FD operators are written in matrix form, using the forms derived in Section 2.2.4.iii and 2.2.5.iii for simply supported boundary conditions.

[16] Note that, e.g., $\delta_{t+}\boldsymbol{\gamma}_q^{n-1/2} = \delta_{t-}\boldsymbol{\gamma}_q^{n+1/2}$.

$$\mathrm{H}_{w,\xi}^{n} \triangleq \frac{h}{2}\sum_{q'=1}^{M'} b'_{q'}a'_{q'}\left|\mathbf{D}_{x-}\boldsymbol{\xi}_{q'}^{n+1/2}\right|^2 \geqslant 0 \tag{3.63b}$$

$$\mathrm{Q}_{w,\gamma}^{n} \triangleq h\sum_{q=1}^{M} b_q\left|\delta_{t+}\boldsymbol{\gamma}_{q}^{n-1/2}\right|^2 \geqslant 0 \tag{3.63c}$$

$$\mathrm{Q}_{w,\xi}^{n} \triangleq h\sum_{q'=1}^{M'} b'_{q'}\left|\delta_{t+}\mathbf{D}_{x-}\boldsymbol{\xi}_{q'}^{n-1/2}\right|^2 \geqslant 0 \tag{3.63d}$$

Since, by definition, $\mathrm{H}_{w,\gamma}^{n}, \mathrm{H}_{w,\xi}^{n} \geqslant 0$, the total energy H_{w}^{n} is positive under the same conditions as for the lossless case; the stability condition for Scheme (3.54) is the same as that of the lossless string, given by (2.91).

As $-\mathrm{Q}_{w}^{n} \leqslant 0$, the discrete energy is decreasing over time.

3.6.4 Scheme update

Scheme (3.58) may be rearranged into an implicit recurrence:

$$\mathbf{L}^{+}\mathbf{u}^{n+1} = \mathbf{L}^{0}\mathbf{u}^{n} + \mathbf{L}^{-}\mathbf{u}^{n-1} \tag{3.64}$$

where the matrices $\mathbf{L}^{+}$, $\mathbf{L}^{0}$, and $\mathbf{L}^{-}$ are obtained by expanding the temporal FD operators in (3.59), directly leading to:

$$\mathbf{L}^{+} \triangleq \left[\begin{array}{c|ccc|ccc}
\frac{\rho S}{k^2}\mathbf{I} & \cdots & \frac{b_q}{k}\mathbf{I} & \cdots & \cdots & \frac{-b'_{q'}}{k}\mathbf{D}_{xx} & \cdots \\
\hline
\vdots & \ddots & & 0 & & & \\
\frac{b_q}{2k}\mathbf{I} & & -\frac{b_q}{2k}(2+a_q k)\mathbf{I} & & & \mathbf{0}_{MN\times M'N} & \\
\vdots & 0 & & \ddots & & & \\
\hline
\vdots & & & & \ddots & & 0 \\
-\frac{b'_{q'}}{2k}\mathbf{D}_{xx} & & \mathbf{0}_{M'N\times MN} & & & \frac{b'_{q'}}{2k}(2+a'_{q'}k)\mathbf{D}_{xx} & \\
\vdots & & & & 0 & & \ddots
\end{array}\right] \tag{3.65a}$$

$$\mathbf{L}^0 \triangleq \left[\begin{array}{c|ccc|ccc}
\frac{2\rho S}{k^2}\mathbf{I} + T\mathbf{D}_{xx} - EI_0\mathbf{D}_{xxxx} & \cdots & \frac{b_q}{k}\mathbf{I} & \cdots & \cdots & \frac{-b'_{q'}}{k}\mathbf{D}_{xx} & \cdots \\
\hline
 & \ddots & & 0 & & & \\
\mathbf{0}_{MN\times N} & & -\frac{b_q}{2k}(2-a_qk)\mathbf{I} & & & \mathbf{0}_{MN\times M'N} & \\
 & 0 & & \ddots & & & \\
\hline
 & & & & \ddots & & 0 \\
\mathbf{0}_{M'N\times N} & & \mathbf{0}_{M'N\times MN} & & & \frac{b'_{q'}}{2k}(2-a'_{q'}k)\mathbf{D}_{xx} & \\
 & & & & 0 & & \ddots
\end{array}\right] \tag{3.65b}$$

$$\mathbf{L}^- \triangleq \left[\begin{array}{c|c}
-\frac{\rho S}{k^2}\mathbf{I} & \\
\hline
\vdots & \\
\frac{b_q}{2k}\mathbf{I} & \\
\vdots & \mathbf{0}_{((1+M+M')N)\times((M+M')N)} \\
\hline
\vdots & \\
-\frac{b'_{q'}}{2k}\mathbf{D}_{xx} & \\
\vdots &
\end{array}\right] \tag{3.65c}$$

The update given by (3.64) therefore takes the form of a sparse linear system, which may be solved efficiently without resorting to compute the inverse of the matrix $\mathbf{L}^+$. Through block Gaussian elimination, System (3.64) may also easily be rearranged such that $\mathbf{w}^{n+1}$ is computed semi-explicitly, in terms of $\mathbf{u}^n$ and $\mathbf{u}^{n-1}$. The resulting update equation for $\mathbf{w}^{n+1}$ is given by:

$$\mathbf{A}\mathbf{w}^{n+1} = \left[\begin{array}{c|c|c} \mathbf{B} & \cdots \; \left(1-\frac{2-a_q}{2+a_q}\right)\frac{b_q}{k}\mathbf{I} \; \cdots & \cdots \; -\left(1-\frac{2-a'_{q'}}{2+a'_{q'}}\right)\frac{b'_q}{k}\mathbf{D}_{xx} \; \cdots \end{array}\right]\mathbf{u}^n + \mathbf{C}\mathbf{w}^{n-1} \tag{3.66}$$

where $\mathbf{A}$, $\mathbf{B}$, and $\mathbf{C}$ are the $N \times N$ matrices given by:

$$\mathbf{A} \triangleq \frac{\rho S}{k^2}\mathbf{I} + \sum_{q=1}^{M}\frac{b_q}{k(2+a_qk)}\mathbf{I} - \sum_{q'=1}^{M'}\frac{b'_{q'}}{k(2+a'_{q'}k)}\mathbf{D}_{xx} \tag{3.67a}$$

$$\mathbf{B} \triangleq \frac{2\rho S}{k^2}\mathbf{I} + T\mathbf{D}_{xx} - EI_0\mathbf{D}_{xxxx} \tag{3.67b}$$

$$\mathbf{C} \triangleq \mathbf{A} - \frac{2\rho S}{k^2}\mathbf{I} \tag{3.67c}$$

This form will be particularly relevant in Chapter 4, and indeed essential to resolve the scheme update when nonlinear bowing excitation is introduced in the model.

3.7 Simulation results and analysis

3.7.1 Reproduction of the theoretical Q-factors

It was seen in Section 3.4 that the number of terms in both $\Gamma(s)$ and $\Xi(s)$ could be chosen to yield a better fit of the Q-factor to its theoretical value Q_{th}. Evidently, each new term added in either Γ or Ξ requires solving for a new state γ_q^n or $\boldsymbol{\xi}_{q'}^n$ in the time domain. It is therefore in one's best interest to evaluate the sensitivity of the simulation results to the quality of the Q-factor fit.

It is not straightforward to quantify how the number of terms in the continuous-domain impedance function will play a role in the simulated frequency-domain loss profile in the different schemes. In order to test this, time-domain simulations of the violin A string, cello D string, and double bass A string presented in Section 3.4 are performed with the scheme presented in Section 3.6. For each of the three strings, 10 simulations are performed for both M, M' pairs corresponding to the optimisation results presented in Figure 3.8. Each of the 10 simulations for all six cases is initiated with a different, randomised initial displacement, and zero initial velocity. In each case, the temporal evolution of modal amplitudes is extracted from the time-domain signals, using an FFT algorithm with a sliding temporal window. The measured peak amplitudes are then plotted against logarithmic time, for all 10 waveforms. The decay rate and Q-factor of a given transverse mode are finally computed by performing a linear regression on the corresponding modal decay curve, each comprised of the collected data points from all 10 simulations.

Figure 3.9 presents the Q-factors measured on simulated waveforms, with the method outlined above, for each string, with both the (M, M') pair yielding a Q-factor fit with 1% error over the frequency range, and the (M, M') pair yielding the closest possible fit. The measured Q-factors are displayed on top of the theoretical profile Q_{th}, given by Cuesta and Valette's model [113].

At first glance, the simulated results seem to closely align to the desired output, most importantly without noticeable difference between a large or small number of $\boldsymbol{\gamma}_q^{n+1/2}$ and $\boldsymbol{\xi}_q^{n+1/2}$ states. Figure 3.10 shows three snapshots of a normalised time-domain output waveform for each string, with randomised initial conditions, read out as the displacement of the string near its termination. Each frame respectively starts at $t = 0$ s, $t = 1$ s, and $t = 2$ s; in each plot, the two superimposed curves correspond to the simulated outputs with fewer or more states. In each case, even after two seconds, the waveforms are almost indistinguishable from one another, indicating that a larger number of terms in the impedance does not seem to have a significant bearing on accuracy.

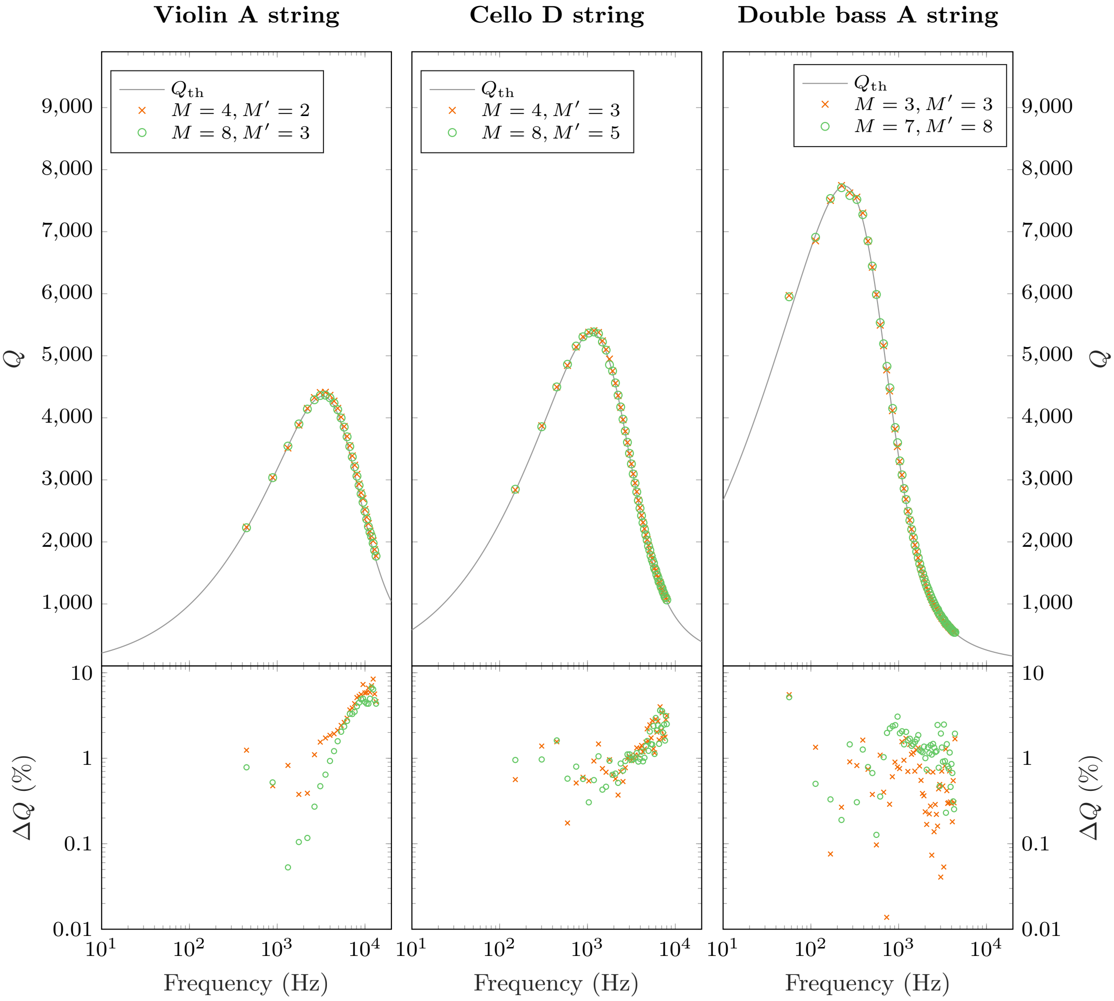

Figure 3.9: Top: Q-factors computed from time-domain simulations, for the violin A string (left), the cello D string (middle), and the double bass A string (right) presented in Section 3.4, superimposed with the theoretical loss profile Q_{th} (in grey). The orange crosses correspond to simulations performed with the minimal number of $\boldsymbol{\gamma}_q^{n+1/2}$, $\boldsymbol{\xi}_{q'}^{n+1/2}$ yielding an acceptable fit (see Figure 3.8, left figures). The green circles correspond to simulations performed with the best fit obtained for each string (see Figure 3.8, right figures). Bottom: error $\Delta Q \triangleq \left|\frac{Q_{\text{th}} - Q_{\mathbf{x}}}{Q_{\text{th}}}\right|$, in percent. — Parameters: see page xxix; $F_s = 44.1$ kHz.

To gain a more concrete understanding of the computational cost of using more or fewer states, Table 3.1 summarises the times required to compute 1 second of output in MATLAB, averaged over the 10 simulations performed for each case. Depending on the string, with the implementation described in Section 3.6.4, employing fewer states yields a computational speedup in the order of 30 to 40 %.

The lower plots in Figure 3.9 illustrate the relative error $\Delta Q \triangleq \left|\frac{Q_{\text{th}} - Q}{Q_{\text{th}}}\right|$, in percent, between the Q-factors measured on simulations and the corresponding theoretical value. The plots seems to confirm, at least for the cello and double bass strings, that seeking a Q-factor fit in the

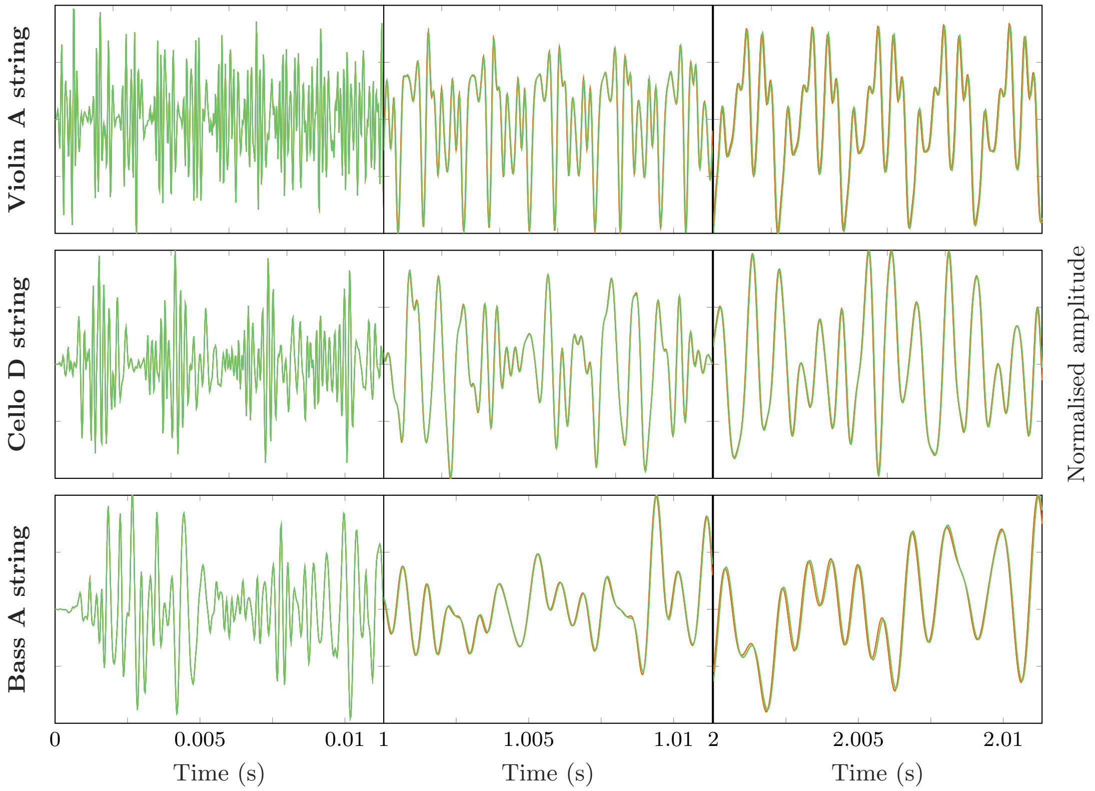

Figure 3.10: Normalised time-domain output waveform computed for a violin A string (top), a cello D string (middle), and a double bass A string (bottom). Three time frames are presented for each string, starting respectively at initial time (left), 1 second later (middle), and 2 seconds later (right). Each plot contains two waveforms, each corresponding to fewer or more impedance terms, colour-coded as in Figure 3.9. — Parameters: see page xxix; $F_s = 44.1$ kHz.

continuous frequency domain with less than 1% error over the frequency range does not achieve significantly better (or even different) results in the time-domain simulations.

The error ΔQ is larger, however, for modal frequencies above a few kHz; in particular, for the violin string, ΔQ seems to approach 10% at the high end of the spectrum. Figure 3.11 provides a closer look at the Q-factor profile obtained for the violin string (see Figure 3.9, top left). At high frequencies, the simulated Q-factors are systematically overestimated, regardless of the number of γ_q^n and $\boldsymbol{\xi}_{q'}^n$ terms used. This indicates that the issue is not related to the quality of the optimisation results; rather, it may have to do with the discretisation process. Note that the drift becomes increasingly prominent with increasing frequency; it is likely fair to assume that it would have shown on the double bass string plot, had the transverse modes with frequency larger than 5 kHz had a large enough decay time to be reliably measured.

A clue as to the cause of this drift, and perhaps a starting point for future work, may be found if the reader recalls the discrepancy, touched upon in Chapter 2, between the continuous and discrete dispersion relations for the lossless stiff string. It was shown in Section 2.2.5.vi that the discretisation of the continuous space-time domain PDEs into the chosen FD scheme

	Violin A	**Cello D**	**Bass A**
Fewer terms	1.49 s	4.24 s	9.68 s
Most terms	2.58 s	6.19 s	14.36 s
Speedup	42.2 %	31.5 %	32.6 %

Table 3.1: Computation times for 1 second of output ($F_s = 44.1$ kHz) in MATLAB, each averaged over 10 simulation runs, with different randomised initial conditions. Substantial speedup is achieved by employing fewer damping terms. — Parameters: see page xxix.

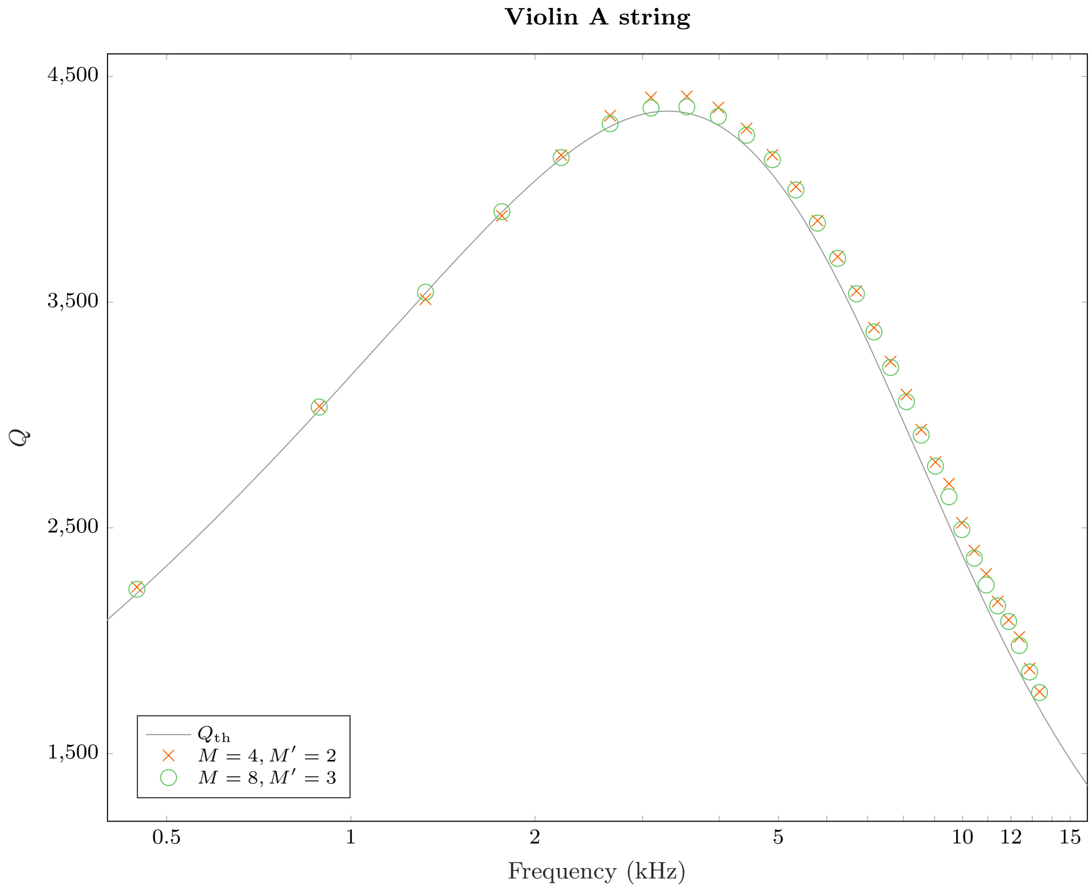

Figure 3.11: Q-factors measured on simulations of a violin A string: detail.

inevitably brought about numerical dispersion, meaning that higher discrete modal frequencies drifted further away from their continuous values. The observed high-frequency drift in Q-factor values may very well arise from a similar issue. Indeed, the optimisation was performed in the continuous frequency domain, assuming that the behaviour of the impedance, function of ω and β along the imaginary axis, would hold after the discretisation of time and space; this is not necessarily accurate. Improving the accuracy of the simulated results may require

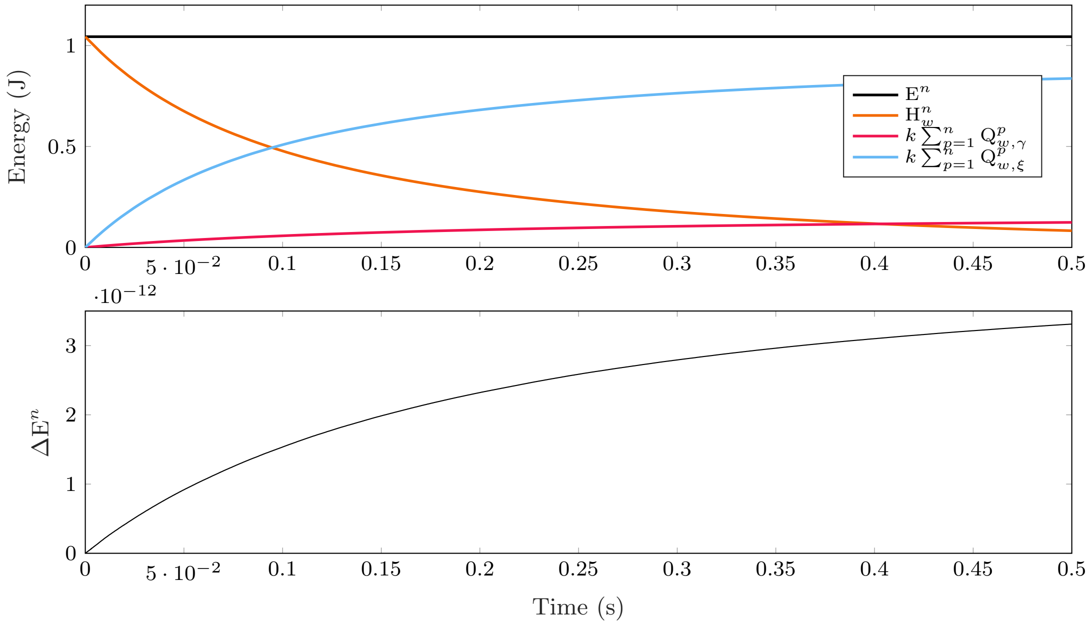

Figure 3.12: Top: total energy E^n for the cello D string (in black), sum of the stored energy H_w^n (in orange) and the cumulated dissipated powers $k\sum_{p=1}^n \mathrm{Q}_{w,\gamma}^p$ (in pink) and $k\sum_{p=1}^n \mathrm{Q}_{w,\xi}^p$ (in light blue). Bottom: normalised energy variations of E^n relative to H_w^0. — Parameters: see Cello D string on page xxix; $F_s = 44.1$ kHz, $M = 4$, $M' = 3$. The corresponding loss profile can be seen in Figure 3.9, top centre plot.

refinement of the optimisation process in order to take the so-called warping of spatial and temporal frequencies into account.

3.7.2 Discrete power balance and invariant quantity

Recall the discrete power balance (3.62) derived for the proposed FD scheme (3.54):

$$\delta_{t-}\mathrm{H}_w^n = -\mathrm{Q}_w^n \tag{3.62}$$

In Chapter 2, the absence of damping meant that $\mathrm{Q}_w^n = 0$, and thus the numerical energy $\mathrm{H}_w^n = \mathrm{H}_w^0$ was conserved over time. This was readily verifiable by checking that the variations of H_w^n did not exceed machine accuracy during the course of a simulation (see Sections 2.2.4.vii and 2.2.5.vii).

With a numerical energy H_w^n now varying over time, a new invariant quantity E^n, with dimensions of energy, may be defined as:

$$\mathrm{E}^n \triangleq \mathrm{H}_w^n + k\sum_{p=1}^{n} \mathrm{Q}_w^p = \mathrm{H}_w^0 \tag{3.68}$$

The relative variations of E^n are given by:

$$\Delta\mathrm{E}^n \triangleq \frac{\mathrm{E}^n - \mathrm{H}_w^0}{\mathrm{H}_w^0} \tag{3.69}$$

Figure 3.12 illustrates the power balance during a simulation of a cello D string, with randomised initial displacement (see Section 2.2.4.vii). Note that the form of E^n makes it difficult to compute accurately in finite precision; despite variations in the order of floating point accuracy ($\Delta\mathrm{E}^n \sim 10^{-12}$), indicating that simulations produce the expected results, a trend is visible, as the cumulated power seems to be systematically overestimated. A bitwise plot like those seen in Chapter 2 (see Figures 2.11 and 2.14) would not be particularly telling here.

Concluding remarks

A method for reproducing frequency-dependent decay times in time-domain simulations of transverse stiff string vibration has been established. The analysis of simulation results shows good agreement with theoretical loss profiles, as established by Valette and Cuesta [113].

It is important to note that the proposed method is relatively independent of the characteristics of the physical model used to represent damping processes. The optimisation of the time-domain damping parameters, as demonstrated in Section 3.4, could well be done with respect to a different theoretical model than that proposed in [113], or indeed directly with respect to experimental measurements.

A solution has been proposed for the time-domain simulation of linear stiff strings with realistic decay times, which is a perceptually important feature of the synthesised sound. The results shown in this Chapter were obtained by initialising string displacements with a randomised shape; this is evidently not a realistic setting, and the question of string excitation logically arises as the next problem to tackle. The incorporation of excitation mechanisms into the framework described in Chapters 2 and 3 will be the subject of Chapter 4.

Chapter 4

Playing the string: a two-polarisation bowed, stopped string model

4.1 Interacting with a string

Chapter 3 describes a physical model for the transverse motion of a linear stiff string, including frequency-dependent loss fitted to a theoretical profile, in order to closely match measurements on real strings. A FD scheme is introduced to simulate the physical system, allowing to reproduce the behaviour of a freely vibrating string, in one polarisation.

A wide variety of sounds can be produced with the same string, depending on how it is excited, and how it interacts with its environment. In particular, this work is concerned with bowing excitation, and seeks to design an algorithm capable of synthesising bowed string gestures; in order to achieve this, the interaction of a string with the left hand of the player and the fingerboard of the instrument must be included.

As will be shown in Section 4.2, these interactions are typically nonlinear; when dealing with a bow or stopping fingers, they are also localised, centred around a potentially time-varying location. The framework described in Chapters 2 and 3 for time-domain numerical modelling is well-suited for these types of interaction. Indeed, on one hand, a FD scheme is an immediate discretisation of the equations of motion, and the algorithm derived from the scheme directly generates an approximate numerical solution. If a scheme can be designed to appropriately discretise a given system of PDEs describing a physical model, provided such scheme is stable, then nonlinear interactions are generally not an issue, local or distributed, at fixed or time-varying locations, since computing the numerical output does not require knowledge of the form of the analytical solutions to the PDE system. Recent work on bowed string simulation using a travelling-wave-based method [73] exemplifies this advantage; as discussed in the article, this method is well-suited for steady-state simulations (e.g., for systematic experimental validation), but quickly encounters limitations when considering simulation of transient behaviour (e.g., with a moving bowing point), and therefore has restricted applications for sound synthesis. Another approach [72] resorts to using a FD scheme to resolve the nonlinear bow friction force at the contact points, and travelling-wave solutions elsewhere.

On the other hand, with a space-time FD scheme, a given point of the discrete system state is only coupled to other points in its vicinity (recall the discussion on stencil size in Section 2.2, notably Figures 2.10 and 2.13). This means that local interactions in the continuous domain can also be treated locally in the discrete domain, and therefore only lead to a marginal increase in computational cost with respect to simulating the isolated system. This is an advantage over, e.g., modal methods [1], for which a pointwise force must be projected onto the entire modal basis in order to compute a solution. Recent work has been concerned with modelling pointwise collision and friction interactions between a two-polarisation string and a unilateral obstacle, including extensive experimental validation [56]. Modelling distributed collisions between string and bridge on tanpura-like instruments has also been attempted with modal decomposition methods [13], where the distributed bridge is discretised in space, in order to derive an expression for the contact force between the string and each point of the bridge, for each string mode.

In this Chapter, Section 4.2 will present a model for a string vibrating linearly in two polarisations, excited by a bow, and stopped between left-hand fingers and a fingerboard; these interactions will be described in terms of nonlinear forces. The description of the physical model will be followed by that of an energy-balanced finite difference scheme in Section 4.3. Details of the implementation of simulations based upon this scheme will be discussed in Section 4.3.5, related in particular to the nonlinear nature of the coupling between the string and the bow, fingers, and fingerboard. Finally, Section 4.4 will present a selection of simulation results.

Some aspects of the model discussed in this Chapter have been described in [27, 28, 29], where nonlinear forces were applied to a simpler model of the isolated string. Simulation data obtained with the bowed string model presented here was used in [78].

4.2 Model description

4.2.1 A two-polarisation model

For the purposes of this work, a dual-polarisation string model yields the ability to simulate impact and contact interactions between the string and any external objects in one direction, which translate directly into tangential friction forces in the other direction. This is a simplified, yet intuitive way to include not only a bow that is able to naturally bounce, but also dynamic left hand fingers stopping the string against a fingerboard, while absorbing some of the string vibrations.

Looking ahead, the model presented here could fairly straightforwardly be connected to a model of a full instrument. The coupling of the two polarisations at the bridge boundary, through a model of the coupled bridge-body system, could be achieved with this model as

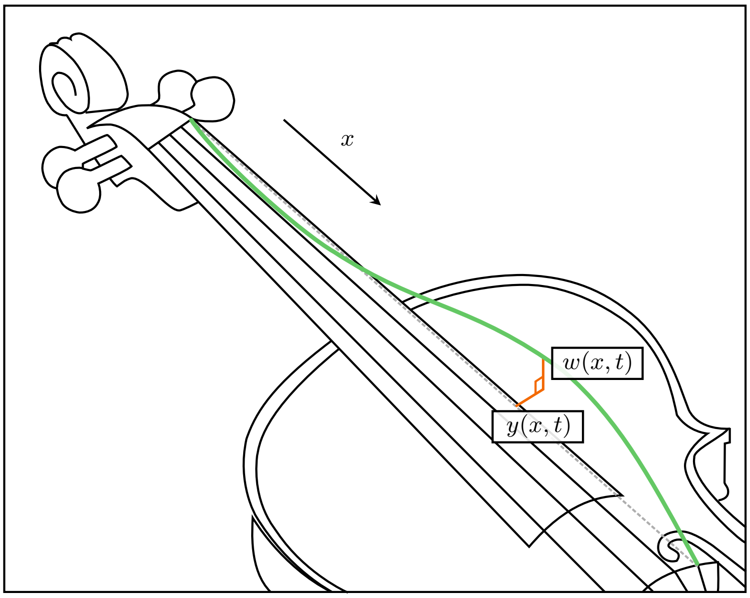

Figure 4.1: String displacement in two polarisations. The displacement $y(x,t)$ in the horizontal polarisation is parallel to the plane formed by the bow and the string; the displacement $w(x,t)$, in the vertical polarisation, is orthogonal to this plane.

a starting point. While the incorporation of the bridge and wooden cavity is undoubtedly crucial to the realism of synthetic sound, and would constitute worthwhile further research, it is beyond the scope of this work. The majority of existing models of the string-bridge-body coupled system in the literature adopt a frequency-domain impedance approach related to that presented in [71].

The proposed model is based on the isolated linear string model presented in Chapter 3. The string displacement in the vertical (or normal) polarisation is denoted by $w(x,t)$, while $y(x,t)$ is the string displacement in the horizontal (or tangential) polarisation. Both are defined, as in the previous Chapters, for abscissa $x \in \mathcal{D} = [0, L]$ and time $t \in \mathbb{R}_{\geqslant 0}$. Figure 4.1 illustrates what this manuscript refers to as the vertical and horizontal polarisations of string motion, labelled as described here; for clearer visualisation, they are shown as if the string was mounted onto a violin.

The temporal evolution of the displacement of the isolated string in each polarisation is governed by a system of PDEs, as described in Section 3.5. For the sake of compactness, such system can be written in matrix-vector form, allowing to henceforth focus on the nonlinear forces exciting the string.

For each polarisation, System (3.33a) can be written as:

$$\boldsymbol{L}\boldsymbol{u}_{(w)} = \mathbf{0} \qquad (4.1a) \qquad\qquad \boldsymbol{L}\boldsymbol{u}_{(y)} = \mathbf{0} \qquad (4.1b)$$

where the zero vector $\mathbf{0}$ has $1 + M + M'$ elements. $\boldsymbol{u}_{(w)}$ and $\boldsymbol{u}_{(y)}$ are column vectors, with

$1 + M + M'$ elements, defined by:

$$\boldsymbol{u}_{(w)} \triangleq \left[\begin{array}{c|ccc|ccc} w & \gamma_{1,(w)} & \cdots & \gamma_{M,(w)} & \xi_{1,(w)} & \cdots & \xi_{M',(w)} \end{array}\right]^{\mathsf{T}} \tag{4.2a}$$

$$\boldsymbol{u}_{(y)} \triangleq \left[\begin{array}{c|ccc|ccc} y & \gamma_{1,(y)} & \cdots & \gamma_{M,(y)} & \xi_{1,(y)} & \cdots & \xi_{M',(y)} \end{array}\right]^{\mathsf{T}} \tag{4.2b}$$

where each $w(x,t)$, $y(x,t)$ is coupled to $M + M'$ states, respectively $\gamma_{q,(w)}(x,t)$, $\xi_{q',(w)}(x,t)$ and $\gamma_{q,(y)}(x,t)$, $\xi_{q',(y)}(x,t)$. The matrix $\boldsymbol{L}$ is that defined by (3.48). Note that the string is assumed to have the same physical properties in both polarisations, hence the matrix $\boldsymbol{L}$ is the same in both Systems (4.1a) and (4.1b).

This compact notation, introduced in Section 3.5.1, allows to treat the linear system (the string) separately from the potentially nonlinear excitation. When an external force $F(x,t)$ per unit length (or force density) is applied onto the string, with vertical component $F_{(w)}(x,t)$ and horizontal component $F_{(y)}(x,t)$, System (4.1) becomes:

$$\boldsymbol{L}\boldsymbol{u}_{(w)} = \begin{bmatrix} F_{(w)}(x,t) \\ \mathbf{0}_{M,1} \\ \mathbf{0}_{M',1} \end{bmatrix} \tag{4.3a}$$

$$\boldsymbol{L}\boldsymbol{u}_{(y)} = \begin{bmatrix} F_{(y)}(x,t) \\ \mathbf{0}_{M,1} \\ \mathbf{0}_{M',1} \end{bmatrix} \tag{4.3b}$$

The total energy balance is the sum of energy balances for both polarisations, each found through the same process as for the linear system (see Equation (3.49)):

$$\begin{aligned} \int\limits_{\mathcal{D}} \left(\left(\partial_t \boldsymbol{u}_{(w)}\right)^{\mathsf{T}} \boldsymbol{L}\boldsymbol{u}_{(w)} + \left(\partial_t \boldsymbol{u}_{(y)}\right)^{\mathsf{T}} \boldsymbol{L}\boldsymbol{u}_{(y)} \right) \mathrm{d}x &= \int\limits_{\mathcal{D}} \left((\partial_t w)\, F_{(w)} + (\partial_t y)\, F_{(y)} \right) \mathrm{d}x \\ \Rightarrow \qquad \dot{H}_w + \dot{H}_y &= -P_w - P_y + P_F \end{aligned} \tag{4.4}$$

where $P_F \triangleq \int_{\mathcal{D}} \left((\partial_t w)F_{(w)} + (\partial_t y)F_{(y)}\right) \mathrm{d}x$ is the power supplied to the string through external excitation.

The next two Sections 4.2.2 and 4.2.3 will describe the forces involved in a bowed and stopped string model, in both polarisations. A full description includes models of a bow, left hand fingers, and a distributed fingerboard.

4.2.2 Vertical polarisation

The vertical polarisation of transverse string motion refers to string motion confined to the direction perpendicular to the bowing plane (see Figure 4.1). In this direction, the forces applied onto the string can be approached with a collision model.

4.2.2.i The collision interaction

The collision model used in this work was formalised in 1975 by Hunt and Crossley [55], who introduced a new law governing the mechanics of nonlinear damped impacts. The undamped power-law model was adopted by the musical acoustics community as a means to describe lumped collisions, in particular hammer-string collisions in the piano [12, 18, 16], and mallet-membrane impacts in drums [88, 19, 112]. A similar model to that of Hunt and Crossley, with hysteretic damping, was used by Stulov [108] for the modelling of the interaction between the piano hammer felt and the piano string, with good concordance with experimental results. A numerical time-domain framework for this particular model has recently been developed [11, 21], which has been proven to give rise to stable schemes.

This type of contact interaction is chosen for modelling two aspects of bowed string playing. First and foremost, a bow having the ability to naturally bounce is a necessary feature for a wide range of the musician's gestural palette, including gestures such as *spiccato* or *ricochet* bowing. Introducing a collision mechanism in the bow model itself allows for this bouncing to occur under realistic playing parameters. A model with one degree of freedom (1-DOF) for bow dynamics in the vertical polarisation is proposed here, in order to allow for compliance of the bow hair. The natural frequency of a bouncing bow varies between 6 and 30 Hz, depending on whether the string is bowed closer to the tip or the frog of the bow [46]; this can be tuned by changing the stiffness and mass parameters of the 1-DOF bow model. It is worth noting that a full model of the dynamics of the bow hair has purposely been excluded from this work; as the primary aim is sound synthesis, it is found here that a dynamic, nonlinear, albeit lumped bow is a satisfying compromise between computational cost and gestural versatility. Detailed studies of bow hair dynamics may be found in the literature; see, for instance, [84, 42].

The second key aspect of the contact interaction lies in the capture of the string between a left hand finger and the fingerboard. The use of the damped impact law allows for realistic simulation of the fingertip reacting against the tension of the string, while significantly absorbing its vibrations. The distributed fingerboard acts as a continuous barrier for fingers to slide along, allowing for *glissando* and *vibrato* gestures on the fly. Finally, the built-in impact model allows to simulate the rattling of the string against the fingerboard [10, 32], used, for instance, in jazz double bass playing; this is also an important aspect of sound production in tanpura-like instruments, and slap/pop gestures in electric bass guitar playing.

4.2.2.ii Finger and bow

In the vertical polarisation, the bow and finger models are essentialy the same—that is, a lumped, flexible body pushing down on the string with a set external force[1]. The distinction lies in the values of the parameters which define the collision force. For instance, the stiffness properties characterising the bow hair may be different from those of the fingertip, and the latter should exhibit much higher damping than the former.

Let $f_{\mathcal{F}}(t)$, $f_{\mathcal{B}}(t)$ be the downwards forces respectively exerted by a fingertip and the bow hair onto the string. Let $J_{\mathcal{F}}(x,t)$, $J_{\mathcal{B}}(x,t)$ denote continuous distributions, defined over $x \in \mathcal{D}$, representing the location of these forces along the string; in the case of pointwise forces, $J_{\mathcal{F}}$ and $J_{\mathcal{B}}$ are defined as Dirac delta functions of x, centred at the location of the contact point. Note that $J_{\mathcal{F}}$ and $J_{\mathcal{B}}$ may be time-varying; this is a requirement to model the bow or fingers moving along the string while a note is played.

---

[1] See the discussion in Section 4.2.2.i about the 1-DOF bow model.

The PDE system describing string motion in the vertical polarisation, including downwards forces[2] exerted by the bow and finger, can be written as:

$$\boldsymbol{L}\boldsymbol{u}_{(w)} = \begin{bmatrix} -J_{\mathcal{F}} f_{\mathcal{F}} - J_{\mathcal{B}} f_{\mathcal{B}} \\ \mathbf{0}_{M \times 1} \\ \mathbf{0}_{M' \times 1} \end{bmatrix} \tag{4.5}$$

The Hunt and Crossley model [55] describes the collision forces $f_{\mathcal{F}}(t)$ and $f_{\mathcal{B}}(t)$ as nonlinear functions of a variable Δ, referred to in [55] as the *deformation* or *approach*, corresponding to the distance by which the colliding object (here, the fingertip and the bow hair, respectively) deforms from its resting shape. Figure 4.2 provides a visual interpretation of the finger and bow deformation variables, $\Delta_{\mathcal{F}}(t)$ and $\Delta_{\mathcal{B}}(t)$, respectively defined as:

$$\Delta_{\mathcal{F}}(t) \triangleq \int_{\mathcal{D}} J_{\mathcal{F}}(x,t)\, w(x,t)\, \mathrm{d}x - w_{\mathcal{F}}(t) \tag{4.6a}$$

$$\Delta_{\mathcal{B}}(t) \triangleq \int_{\mathcal{D}} J_{\mathcal{B}}(x,t)\, w(x,t)\, \mathrm{d}x - w_{\mathcal{B}}(t) \tag{4.6b}$$

where $w_{\mathcal{F}}(t)$, $w_{\mathcal{B}}(t)$ are the respective vertical positions of the finger and bow above the string. The expression for the forces $f_{\mathcal{F}}$ and $f_{\mathcal{B}}$ as a function of $\Delta_{\mathcal{F}}(t)$ and $\Delta_{\mathcal{B}}(t)$ is given by:

$$f_{\mathcal{F}}(\Delta_{\mathcal{F}}) \triangleq \frac{\dot{\Phi}_{\mathcal{F}}}{\dot{\Delta}_{\mathcal{F}}} + \dot{\Delta}_{\mathcal{F}} \Psi_{\mathcal{F}} \tag{4.7a}$$

$$f_{\mathcal{B}}(\Delta_{\mathcal{B}}) \triangleq \frac{\dot{\Phi}_{\mathcal{B}}}{\dot{\Delta}_{\mathcal{B}}} + \dot{\Delta}_{\mathcal{B}} \Psi_{\mathcal{B}} \tag{4.7b}$$

where $\Phi_{\mathcal{F}}(\Delta_{\mathcal{F}})$, $\Phi_{\mathcal{B}}(\Delta_{\mathcal{B}})$ are nonlinear potentials, related to the stored collision energy, and $\Psi_{\mathcal{F}}(\Delta_{\mathcal{F}})$, $\Psi_{\mathcal{B}}(\Delta_{\mathcal{B}})$ are nonlinear damping terms, with dimensions of mechanical resistance. They are defined as:

$$\Phi_{\mathcal{F}}(\Delta_{\mathcal{F}}) \triangleq \frac{K_{\mathcal{F}}}{\alpha_{\mathcal{F}}+1} [\Delta_{\mathcal{F}}]_+^{\alpha_{\mathcal{F}}+1} \tag{4.8a}$$

$$\Psi_{\mathcal{F}}(\Delta_{\mathcal{F}}) \triangleq K_{\mathcal{F}} \beta_{\mathcal{F}} [\Delta_{\mathcal{F}}]_+^{\alpha_{\mathcal{F}}} \tag{4.8b}$$

$$\Phi_{\mathcal{B}}(\Delta_{\mathcal{B}}) \triangleq \frac{K_{\mathcal{B}}}{\alpha_{\mathcal{B}}+1} [\Delta_{\mathcal{B}}]_+^{\alpha_{\mathcal{B}}+1} \tag{4.9a}$$

$$\Psi_{\mathcal{B}}(\Delta_{\mathcal{B}}) \triangleq K_{\mathcal{B}} \beta_{\mathcal{B}} [\Delta_{\mathcal{B}}]_+^{\alpha_{\mathcal{B}}} \tag{4.9b}$$

where $[\cdot]_+$ means $\max(\cdot, 0)$. The parameters $K_{\mathcal{F}}$ and $K_{\mathcal{B}}$, strictly positive, define the respective stiffnesses of the fingertip and bow hair; $\alpha_{\mathcal{F}}$ and $\alpha_{\mathcal{B}}$ are power law exponents, both larger than

---

[2] Note that the adopted sign convention indicates that downwards forces are negative.

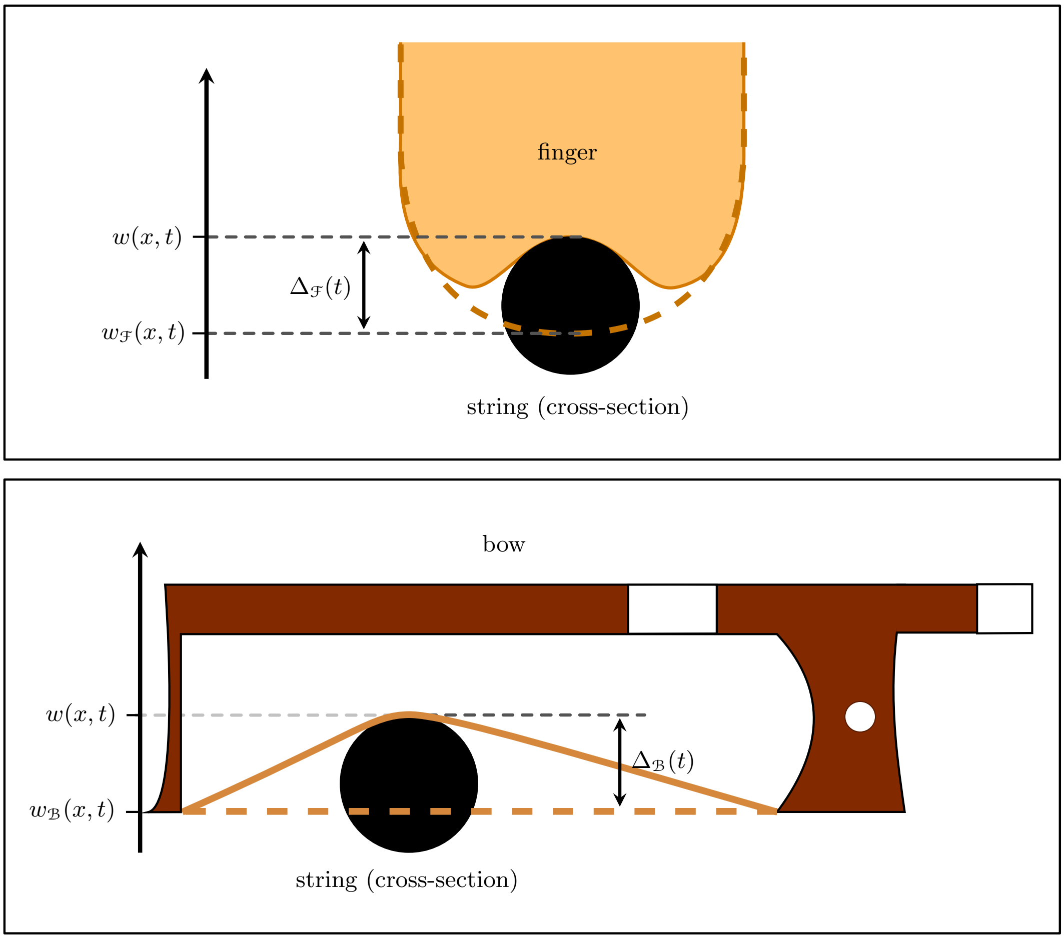

Figure 4.2: Visualisation of the deformation variables $\Delta_{\mathcal{F}}$ and $\Delta_{\mathcal{B}}$. Top: $\Delta_{\mathcal{F}}(t)$ represents the distance by which the fingertip deforms upon contact with the string surface. Bottom: $\Delta_{\mathcal{B}}(t)$ can be interpreted as the deformation of the flexible bow hair against the string[3].

1, characterising the nonlinearity of the impact interaction. The damping factors $\beta_{\mathcal{F}}$ and $\beta_{\mathcal{B}}$ are positive.

Finally, the temporal evolution of the vertical positions of the finger ($w_{\mathcal{F}}(t)$) and bow ($w_{\mathcal{B}}(t)$) is governed by a pair of ordinary differential equations:

$$m_{\mathcal{F}}\ddot{w}_{\mathcal{F}} = f_{\mathcal{F}} + f_{\text{ext}\mathcal{F},(w)} \tag{4.10a}$$

$$m_{\mathcal{B}}\ddot{w}_{\mathcal{B}} = f_{\mathcal{B}} + f_{\text{ext}\mathcal{B},(w)} \tag{4.10b}$$

where $m_{\mathcal{F}}$, $m_{\mathcal{B}}$ are the finger and bow masses, respectively, and $f_{\text{ext}\mathcal{F},(w)}(t)$, $f_{\text{ext}\mathcal{B},(w)}(t)$ are the time-varying external forces applied vertically onto the finger and bow (by the player). These forces are the input streams through which the player supplies energy to the string;

---

[3] Note that the proposed model implies a single degree of freedom for bow hair flexibility in the vertical polarisation. The model does not presently include wave propagation in the bow hair; the strand represented here is simply a visual aid.

in the numerical implementation, these will be the control signals. Instead of applying a force directly to the string, incorporating a dynamic bow and finger model allows to simulate observed behaviours (bouncing, damping. . .) as a result of certain inputs on a physical model, rather than through manual ad-hoc implementation.

4.2.2.iii Fingerboard

The fingerboard is modelled as a distributed barrier underneath the string. Let $F_{\mathcal{N}}(x,t)$ denote the contact force density between the fingerboard and the string (in N/m)[4]. Incorporating the fingerboard model into System (4.5) yields:

$$\boldsymbol{L}\boldsymbol{u}_{(w)} = \begin{bmatrix} F_{\mathcal{N}} - J_{\mathcal{F}} f_{\mathcal{F}} - J_{\mathcal{B}} f_{\mathcal{B}} \\ \mathbf{0}_{M,1} \\ \mathbf{0}_{M',1} \end{bmatrix} \tag{4.11}$$

The force density $F_{\mathcal{N}}$ is a nonlinear function of the fingerboard deformation $\Delta_{\mathcal{N}}(x,t)$, defined over the spatial domain $\mathcal{D}$:

$$\Delta_{\mathcal{N}}(x,t) \triangleq \varepsilon(x) - w(x,t) \tag{4.12}$$

where $\varepsilon(x)$ is the position of the fingerboard with respect to the string's resting position (coinciding with the x-axis). A diagram summarising the forces at play in the vertical polarisation can be seen in Figure 4.3.

As for the finger and bow, the expression for the fingerboard force density $F_{\mathcal{N}}$ as a function of $\Delta_{\mathcal{N}}(x,t)$ is derived from the Hunt and Crossley model, which is now used as a smooth approximation to a rigid collision:

$$F_{\mathcal{N}}(x,t) \triangleq \frac{\partial_t \Phi_{\mathcal{N}}}{\partial_t \Delta_{\mathcal{N}}} + (\partial_t \Delta_{\mathcal{N}})\, \Psi_{\mathcal{N}} \tag{4.13}$$

The potential density $\Phi_{\mathcal{N}}(\Delta_{\mathcal{N}})$ and mechanical resistance per unit length $\Psi_{\mathcal{N}}(\Delta_{\mathcal{N}})$ are given by:

$$\Phi_{\mathcal{N}}(\Delta_{\mathcal{N}}) \triangleq \frac{K_{\mathcal{N}}}{\alpha_{\mathcal{N}}+1} [\Delta_{\mathcal{N}}]_+^{\alpha_{\mathcal{N}}+1} \tag{4.14a}$$

$$\Psi_{\mathcal{N}}(\Delta_{\mathcal{N}}) \triangleq K_{\mathcal{N}} \beta_{\mathcal{N}} [\Delta_{\mathcal{N}}]_+^{\alpha_{\mathcal{N}}} \tag{4.14b}$$

where $\alpha_{\mathcal{N}} > 1$, and the stiffness parameter $K_{\mathcal{N}} > 0$ is chosen to be very large so as to approach an ideally rigid collision. Such a choice ensures that the deformation $\Delta_{\mathcal{N}}$ remains very small, as it should for fingerboard-like structures [10].

---

[4] Note that the index $\cdot_{\mathcal{N}}$ indicates "neck", in order to avoid confusion between fingers and fingerboard.

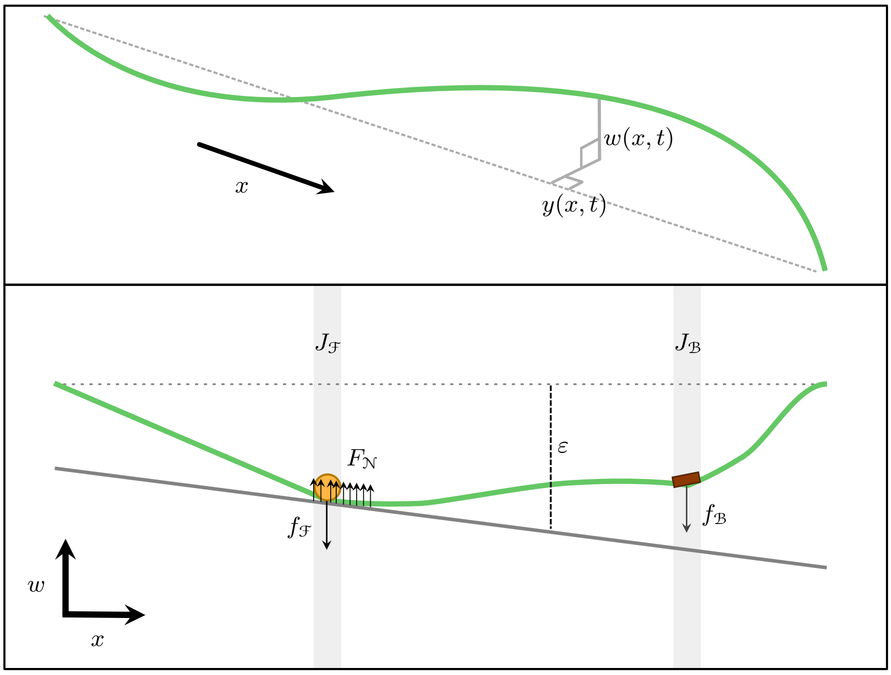

Figure 4.3: Diagram summarising the forces applied onto the string by the finger, bow, and fingerboard, in the vertical polarisation.

4.2.3 Horizontal polarisation

4.2.3.i The friction model

When the string is set into motion in the horizontal polarisation, the vertical contact forces described in Section 4.2.2 give rise to corresponding tangential friction forces.

A classic dry friction model is employed to compute tangential friction force:

$$F_{\leftrightarrow} \triangleq \left[F_{\updownarrow}\right]_{+} \varphi \tag{4.15}$$

where the tangential force $F_{\leftrightarrow}$ (in N) in the horizontal polarisation is directly proportional to the normal contact force $F_{\updownarrow}$ applied in the vertical polarisation. The ratio φ of tangential to normal force is a dimensionless friction coefficient, which is not necessarily constant; as will be seen in Section 4.2.3.ii, it may depend on a state variable. In the bowed string system presented here, neither the bow, fingers, nor fingerboard are considered adhesive, therefore friction only arises for positive normal forces.

It is important to note that, in this particular system, the vertical and horizontal polarisations are coupled through the modulation of the tangential friction force by the normal force, at the contact points between the string and the external objects. In the present model, there is no other form of polarisation coupling.

The next two Sections 4.2.3.ii and 4.2.3.iii will describe the incorporation of frictional forces in the horizontal polarisation. As the nature of the friction interaction for the rosin-coated bow hair is rather different from that characterising the fingers and fingerboard, they will be treated separately.

4.2.3.ii Bow

The primary instance of friction in the system, which constitutes the core mechanism of bowed string excitation, is the interaction between the bow hair, coated with rosin, and the surface of the string. This interaction is at the source of the sound production mechanism in bowed string instruments. The motion of a bowed string in normal playing conditions is referred to as Helmholtz motion [115], and has been the subject of many studies (see, e.g., [90, 93]). One period of transverse bowed string oscillations in the Helmholtz regime consists of a *sticking* phase, during which the bow sticks to the string at the contact point, and a shorter *slipping* phase, when the string slides against the bow. At any time, the string is approximately divided into two straight segments, connected at the Helmholtz corner; the trajectory of this corner is lens-shaped. Figure 4.4 illustrates one so-called stick-slip cycle during Helmholtz motion.

The friction force between string and bow can be incorporated into the PDE describing string motion in the horizontal polarisation, as follows:

$$\boldsymbol{L}\boldsymbol{u}_{(y)} = \begin{bmatrix} -J_{\mathcal{B}} \left[f_{\mathcal{B}}\right]_{+} \varphi_{\mathcal{B}} \\ \mathbf{0}_{M,1} \\ \mathbf{0}_{M',1} \end{bmatrix} \tag{4.16}$$

where $J_{\mathcal{B}}(x,t)$ is the same spatial distribution described in Section 4.2.2.ii, used to place the bow at a given location along the string. The force $f_{\mathcal{B}}(t)$ is the contact force between the bow hair and the string, in the vertical polarisation, defined by (4.7b). Note the minus sign in the friction term, reflecting the opposition of the sliding friction force to the motion of the string.

The dimensionless friction coefficient $\varphi_{\mathcal{B}}\left(v_{\mathrm{rel},\mathcal{B}}\right)$ depends on the relative velocity $v_{\mathrm{rel},\mathcal{B}}(t)$ between the bow hair and the string, which is defined as:

$$v_{\mathrm{rel},\mathcal{B}}(t) \triangleq \frac{d}{dt} \int\limits_{\mathcal{D}} J_{\mathcal{B}}(x,t) y(x,t) \mathrm{d}x - \dot{y}_{\mathcal{B}}(t) \tag{4.17}$$

where $y_{\mathcal{B}}(t)$ is the transverse displacement of the bow. The friction coefficient $\varphi_{\mathcal{B}}(v_{\mathrm{rel},\mathcal{B}})$ is defined as:

$$\begin{cases} \left|\varphi_{\mathcal{B}}\right| \leqslant 1.2 & \text{if } v_{\mathrm{rel},\mathcal{B}} = 0 \text{ (static)} \\ \varphi_{\mathcal{B}} \triangleq \operatorname{sign}\left(v_{\mathrm{rel},\mathcal{B}}\right) \left(0.4 e^{\frac{-\left|v_{\mathrm{rel},\mathcal{B}}\right|}{0.01}} + 0.45 e^{\frac{-\left|v_{\mathrm{rel},\mathcal{B}}\right|}{0.1}} + 0.35\right) & \text{if } v_{\mathrm{rel},\mathcal{B}} \neq 0 \text{ (kinetic)} \end{cases} \tag{4.18}$$

The graph of $\varphi_{\mathcal{B}}$ against $v_{\mathrm{rel},\mathcal{B}}$ constitutes a so-called *friction curve.* This particular model was derived by Smith *et al.* [100], who measured the ratio of normal load to resulting friction force experienced by a mass sliding steadily against a rosin-coated conveyor belt. It is fair to say that this model is flawed, as bowed string motion does not involve a steady sliding regime. Indeed,

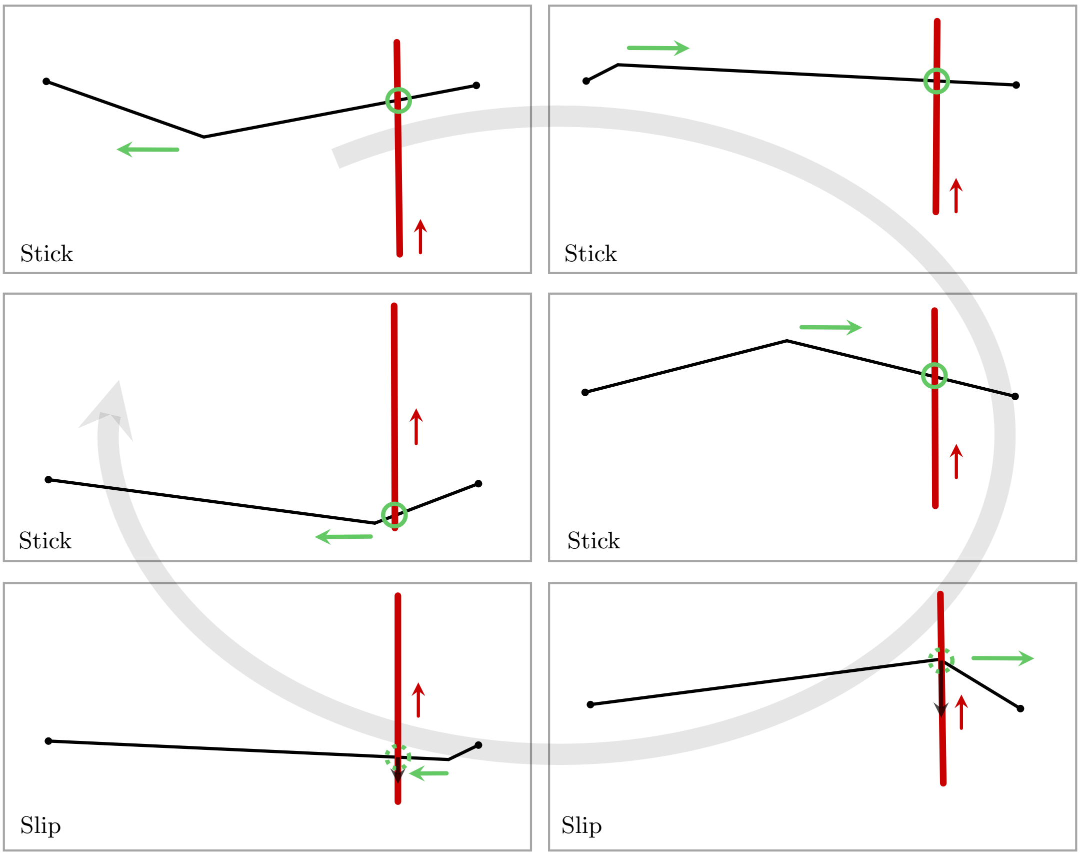

Figure 4.4: Description of a stick-slip cycle in the Helmholtz regime. The bow (in red) is moving upwards. A solid green circle indicates that the bow is sticking to the string; a dashed circle indicates slipping in the direction of the black arrow. The green arrows indicate the travel direction of the Helmholtz corner. As indicated by the grey arrow, the figures should be read clockwise.

the authors of [100] found that the temperature variations of the rosin layer during a stick-slip cycle played an important role in the frictional force exerted onto the string. This friction curve model is, however, a commonly used approximation, and the study of this particular interaction is not the subject of this manuscript. The reader is invited to consult a recent publication by Galluzzo *et al.* [41], which offers an in-depth assessment of the state of the art for bow friction models, including friction curve and temperature-dependent models, based on experimental and simulated results. Furthermore, considerations of computational cost must be kept in mind; while such a nonlinear friction curve may already be fairly costly to incorporate into a model, it nonetheless constitutes somewhat of a trade-off between computational simplification and physical realism. A model taking into account viscothermal effects in the rosin layer coating the bow hair would require significantly more advanced implementations, in order to keep track of heat exchanges in the system. Bowed string simulation results will be discussed extensively

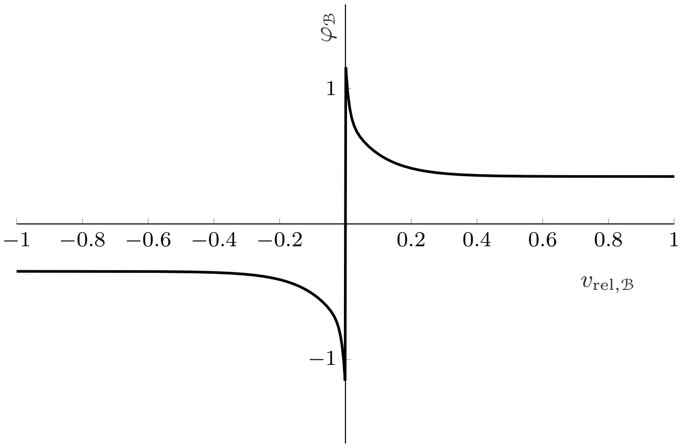

Figure 4.5: Friction curve $\varphi_{\mathcal{B}}\left(v_{\mathrm{rel},\mathcal{B}}\right)$ for the bow, from [100].

in Chapter 5, including an exploration of the available control parameter space; it will be seen that the friction curve model is able to produce results consistent with previous studies.

Figure 4.5 illustrates the friction curve $\varphi_{\mathcal{B}}\left(v_{\mathrm{rel},\mathcal{B}}\right)$; the vertical section at $v_{\mathrm{rel},\mathcal{B}} = 0$ corresponds to the sticking phase, while the rest of the curve, defined by (4.18), yields a kinetic friction coefficient for $|v_{\mathrm{rel},\mathcal{B}}| > 0$.

Finally, as the bow is pushed across the string, the equation governing the temporal evolution of $y_{\mathcal{B}}(t)$ is given by:

$$m_{\mathcal{B}}\ddot{y}_{\mathcal{B}} = -\lambda_{\mathcal{B}}\dot{y}_{\mathcal{B}} + \left[f_{\mathcal{B}}\right]_{+}\varphi_{\mathcal{B}} + f_{\mathrm{ext}\mathcal{B},(y)} \tag{4.19}$$

$\lambda_{\mathcal{B}} \geqslant 0$ is a coefficient quantifying the linear energy dissipation into the bow in the horizontal polarisation. The corresponding linear damping is negligible compared to the losses brought about by friction, when the string is in contact with the bow. Indeed, the purpose of this linear term is mainly practicality in the numerical simulations; when the bow is lifted up from the string at the end of a note, it may drift far away from the origin if not stopped, yielding large numbers which may be detrimental to computational accuracy of the numerical energy balance.

$f_{\mathrm{ext}\mathcal{B},(y)}(t)$ is the force applied tangentially onto the bow by the player, in order to establish the desired bow velocity. The use of a shear force as a control parameter sets this work slightly apart from most existing bowed string studies, including all those cited so far, which impose a bow velocity $v_{\mathcal{B}}(t)$ as a control signal; here, the resultant force applied by the player onto the bow is employed, leading to a variable bow velocity $\dot{y}_{\mathcal{B}}(t)$. The consequences on the playability of a sound synthesis tool using this model as an engine will be discussed in Chapter 5.

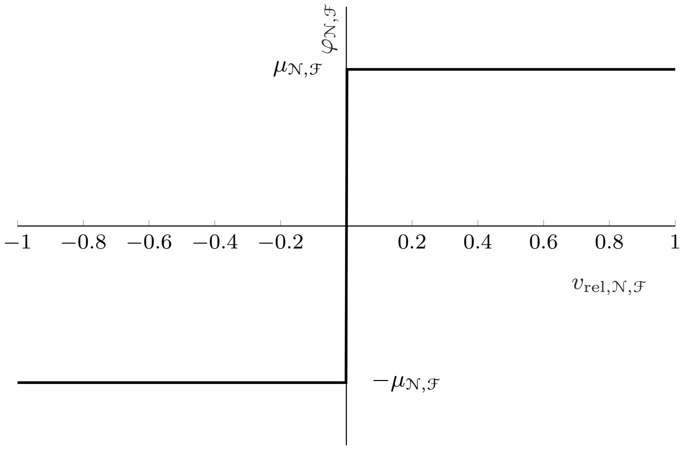

Figure 4.6: Coulomb step friction curve $\varphi_{\mathcal{N},\mathcal{F}}\left(v_{\mathrm{rel},\mathcal{N},\mathcal{F}}\right)$ for the finger and fingerboard.

4.2.3.iii Fingerboard and fingers

The tangential friction force exerted by the finger and fingerboard may be incorporated in System (4.16), as follows:

$$\boldsymbol{L}\boldsymbol{u}_{(y)} = \begin{bmatrix} -\left[F_{\mathcal{N}}\right]_{+}\varphi_{\mathcal{N}} - J_{\mathcal{F}}\left[f_{\mathcal{F}}\right]_{+}\varphi_{\mathcal{F}} - J_{\mathcal{B}}\left[f_{\mathcal{B}}\right]_{+}\varphi_{\mathcal{B}} \\ \mathbf{0}_{M\times 1} \\ \mathbf{0}_{M'\times 1} \end{bmatrix} \tag{4.20}$$

where $J_{\mathcal{F}}(x,t)$ is the distribution described in Section 4.2.2.i to place the finger along the string; $f_{\mathcal{F}}(t)$ is the normal contact force between finger and string, defined by (4.7a); $F_{\mathcal{N}}(x,t)$ is the normal force exerted by the fingerboard, defined by (4.13); $\varphi_{\mathcal{F}}\left(v_{\mathrm{rel},\mathcal{F}}\right)$ and $\varphi_{\mathcal{N}}\left(v_{\mathrm{rel},\mathcal{N}}\right)$ are dimensionless friction coefficients. Note that, as for the vertical polarisation, the tangential finger force is lumped, while the force exerted by the fingerboard is distributed along the string's length.

To a crude approximation, the function of the fingers and fingerboard is to capture the string to reduce its speaking length. To the author's knowledge, there does not exist experimental data against which to calibrate a velocity-dependent friction curve for the fingertips or the fingerboard. In the absence of such data, a Coulomb-like friction characteristic may be assumed, as illustrated in Figure 4.6, where the friction coefficient is constant for all sliding velocities. In most playing situations, static friction pins the string in place between the fingerboard and the fingertip; however, this simple model enables the string to slip under the finger if the left hand grip is too loose. The Coulomb characteristic for the finger and fingerboard is defined as:

$$\begin{cases} \left|\varphi_{\mathcal{F}}\left(v_{\mathrm{rel},\mathcal{F}}\right)\right| \leqslant \mu_{\mathcal{F}} & \text{if } v_{\mathrm{rel},\mathcal{F}} = 0 \text{ (static)} \\ \varphi_{\mathcal{F}}\left(v_{\mathrm{rel},\mathcal{F}}\right) \triangleq \mu_{\mathcal{F}} \operatorname{sign}\left(v_{\mathrm{rel},\mathcal{F}}\right) & \text{if } v_{\mathrm{rel},\mathcal{F}} \neq 0 \text{ (kinetic)} \end{cases} \tag{4.21a}$$

$$\begin{cases} \left|\varphi_{\mathcal{N}}\left(v_{\mathrm{rel},\mathcal{N}}\right)\right| \leqslant \mu_{\mathcal{N}} & \text{if } v_{\mathrm{rel},\mathcal{N}} = 0 \text{ (static)} \\ \varphi_{\mathcal{N}}\left(v_{\mathrm{rel},\mathcal{N}}\right) \triangleq \mu_{\mathcal{N}} \operatorname{sign}\left(v_{\mathrm{rel},\mathcal{N}}\right) & \text{if } v_{\mathrm{rel},\mathcal{N}} \neq 0 \text{ (kinetic)} \end{cases} \tag{4.21b}$$

where $\mu_{\mathcal{F}}$, $\mu_{\mathcal{N}} > 0$ are the friction coefficients characterising the finger and fingerboard, respectively. The relative velocities $v_{\mathrm{rel},\mathcal{F}}(t)$ and $v_{\mathrm{rel},\mathcal{N}}(x,t)$ of the finger and fingerboard with respect to the string are respectively defined as:

$$v_{\mathrm{rel},\mathcal{F}}(t) \triangleq \frac{d}{dt} \int\limits_{\mathcal{D}} J_{\mathcal{F}}(x,t) y(x,t) \mathrm{d}x - \dot{y}_{\mathcal{F}}(t) \tag{4.22a}$$

$$v_{\mathrm{rel},\mathcal{N}}(x,t) \triangleq \partial_t y(x,t) \tag{4.22b}$$

The position of the fingertip in the horizontal polarisation is denoted by $y_{\mathcal{F}}(t)$; it is hypothesised that the fingertip oscillates about the third knuckle, while simultaneously damping the vibrations of the string in the bowing plane. The behaviour of $y_{\mathcal{F}}(t)$ can therefore be modelled with a simple ODE:

$$m_{\mathcal{F}} \ddot{y}_{\mathcal{F}} = -K_{\mathcal{F}} y_{\mathcal{F}} - \lambda_{\mathcal{F}} \dot{y}_{\mathcal{F}} + \left[f_{\mathcal{F}}\right]_{+} \varphi_{\mathcal{F}} \tag{4.23}$$

where $K_{\mathcal{F}} \geqslant 0$ is a spring constant, characterising the restoring force exerted by the fingertip in reaction to being displaced by the moving string, and $\lambda_{\mathcal{F}} \geqslant 0$ is a damping coefficient. When the fingertip is concerned, the choice of a more elaborate contact model such as that used in the vertical polarisation seems excessive. Impacts are dominant in the vertical polarisation, and the modelling of collisions is important for accurate simulation of transients, e.g., when hammering the string with the left hand fingers in *legato* playing. Conversely, it is clear that collisions only have an auxiliary effect in the tangential polarisation.

A summary of the forces exerted onto the string in the horizontal polarisation is illustrated in Figure 4.7.

4.2.4 Energy analysis

Since the two polarisations of string motion are not intrinsically coupled in the proposed model, an energy balance can be derived separately for each polarisation. As will be seen in Section 4.3, this separation indeed follows the numerical implementation; contact forces are computed first in the vertical polarisation, then supplied as known parameters into the second polarisation system.

4.2.4.i Vertical polarisation

As described in Section 4.2.1 for the linear case, the energy balance for the vertical polarisation is derived by left-multiplying System (4.11) by $\left(\partial_t \boldsymbol{u}_{(w)}\right)^{\intercal}$, and integrating the result over $\mathcal{D}$, yielding:

$$\dot{H}_w = -Q_w + P_w \tag{4.24}$$

where $H_w(t)$ is the stored energy in the vertical polarisation, $Q_w(t)$ is the power dissipated through damping processes, and $P_w(t)$ is the power supplied to excite the system.

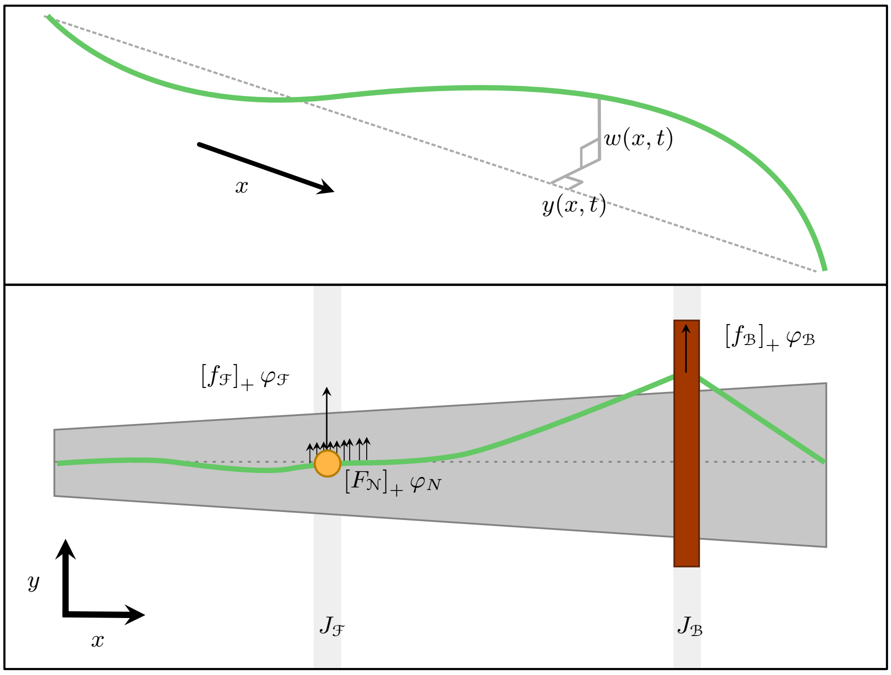
$w(x,t)$
x
$y(x,t)$
$[f_{\mathcal{B}}]_+\,\varphi_{\mathcal{B}}$
$[f_{\mathcal{F}}]_+\,\varphi_{\mathcal{F}}$
$[F_{\mathcal{N}}]_+\,\varphi_{N}$
y
x
$J_{\mathcal{F}}$
$J_{\mathcal{B}}$

Figure 4.7: Diagram summarising the forces applied onto the string by the finger, bow, and fingerboard, in the horizontal polarisation. The tangential friction forces arise from the normal contact forces described in Section 4.2.2.

The energy $H_w(t)$ is defined as:

$$H_w \triangleq H_{w,s} + H_{w,\gamma} + H_{w,\xi} + H_{w,\mathcal{N}} + H_{w,\mathcal{F}} + H_{w,\mathcal{B}} \tag{4.25a}$$

$$H_{w,\mathcal{N}} \triangleq \int_{\mathcal{D}} \Phi_{\mathcal{N}} \mathrm{d}x \geqslant 0 \tag{4.25b}$$

$$H_{w,\mathcal{F}} \triangleq \Phi_{\mathcal{F}} + \frac{m_{\mathcal{F}}}{2}\dot{w}_{\mathcal{F}}^2 \geqslant 0 \tag{4.25c}$$

$$H_{w,\mathcal{B}} \triangleq \Phi_{\mathcal{B}} + \frac{m_{\mathcal{B}}}{2}\dot{w}_{\mathcal{B}}^2 \geqslant 0 \tag{4.25d}$$

where $H_{w,s}(t)$ is the energy of the lossless stiff string, defined by (2.28); $H_{w,\gamma}(t)$, $H_{w,\xi}(t)$ are the energy terms related to the linear loss model presented in Chapter 3, and are defined by (3.49). The new terms $H_{w,\mathcal{N}}(t)$, $H_{w,\mathcal{F}}(t)$, $H_{w,\mathcal{B}}(t)$ constitute the energy stored during the collision with the neck, finger, and bow, as well as the kinetic energies of the finger and bow. The total energy $H_w(t)$ is positive.

The power $Q_w(t)$ dissipated within the string and through collision with the fingerboard, finger, and bow, is defined as:

$$Q_w \triangleq Q_{w,\gamma} + Q_{w,\xi} + Q_{\Psi,\mathcal{N}} + Q_{\Psi,\mathcal{F}} + Q_{\Psi,\mathcal{B}} \tag{4.26a}$$

$$Q_{\Psi,\mathcal{N}} \triangleq \int_{\mathcal{D}} \left(\partial_t \Delta_{\mathcal{N}}\right)^2 \Psi_{\mathcal{N}} \,\mathrm{d}x \geqslant 0 \tag{4.26b}$$

$$Q_{\Psi,\mathcal{F}} \triangleq \dot{\Delta}_{\mathcal{F}}^2 \Psi_{\mathcal{F}} \geqslant 0 \tag{4.26c}$$

$$Q_{\Psi,\mathcal{B}} \triangleq \dot{\Delta}_{\mathcal{B}}^2 \Psi_{\mathcal{B}} \geqslant 0 \tag{4.26d}$$

where $Q_{w,\gamma}$, $Q_{w,\xi}$ are defined in (3.51). Since $Q_w(t) \geqslant 0$, in the absence of external excitation, the energy $H_w(t)$ of the system decreases.

The power $P_w(t)$ supplied to the system is defined as:

$$P_w \triangleq P_{w,\mathcal{F}} + P_{w,\mathcal{B}} \tag{4.27a}$$

$$P_{w,\mathcal{F}} \triangleq \dot{w}_{\mathcal{F}} f_{\mathrm{ext}\mathcal{F},(w)} + f_{\mathcal{F}} \int\limits_{\mathcal{D}} w\, \partial_t J_{\mathcal{F}} \, \mathrm{d}x \tag{4.27b}$$

$$P_{w,\mathcal{B}} \triangleq \dot{w}_{\mathcal{B}} f_{\mathrm{ext}\mathcal{B},(w)} + f_{\mathcal{B}} \int\limits_{\mathcal{D}} w\, \partial_t J_{\mathcal{B}} \, \mathrm{d}x \tag{4.27c}$$

Note that the second term in (4.27b) and (4.27c) accounts for the energy supplied to the system by changing the position of the bow or finger along the string.

4.2.4.ii Horizontal polarisation

For the horizontal polarisation, left-multiplying System (4.20) by $\left(\partial_t \boldsymbol{u}_{(y)}\right)^{\mathsf{T}}$, and integrating the resulting equation over $\mathcal{D}$, leads to the energy balance:

$$\dot{H}_y = -Q_y + P_y \tag{4.28}$$

where $H_y(t)$ is the stored energy in the horizontal polarisation, $Q_y(t)$ is the power dissipated by linear damping and friction, and $P_y(t)$ is the supplied power.

The energy $H_y(t)$ is defined as:

$$H_y \triangleq H_{y,s} + H_{y,\gamma} + H_{y,\xi} + H_{y,\mathcal{F}} + H_{y,\mathcal{B}} \tag{4.29a}$$

$$H_{y,\mathcal{F}} \triangleq \frac{m_{\mathcal{F}}}{2} \dot{y}_{\mathcal{F}}^2 + \frac{K_{\mathcal{F}}}{2} y_{\mathcal{F}}^2 \geqslant 0 \tag{4.29b}$$

$$H_{y,\mathcal{B}} \triangleq \frac{m_{\mathcal{B}}}{2} \dot{y}_{\mathcal{B}}^2 \geqslant 0 \tag{4.29c}$$

where $H_{y,s}(t)$, $H_{y,\gamma}(t)$, $H_{y,\xi}(t)$ have the same respective expressions as $H_{w,s}(t)$ (defined by (2.28)), $H_{w,\gamma}(t)$, and $H_{w,\xi}(t)$ (both defined by (3.49)), with the appropriate substitutions of w by y. The energy $H_y(t)$ in the second polarisation is positive.

The dissipated power $Q_y(t)$ is defined as:

$$Q_y \triangleq Q_{y,\gamma} + Q_{y,\xi} + Q_{\varphi,\mathcal{N}} + Q_{\varphi,\mathcal{F}} + Q_{\varphi,\mathcal{B}} + Q_{y,\mathcal{F}} + Q_{y,\mathcal{B}} \tag{4.30a}$$

$$Q_{\varphi,\mathcal{N}} \triangleq \int\limits_{\mathcal{D}} v_{\mathrm{rel},\mathcal{N}} [F_{\mathcal{N}}]_+ \varphi_{\mathcal{N}} \, \mathrm{d}x \tag{4.30b}$$

$$Q_{\varphi,\mathcal{F}} \triangleq v_{\mathrm{rel},\mathcal{F}} [f_{\mathcal{F}}]_+ \varphi_{\mathcal{F}} \tag{4.30c}$$

$$Q_{\varphi,\mathcal{B}} \triangleq v_{\mathrm{rel},\mathcal{B}}[f_{\mathcal{B}}]_{+}\varphi_{\mathcal{B}} \tag{4.30d}$$
$$Q_{y,\mathcal{F}} \triangleq \lambda_{\mathcal{F}}\dot{y}_{\mathcal{F}}^2 \tag{4.30e}$$
$$Q_{y,\mathcal{B}} \triangleq \lambda_{\mathcal{B}}\dot{y}_{\mathcal{B}}^2 \tag{4.30f}$$

Note that, for the system to be dissipative in the absence of external excitation, $Q_y(t)$ must be positive. This condition is satisfied if:

$$\begin{aligned} v_{\mathrm{rel},\mathcal{N}} \cdot \varphi_{\mathcal{N}}(v_{\mathrm{rel},\mathcal{N}}) &\geqslant 0 \\ v_{\mathrm{rel},\mathcal{F}} \cdot \varphi_{\mathcal{F}}(v_{\mathrm{rel},\mathcal{F}}) &\geqslant 0 \\ v_{\mathrm{rel},\mathcal{B}} \cdot \varphi_{\mathcal{B}}(v_{\mathrm{rel},\mathcal{B}}) &\geqslant 0 \end{aligned} \tag{4.31}$$

This is to say that the friction curves must lie in the top-right and bottom-left quarter-planes of the $(v_{\mathrm{rel}}, \varphi(v_{\mathrm{rel}}))$ plane; all three $\varphi_{\mathcal{N}}$, $\varphi_{\mathcal{F}}$, and $\varphi_{\mathcal{B}}$ comply.

The power supplied through external excitation is defined as:

$$P_y \triangleq P_{y,\mathcal{F}} + P_{y,\mathcal{B}} \tag{4.32a}$$
$$P_{y,\mathcal{F}} \triangleq [f_{\mathcal{F}}]_{+}\varphi_{\mathcal{F}} \int_{\mathcal{D}} y\, \partial_t J_{\mathcal{F}}\, \mathrm{d}x \tag{4.32b}$$
$$P_{y,\mathcal{B}} \triangleq [f_{\mathcal{B}}]_{+}\varphi_{\mathcal{B}} \int_{\mathcal{D}} y\, \partial_t J_{\mathcal{B}}\, \mathrm{d}x + \dot{y}_{\mathcal{B}} f_{\mathrm{ext}\mathcal{B},(y)} \tag{4.32c}$$

4.2.4.iii Global power balance

The total power balance of the full system, including both polarisations, is obtained by summing (4.24) and (4.28):

$$\dot{H} = -Q + P \tag{4.33}$$
$$H \triangleq H_w + H_y \qquad Q \triangleq Q_w + Q_y \qquad P \triangleq P_w + P_y$$

A power balance equation of the same type as (4.33) generally forms the basis for another class of modelling methods, mentioned in Chapter 2 (see Section 2.1.1.iv), based on so-called port-Hamiltonian systems [114]. The discretisation of such systems has recently been successfully implemented for time-domain physical modelling of acoustic and electroacoustic systems [34, 35].

4.3 Finite difference scheme

The continuous-time system presented in Section 4.2 describes a physical model of a two-polarisation linear string, nonlinearly coupled to a bow, left-hand fingers, and a fingerboard.

Sections 4.3.1—4.3.3 will describe the finite difference scheme arising from the discretisation of the PDE system, based on the same principles and framework as that used in Chapters 2 and 3.

The PDE system now includes nonlinear elements; the scheme update can no longer be computed as the solution of a linear system. Section 4.3.5 will focus on the resolution of the discrete nonlinear system, in each polarisation, required to perform each iteration of the scheme.

4.3.1 Localising interactions in the discrete spatial domain

The interaction of the string with the finger and bow is localised onto a small interval (or, in the lumped case, a single point) of the spatial domain of definition $\mathcal{D}$ of $w(x,t)$ and $y(x,t)$. In the continuous system, such localisation is achieved through the normalised distributions $J_{\mathcal{F}}(x,t)$ and $J_{\mathcal{B}}(x,t)$.

These distributions may be approximated by the grid functions $\mathbf{j}_{\mathcal{F}}^n$ and $\mathbf{j}_{\mathcal{B}}^n$ (in vector notation), defined over the same discrete spatial domain $\mathfrak{D}$ as are $\mathbf{w}^n$ and $\mathbf{y}^n$, at coinciding time step $n \in \mathbb{N}$, and normalised by the grid spacing h.

In the discrete spatial domain, centring the bow and finger forces at a specific point requires careful consideration. If the desired location at which to apply a force lies between two grid points, one must resort to interpolation; hence, a pointwise distribution in the continuous domain will only result in a pointwise distribution in the discrete domain if the location $x_{\mathcal{F}}, x_{\mathcal{B}} \in \mathcal{D}$ of the finger or bow is rounded to that of the nearest grid point (that is, using 0th order interpolation). This obviously leads to inaccuracies in simulations; for instance, on a fretless stringed instrument, the location of the stopping finger determines the pitch of a note, and an inaccurate approximation will lead to mistunings. Furthermore, a great deal of the expressivity in bowed string instrument playing comes from the continuous variations of playing parameters, directed by the musician. Such parameters include the bow-bridge distance, varied to affect timbre, and the location of the left hand fingers during *vibrato* and *glissando* gestures. When they are time-varying, truncating the locations of applied forces to the nearest grid point would undoubtedly lead to audible grid effects.

A better approach makes use of Lagrange interpolation polynomials. The effect of a lumped excitation is spread over a number of grid points, with different weightings depending on the relative location of the excitation between two grid points [8, pp. 101—103]. For m^{th} order interpolation, the resulting discrete distributions $\mathbf{j}_{\mathcal{F}}^n$ and $\mathbf{j}_{\mathcal{B}}^n$ contain m consecutive non-zero elements, centred around the desired position of the excitation.

Recall that, for a pointwise (Dirac delta) distribution $J_{\mathcal{F}}(x,t) \triangleq \delta(x - x_{\mathcal{F}}, t)$ defining the location of a finger along the string in the continuous domain:

$$\int_{\mathcal{D}} J_{\mathcal{F}}(x,t)\, w(x,t)\, \mathrm{d}x = w(x_{\mathcal{F}}, t) \tag{4.34}$$

In the same manner, left-multiplying $\mathbf{w}^n$ by $h\left(\mathbf{j}_{\mathcal{F}}^n\right)^{\mathsf{T}}$ will yield an mth order interpolated estimate of the string displacement at the finger location:

$$\begin{aligned} h\left(\mathbf{j}_{\mathcal{B}}^{n}\right)^{\mathsf{T}}\mathbf{w}^{n} &= \sum_{l=l_0}^{l_0+m} c_l w_l^n \\ &\approx w(x_{\mathcal{F}},t) \end{aligned} \tag{4.35}$$

where the $c_l, l \in [l_0, ..., l_0+m]$ are the mth order Lagrange basis polynomials, evaluated at $x = x_{\mathcal{F}}$, between data points $l_0, \ldots, l_0+m$. $\mathbf{j}_{\mathcal{B}}^n$ is hence defined as:

$$\mathbf{j}_{\mathcal{B}}^{n} \triangleq \frac{1}{h}\begin{bmatrix} \cdots & 0 & c_{l_0} & c_{l_0+1} & \cdots & c_{l_0+m} & 0 & \cdots \end{bmatrix}^{\mathsf{T}} \tag{4.36}$$

The magnitude of $\mathbf{j}_{\mathcal{B}}^n$ is thus bounded by $\frac{1}{h}$[5].

4.3.2 Vertical polarisation

Let $\mathbf{u}_{(w)}^n$ be defined as the discrete counterpart of $\boldsymbol{u}_{(w)}$, as per (3.57):

$$\mathbf{u}_{(w)}^{n} \triangleq \left[\begin{array}{c|ccc|ccc} \mathbf{w}^{n\,\mathsf{T}} & \boldsymbol{\gamma}_{1,(w)}^{n-1/2\,\mathsf{T}} & \cdots & \boldsymbol{\gamma}_{M,(w)}^{n-1/2\,\mathsf{T}} & \boldsymbol{\xi}_{1,(w)}^{n-1/2\,\mathsf{T}} & \cdots & \boldsymbol{\xi}_{M',(w)}^{n-1/2\,\mathsf{T}} \end{array}\right]^{\mathsf{T}} \tag{4.37}$$

The continuous PDE system (4.11) describing the behaviour of a linear string in contact with a fingerboard, a finger, and a bow, may be discretised with the following FD scheme:

$$\mathbf{L}\mathbf{u}_{(w)}^{n} = \begin{bmatrix} \mu_{t\cdot}\mathbf{J}_{(w)}^{n}\mathbf{f}_{(w)}^{n} \\ \mathbf{0}_{M\times 1} \\ \mathbf{0}_{M'\times 1} \end{bmatrix} \tag{4.38}$$

where $\mathbf{J}_{(w)}^n$ is a $N \times (N+2)$ distribution matrix[6], defined as:

$$\mathbf{J}_{(w)}^{n} \triangleq \left[\begin{array}{c|c|c} \frac{1}{h}\mathbf{I} & -\mathbf{j}_{\mathcal{F}}^{n} & -\mathbf{j}_{\mathcal{B}}^{n} \end{array}\right] \tag{4.39}$$

and $\mathbf{f}_{(w)}^n$ is a $(N+2) \times 1$ column vector, containing the discrete contact forces exerted by the fingerboard, finger, and bow, onto the string:

$$\mathbf{f}_{(w)}^{n} \triangleq \left[\begin{array}{c|c|c} \left(h\mathbf{f}_{\mathcal{N}}^{n}\right)^{\mathsf{T}} & f_{\mathcal{F}}^{n} & f_{\mathcal{B}}^{n} \end{array}\right]^{\mathsf{T}} \tag{4.40}$$

---

[5] It is easy to show that $\left|\mathbf{j}_{\mathcal{B}}^n\right| = \frac{1}{h}$ if and only if $x_{\mathcal{B}}$ lies exactly on a grid point.

[6] Recall that N is the number of elements in the truncated state vector $\mathbf{w}^n$.

The N elements of the vector $\mathbf{f}^n_{\mathcal{N}}$ each approximate the fingerboard force density $F_{\mathcal{N}}(x,t)$, as defined in Section 4.2.2.iii, at $x = lh$; the time series $f^n_{\mathcal{F}}$, $f^n_{\mathcal{B}}$ respectively approximate $f_{\mathcal{F}}(t)$ and $f_{\mathcal{B}}(t)$, the finger and bow forces, as defined in Section 4.2.2.ii.

Note the use of the centred averaging operator $\mu_{t\cdot}$ in (4.38); as will be seen in Section 4.3.4, this is necessary to derive the appropriate discrete energy balance for this scheme, ultimately yielding the stability condition.

Given the definitions of the nonlinear collision forces given in Section 4.2.2, the force vector $\mathbf{f}^n_{(w)}$ can be directly written as:

$$\mathbf{f}^n_{(w)} \triangleq \operatorname{diag}(\mathbf{h}) \left(\frac{\delta_{t\cdot}\boldsymbol{\Phi}^n}{\delta_{t\cdot}\boldsymbol{\Delta}^n} + \left(\delta_{t\cdot}\boldsymbol{\Delta}^n\right) \odot \boldsymbol{\Psi}^n \right) \tag{4.41}$$

where the vector $\mathbf{h} \triangleq [\ldots\ h\ \ldots|1|1]^{\mathsf{T}}$ has $N+2$ elements. Here, the division is element-wise, and the notation $\odot$ indicates the element-wise product of two matrices of equal size. The force vector $\mathbf{f}^n_{(w)}$ is written as a function of a vector deformation $\boldsymbol{\Delta}^n$, defined as:

$$\boldsymbol{\Delta}^n \triangleq \left[\begin{array}{c} \\ \boldsymbol{\Delta}^n_{\mathcal{N}} \\ \\ \hline \Delta^n_{\mathcal{F}} \\ \hline \Delta^n_{\mathcal{B}} \end{array}\right] \tag{4.42a}$$

$$\boldsymbol{\Delta}^n_{\mathcal{N}} \triangleq \boldsymbol{\varepsilon} - \mathbf{w}^n \tag{4.42b}$$

$$\Delta^n_{\mathcal{F}} \triangleq h\,{\mathbf{j}^n_{\mathcal{F}}}^{\mathsf{T}}\mathbf{w}^n - w^n_{\mathcal{F}} \tag{4.42c}$$

$$\Delta^n_{\mathcal{B}} \triangleq h\,{\mathbf{j}^n_{\mathcal{B}}}^{\mathsf{T}}\mathbf{w}^n - w^n_{\mathcal{B}} \tag{4.42d}$$

where the elements of the vector $\boldsymbol{\varepsilon}$ are $\varepsilon_l \triangleq \varepsilon(lh)$, with $\varepsilon(x)$ the position of the fingerboard with respect to the string at rest, as presented in Section 4.2.2.iii. The time series $w^n_{\mathcal{F}}$ and $w^n_{\mathcal{B}}$ approximate the respective vertical positions of the finger and bow.

$\boldsymbol{\Phi}^n(\boldsymbol{\Delta}^n)$ and $\boldsymbol{\Psi}^n(\boldsymbol{\Delta}^n)$ are now vector functions of $\boldsymbol{\Delta}^n$:

$$\boldsymbol{\Phi}^n(\boldsymbol{\Delta}^n) \triangleq \frac{\boldsymbol{K}}{\boldsymbol{\alpha}+1} \odot [\boldsymbol{\Delta}^n]_+^{\boldsymbol{\alpha}+1} \tag{4.43a}$$

$$\boldsymbol{\Psi}^n(\boldsymbol{\Delta}^n) \triangleq \boldsymbol{K} \odot \boldsymbol{\beta} \odot [\boldsymbol{\Delta}^n]_+^{\boldsymbol{\alpha}} \tag{4.43b}$$

$$\tag{4.43c}$$

where the exponentiation operation is also element-wise, and the nonlinearity parameters $\boldsymbol{K}$, $\boldsymbol{\alpha}$, and $\boldsymbol{\beta}$ are themselves in vector form:

$$\boldsymbol{K} \triangleq \left[\begin{array}{c} \vdots \\ K_{\mathcal{N}} \\ \vdots \\ \hline K_{\mathcal{F}} \\ \hline K_{\mathcal{B}} \end{array}\right] \quad (4.44a) \qquad \boldsymbol{\alpha} \triangleq \left[\begin{array}{c} \vdots \\ \alpha_{\mathcal{N}} \\ \vdots \\ \hline \alpha_{\mathcal{F}} \\ \hline \alpha_{\mathcal{B}} \end{array}\right] \quad (4.44b) \qquad \boldsymbol{\beta} \triangleq \left[\begin{array}{c} \vdots \\ \beta_{\mathcal{N}} \\ \vdots \\ \hline \beta_{\mathcal{F}} \\ \hline \beta_{\mathcal{B}} \end{array}\right] \quad (4.44c)$$

Finally, the ODEs (4.10) governing the temporal evolution of the vertical displacements of the finger and bow may be discretised as:

$$\mathbf{M}_{\mathcal{F}\mathcal{B}} \delta_{tt} \mathbf{w}^n_{\mathcal{F}\mathcal{B}} = \mathbf{f}^n_{\mathcal{F}\mathcal{B},(w)} + \mathbf{f}^n_{\mathrm{ext}\mathcal{F}\mathcal{B},(w)} \tag{4.45}$$

where the 2×2 matrix $\mathbf{M}_{\mathcal{F}\mathcal{B}}$, and the 2×1 vectors $\mathbf{w}^n_{\mathcal{F}\mathcal{B}}$, $\mathbf{f}^n_{\mathcal{F}\mathcal{B},(w)}$, and $\mathbf{f}^n_{\mathrm{ext}\mathcal{F}\mathcal{B},(w)}$ are defined as:

$$\mathbf{M}_{\mathcal{F}\mathcal{B}} \triangleq \begin{bmatrix} m_{\mathcal{F}} & 0 \\ 0 & m_{\mathcal{B}} \end{bmatrix} \quad (4.46a) \qquad \mathbf{f}^n_{\mathcal{F}\mathcal{B},(w)} \triangleq \begin{bmatrix} f^n_{\mathcal{F}} \\ f^n_{\mathcal{B}} \end{bmatrix} \quad (4.46c)$$

$$\mathbf{w}^n_{\mathcal{F}\mathcal{B}} \triangleq \begin{bmatrix} w^n_{\mathcal{F}} \\ w^n_{\mathcal{B}} \end{bmatrix} \quad (4.46b) \qquad \mathbf{f}^n_{\mathrm{ext}\mathcal{F}\mathcal{B},(w)} \triangleq \begin{bmatrix} f^n_{\mathrm{ext}\mathcal{F},(w)} \\ f^n_{\mathrm{ext}\mathcal{B},(w)} \end{bmatrix} \quad (4.46d)$$

4.3.3 Horizontal polarisation

Let $\mathbf{u}^n_{(y)}$ the discrete state vector in the horizontal polarisation, defined as:

$$\mathbf{u}^n_{(y)} \triangleq \left[\begin{array}{c|ccc|ccc} \mathbf{y}^{n\,\mathsf{T}} & \boldsymbol{\gamma}^{n-1/2\,\mathsf{T}}_{1,(y)} & \cdots & \boldsymbol{\gamma}^{n-1/2\,\mathsf{T}}_{M,(y)} & \boldsymbol{\xi}^{n-1/2\,\mathsf{T}}_{1,(y)} & \cdots & \boldsymbol{\xi}^{n-1/2\,\mathsf{T}}_{M',(y)} \end{array}\right]^{\mathsf{T}} \tag{4.47}$$

In the horizontal polarisation, consider the following FD scheme as a discretisation of System (4.20):

$$\mathbf{L}\mathbf{u}^n_{(y)} = \begin{bmatrix} -\mu_{t\cdot}\mathbf{J}^n_{(y)}\mathbf{f}^n_{(y)} \\ \mathbf{0}_{M\times 1} \\ \mathbf{0}_{M'\times 1} \end{bmatrix} \tag{4.48}$$

where the distribution matrix $\mathbf{J}^n_{(y)}$ is defined as:

$$\mathbf{J}^n_{(y)} \triangleq \left[\begin{array}{c|c|c} \frac{1}{h}\mathbf{I} & \mathbf{j}^n_{\mathcal{F}} & \mathbf{j}^n_{\mathcal{B}} \end{array}\right] \tag{4.49}$$

The $(N+2) \times 1$ force vector $\mathbf{f}^n_{(y)}$ is defined as:

$$\mathbf{f}^n_{(y)} \triangleq \left[\mathbf{f}^n_{(w)}\right]_+ \odot \left[\begin{array}{c} \varphi_{\mathcal{N}}\left(\mathbf{v}^n_{\mathrm{rel},\mathcal{N}}\right) \\ \hline \varphi_{\mathcal{F}}\left(v^n_{\mathrm{rel},\mathcal{F}}\right) \\ \hline \varphi_{\mathcal{B}}\left(v^n_{\mathrm{rel},\mathcal{B}}\right) \end{array}\right] \tag{4.50a}$$

$$\mathbf{v}^n_{\mathrm{rel},\mathcal{N}} \triangleq \delta_{t\cdot}\mathbf{y}^n \tag{4.50b}$$

$$v^n_{\mathrm{rel},\mathcal{F}} \triangleq h\delta_{t\cdot}\left({\mathbf{j}^n_{\mathcal{F}}}^{\mathsf{T}}\mathbf{y}^n\right) - \delta_{t\cdot}y^n_{\mathcal{F}} \tag{4.50c}$$

$$v^n_{\mathrm{rel},\mathcal{B}} \triangleq h\delta_{t\cdot}\left({\mathbf{j}^n_{\mathcal{B}}}^{\mathsf{T}}\mathbf{y}^n\right) - \delta_{t\cdot}y^n_{\mathcal{B}} \tag{4.50d}$$

where the friction curves $\varphi_{\mathcal{N}}$, $\varphi_{\mathcal{F}}$, and $\varphi_{\mathcal{B}}$ are those defined in (4.21) and (4.18). The time series $y^n_{\mathcal{F}}$ and $y^n_{\mathcal{B}}$ approximate the respective horizontal displacements of the finger and bow. One can define a vector relative velocity:

$$\mathbf{v}^n_{\mathrm{rel}} \triangleq \left[\begin{array}{c|c|c} \left(\mathbf{v}^n_{\mathrm{rel},\mathcal{N}}\right)^{\mathsf{T}} & v^n_{\mathrm{rel},\mathcal{F}} & v^n_{\mathrm{rel},\mathcal{B}} \end{array}\right]^{\mathsf{T}} \tag{4.51}$$

The ODEs (4.23) and (4.19) may be discretised as:

$$\mathbf{M}_{\mathcal{F}\mathcal{B}}\delta_{tt}\mathbf{y}^n_{\mathcal{F}\mathcal{B}} = -\mathbf{K}_{\mathcal{F}\mathcal{B}}\mu_{t\cdot}\mathbf{y}^n_{\mathcal{F}\mathcal{B}} - \boldsymbol{\lambda}_{\mathcal{F}\mathcal{B}}\delta_{t\cdot}\mathbf{y}^n_{\mathcal{F}\mathcal{B}} + \mathbf{f}^n_{\mathcal{F}\mathcal{B},(y)} + \mathbf{f}^n_{\mathrm{ext}\mathcal{F}\mathcal{B},(y)} \tag{4.52}$$

where $\mathbf{M}_{\mathcal{F}\mathcal{B}}$ is the mass matrix defined by (4.46a), and the remaining vectors and matrices are defined as:

$$\mathbf{y}^n_{\mathcal{F}\mathcal{B}} \triangleq \begin{bmatrix} y^n_{\mathcal{F}} \\ y^n_{\mathcal{B}} \end{bmatrix} \tag{4.53a}$$

$$\mathbf{K}_{\mathcal{F}\mathcal{B}} \triangleq \begin{bmatrix} K_{\mathcal{F}} & 0 \\ 0 & 0 \end{bmatrix} \tag{4.53b}$$

$$\boldsymbol{\lambda}_{\mathcal{F}\mathcal{B}} \triangleq \begin{bmatrix} \lambda_{\mathcal{F}} & 0 \\ 0 & \lambda_{\mathcal{B}} \end{bmatrix} \tag{4.53c}$$

$$\mathbf{f}^n_{\mathcal{F}\mathcal{B},(y)} \triangleq \left[\mathbf{f}^n_{\mathcal{F}\mathcal{B},(w)}\right]_+ \odot \begin{bmatrix} \varphi_{\mathcal{F}}(v^n_{\mathrm{rel},\mathcal{F}}) \\ \varphi_{\mathcal{B}}(v^n_{\mathrm{rel},\mathcal{B}}) \end{bmatrix} \tag{4.53d}$$

$$\mathbf{f}^n_{\mathrm{ext}\mathcal{F}\mathcal{B},(y)} \triangleq \begin{bmatrix} 0 \\ f^n_{\mathrm{ext}\mathcal{B},(y)} \end{bmatrix} \tag{4.53e}$$

As will be seen in Section 4.3.4.ii, the centred averaging operator $\mu_{t\cdot}$ in (4.52) is used as a means to avoid restricting the stability limit of the FD scheme any further.

4.3.4 Energy and stability analysis

4.3.4.i Vertical polarisation

Left-multiplying Equation (4.38) by $\left(h\delta_{t\cdot}\mathbf{u}^n_{(w)}\right)^{\mathsf{T}}$, and using (4.41), (4.42), and (4.45), yields the following discrete power balance for the vertical polarisation:

$$\delta_{t-}\mathrm{H}^n_w = \mathrm{P}^n_w - \mathrm{Q}^n_w \tag{4.54}$$

where H^n_w is the discrete energy, while Q^n_w and P^n_w are the power respectively dissipated from and supplied to the discrete system at time step n. The energy H^n_w is defined as:

$$\mathrm{H}^n_w \triangleq \mathrm{H}^n_{w,s} + \mathrm{H}^n_{w,\gamma} + \mathrm{H}^n_{w,\xi} + \mathrm{H}^n_{w,\Phi} + \mathrm{H}^n_{w,\mathcal{F}\mathcal{B}} \tag{4.55a}$$

$$\mathrm{H}^n_{w,\Phi} \triangleq \mathbf{h}^{\mathsf{T}}\mu_{t+}\mathbf{\Phi}^n \tag{4.55b}$$

$$\mathrm{H}^n_{w,\mathcal{F}\mathcal{B}} \triangleq \frac{1}{2}\left(\mathbf{M}_{\mathcal{F}\mathcal{B}}\delta_{t+}\mathbf{w}^n_{\mathcal{F}\mathcal{B}}\right)^{\mathsf{T}}\delta_{t+}\mathbf{w}^n_{\mathcal{F}\mathcal{B}} \tag{4.55c}$$

The energy terms relating to the string, $\mathrm{H}^n_{w,s}$, $\mathrm{H}^n_{w,\gamma}$, and $\mathrm{H}^n_{w,\xi}$, are the same as defined in (2.84b), (3.63a) and (3.63b). The term $\mathrm{H}^n_{w,\Phi}$ is the energy stored during collision of the string with the fingerboard, finger and bow. Finally, $\mathrm{H}^n_{w,\mathcal{F}\mathcal{B}}$ is the kinetic energy of the bow and the finger.

The power $\mathrm{Q}^n_w \geqslant 0$ dissipated by damping processes is defined by:

$$\mathrm{Q}^n_w \triangleq \mathrm{Q}^n_{w,\gamma} + \mathrm{Q}^n_{w,\xi} + \mathrm{Q}^n_{w,\Psi} \tag{4.56a}$$

$$\mathrm{Q}^n_{w,\Psi} \triangleq \left(\mathbf{h}\odot\delta_{t\cdot}\mathbf{\Delta}^n\right)^{\mathsf{T}}\left(\left(\delta_{t\cdot}\mathbf{\Delta}^n\right)\odot\mathbf{\Psi}^n\right) \tag{4.56b}$$

The power $\mathrm{Q}^n_{w,\gamma}$, $\mathrm{Q}^n_{w,\xi}$ dissipated by mechanisms specific to the linear string is the same as defined in (3.63c) and (3.63d). The power dissipated during nonlinear collision is $\mathrm{Q}^n_{w,\Psi}$.

The power P^n_w supplied by external excitation is given by:

$$\mathrm{P}^n_w \triangleq \left(\delta_{t\cdot}\mathbf{w}^n_{\mathcal{F}\mathcal{B}}\right)^{\mathsf{T}}\mathbf{f}^n_{\mathrm{ext}\mathcal{F}\mathcal{B},(w)} - h\left(\left(\mu_{t\cdot}\mathbf{w}^n\right)^{\mathsf{T}}\left(\delta_{t\cdot}\mathbf{J}^n_{(w)}\right)\right)\mathbf{f}^n_{(w)} \tag{4.57}$$

4.3.4.ii Horizontal polarisation

The numerical power balance for the horizontal polarisation is obtained by left-multiplying Equation (4.48) by $\left(h\delta_{t\cdot}\mathbf{u}^n_{(y)}\right)^{\mathsf{T}}$:

$$\delta_{t-}\mathrm{H}^n_y = \mathrm{P}^n_y - \mathrm{Q}^n_y \tag{4.58}$$

where the numerical energy H_y^n is given by:

$$\mathrm{H}_y^n \triangleq \mathrm{H}_{y,s}^n + \mathrm{H}_{y,\gamma}^n + \mathrm{H}_{y,\xi}^n + \mathrm{H}_{y,\mathcal{FB}}^n \tag{4.59a}$$

$$\mathrm{H}_{y,\mathcal{FB}}^n \triangleq \frac{1}{2}\left(\mathbf{M}_{\mathcal{FB}}\delta_{t+}\mathbf{y}_{\mathcal{FB}}^n\right)^{\mathsf{T}}\delta_{t+}\mathbf{y}_{\mathcal{FB}}^n + \frac{1}{2}\mu_{t+}\left(\left(\mathbf{K}_{\mathcal{FB}}\mathbf{y}_{\mathcal{FB}}^n\right)\mathbf{y}_{\mathcal{FB}}^n\right) \tag{4.59b}$$

and $\mathrm{H}_{y,s}^n$, $\mathrm{H}_{y,\gamma}^n$, and $\mathrm{H}_{y,\xi}^n$ take the same form as those defined by (2.84b), (3.63a), and (3.63b), with the appropriate substitutions of $w, \mathbf{w}^n$ by $y, \mathbf{y}^n$.

Q_y^n is the power dissipated by friction and damping, defined by:

$$\mathrm{Q}_y^n \triangleq \mathrm{Q}_{y,\gamma}^n + \mathrm{Q}_{y,\xi}^n + \mathrm{Q}_{y,\varphi}^n + \mathrm{Q}_{y,\mathcal{FB}}^n \tag{4.60a}$$

$$\mathrm{Q}_{y,\varphi}^n \triangleq \left(\mathbf{h}\odot\mathbf{v}_{\mathrm{rel}}^n\right)^{\mathsf{T}}\mathbf{f}_{(y)}^n \tag{4.60b}$$

$$\mathrm{Q}_{y,\mathcal{FB}}^n \triangleq \left(\lambda_{\mathcal{FB}}\delta_{t\cdot}\mathbf{y}_{\mathcal{FB}}^n\right)^{\mathsf{T}}\delta_{t\cdot}\mathbf{y}_{\mathcal{FB}}^n \tag{4.60c}$$

The power quantities $\mathrm{Q}_{y,\gamma}^n$, $\mathrm{Q}_{y,\xi}^n$ take the same form as (3.63c) and (3.63d), once again with the appropriate substitutions.

The power P_y^n supplied from external excitation is given by:

$$\mathrm{P}_y^n \triangleq \left(\delta_{t\cdot}\mathbf{y}_{\mathcal{FB}}^n\right)^{\mathsf{T}}\mathbf{f}_{\mathrm{ext}\mathcal{FB},(y)}^n + h\left(\left(\mu_{t\cdot}\mathbf{y}^n\right)^{\mathsf{T}}\left(\delta_{t\cdot}\mathbf{J}_{(y)}^n\right)\right)\mathbf{f}_{(y)}^n \tag{4.61}$$

4.3.4.iii Global power balance and invariant quantity

The total numerical energy H^n of the system is balanced by:

$$\delta_{t-}\mathrm{H}^n = \mathrm{P}^n - \mathrm{Q}^n \tag{4.62a}$$

$$\mathrm{H}^n \triangleq \mathrm{H}_y^n + \mathrm{H}_w^n \quad (4.62\mathrm{b}) \qquad \mathrm{P}^n \triangleq \mathrm{P}_y^n + \mathrm{P}_w^n \quad (4.62\mathrm{c}) \qquad \mathrm{Q}^n \triangleq \mathrm{Q}_y^n + \mathrm{Q}_w^n \quad (4.62\mathrm{d})$$

An invariant quantity E^n may be defined for the full system, as was done in Section 3.7.2 (see Equation (3.68)), this time also including the cumulated supplied power:

$$\mathrm{E}^n \triangleq \mathrm{H}^n + k\sum_{p=1}^{n}\left(\mathrm{Q}^p - \mathrm{P}^p\right) \tag{4.63}$$

As will be seen in Section 4.4, examining the temporal evolution of the separate contributions of each component of (4.63) provides a practical visualisation of the power exchanges between the various parts of the system.

4.3.4.iv Stability condition

The stability of the proposed FD scheme now reduces to the condition of non-negativity of H^n. For the vertical polarisation, as $\boldsymbol{\Phi}^n \geqslant 0$ by construction, it is straightforward to see from Equation (4.55b) that $\mathrm{H}_{w,\Phi}^n \geqslant 0$. The quantity $\mathrm{H}_{w,\mathcal{FB}}^n$, corresponding to the combined kinetic energies of the finger and bow in the vertical polarisation, is also unconditionally positive;

the introduction of collision forces hence does not have an effect on numerical stability. In the horizontal polarisation, the kinetic and potential energies of the finger and bow, given by $\mathrm{H}^n_{y,\mathcal{FB}}$, are also positive.

This implies that the total discrete energy H^n for the scheme given by (4.38) and (4.48) is positive under the same stability condition as that derived for the isolated string, and given by (2.91).

4.3.5 Scheme update: vertical polarisation

As the horizontal friction forces depend on the normal contact forces, the vertical polarisation is updated first. The resulting normal forces are then supplied to the horizontal polarisation system, which is subsequently updated.

The scheme update for the vertical polarisation takes the form of a nonlinear system. Firstly, the update for the string state is obtained from (4.38), considering (3.66):

$$\begin{aligned}\mathbf{A}\mathbf{w}^{n+1} = {} & \overbrace{\left[\begin{array}{c|ccc|ccc} \mathbf{B} & \cdots & \left(1-\frac{2-a_q}{2+a_q}\right)\frac{b_q}{k}\mathbf{I} & \cdots & \cdots & -\left(1-\frac{2-a'_{q'}}{2+a'_{q'}}\right)\frac{b'_q}{k}\mathbf{D}_{xx} & \cdots \end{array}\right]}^{\triangleq \mathbf{B_u}}\mathbf{u}^n_{(w)} \\ & + \mathbf{C}\mathbf{w}^{n-1} + \mu_{t\cdot}\mathbf{J}^n_{(w)}\mathbf{f}^n_{(w)} \end{aligned} \tag{4.64}$$

where $\mathbf{A}$, $\mathbf{B}$, and $\mathbf{C}$ are defined in (3.67). The update for $\boldsymbol{\gamma}^{n+1/2}_{q,(w)}$ and $\boldsymbol{\xi}^{n+1/2}_{q',(w)}$ is then computed from (3.64), as for the unforced case.

The update equation for the bow and finger displacements are obtained after expanding the FD operators in Equation (4.45):

$$\mathbf{w}^{n+1}_{\mathcal{FB}} = 2\mathbf{w}^n_{\mathcal{FB}} - \mathbf{w}^{n-1}_{\mathcal{FB}} + k^2\mathbf{M}^{-1}_{\mathcal{FB}}\left(\mathbf{f}^n_{\mathcal{FB},(w)} + \mathbf{f}^n_{\mathrm{ext}\mathcal{FB},(w)}\right) \tag{4.65}$$

The nonlinearity of the contact forces $\mathbf{f}^n_{(w)}$ does not allow for a direct resolution of the system given by Equations (4.64) and (4.65). It is useful to rewrite such system in terms of an unknown vector $\mathbf{r}^n \triangleq \boldsymbol{\Delta}^{n+1} - \boldsymbol{\Delta}^{n-1}$. To do so requires left-multiplying (4.64) by $-\left(h\mathbf{J}^{n+1}_{(w)}\right)^{\mathsf{T}}\mathbf{A}^{-1}$, and using (4.65) to rearrange the result, yielding the following nonlinear system:

$$\boldsymbol{\Lambda}^n_{1,(w)}\mathbf{r}^n + \boldsymbol{\Lambda}^n_{2,(w)}\mathbf{f}^n_{\Phi}\left(\mathbf{r}^n\right) + \boldsymbol{\zeta}^n_{(w)} = \mathbf{0} \tag{4.66}$$

where the matrices $\boldsymbol{\Lambda}^n_{1,(w)}$, $\boldsymbol{\Lambda}^n_{2,(w)}$ and the vectors $\mathbf{f}^n_{\Phi}$, $\boldsymbol{\zeta}^n_{(w)}$ are given by:

$$\boldsymbol{\Lambda}^n_{2,(w)} \triangleq \left(h\mathbf{J}^{n+1}_{(w)}\right)^{\mathsf{T}}\mathbf{A}^{-1}\mu_{t\cdot}\mathbf{J}^n_{(w)} + k^2\mathbf{M}_{\mathrm{inv}} \tag{4.67a}$$

$$\boldsymbol{\Lambda}^n_{1,(w)} \triangleq \mathbf{I}_{N+2} + \frac{1}{2k}\boldsymbol{\Lambda}^n_{2,(w)}\,\mathrm{diag}\left(\boldsymbol{\Psi}^n\right) \tag{4.67b}$$

$$\mathbf{f}^n_{\Phi} \triangleq \frac{\delta_{t\cdot}\boldsymbol{\Phi}^n}{\delta_{t\cdot}\boldsymbol{\Delta}^n} = \frac{\boldsymbol{\Phi}\left(\mathbf{r}^n + \boldsymbol{\Delta}^{n-1}\right) - \boldsymbol{\Phi}\left(\boldsymbol{\Delta}^{n-1}\right)}{\mathbf{r}^n} \tag{4.67c}$$

$$\boldsymbol{\zeta}^n_{(w)} \triangleq \left[\begin{array}{c|c} \mathbf{0}_{1\times N} & 2\left(\mathbf{w}^n_{\mathcal{FB}} - \mathbf{w}^{n-1}_{\mathcal{FB}}\right)^{\mathsf{T}} + k^2\left(\mathbf{M}^{-1}_{\mathcal{FB}}\mathbf{f}^n_{\mathrm{ext}\mathcal{FB},(w)}\right)^{\mathsf{T}} \end{array}\right]^{\mathsf{T}}$$

$$+ h\left(\left(\mathbf{J}_{(w)}^{n+1}\right)^{\mathsf{T}}\mathbf{A}^{-1}\left(\mathbf{B}_{\mathbf{u}}\mathbf{u}_{(w)}^{n}+\mathbf{C}\mathbf{w}^{n-1}\right)-\left(\mathbf{J}_{(w)}^{n-1}\right)^{\mathsf{T}}\mathbf{w}^{n-1}\right) \tag{4.67d}$$

where $\mathbf{M}_{\text{inv}}$ is a $(N+2)\times(N+2)$ matrix with $\mathbf{M}_{\mathcal{FB}}^{-1}$ at its bottom right corner, and all zeros elsewhere.

System (4.66) is solved for $\mathbf{r}^n$ with an iterative nonlinear system solver. Care must be taken with computing $\mathbf{f}_{\Phi}^{n}$ when values of the elements of $\mathbf{r}^n$ tend towards zero. In this case, $\mathbf{f}_{\Phi}^{n}$ reduces to the derivative of $\boldsymbol{\Phi}$ with respect to $\boldsymbol{\Delta}$, evaluated at $\boldsymbol{\Delta}^{n-1}$; the analytical expression for this derivative can be used instead. Once the contact forces are found, the system state is updated with (4.64) and (4.65).

4.3.6 Scheme update: horizontal polarisation

4.3.6.i Nonlinear system

The update equation for the string, bow, and finger states in the horizontal polarisation is derived in the same manner as in the vertical direction. For the string state, (3.66) is used (with the appropriate variable name substitutions) in conjunction with (4.48), yielding a similar update to (4.64):

$$\mathbf{A}\mathbf{y}^{n+1} = \mathbf{B}_{\mathbf{u}}\mathbf{u}_{(y)}^{n} + \mathbf{C}\mathbf{y}^{n-1} - \mu_{t\cdot}\mathbf{J}_{(y)}^{n}\mathbf{f}_{(y)}^{n} \tag{4.68}$$

Recall the definition of $\mathbf{f}_{(y)}^{n}$ given in (4.50a); the normal contact forces $\mathbf{f}_{(w)}^{n}$, computed in the vertical polarisation update, are now inserted into (4.68) as known parameters, modulating the amplitude of the tangential friction forces. The update for $\gamma_{q,(y)}^{n+1/2}$ and $\boldsymbol{\xi}_{q',(y)}^{n+1/2}$ is computed from (3.64).

The bow and finger updates are directly obtained from Equation (4.52):

$$\mathbf{A}_{\mathcal{FB}}\mathbf{y}_{\mathcal{FB}}^{n+1} = \mathbf{B}_{\mathcal{FB}}\mathbf{y}_{\mathcal{FB}}^{n} + \mathbf{C}_{\mathcal{FB}}^{n-1}\mathbf{y}_{\mathcal{FB}}^{n-1} + k^2\left(\mathbf{f}_{\mathcal{FB},(y)}^{n} + \mathbf{f}_{\text{ext}\mathcal{FB},(y)}^{n}\right) \tag{4.69}$$

where the matrices $\mathbf{A}_{\mathcal{FB}}$, $\mathbf{B}_{\mathcal{FB}}$, and $\mathbf{C}_{\mathcal{FB}}$ are 2×2 diagonal matrices, defined as:

$$\mathbf{A}_{\mathcal{FB}} \triangleq \mathbf{M}_{\mathcal{FB}} + \frac{k^2}{2}\mathbf{K}_{\mathcal{FB}} + \frac{k}{2}\boldsymbol{\lambda}_{\mathcal{FB}} \tag{4.70a}$$

$$\mathbf{B}_{\mathcal{FB}} \triangleq 2\mathbf{M}_{\mathcal{FB}} \tag{4.70b}$$

$$\mathbf{C}_{\mathcal{FB}} \triangleq -\mathbf{M}_{\mathcal{FB}} - \frac{k^2}{2}\mathbf{K}_{\mathcal{FB}} + \frac{k}{2}\boldsymbol{\lambda}_{\mathcal{FB}} \tag{4.70c}$$

The horizontal polarisation update is nonlinear and implicit. As was done for the vertical direction, Equations (4.68) and (4.69) can be rewritten as a nonlinear system in terms of the vector $\mathbf{v}_{\text{rel}}^{n}$. Pre-multiplying (4.68) by $\left(h\mathbf{J}_{(y)}^{n+1}\right)^{\mathsf{T}}\mathbf{A}^{-1}$, and rearranging with (4.69), leads to the following system:

$$\mathbf{v}_{\text{rel}}^{n} + \boldsymbol{\Lambda}_{(y)}^{n}\mathbf{f}_{(y)}^{n} + \boldsymbol{\zeta}_{(y)}^{n} = \mathbf{0} \tag{4.71}$$

where the matrix $\boldsymbol{\Lambda}^n_{(y)}$ and the vector $\boldsymbol{\zeta}^n_{(y)}$ are defined as:

$$\boldsymbol{\Lambda}^n_{(y)} \triangleq \frac{1}{2k}\left(\left(h\mathbf{J}^{n+1}_{(y)}\right)^{\mathsf{T}}\mathbf{A}^{-1}\mu_t.\mathbf{J}^n_{(y)} + k^2\mathbf{A}_{\text{inv}}\right) \tag{4.72a}$$

$$\boldsymbol{\zeta}^n_{(y)} \triangleq \frac{h}{2k}\left(\left(\mathbf{J}^{n-1}_{(y)}\right)^{\mathsf{T}}\mathbf{y}^{n-1} - \left(\mathbf{J}^{n+1}_{(y)}\right)^{\mathsf{T}}\mathbf{A}^{-1}\left(\mathbf{B}_{\mathbf{u}}\mathbf{u}^n_{(y)} + \mathbf{C}\mathbf{y}^{n-1}\right)\right) + \left[\begin{array}{c|c}\mathbf{0}_{1\times N} & \left(\boldsymbol{\zeta}^n_{\mathcal{F}\mathcal{B},(y)}\right)^{\mathsf{T}}\end{array}\right]^{\mathsf{T}} \tag{4.72b}$$

$$\boldsymbol{\zeta}^n_{\mathcal{F}\mathcal{B},(y)} \triangleq \frac{1}{2k}\left(\mathbf{A}^{-1}_{\mathcal{F}\mathcal{B}}\left(\mathbf{B}_{\mathcal{F}\mathcal{B}}\mathbf{y}^n_{\mathcal{F}\mathcal{B}} + \mathbf{C}_{\mathcal{F}\mathcal{B}}\mathbf{y}^{n-1}_{\mathcal{F}\mathcal{B}} + k^2\mathbf{f}^n_{\text{ext}\mathcal{F}\mathcal{B},(y)}\right) - \mathbf{y}^{n-1}_{\mathcal{F}\mathcal{B}}\right) \tag{4.72c}$$

where $\mathbf{A}_{\text{inv}}$ is a $(N+2)\times(N+2)$ matrix with $\mathbf{A}^{-1}_{\mathcal{F}\mathcal{B}}$ in the bottom right corner and zeros elsewhere.

Conversely to the vertical contact forces, the nonlinear friction characteristics are not smooth (see Figures 4.5 and 4.6). Incidentally, a direct attempt to solve System (4.71) with an iterative method will rarely be successful. The next Section 4.3.6.ii will describe the method employed to compute the friction forces and update the state variables in the horizontal polarisation, drawing in particular from known aspects of the friction curve model for the bow-string interaction.

4.3.6.ii Resolution: Friedlander's construction

Consider the last equation of System (4.71), in terms of the relative velocity $v^n_{\text{rel},\mathcal{B}}$ between the bow and the string:

$$v^n_{\text{rel},\mathcal{B}} + \boldsymbol{\sigma}^n_{\mathcal{N}}\left[\mathbf{f}^n_{\mathcal{N}}\right]_+\varphi_{\mathcal{N}} + \sigma^n_{\mathcal{F}}\left[f^n_{\mathcal{F}}\right]_+\varphi_{\mathcal{F}} + \sigma^n_{\mathcal{B}}\left[f^n_{\mathcal{B}}\right]_+\varphi_{\mathcal{B}} + \zeta^n_{\mathcal{B}} = 0 \tag{4.73}$$

where $\zeta^n_{\mathcal{B}}$ is the last element of $\boldsymbol{\zeta}^n_{(y)}$, and the vector $\boldsymbol{\sigma}^n_{\mathcal{N}}$ and scalars $\sigma^n_{\mathcal{F}}$ and $\sigma^n_{\mathcal{B}}$ are defined as:

$$\boldsymbol{\sigma}^n_{\mathcal{N}} \triangleq \frac{1}{2k}\left(h\mathbf{j}^{n+1}_{\mathcal{B}}\right)^{\mathsf{T}}\mathbf{A}^{-1} \tag{4.74a}$$

$$\sigma^n_{\mathcal{F}} \triangleq \frac{1}{2k}\left(h\mathbf{j}^{n+1}_{\mathcal{B}}\right)^{\mathsf{T}}\mathbf{A}^{-1}\mu_t.\mathbf{j}^n_{\mathcal{F}} \tag{4.74b}$$

$$\sigma^n_{\mathcal{B}} \triangleq \frac{1}{2k}\left(h\mathbf{j}^{n+1}_{\mathcal{B}}\right)^{\mathsf{T}}\mathbf{A}^{-1}\mu_t.\mathbf{j}^n_{\mathcal{B}} \tag{4.74c}$$

In any standard bowed string playing situation, it is safe to assume that the bowing point is located some distance away from the stopping fingers. In this case, the locations of the non-zero values in the vectors $\mathbf{j}^n_{\mathcal{F}}$ and $\mathbf{j}^n_{\mathcal{B}}$ likely do not overlap[7]; in other words, $\mathbf{j}^n_{\mathcal{F}}$ and $\mathbf{j}^n_{\mathcal{B}}$ are orthogonal.

Recall the form of the matrix $\mathbf{A}$, defined in Section 3.6.4:

$$\mathbf{A} \triangleq \underbrace{\left(\frac{\rho S}{k^2} + \sum_{q=1}^{M}\frac{b_q}{k(2+a_q k)}\right)}_{\triangleq A_{(\mathbf{I})}}\mathbf{I} - \underbrace{\sum_{q'=1}^{M'}\frac{b'_{q'}}{k(2+a'_{q'}k)}}_{\triangleq A_{(xx)}}\mathbf{D}_{xx} \tag{4.75}$$

---

[7] Recall, from Section 4.3.1, that the discrete distributions $\mathbf{j}^n_{\mathcal{F}}$ and $\mathbf{j}^n_{\mathcal{B}}$ approximate a continuous Dirac delta function. If m^{th} order interpolation is employed, they contain only m contiguous non-zero values, located around the contact point.

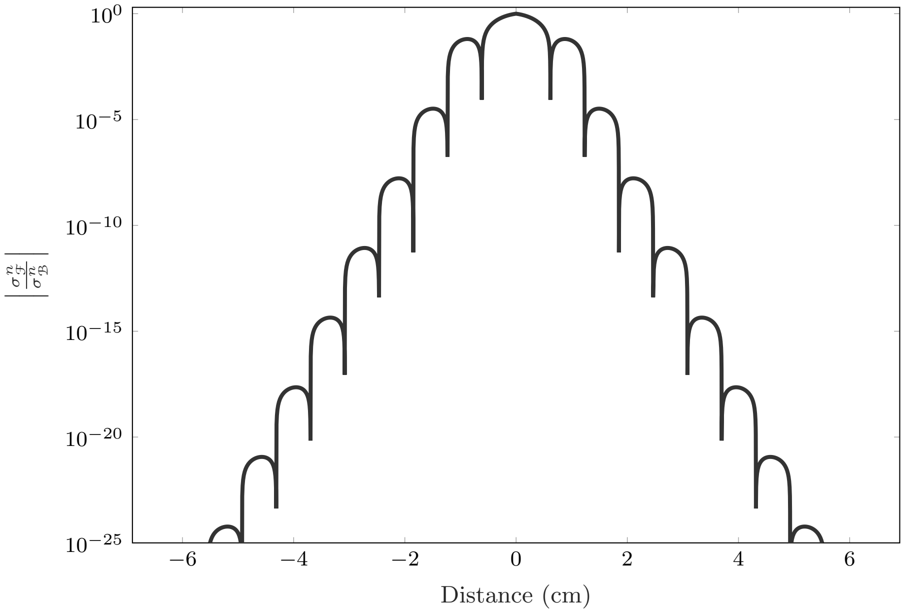

Figure 4.8: Magnitude of $\sigma_{\mathcal{F}}^{n}$ relative to that of $\sigma_{\mathcal{B}}^{n}$, as a function of distance between the bow and finger contact points, for a simulated cello D string. The magnitude of $\sigma_{\mathcal{F}}^{n}$ decays exponentially with increasing distance. The friction force exerted by a finger a few centimetres away from the bowing point is negligible in the calculation of the bow friction force. — Parameters: see Cello D string on page xxix; $F_s = 44.1$ kHz.

$\mathbf{A}$ is a symmetric Toeplitz tridiagonal matrix, due to the presence of the discrete Laplacian matrix $\mathbf{D}_{xx}$ (defined in (2.71b)). For a typical string, the coefficient $A_{(xx)}$ is small relative to $A_{(\mathbf{I})}$; $\mathbf{A}$ is therefore diagonally dominant, and indeed the off-diagonal entries of $\mathbf{A}$, all negative, are typically several orders of magnitude smaller (in absolute value) than its diagonal entries.

This means that, while $\mathbf{A}^{-1}$ will be a full matrix, the magnitude of its entries will decay along a column away from the diagonal, at an exponential rate [77]. It is therefore fair to assume that $\sigma_{\mathcal{F}}^{n}$, defined by (4.74b), will be very small in practice. To illustrate this, Figure 4.8 shows the relative magnitude $\left|\sigma_{\mathcal{F}}^{n}/\sigma_{\mathcal{B}}^{n}\right|$ of the finger force weighting with respect to that of the bow force, as a function of distance between bowing point and finger location. The parameters are those of a cello D string, where the grid spacing h was chosen as close as possible to the stability limit, with sample rate $F_s = 44.1$ kHz. This graph demonstrates that, for most realistic playing situations, where the stopping fingers are more than a few centimetres away from the bowing point, the finger friction force term in (4.73) is completely negligible in the computation of the bow friction force at a given time step.

The same can be said about the friction force exerted by the fingerboard onto the string. One can safely assume that the non-zero values of $[\mathbf{f}_{\mathcal{N}}^{n}]_+$ will not coincide with the non-zero values of $\mathbf{j}_{\mathcal{B}}^{n}$; in other words, the string is not bowed at a point where it is touching the fingerboard. In this case, the same argument can be made on the relative magnitude of $\boldsymbol{\sigma}_{\mathcal{N}}^{n}\,[\mathbf{f}_{\mathcal{N}}^{n}]_+$ compared to that of $\sigma_{\mathcal{B}}^{n}\,[f_{\mathcal{B}}^{n}]_+$.

Under these assumptions, the update equation (4.73) for the bow friction force and relative

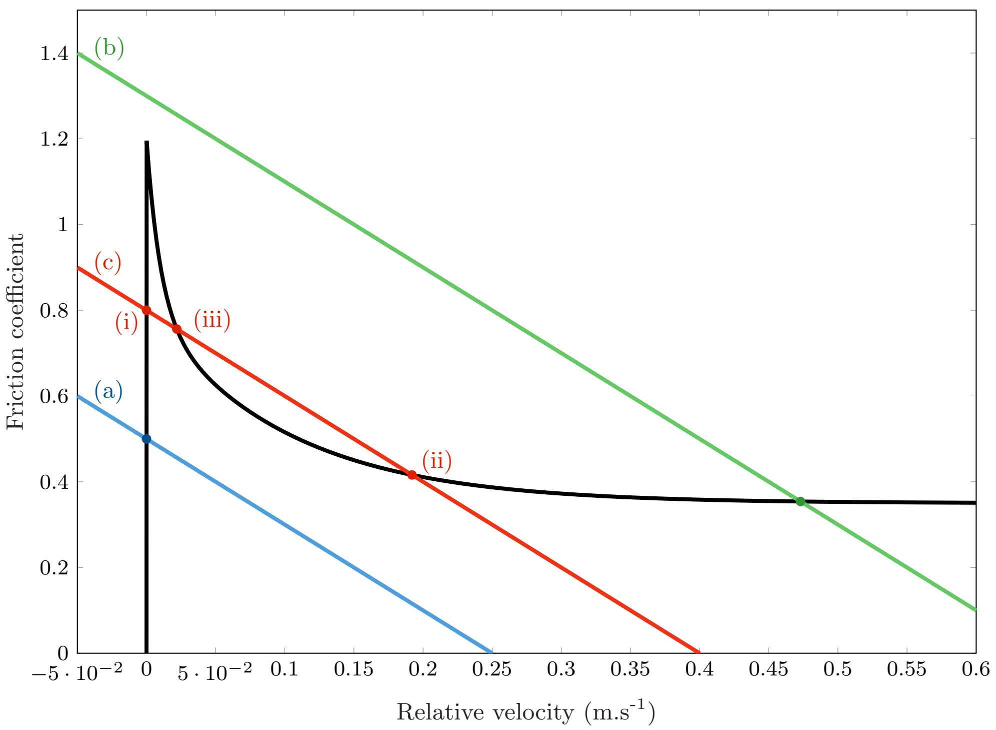

Figure 4.9: Friedlander's graphical construction to solve for the bow relative velocity. The solutions for $v^n_{\mathrm{rel},\mathcal{B}}$ lie at the intersections of the friction curve $\varphi_{\mathcal{B}}$ (in black) and the straight line $\eta_{\mathcal{B}}$; three cases are illustrated, with a different intercept value. In case (a), in blue, the solution is given by $v^n_{\mathrm{rel},\mathcal{B}} = 0$; the bow is sticking to the string. In case (b), in green, the solution for $v^n_{\mathrm{rel},\mathcal{B}}$ is strictly positive; the string is slipping against the bow. Under certain conditions (case (c), in red), there are multiple solutions to Equation (4.76); this ambiguity is resolved by choosing the solution on the same branch of φ_B as the previous time step. (i) corresponds to the sticking phase; (ii) corresponds to the slipping phase; (iii) is physically unstable, and not seen in bowed string motion [75].

velocity reduces to a scalar, nonlinear ODE:

$$v^n_{\mathrm{rel},\mathcal{B}} + \sigma^n_{\mathcal{B}} \left[f^n_{\mathcal{B}}\right]_+ \varphi_{\mathcal{B}} + \zeta^n_{\mathcal{B}} = 0 \tag{4.76}$$

The solutions of Equation (4.76) can be represented graphically, as the intersections of the friction curve $\varphi_{\mathcal{B}}\left(v^n_{\mathrm{rel},\mathcal{B}}\right)$ with a straight line with negative slope, defined by:

$$\eta_{\mathcal{B}}\left(v^n_{\mathrm{rel},\mathcal{B}}\right) \triangleq -\frac{1}{\sigma^n_{\mathcal{B}}\left[f^n_{\mathcal{B}}\right]_+}\left(v^n_{\mathrm{rel},\mathcal{B}} + \zeta^n_{\mathcal{B}}\right) \tag{4.77}$$

This graphical representation is referred to as Friedlander's construction [39], and illustrated in Figure 4.9 for positive values of $v^n_{\mathrm{rel},\mathcal{B}}$[8]. A solution on the vertical part of the curve corresponds to the sticking state ($v^n_{\mathrm{rel},\mathcal{B}} = 0$); otherwise, the string is slipping against the bow ($\left|v^n_{\mathrm{rel},\mathcal{B}}\right| > 0$). As Figure 4.9 shows (case (c)), one must beware of the possibility of multiple solutions. With this force-velocity curve model, this possibility is seemingly brought about by the particular FD discretisation chosen for the bowed string equations. However, it does resemble Friedlander's so-called ambiguity, which he derived in [39] from travelling-wave solutions of the continuous 1D wave equation.

---

[8] The problem is origin-symmetric; the same analysis can be performed for negative relative velocities.

It is straightforward to see that if the slope of $\eta_{\mathcal{B}}$ is negative enough, then (4.76) has a unique solution. This condition is formulated as:

$$-\frac{1}{\sigma_{\mathcal{B}}^{n}\left[f_{\mathcal{B}}^{n}\right]_{+}} \leqslant \min\left(\varphi_{\mathcal{B}}'\right) \tag{4.78}$$

where $\min\left(\varphi_{\mathcal{B}}'\right)$ is the minimum (i.e. largest negative) value of the gradient of the friction curve. For this particular model, as per (4.18), it is equal to the slope of $\varphi_{\mathcal{B}}$ at $v_{\mathrm{rel},\mathcal{B}}^{n} = 0$[9], and its value is -44.5. Given the definition of $\sigma_{\mathcal{B}}^{n}$, given by (4.74c), the condition under which the solution is unique depends on the string physical parameters (through $\mathbf{A}^{-1}$), the time step k, the grid spacing h, and most importantly on the normal force $\left[f_{\mathcal{B}}^{n}\right]_{+}$ exerted by the bow.

When this condition is not met, and $\eta_{\mathcal{B}}$ intersects $\varphi_{\mathcal{B}}$ in three places, the method to resolve Equation (4.76) was discussed by McIntyre *et al.* [75]. They showed that the "correct" solution is the one that preserves the current regime, sticking (Figure 4.9, (i)) or slipping (Figure 4.9, (ii)), for the longest time, and that the "middle" solution (Figure 4.9, (iii)) was always physically unstable, and never seen in practice. This gives rise to hysteretic behaviour: the relative velocity jumps back and forth between the two branches of $\varphi_{\mathcal{B}}$ at different points depending on whether the transition is from stick to slip, or the other way around. This manifests as a lengthening of the stick/slip cycles, and therefore a flattening of the pitch. This effect has later been found to be due to the naturally hysteretic viscothermal behaviour of the melting rosin, which is somewhat approximated by this hysteresis rule on the simpler friction curve model [100].

The slope of $\eta_{\mathcal{B}}$ depends directly on the normal bow force; a larger value of $\left[f_{\mathcal{B}}^{n}\right]_{+}$ means less steep a slope, and in turn a more pronounced hysteresis loop. For the proposed system, the pitch flattening effect therefore results from excessive downwards bow force; this indeed corresponds to musicians' experience in real bowed string playing. For a given string, an expression for the maximal bow force beyond which pitch flattening can occur may be derived. As will be demonstrated in Appendix A, for an *ideal* bowed string (i.e. without bending stiffness or damping), the analytical expression derived by Friedlander for this maximal bow force is found to be the same as that obtained with a FD scheme analogous to that presented here, at the stability limit. This is an encouraging indicator of the validity of using a physical hysteresis rule such as that used by McIntyre *et al.* to resolve this seemingly numerical ambiguity, albeit not a definitive proof that the expression for the maximal bow force will be the same, in practice, for different choices of discretisation.

Once Equation (4.76) has been solved for $v_{\mathrm{rel},\mathcal{B}}^{n}$, and the friction coefficient $\varphi_{\mathcal{B}}$ has been computed, they can be substituted into System (4.71). The system is finally solved for the bow and finger relative velocities, allowing the discrete state to be updated, with (4.68) and (4.69).

---

[9] Approaching the discontinuity from the positive or negative $v_{\mathrm{rel},\mathcal{B}}^{n}$ axis; otherwise, the slope is infinite.

4.4 Simulation results

Through the proposed control parameter space, the bowed string model presented here allows the reproduction of a wide range of bowed string gestures. A more complete review of the musical sound synthesis capabilities of the algorithm described in this Chapter will be presented in Chapter 5.

Before moving on to "playing" the virtual string, however, it is useful to ensure that the algorithm derived from the FD scheme proposed in Section 4.3 functions as expected. As was discussed in Chapters 2 and 3, the numerical power balance provides insight on the energetic contributions of each subsystem (string, bow, finger, fingerboard, in each polarisation), as well as the power exchanges between them. A global energy variable E^n was defined by (4.63) for the bowed string system, which should remain conserved throughout a simulation.

Figure 4.10 presents the evolution of the energy and cumulated power for each subsystem, in both polarisations, during a 2-second simulation of a cello D string, initially at rest. One finger then pushes the string down onto the fingerboard, in order to stop it. The bow is then lowered onto the string. After a short time, the bow is pushed across the string, in the horizontal direction, exciting periodic motion.

While the string is bowed, all control parameters are made to continuously vary over time, in order to demonstrate global energy conservation in the most general case. The finger slides down the string towards a higher position and downwards force, simulating a glissando; the bow downwards and transverse force are continuously increased, while the bowing point is brought closer to the bridge. The bow is finally lifted away from the string, and the string oscillations between the stopping finger and the bridge boundary are left to decay. The middle row of plots in Figure 4.10 displays the external forces applied onto the bow and finger, in the vertical polarisation ($f^n_{\mathrm{ext},\mathcal{F},(w)}$ in blue, $f^n_{\mathrm{ext},\mathcal{B},(w)}$ in red, LHS) and in the horizontal direction ($f^n_{\mathrm{ext},\mathcal{B},(y)}$ in red, RHS). The bottom plots are the same for both polarisations; they display the respective positions $x^n_{\mathcal{F}}$ and $x^n_{\mathcal{B}}$ of the finger and bow with respect to the nut boundary of the string, in cm.

As a visualisation aid, the energy balance plots of Figure 4.10 (top row) are reproduced, for each polarisation, in Figures 4.11 and 4.12, and are each accompanied by simulation snapshots at relevant timestamps (indicated with the numbered grey markers on each plot).

Since the system starts at rest, the total initial energy H^0 is zero, and computing the relative variations of E^n as done in (3.69) becomes an issue. Instead, in this case, recall the definition of E^n given by (4.63):

$$\mathrm{E}^n \triangleq \mathrm{H}^n + k \sum_{p=1}^{n} \left(\mathrm{Q}^p - \mathrm{P}^p\right) = 0 \tag{4.63}$$

As the power is balanced separately for each polarisation (see Section 4.3.4), the equation may be split as follows:

$$\mathrm{H}^n_w = -k \sum_{p=1}^{n} \left(\mathrm{Q}^p_w - \mathrm{P}^p_w\right) \tag{4.79a}$$

$$\mathrm{H}_u^n = -k \sum_{p=1}^{n} (\mathrm{Q}_u^p - \mathrm{P}_u^p) \tag{4.79b}$$

$$\tag{4.79c}$$

One can define a dimensionless invariant for each polarisation, given as the ratio of energy to cumulated power:

$$\mathrm{R}_w^n \triangleq \begin{cases} 1 & \text{if } \mathrm{H}_w^n = 0 \\ -\dfrac{\mathrm{H}_w^n}{k \sum_{p=1}^{n} (\mathrm{Q}_w^p - \mathrm{P}_w^p)} & \text{otherwise} \end{cases} \tag{4.80a}$$

$$\mathrm{R}_u^n \triangleq \begin{cases} 1 & \text{if } \mathrm{H}_u^n = 0 \\ -\dfrac{\mathrm{H}_u^n}{k \sum_{p=1}^{n} (\mathrm{Q}_u^p - \mathrm{P}_u^p)} & \text{otherwise} \end{cases} \tag{4.80b}$$

The variations of R_w^n and R_u^n away from 1 should then be independent from the absolute magnitudes of the energy and cumulated power. In practice, to avoid dividing by very small numbers, the condition under which R_w^n and R_u^n are set to 1 may depend on a threshold value. Figure 4.13 displays the values of $\mathrm{R}_w^n - 1$ and $\mathrm{R}_u^n - 1$ over time; the total numerical energy (including cumulated power) is indeed conserved, to the 9th significant digit.

Concluding remarks

The isolated string model presented in Chapter 3 has now been completed with the addition of nonlinear excitation mechanisms, through coupling with a bow, a stopping finger, and a distributed fingerboard. A nonlinear power-balanced FD scheme was proposed for the full system, used to numerically solve the equations of motion in both polarisations; the scheme was shown to be stable under the same condition as the scheme used for the isolated string.

At each time step, the order of the full scheme update is as follows:

1. The linear update is computed for the string state grid functions $\mathbf{w}^{n+1}$ and $\mathbf{y}^{n+1}$ in each polarisation, using Equation (3.66).
2. The nonlinear system (4.66) is solved in the vertical polarisation with an iterative method, in order to obtain the values of the normal contact forces between the string and the fingerboard, finger, and bow.
3. The normal forces are substituted into the nonlinear system (4.71) for the horizontal polarisation.
4. Equation (4.76) is solved first for the bow friction force, using Friedlander's construction, and a nonlinear iterative method if the bow-string system is in the slipping phase. The result is substituted into the rest of System (4.71).
5. System (4.71) is solved for the fingerboard and finger friction forces.

6. The full nonlinear update is computed for $\mathbf{w}^{n+1}$ with Equation (4.64), and for $\mathbf{y}^{n+1}$ with Equation (4.68).
7. The states $\boldsymbol{\gamma}_{q,(w)}^{n+1/2}$, $\boldsymbol{\xi}_{q',(w)}^{n+1/2}$, $\boldsymbol{\gamma}_{q,(y)}^{n+1/2}$, and $\boldsymbol{\xi}_{q',(y)}^{n+1/2}$ are updated with (3.64), in each polarisation.
8. The displacements $\mathbf{w}_{\mathcal{FB}}^{n+1}$, $\mathbf{y}_{\mathcal{FB}}^{n+1}$ of the finger and bow are updated in both polarisations, with (4.65) and (4.69).

The output of the algorithm depends on the external force and position control signals for the bow and finger. The focus of the next Chapter 5 will centre on these control signals. It will be shown that all bowed string vibration regimes and many bowed string gestures can be reproduced with the proposed model, by simply using different combinations of time profiles and patterns for the control signals.

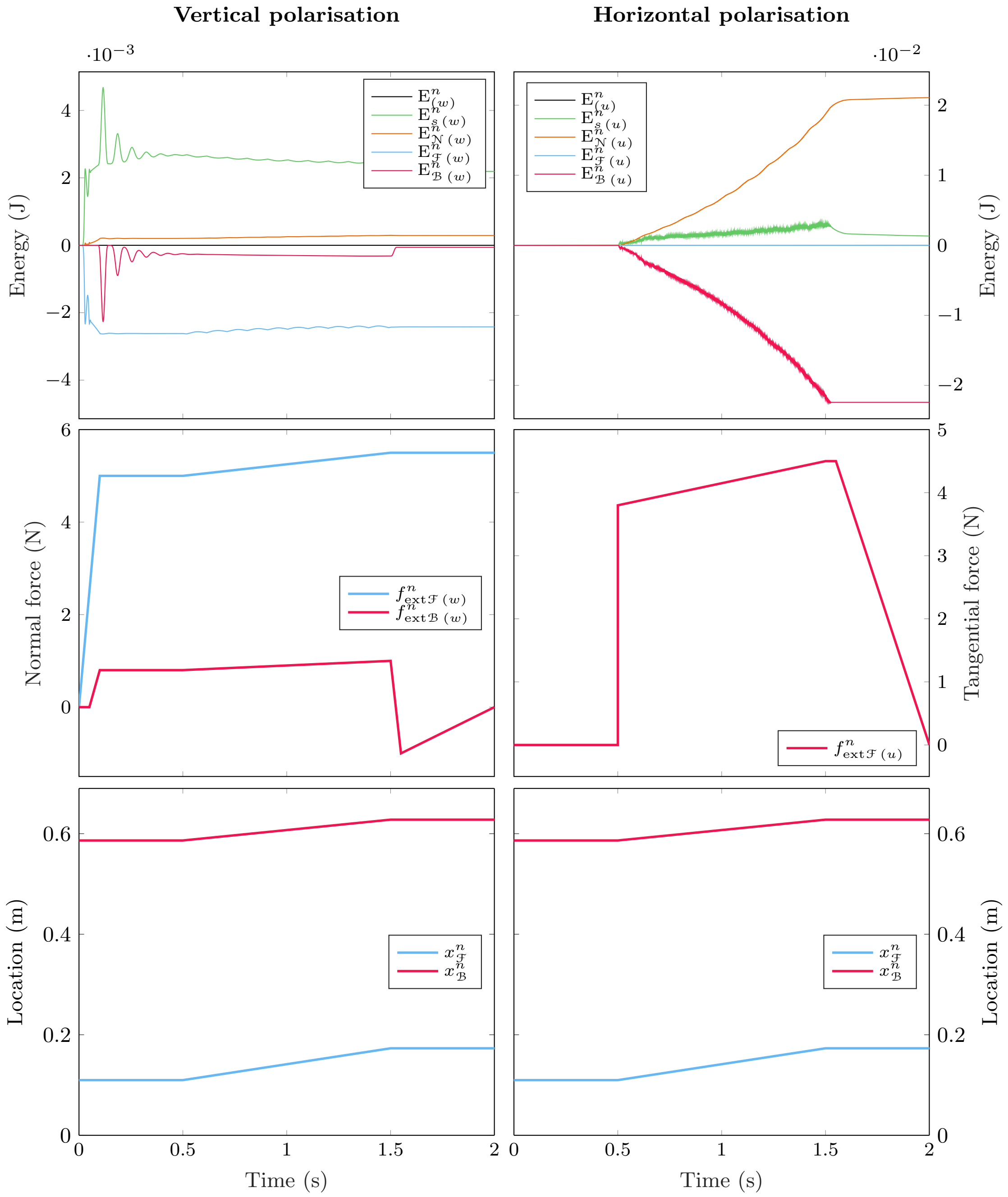

Figure 4.10: Top row: energy balance plots for a 2-second simulation of a bowed cello D string, with a stopping finger pressing the string against the fingerboard. The vertical polarisation is shown on the left, the horizontal polarisation on the right. For each polarisation, the energy and cumulated power is shown for the string (in green), the bow (in red), the finger (in blue), and the fingerboard (in orange); the total energy and cumulated power is drawn in black (note that, for the horizontal polarisation, the black curve is masked by the blue curve). Middle row: on the same time scale, force control signals for the bow (in red) and the finger (in blue), in each polarisation. Bottom row: locations $x_{\mathcal{B}}$, $x_{\mathcal{F}}$ of the bow and finger (same for both polarisations). — Sample rate: $F_s = 44.1$ kHz.

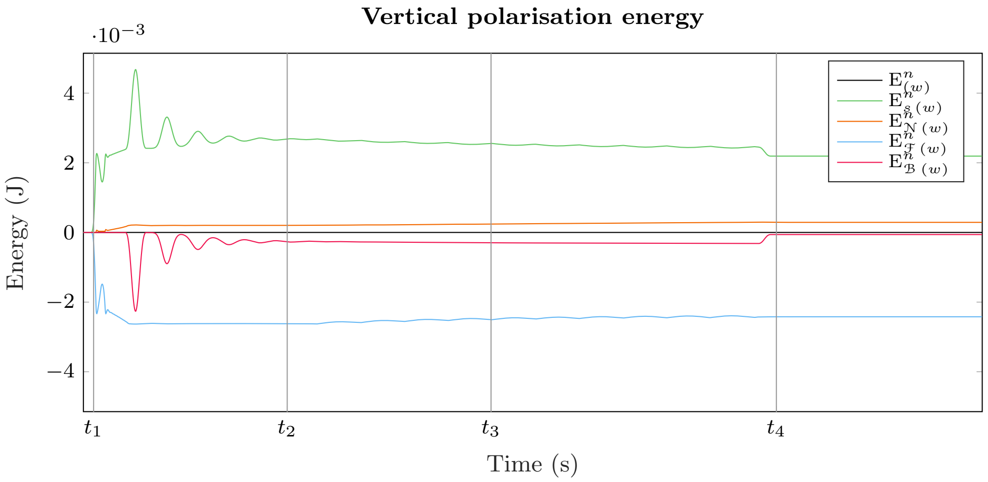

(a) Total energy and cumulated power for each subsystem: string (in green), fingerboard (in orange), finger (in blue), and bow (in red), in the vertical polarisation. The total energy and cumulated power (in black) remains constant.

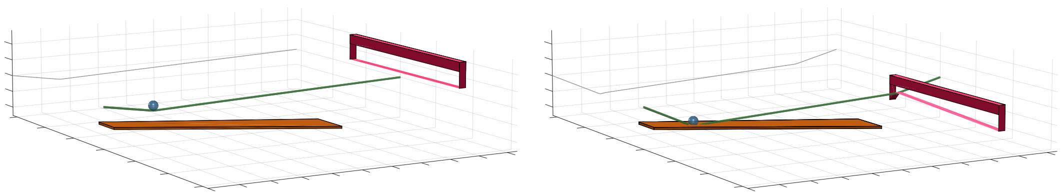

(b) $t = t_1$: the finger is pushed down onto the string.

(c) $t = t_2$: the string is stopped between finger and fingerboard, the bow is pushed down onto the string.

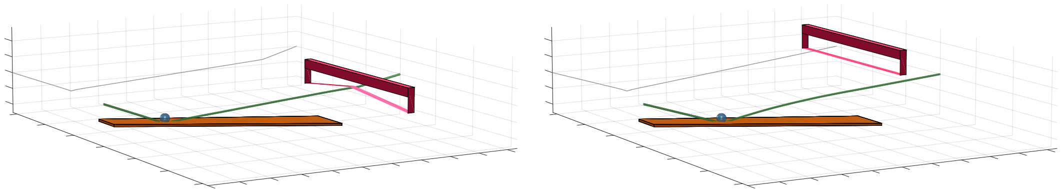

(d) $t = t_3$: the bow is pushed down onto and across the string with increasing force, and is brought closer to the bridge termination; the finger moves down the fingerboard, also with increasing force.

(e) $t = t_4$: the bow is lifted up from the string.

Figure 4.11: Energy transfers in the vertical polarisation during a 2-second simulation (top), with visualisations of the system state (not to scale) at different timestamps. The shadow of the string displacement in the vertical polarisation is displayed in grey, at the back of the graph.

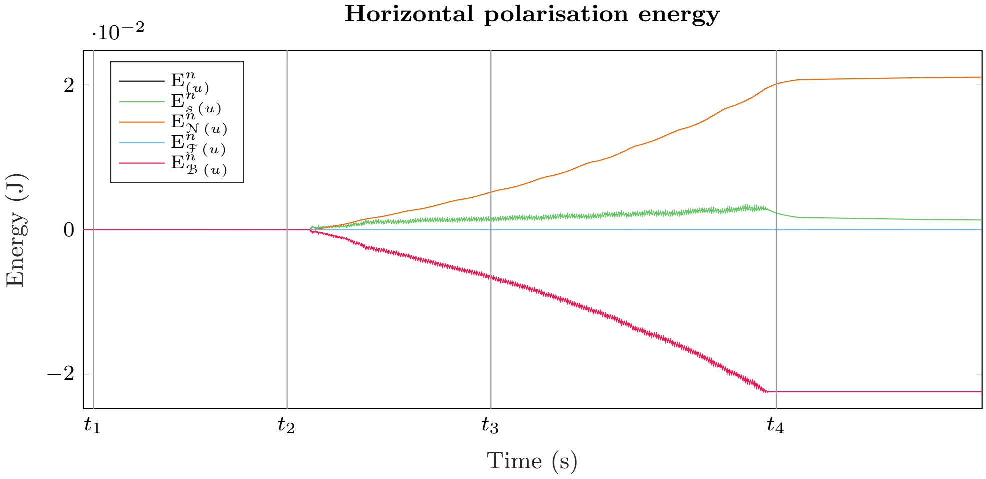

(a) Total energy and cumulated power for each subsystem: string (in green), fingerboard (in orange), finger (in blue), and bow (in red), in the horizontal polarisation. The total energy and cumulated power (in black) remains constant.

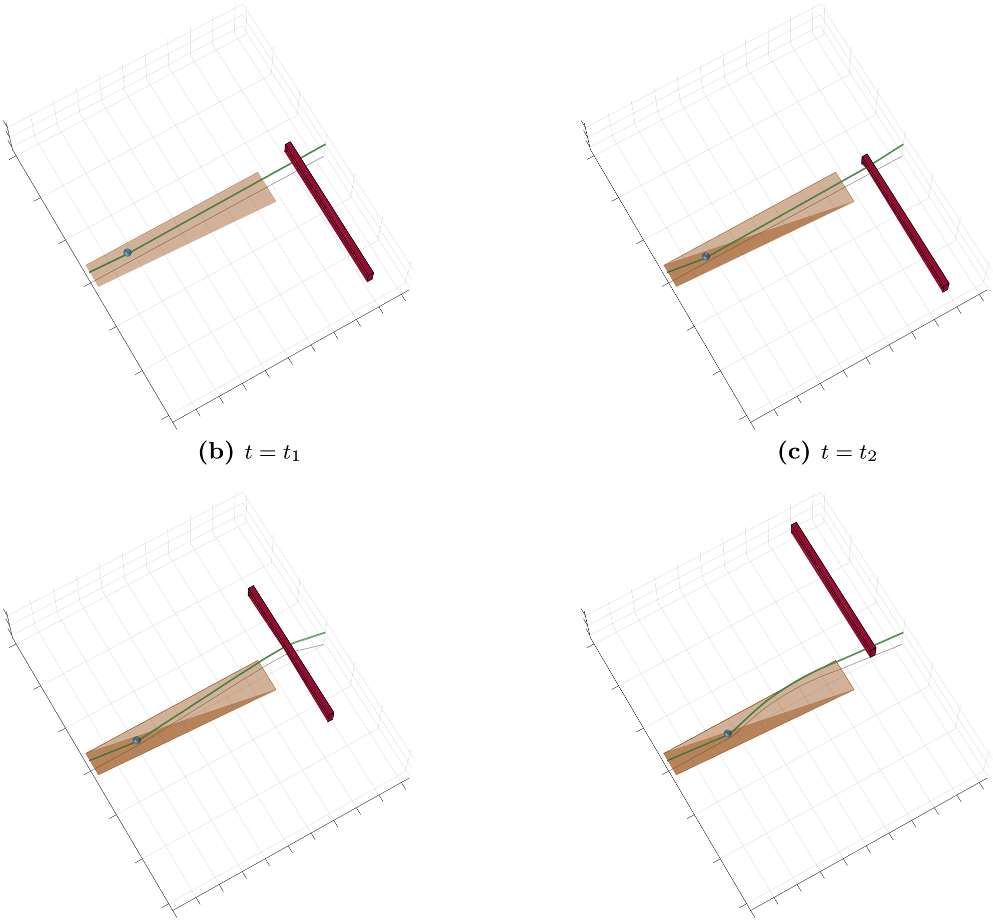

(b) $t = t_1$

(c) $t = t_2$

(d) $t = t_3$

(e) $t = t_4$

Figure 4.12: Energy transfers in the horizontal polarisation during a 2-second simulation (top), with visualisations of the system state (not to scale) at different timestamps. The shadow of the string displacement in the horizontal polarisation is displayed in grey, at the bottom of the graph; the fingerboard is transparent. Timestamps are the same as that shown for the vertical polarisation in Figure 4.11.

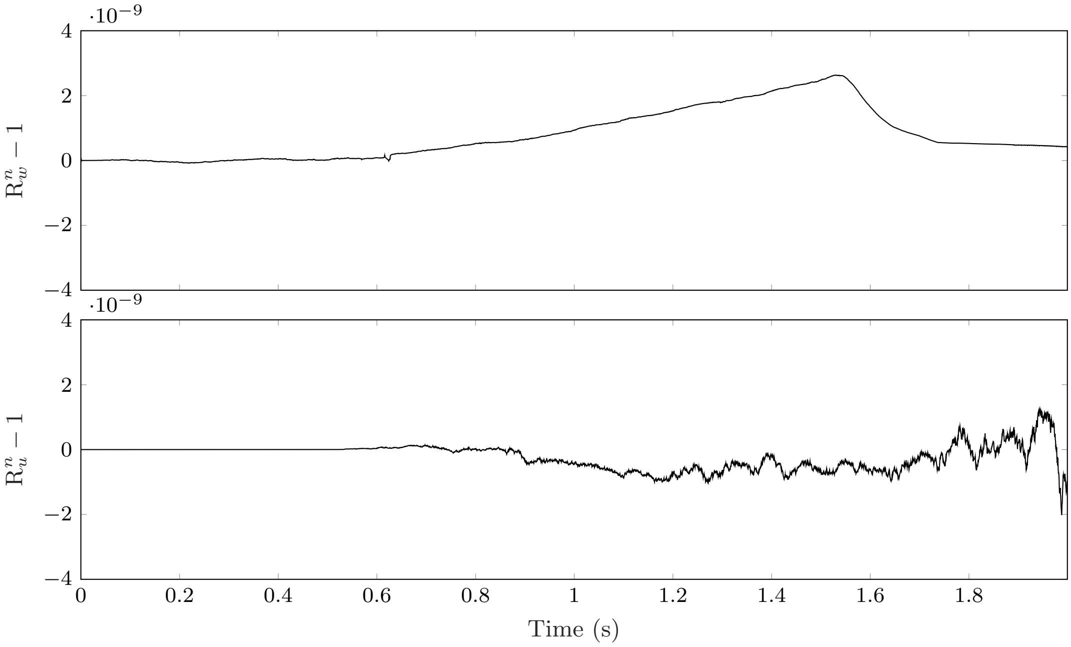

Figure 4.13: Variations of R_w^n (top, vertical polarisation) and R_u^n (bottom, horizontal polarisation) away from 1; small values indicate that the numerical energy is indeed balanced.

Chapter 5

Control and gesture-based sound synthesis

In Chapter 4, a numerical model of a two-polarisation bowed string was presented, including stopping fingers and a fingerboard. Given a set of time-varying control parameters, the algorithm can be used to simulate a musician's gesture. The computed output can then be read out at one or more locations along the string[1] in order to generate synthetic sound.

The problem explored in the present Chapter is that of user control[2]. A numerical model based on the behaviour of real instruments should exhibit both musically desirable and undesirable responses to user input, as seen in the physical objects they imitate. This means that, although the sound synthesis possibilities from such an algorithm are vast, the musically useful region may only be a small subset of the control parameter space, the dimensions and location of which are not trivial to determine.

The first part of this Chapter (Section 5.1) seeks to address some of these issues, with a systematic exploration of the bowing parameter space made available by the proposed bowing model. This analysis hinges on the concept of *playability*, a description of which will be given in Section 5.1.1. After describing the principal vibration regimes observed in a bowed string, a graphical representation of the parameter space will be proposed in Section 5.1.2, closely related to those present in the literature, and adapted for the proposed model of the bow-string system. Section 5.1.3 will describe the method employed to generate and analyse numerical data from simulations. The results of this analysis will be presented in 5.1.4, and their usability in guiding sound synthesis will be discussed in Section 5.1.5.

The second part of this Chapter (Section 5.2), informed by the results of 5.1, will then give an overview of the capability of this algorithm to simulate bowed string gestures. A summary of the user control streams will be presented, and simple gesture examples will be demonstrated.

---

[1] Recall that the model presented throughout this work assumes an isolated string, with perfectly reflecting boundary conditions, uncoupled to any bridge/body structure; computational output must therefore be read out on the string itself.

[2] Note that, here, "control" is meant in a computational sense; the user interface problem is a wholly different topic.

The work presented in Section 5.1 has been described in [31]. Note that the results were obtained before the development of the frequency-dependent damping model presented in Chapter 3. The loss model employed for the playability study in the present chapter is described in [7], and is summarised by Equation (3.27). The other aspects of the model are identical to those presented in this manuscript, namely the nonlinear interactions with the bow, finger, and fingerboard in two polarisations. Indeed, all derivations exposed in Chapter 4 still stand with the former loss model; the only discrepancies lie in the linear part of Systems (4.11) and (4.20), and are therefore all encapsulated in the $\boldsymbol{L}\boldsymbol{u}_{(w)}$ and $\boldsymbol{L}\boldsymbol{u}_{(y)}$ terms.

An overview of the gestural control attainable with the same model was described in [29]. Sound and video examples, compiled directly from simulated data, are available online[3].

5.1 Control parameter space and playability of the virtual bowed string

Section 5.1 focuses on the problem of bow control within the available parameter space defined by the numerical model proposed in Chapter 4. Throughout this Section, the fingerboard and finger models will be omitted, reducing the study to that of open bowed strings.

5.1.1 The concept of playability of a bowed string instrument

Bowed string playing is characterised by the high sensitivity of the tonal quality of a produced note to small variations of playing parameters. While this grants remarkable expressive control to an experienced player, the requirement for such fine execution presents the novice musician with significant challenges.

The ease with which a stable note (i.e. in the Helmholtz regime) can be produced on a bowed string instrument is often referred to as the *playability* of the instrument [117]. Playability can be quantified by the breadth of the bowing parameter space that gives rise to Helmholtz motion [115] in the bowed string (see Figure 4.4).

Many studies have investigated the playability of bowed strings, both experimentally and on virtual strings; see, for instance, [94, 85, 96, 95, 97, 117]. Three control parameters have most frequently been used: the downwards bow force, transverse bow velocity, and bow-bridge distance. Schelleng [90] was the first to formulate analytical limits for the minimum and maximum downwards bow force, for given values of the two other parameters, outwith which Helmholtz motion is unattainable. He introduced a well-known graphical representation of the playable region in the bowing parameter space, now commonly referred to as a “Schelleng diagram”; the original figure in [90] is reproduced in Figure 5.1. Schelleng’s analysis was then

---

[3] `https://charlottedesvages.com/companion/appl-sci-16/`

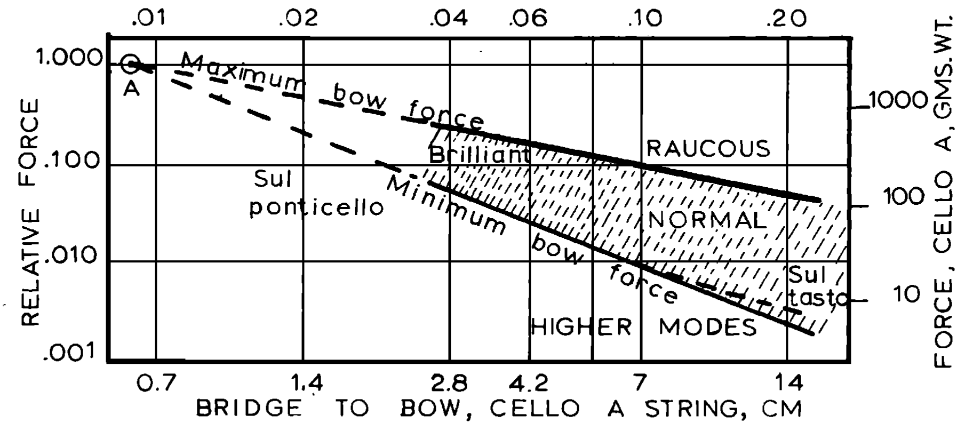

Figure 5.1: Schelleng diagram, reproduced from [90], showing the minimal and maximal downwards bow forces delimiting the Helmholtz playable region, as a function of the bow-bridge distance, for a given bow velocity.

revised by Schoonderwaldt *et al.* [93] who found, through extensive analysis of experimental measurements, no clear relation between minimum bow force and bow velocity.

Schelleng's diagram is the standard tool for playability analysis of bowed strings, in the steady state regime. It is a two-dimensional logarithmic plot of the theoretical minimal and maximal bow force limits versus bow-bridge distance, for a given bow velocity. Each of these limits forms a straight line in this logarithmic parameter space, delimiting a triangular area within which Helmholtz motion is achievable. Beyond these limits, other vibration regimes arise, such as:

- Raucous motion, when the downwards bow force is high for a given transverse bow velocity and bow-bridge distance, preventing the string from detaching from the bow at the end of the sticking phase[4], hence giving rise to a rough, noisy sound.

- Multiple slipping, when the downwards bow force is too low for a given transverse bow velocity and bow-bridge distance, preventing the bow from sticking to the string for the full duration of the nominal sticking phase. Multiple slipping is often characterised by strong harmonics in the produced note, as the string slips several times per nominal period.

- Anomalous low frequencies (ALF), beyond the maximal downwards bow force limit, when the Helmholtz corner is reflected once or more between the bow and nut before triggering the slipping phase, resulting in oscillations below the fundamental frequency of the string. The frequency of these oscillations depends on the distance between the nut (or stopping finger) and the bow. There do exist so-called secondary waves (ripples), reflecting between the bow and the bridge; these ripples could also yield another type of ALF, with a shorter period lengthening, correlated to the bow-bridge distance [91].

---

[4] See Section 4.2.3.ii for a description of the stick/slip cycle.

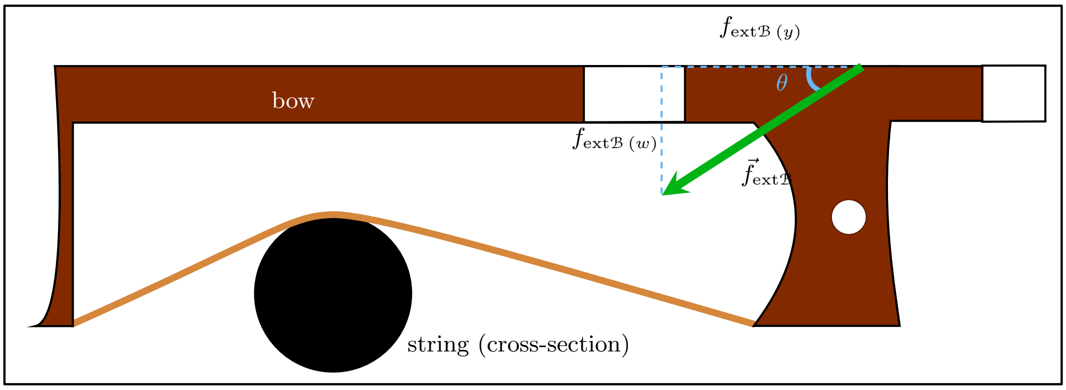
$f_{\text{ext}\mathfrak{B}\,(y)}$
bow
θ
$f_{\text{ext}\mathfrak{B}\,(w)}$
$\vec{f}_{\text{ext}\mathfrak{B}}$
string (cross-section)

Figure 5.2: Bow control for the present model is characterised by the magnitude $\left|\vec{f}_{\text{ext}\mathfrak{B}}\right|$ and angle θ of an external resultant force vector applied onto the bow.

- S-motion, observed for high downwards bow forces and bow-bridge distances, characterised by high-amplitude ripples [66].

A Schelleng diagram can be replicated from experimental and simulated data, in order to test a particular bowed string model. In this case, a large number of measurements must be taken, spanning the available parameter space. This is evidently much easier to do with simulations than it is with an experimental rig, having the advantage of perfect repeatability, and the ability to run a very large number of simulations at virtually no cost.

5.1.2 The force-force control parameters

In addition to the bow position $x_{\mathfrak{B}}$ along the string, made static during each simulation in this study, the available dynamic control parameters are the forces exerted onto the bow by the player in the two polarisations, $f^n_{\text{ext}\mathfrak{B},(w)}$ and $f^n_{\text{ext}\mathfrak{B},(y)}$. The former directly determines the steady-state normal bow force, often referred to as "bowing pressure" by musicians. The latter dictates the transverse bow velocity, depending on the bow hair's friction characteristics.

Consequently, a bow force vector $\vec{f}_{\text{ext}\mathfrak{B}}$ may be defined, the orthogonal components of which are given by the vertical and horizontal components of the bow force; Figure 5.2 illustrates such a vector. This description emphasises the role of the player in providing control through application of a force onto the bow, from which the string and bow dynamics eventually arise.

The main difference between the control of classic bowed string models, and the model presented here, is the transverse bow control. In the horizontal polarisation, at least, the conventional control parameter is an imposed transverse bow velocity. The present model, however, uses a time series describing the force applied to the bow, in the transverse direction. A parameter exploration study will therefore seek the regions of the parameter space giving rise to a given bowed string vibration regime, not along force-velocity axes, but along force-force axes; at a given bowing position, the entire parameter space can be described in terms of the magnitude and angle of the bow force vector $\vec{f}_{\text{ext}\mathfrak{B}}$.

Clearly, the availability of three control parameters implies to make a choice if a 2D

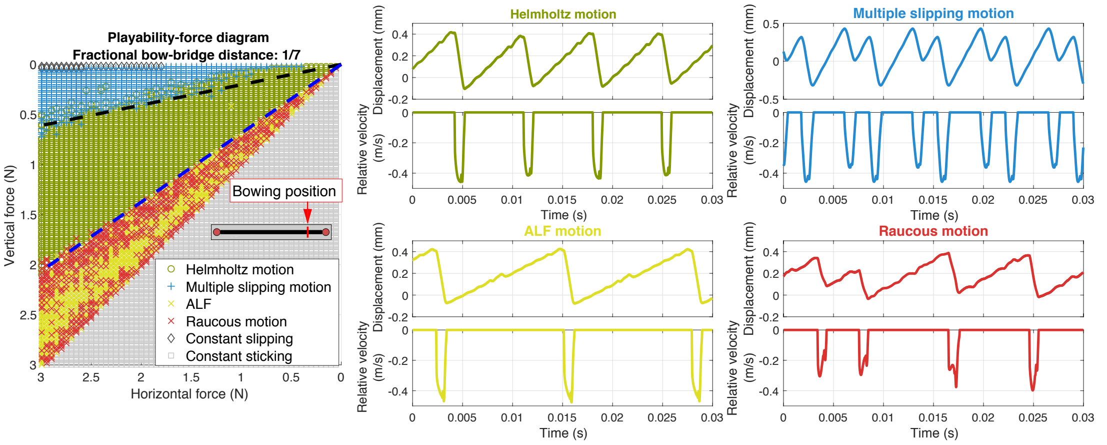

Figure 5.3: An example playability-force diagram. Each marker on the left plot represents one simulation, performed with one combination of transverse and normal bow force. Each simulation was examined 1.8 s after initial application of the horizontal bow force, and categorised into one of four playing regimes (excluding constant sticking and constant slipping). Typical string displacement and associated relative velocity waveforms are shown for each of the four detected regimes. The diagonal black and blue lines on the diagram respectively mark the estimated minimum and maximum bow force angles, between which Helmholtz motion is reliably obtained in the simulation, regardless of bow force magnitude. — Parameters: see Cello D string on page xxix. — Figure reproduced from [31].

representation is sought. In his study of steady-state bowed string oscillations, Schelleng [90] chose a particular representation of the parameter space and bow force limits, as a function of the bow-bridge distance, for a given bow velocity. However, as noted in his original work, one could also plot the vertical bow force as a function of the bow velocity, for a given bow-bridge distance. A possible layout for visualising the parameter space in the present framework immediately arises: the bow force vector can be represented in a playability diagram, with its transverse component $f_{\mathrm{ext}\mathcal{B},(y)}$ on the horizontal axis, and $f_{\mathrm{ext}\mathcal{B},(w)}$ on the vertical axis. The origin of the graph (chosen to lie at the top right of the axes) then corresponds to the origin of $\vec{f}_{\mathrm{ext}\mathcal{B}}$ (i.e. application of zero force). An example of such a “playability-force diagram” is shown in Figure 5.3. The apex of the bow force vector is then expected to navigate a two-dimensional valley in the bow force parameter space, within which steady Helmholtz motion is attainable.

5.1.3 Exploring the parameter space: a numerical experiment

A large number of simulations were computed on a cello D string, using the algorithm described in Section 4.3[5]. 10 data sets were obtained, for 10 static bow positions $x_{\mathcal{B}}$, all chosen as integer ratios $x_{\mathcal{B}}^{\mathrm{int}}$ of the string length, for $x_{\mathcal{B}}^{\mathrm{int}}$ values ranging from 5 to 14, so that the bow was positioned at a fraction $1/x_{\mathcal{B}}^{\mathrm{int}}$ of the string length away from the bridge termination.

For each of the 10 positions, the downwards bow force $f_{\mathrm{ext}\mathcal{B},(w)}$ was incrementally varied from 0.02 to 3 N, in 0.02 N steps (150 different force values), and the transverse bow force $f_{\text{ext}\mathcal{B},(y)}$ was varied between 0.05 and 6 N, in 0.05 N steps (120 different values), amounting to 18,000 simulations for each bow position. Each simulation lasted for 3 seconds, with the downwards bow force applied at $t = 0$, and the transverse bow force stepped up to its target value at $t = 1$ s. This delay was implemented so that any initial string oscillations, caused by the application of the downwards bow force, had time to settle. As this study was focused on the steady-state regime, the resulting output waveforms were analysed from 1.8 s after application of the transverse bow force, i.e. well after the end of the initial transient phase.

---

[5] Recall that, for this study, the linear part of the string model employed a simpler representation of damping processes.

The automatic classification of bowed string playing regimes is described in [31]; a brief outline of the methodology is given here. It should be disclosed that this particular aspect of the study was led by the co-author of [31].

The classification routine is based upon analysis of the relative velocity signal $v^n_{\text{rel},\mathcal{B}}$, computed from the simulations. The approach uses autocorrelation to identify periodicity, and is largely inspired by a methodology employed in the literature for similar studies [116], with one notable difference. Rather than applying an autocorrelation analysis directly to $v^n_{\text{rel},\mathcal{B}}$, a peak-finding algorithm is first applied to the signal to identify times of maximal slip velocity. The timing and amplitude of these peaks are then used to create the signal $v^n_{\text{rel},\mathcal{B},\mathtt{q}}$, a quantised version of $v^n_{\text{rel},\mathcal{B}}$ consisting of zeros everywhere except at moments of maximum slip velocity, where $v^n_{\text{rel},\mathcal{B},\mathtt{q}}$ takes the value of such velocity.

Autocorrelation analysis is then applied to $v^n_{\text{rel},\mathcal{B},\mathtt{q}}$, producing an autocorrelation function that is itself of a quantised nature. Analysis of the location, spacing, and spread of the autocorrelation peaks leads to a set of relatively simple rules, allowing classification of each simulated waveform into one of six categories:

- constant slipping, where the bow slides smoothly over the string, with no clear stick/slip cycle;
- constant sticking, where the transverse bow force is too small to keep the bow moving, the bow stops and remains permanently stuck to the string;
- Helmholtz motion;
- multiple slipping;
- anomalous low frequencies (ALF);
- raucous motion.

The detection of S-motion was not included in this study.

5.1.4 Results

This Section summarises the key observations made on the playability diagrams compiled with simulation output data.

5.1.4.i Bow force vector range and areas of interest

The playability-force diagrams mostly appear divided into approximately triangular regions. Observation of sampled data on either side of the limits between the various regions suggests that the classification algorithm is robust. The following observations are common to all generated diagrams (i.e., for all bowing positions).

- The Helmholtz-playable region (Figure 5.3, in green) is circumscribed by two limits. The lower separation segregates the Helmholtz region from the raucous region (in red). In this representation of the parameter space, it is almost linear; it therefore corresponds to a particular angle of the bow force vector.
- Above the Helmholtz region, the transition into the multiple slipping region is generally less distinct, especially for very high and very low bow force vector magnitudes (i.e., close to, or far away from, the origin). This suggests a more ambiguous transition between Helmholtz motion and multiple slipping at low downwards forces.
- Within the raucous region, one or more wedge-shaped ALF areas (in yellow) are visible.

The clearly defined (and seemingly linear) maximum downwards bow force limit, within the analysis framework used here, suggests a possible definition of the lower limit of the playable space in terms of only the angle of the bow force vector, and independent of its magnitude. With the aim of clarifying the playability of the proposed algorithm as a sound synthesis tool, a “soft” upper bound of the Helmholtz region can similarly be drawn from the origin, bounding an angle range where Helmholtz motion is reliably achieved regardless of bow force magnitude, and excluding all occurrences of multiple slipping. Figure 5.3 shows these upper (in black) and lower (in blue) limits, in dashed lines.

5.1.4.ii Evolution of the playable range with bow position

Figure 5.4 presents all 10 playability-force diagrams for fractional bow-bridge distances from $\frac{1}{5}$ to $\frac{1}{14}$ of the length of the string. All regions of the diagram seem to rotate counter-clockwise around the origin as the bow gets closer to the bridge. Both lower and upper downwards force limits shift towards higher values.

The raucous/ALF section narrows, as the multiple slipping area expands, confirming the need for higher downwards forces to trigger Helmholtz motion as the bow-bridge distance decreases.

The lower downwards bow force limit, separating multiple slipping and Helmholtz regimes, appears to become increasingly linear as the string is bowed nearer the bridge. Within the multiple slipping region, various “pockets” of Helmholtz motion seem to appear, change shape, and generally rotate anti-clockwise with decreasing bow-bridge distance.

To get a better sense of how playability might evolve as the string is bowed closer to the bridge, and to relate the results to a more conventional Schelleng analysis, two quantities are plotted against bow position. Figure 5.5 shows the evolution of the relative area of each

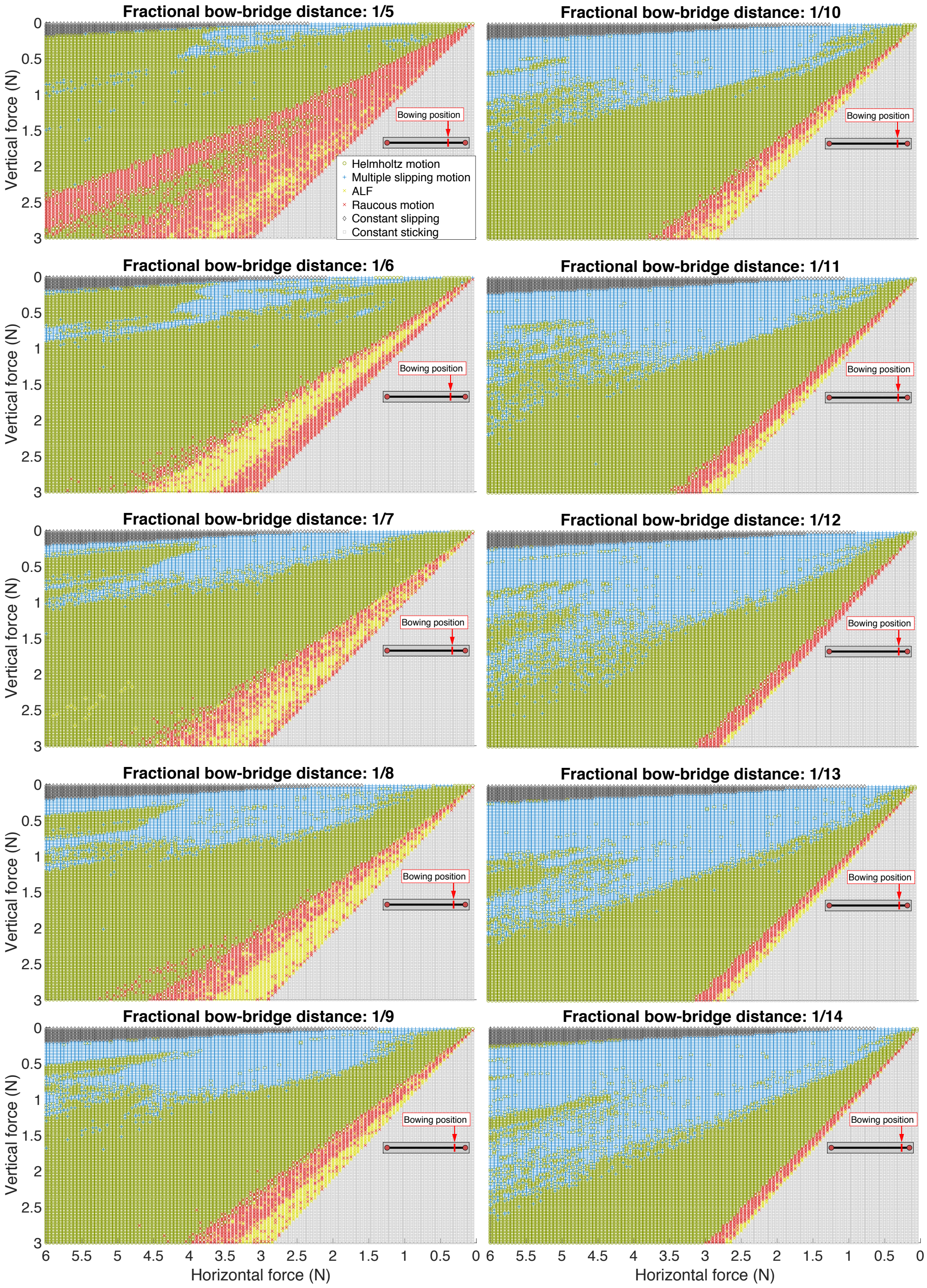

Figure 5.4: Playability-force diagrams for different bowing positions. The axes have been adjusted so that zero force is at the top right of each plot, so as to reflect the diagram shown in Figure 5.2. Note that, while the bow force vector angle changes, rotation of the bow itself is not implied. — Parameters: see Cello D string on page xxix. — Figure reproduced from [31].

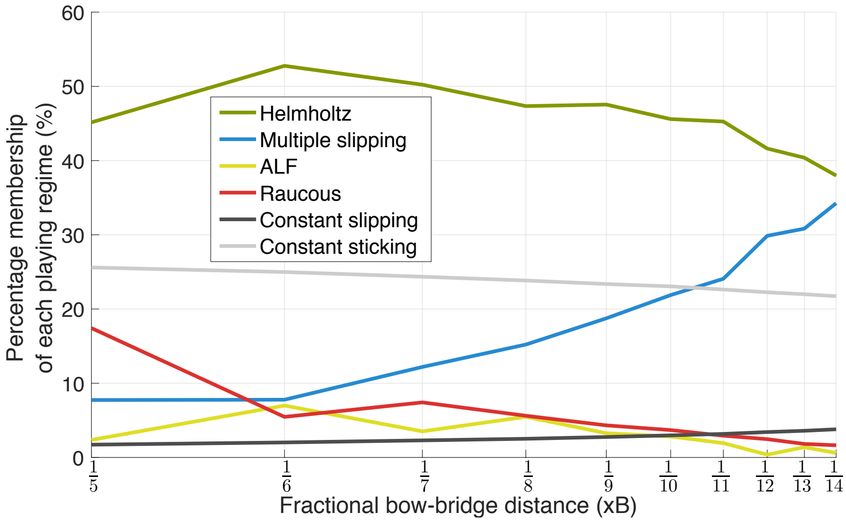

Figure 5.5: Relative membership counts for detected playing regimes, plotted against decreasing bow-bridge distance. — Figure reproduced from [31].

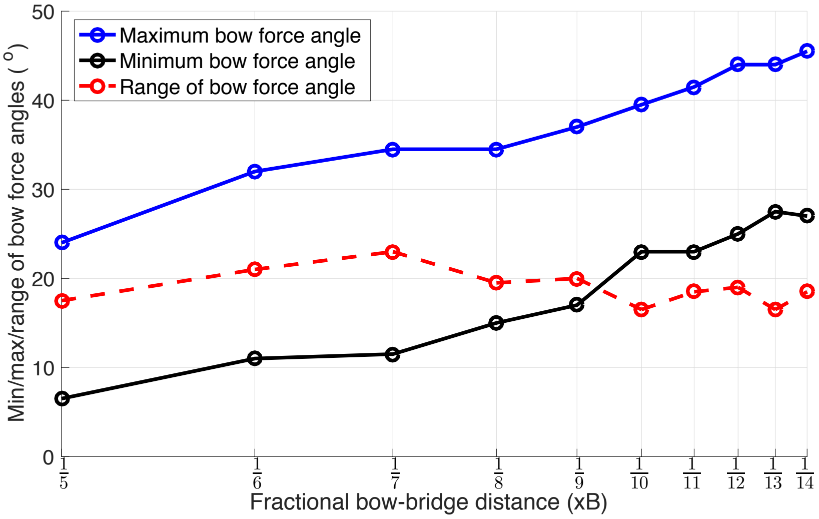

Figure 5.6: Estimated minimum, maximum, and implied range of bow force angles that produce reliable Helmholtz motion, as a function of bow position. — Figure reproduced from [31].

detected regime versus bow position, by counting, in each diagram of Figure 5.4, the number of waveforms classified into a particular category. The result summarises one of the obvious trends seen in Figure 5.4, which is the progressive rise in the number of multiple slipping cases with decreasing bow-bridge distance. Furthermore, after a peak at $x_{\mathcal{B}} = \frac{L}{6}$, the Helmholtz region gradually narrows as the bow is brought closer to the bridge.

Figure 5.6 plots the angular range of the bow force vector giving reliable Helmholtz motion, as a function of bow-bridge distance. This range is evaluated by measuring the respective angles of the dark blue and black dashed lines used to delimit a reliable Helmholtz-playable range independently of the bow force magnitude (see Figure 5.3), as described in Section 5.1.4.i. While the minimum and maximum bow force angles both increase with decreasing bow-bridge distance, the playable angular range does not seem to follow such a clear trend. Indeed, as seen on the red dashed curve in Figure 5.6, the playable angular range only narrows or expands by a few degrees; such variations are practically indistinguishable from those arising from the uncertainty in the assignment of the upper (black) line, separating the Helmholtz and multiple slipping regions. This means that, in terms of the bow force vector control, the breadth of the Helmholtz playable space remains relatively constant with varying bow-bridge distance. Note that this observation will, perhaps, not seem familiar to a bowed string player; a possible explanation could be that smaller bow-bridge distances require steeper bow force angles (i.e. larger downwards forces), for which finer control is more difficult to achieve.

5.1.4.iii Anomalous low frequencies

A noteworthy feature of all the playability diagrams in Figure 5.4 is the presence of an ALF band (in yellow), suggesting a "playable ALF region" rather than random, sparsely distributed cases; this was also observed experimentally by Schoonderwaldt [93]. This ALF region moves within the raucous region with varying bow position, surrounded by raucous cases when the string is bowed further from the bridge, and progressively shifting in an anti-clockwise direction when the bowing point gets closer to the bridge. Eventually, the ALF band provides a clear separation between raucous motion and constant sticking.

For $x_{\mathcal{B}} = \frac{L}{5}$ (Figure 5.4, top left), two triangle-shaped bands can be observed within the raucous area. One of them, in yellow, corresponds to the first type of ALF described in Section 5.1.1, for which the fundamental stick/slip period is almost doubled. The second wedge, in green, was automatically classified as Helmholtz motion, as the classification algorithm tolerates a moderate amount of pitch flattening. However, closer inspection of the waveforms shows what could be the second type of ALF described in 5.1.1, due to ripples reflecting between the bridge and bow, and for which the resulting pitch is lowered by about one semitone. Without further analysis, this second band becomes indistinguishable from pitch-flattened Helmholtz motion for smaller bow-bridge distances.

5.1.4.iv Regime segregation

As a more general comment, it is worth noting that the separation between the different vibration regimes for all plots of Figure 5.4 is clearly defined, in particular the separation between Helmholtz and raucous motion, and the boundaries of the ALF regions. This highlights once again the strong nonlinearity of the bow-string interaction, as it is shown that very small, incremental shifts in control parameter values can result in drastic pattern changes in the output signal. In the literature pertaining to nonlinear dynamics, these events are referred to as bifurcations [63]. Amongst existing studies of the bowed string as a nonlinear dynamical system, an interesting example is that of an experimental study by Müller and Lauterborn [76], who investigated these bifurcations by applying gradually increasing bow velocities. Such phenomena are difficult to approach analytically, hence reaffirming the suitability of a time-stepping numerical method based on a physical model to simulate the bowed string system.

5.1.5 A tool for sound synthesis control

The results presented above are qualitative in nature. It is not the ambition of this study to validate theoretical models or experimental measurements in a quantitative manner; rather, it is to provide a tool for guiding sound synthesis with the proposed bow-force-controlled algorithm. Before any comparison can be made with experimental data, it must be considered that the physical model used in this work is missing arguably essential features, potentially having great influence on playability. Some of these features may include the finite width of the bow, the presence of torsional waves [6], or a mobile bridge boundary, dynamically coupled to a realistic bridge-body model. Schoonderwaldt [93] has experimentally demonstrated that damping conditions have significant influence on the bow force limits defining the playable region; specifically, he outlines the intrinsic string damping, the coupling to the body, and the stopping finger as the factors most influential on playability. It would therefore be appropriate to derive results as those presented here, using accurate calibration of the frequency-dependent loss profile of the string, as described in Chapter 3, and to explore the influence of an absorbing stopping finger on playability; this is left, for now, as further work.

Qualitatively, nonetheless, the diagrams compiled for the proposed model indeed show similarities with Schelleng diagrams, in that a triangular Helmholtz-playable area is visible, in terms of downwards and transverse bow force components. As observed experimentally [93], the transition between the Helmholtz and multiple slipping regions is not clearly defined; this could result from the progressive character of this transition, and perhaps from its dependency on initial transient response. Further observation of the waveforms lying in the vicinity of the minimum bow force limit confirms that many continuously transitioned between multiple slipping and Helmholtz motion; this suggests that results computed from a delayed analysis window would certainly produce a different set of diagrams.

Following this observation, it is straightforward to see how this analysis could be applied to the characterisation of transient behaviour. In addition to the quality of the steady-state regime, the initial bowed string transient characteristic, and particularly its duration [47], plays a major part in the evaluation of playability. In this respect, the force vector representation for bow control offers a significant advantage; a step onset of transverse bow force is arguably comparable to the application of an initial transverse acceleration to the bow, which is the control parameter used by Guettler for his pioneering transient analysis [45]. The same method as that described in Section 5.1.3 can therefore be used for the evaluation of transient behaviour, if applied to many analysis windows, each centred at a different time; most importantly, the analysis can be performed on the same simulated dataset, without the need to recompute thousands of simulations with a different set of control parameters.

The steady-state playability diagrams presented here, possibly coupled with a future transient characterisation study, could constitute a collection of presets for the sound synthesis of a range of strings with known physical parameters. Options to compile playability diagrams for any virtual string, outside of such database, could perhaps be explored in further refinements. The relatively consistent triangular structures observed in Figure 5.4 could be the starting point for a much more targeted (and time-efficient) analysis, over a few carefully selected combinations of control parameters, aiming at determining approximate minimum and maximum bow force angles as a function of bowing position.

5.2 Gesture reproduction for sound synthesis

This section, and the concluding part of this thesis, aims to illustrate the range of sound synthesis possibilities offered by the bowed string numerical model presented throughout Chapters 3 and 4. All the simulations presented here were run in MATLAB, at a standard audio sample rate ($F_s = 44.1$ kHz)[6], with the grid spacing h set as close as possible to the stability limit. The output waveforms, in the form of string displacement time histories, were read out from the discrete string point immediately adjacent to the bridge termination.

5.2.1 Summary of the control parameters

5.2.1.i Physical parameters

The first aspect of user control for the proposed algorithm lies in the physical parameters of the system. An end user has total and independent control over every constant physical parameter defined in this work, summarised in the table on page xxv. The parameters are manually input into a MATLAB script, referred to as the *instrument file*. For a given audio sample rate, the grid spacing can then be set according to the stability condition given in (2.91).

The table of physical parameter values given on page xxix may be used as a safeguard, if one is concerned with the synthesis of realistic bowed string instrument sounds; the more adventurous composer can experiment with different parameter combinations, not limited by physical constraints. Recalling the results of Section 5.1, it is important to note that, given the nature of bowed string motion, unusual combinations of physical parameters may drastically limit playability.

5.2.1.ii Control signals

The second aspect of user input, and the focus of the rest of this Section 5.2, is gestural control, defined by a set of dynamically varying parameters for each bow and finger:

- Bow parameters:
    - bow position $x^n_{\mathcal{B}}$ along the string, closer to or further away from the bridge;
    - downwards bow force $f^n_{\text{ext}\mathcal{B},(w)}$, often referred to as “bowing pressure”;

---

[6] With the exception of those for which spectrograms were computed, where the sampling rate was increased in order to enhance resolution.

  - tangential bow force $f^n_{\mathrm{ext}\mathcal{B},(y)}$, which will determine the bowing velocity, and, in turn, the amplitude of bowed string motion.

- Finger parameters:
  - finger position $x^n_{\mathcal{F}}$ along the string, determining the (possibly time-varying) pitch of the produced note;
  - downwards finger force $f^n_{\mathrm{ext}\mathcal{F},(w)}$, used to capture the string against the fingerboard, or to lightly push the finger against the string in order to play natural harmonics or to damp residual oscillations.

It should be noted that, if the string model was designed to include a geometric nonlinearity (leading to, e.g., tension modulation), the application of a transverse finger force $f^n_{\mathrm{ext}\mathcal{F},(y)}$ would suffice to reproduce pitch-bending gestures, often used in guitar playing.

In a second MATLAB script, referred to as the *score file*, the user inputs a list of breakpoint times and values for each of the five control parameters cited above. Time series are then generated for all parameters, using linear interpolation between breakpoints. The resulting piecewise linear control signals can then be modified at will; a representative example is the addition of an oscillatory term in the finger position signal, so as to simulate a vibrato sound, as will be seen in Section 5.2.2.iv.

5.2.2 Example gestures

5.2.2.i Varying bow forces and position

As long as the combination of bow force and bow position remains within the playable area of the control parameter space (see Section 5.1), the bow control parameters can be updated dynamically during the course of a simulation, while keeping Helmholtz motion sustained. This allows for dynamic variations of a note's timbre and loudness, directly mapped to the same parameters that a player would handle on a real instrument, as opposed to a more abstract representation of their influence over the output sound. For instance, a sharper, more brilliant sound is achieved by bowing the string closer to the bridge termination; loudness is controlled by adjusting the bow tangential force, in order to increase or decrease the bow velocity. Figure 5.7 illustrates the spectral variations associated with dynamic changes to the bow downwards force, tangential force, and position along the string, during a simple synthesised bowed string gesture.

5.2.2.ii Natural harmonics

It is possible to bow natural string harmonics by placing the finger at an integer fraction of the string length. The finger downwards force $f^n_{\mathrm{ext}\mathcal{F},(w)}$ must be small enough that the string does not touch the fingerboard, but large enough that the finger has a grip on the string. Figure 5.8 shows the spectrogram of a simulated bowed harmonic on a violin A string, where the string is stopped at its mid-point ($x_{\mathcal{F}} = \frac{L}{2}$ m), and bowed at $x_{\mathcal{B}} = \frac{3L}{4}$ m. As expected, the second

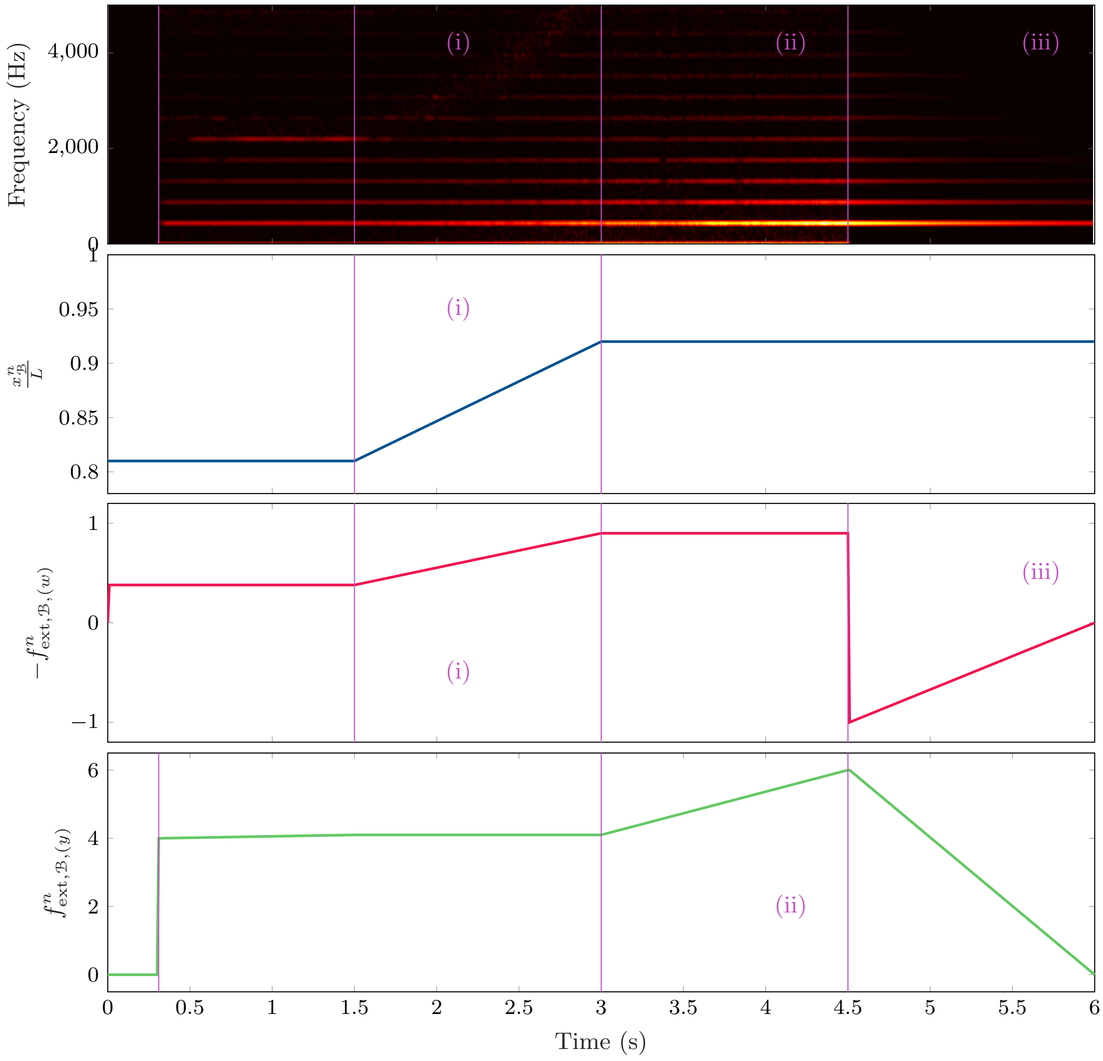

Figure 5.7: Spectrogram (1st plot) of the synthetic sound produced by bowing a violin A string with varying bow position $x^n_{\mathcal{B}}$ (2nd plot), bow downwards force $f^n_{\text{ext}\mathcal{B},(w)}$ (3rd plot), and bow tangential force $f^n_{\text{ext}\mathcal{B},(w)}$ (4th plot). (i) Higher harmonics appear when increasing the bow force and bowing closer to the bridge. (ii) An increase in bow tangential force does not influence the spectral content of the sound, but globally increases its amplitude. (iii) The free string oscillations decay as soon as the bow is lifted up, at frequency-dependent rates. — Parameters: see Violin A string on page xxix.

harmonic is the strongest; there are also partials at odd multiples of its frequency[7]. Some beating is observed when the string oscillations are left to decay, perhaps related to the finger's own resonant frequency being excited.

---

[7] Partials at even multiples of the second harmonic's frequency are not excited here, since their modal shapes comprise a node at the location of the bowing point.

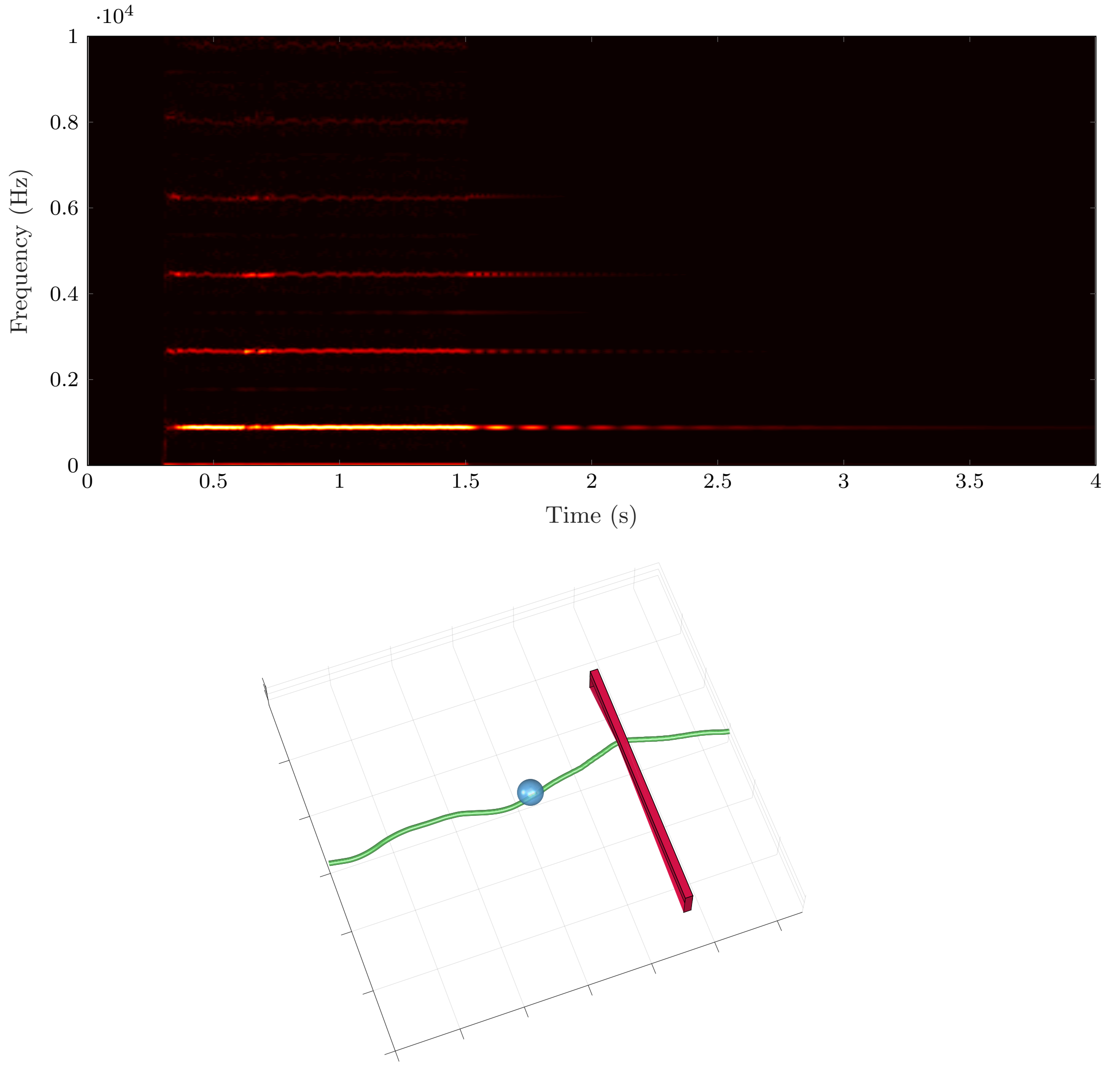

Figure 5.8: Top: spectrogram of the bowed first harmonic on a violin A string. Bottom: simulation snapshot, showing the bow and finger positions. — Parameters: see Violin A string on page xxix.

5.2.2.iii Bouncing bow

The bow spontaneously bounces against the string, if the initial vertical bow velocity is high enough (i.e., if the bow is pushed down too quickly onto the string, typically with a downwards initial velocity of 1—10 m/s), and the downwards force $f^n_{\mathrm{ext}\mathcal{B},(w)}$ is too small to immediately compensate the restoring force due to the tension of the string. A video of a bouncing bow simulation is available online[8]. With more refined control over the gesture parameters, it is indeed possible to simulate *spiccato* playing. Exploration of the full potential of the proposed model to reproduce these more complex gestures would greatly benefit from a real-time implementation, where dynamic parameters are mapped to a controller; this is out of the

---

[8] `https://charlottedesvages.com/companion/appl-sci-16/`

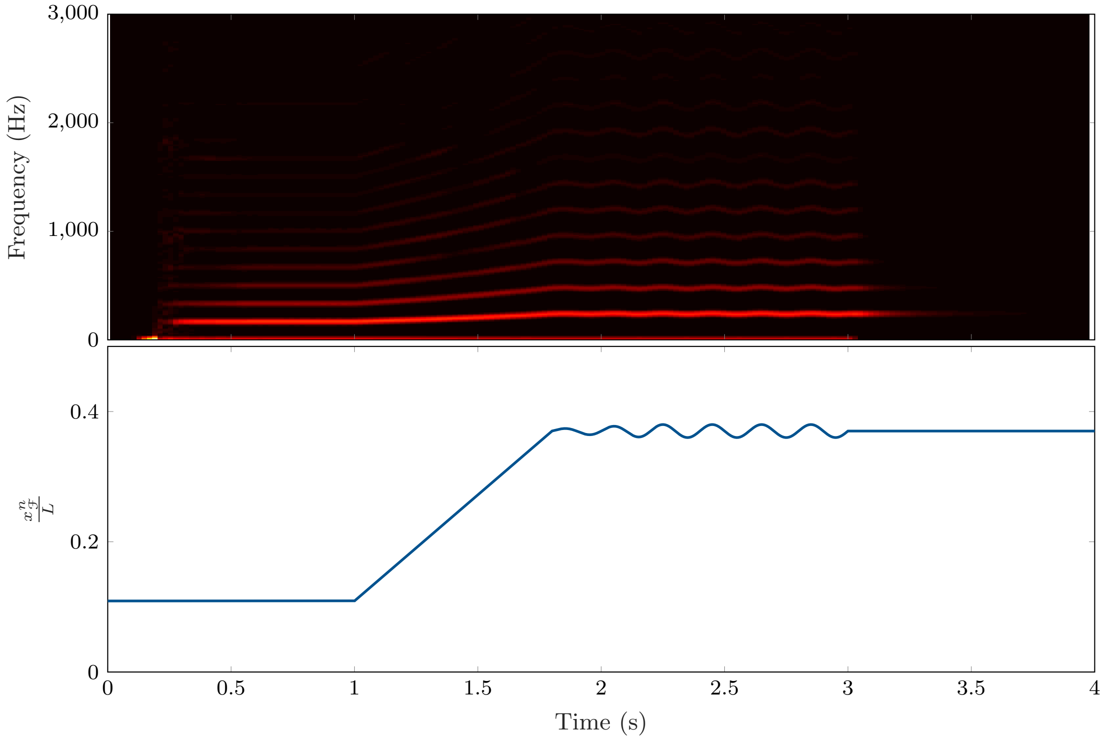

Figure 5.9: Top: spectrogram of a synthesised gesture, showing a glissando along a cello D string followed by a vibrato; the stopped string vibrations are then left to decay. Bottom: corresponding finger position along time. — Parameters: see Cello D string on page xxix.

scope of this thesis, and it is simply pointed out here that the numerical model enables such gestures.

5.2.2.iv Moving finger

The left hand finger can be moved along the string while pressed down against the fingerboard. It is therefore straightforward to introduce gestures such as *glissando*, where the finger slides up or down along a significant portion of the string, and *vibrato*, by oscillating the finger around a central position, at a sub-audio rate. Figure 5.9 shows the spectrogram for a *glissando* gesture, followed by a *vibrato*; the corresponding finger position is displayed underneath the spectrogram for reference.

5.2.2.v Rattling

In the absence of a bow, it is possible to reproduce a pluck gesture, for instance, by initialising the string displacement and velocity away from the string's resting state, or feeding an additional external force directly into the string as a time series, at the desired plucking point, with the help of a pointwise distribution akin to $\mathbf{j}_{\mathcal{F}}^n$ or $\mathbf{j}_{\mathcal{B}}^n$ [10]. A pluck at the same position in both polarisations, with large enough amplitude, will excite the string with enough energy to collide and rub against the fingerboard, possibly repeatedly; the resulting sound is that of the string

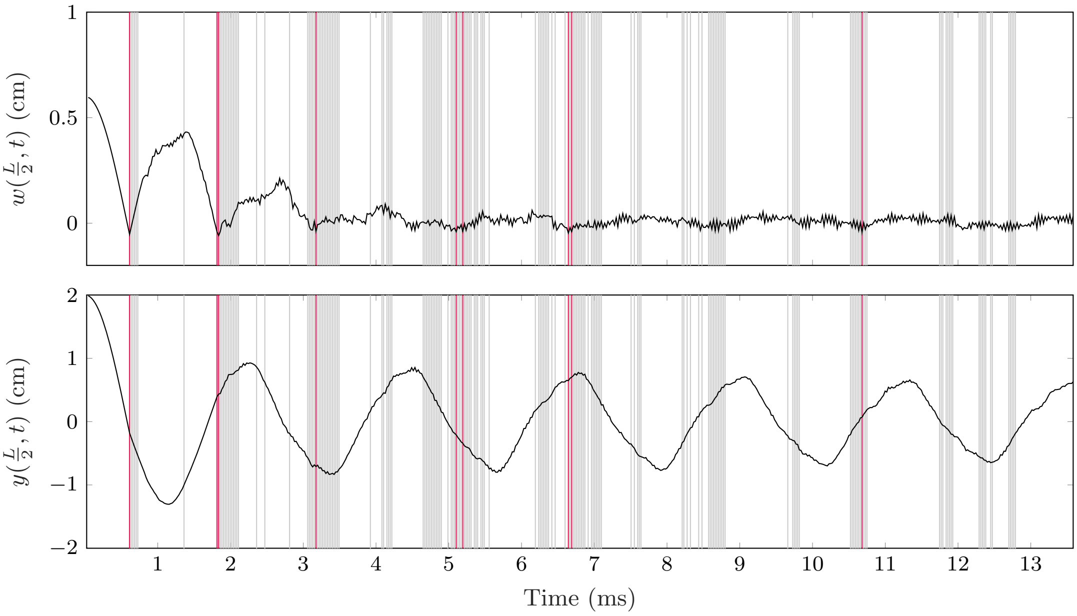

Figure 5.10: Large amplitude oscillations of a violin A string, resulting in repeated collisions and friction with the fingerboard. Top: vertical polarisation; bottom: horizontal polarisation. The grey vertical lines mark times when the string is anywhere in contact with the fingerboard; the red lines denote contact events at the readout position ($x = L/2$). The displacement of the string was initialised with the shape of the fundamental transverse mode, in both polarisations, to emulate a "diagonal" pluck; collision and friction both generate higher partials. — Parameters: see Violin A string on page xxix.

rattling against the fingerboard. Figure 5.10 shows the waveform obtained by a large amplitude pluck of a violin string, in both polarisations, where the times where the string is in contact with the fingerboard are highlighted.

Concluding remarks

This chapter has taken the first steps towards demonstrating the usability of the numerical bowed string model developed in this work as a tool for musical sound synthesis. An exploration of the control parameter space has provided a graphical representation of the playable space in terms of bow control. This parameter map showed qualitative resemblance with others obtained with experimental data, although further refinements are necessary in order to generalise the analysis of the results presented here.

The inclusion of lumped and distributed interactions with the player (through the bow and finger) and fingerboard allows to simulate articulated gestures in a relatively instinctive and concrete manner, without having to rely on somewhat abstract hypotheses. An eloquent example to illustrate this point is the versatility of the finger model, which accounts for several important phenomena which would be difficult (or impossible) to model with a simple absorbing string termination. Here, the simple action of pushing a finger down onto the string results in damped dynamic behaviour in both polarisations, control of the string's speaking length, possible slipping of the string under the fingertip while captured, and allows to play natural harmonics. The portion of the string between nut and finger is also excited, and participates in the overall dynamic behaviour of the system. The adaptation of this work to a more realistic situation, with multiple fingers, is trivial, as well as the design of a multiple string environment (provided the strings are independent).

Chapter 6

Conclusions and perspectives

This work outlines the development of a time-domain numerical model of a dual polarisation bowed string system, with the aim of designing a new tool for the synthesis of stringed instrument sounds. After a brief summary of the research contributions proposed in each Chapter, a review of remaining open problems is presented; finally, possible paths for future work are put forward.

6.1 Summary and contributions

Chapter 2 serves to describe the physical and numerical framework used in the rest of this thesis. Mathematical tools and notations are introduced with a case study of a simplified physical system: the lossless, stiff, isolated, linear string. Relevant aspects of the discretisation of the physical model into a space-time domain FD scheme are described for this simplified system, in order to later facilitate analysis. The procedure to derive a stable time-stepping algorithm from the numerical scheme is outlined.

Chapter 3 introduces modelling of frequency-dependent losses in the stiff linear string, adapting a frequency-domain model to a time-domain framework. The Q-factors of the string transverse modes constitute a particular loss profile in the frequency domain, depending on known (or measurable) physical parameters [113]. This profile is approximated by the means of a passive network, with a driving-point impedance determined by a set of positive, adjustable parameters. These parameters are then optimised in order to closely fit the known loss profile characterising a particular string. The equivalent time-domain system requires coupling the string displacement to a number of additional state variables. It is shown that only a small number of these additional states is required in order for the Q-factors computed on simulations to match the theoretical loss profile to a satisfactory level. The method described in Chapter 3 hence offers a reliable means to simulate linear string vibration with accurate decay times, all within a time-domain framework.

The benefits of working fully in the space-time domain are best illustrated in Chapter 4, where the linear string model presented in Chapter 3 is coupled, in two polarisations, to a dynamic bow and finger, as well as a rigid, distributed fingerboard; the interaction forces are nonlinear in both polarisations. In one direction, the finger, bow, and fingerboard are coupled to the string through a penalty impact model. When the string is excited in the other, perpendicular direction, the normal contact forces result in tangential friction. The friction model for the rosin-coated bow hair enables the various well-established bowed string regimes to take place; for the finger and fingerboard, friction keeps the string pinned in place, allowing to play stopped notes. Control parameters, such as the position of the finger and bow, as well as the normal and transverse forces exerted on them, are time-varying; they can be dynamically updated at each time step, without at all upsetting the stability of the algorithm.

The focus of Chapter 5 is the use of the algorithm detailed in Chapters 3 and 4 for sound synthesis purposes. A qualitative, exploratory study of playability of the virtual bowed string is first presented, in order to provide a visual representation of the control parameter map, highlighting musically useful regions. A number of qualitative similarities are found with previous experimental studies of bowed string playability, indicating, to a certain extent, that the proposed algorithm reproduces expected bowed string behaviour. The primary purpose of the playability diagrams compiled with simulation outputs is to provide a guiding hand to sound synthesis, by aiding the manual setting of input control parameters.

Finally, the second part of Chapter 5 gives an overview of the synthetic sound possibilities offered by the bowed, stopped string algorithm. A major advantage of the numerical model described throughout this work, perhaps with respect to other existing bowed string synthesis engines, is that of gestural flexibility. A wide variety of gestures can be reproduced with only a handful of control streams, each corresponding to a parameter familiar to a musician playing a real instrument (for instance, finger position, or bow force). In particular, gestures such as *vibrato* and *glissando* are readily available through the finger location parameter. Moreover, the timbre of a played note can be made to evolve, with varying degrees of subtlety, by introducing variations in bow force and position. *Pizzicato* playing at high amplitudes induces repeated collisions and friction between the string and the distributed fingerboard, significantly affecting the timbre. Bouncing of the bow against the string occurs spontaneously, opening the door to the synthesis of yet more advanced gestures.

6.2 Open questions

6.2.1 Frequency-dependent losses in the linear string

The time-domain approach to frequency-dependent loss modelling for the transverse modes of the linear string, described in Chapter 3, uses Valette's model [113] as a starting point, as have a number of recent works on (modal-based) string numerical modelling [80, 56]. This model contains a number of free parameters, difficultly adjustable for a particular string without experimental data. Furthermore, the measurements in [113] were taken on harpsichord strings; had the experiment been performed on strings with physical properties such as those described in this work, used on bowed string instruments, the theoretical model proposed by Valette and

Cuesta might not have been the best possible fit. A more accurate representation of the loss profile of a particular string would arise from experimental measurements performed on that string. Fortunately, the method described in Chapter 3 could straightforwardly be adapted to take a set of experimental data as a reference for optimisation, rather than an analytical curve.

One particular design was proposed for time-domain modelling of losses, making use of the Foster structure illustrated in Figure 3.4. It may be worth exploring other designs giving rise to positive-real impedances, in the hope of improving the quality of the simulated results, and/or further simplifying the synthesis algorithm, by achieving a comparable fit quality with potentially fewer damping terms.

As seen in the simulation results presented in Section 3.7.1, the Q-factors computed from the time-domain output signals seem to drift away from their theoretical value, as frequency increases. It is strongly suspected that frequency warping associated with the transfer from continuous to discrete domain plays an important role in this drift. Further analysis is required in order to locate the sources of frequency warping, both spatial and temporal, leading to the observed discrepancy between theory and results.

6.2.2 Impact parameters

The Hunt and Crossley penalty contact model [55] used to describe interactions in the vertical polarisation between the string and the bow, fingerboard, and finger, relies on three parameters for each object, defining stiffness and dissipated energy during contact; they have not presently been calibrated to experimental data. The collision parameter values could be determined, for instance, through a procedure akin to a load/unload test.

6.2.3 Friction force

As touched upon in Section 4.2.3.ii, the force-velocity curve given by (4.18) for the bow friction coefficient has been shown to be a flawed model [100, 41], failing to take into account an apparent temperature dependence of the friction force. Beyond this fundamentally physical question, as detailed in Section 4.3.6.ii, the form of the friction curve leads to an issue in the resolution of the nonlinear system obtained after discretisation. Fortunately, here, the description of the string's behaviour in the discrete domain allows for the bow equation to be decoupled from the rest of the nonlinear system, if the bowing point is far enough away from any other contact points between the string and the fingerboard or finger. The scalar nonlinear equation for bow friction force, with three potential solutions, can then be resolved with Friedlander's ambiguity (see Figure 4.9).

Isolating the bow equation to solve it graphically may not be a possibility with more advanced string models, however; a geometric nonlinearity, a more advanced damping model, the introduction of longitudinal and torsional wave modelling, could all become major obstacles to the ad-hoc resolution of Friedlander's ambiguity. A model based upon rosin temperature for the bow friction coefficient, the validity of which is although still debated [41], provides a single deterministic solution, removing the need for graphical resolution of the friction force. Such a representation may be worth investigating, as a more robust (yet perhaps more computationally expensive) alternative to the relative velocity curve for the proposed bowed string synthesis algorithm.

The question of finger and fingerboard friction characteristics has been approached heuristically in this work. Extensive experimental measurements would be necessary in order to determine such properties, and to clarify the extent of their influence on the behaviour of the full system.

6.2.4 Aliasing

The strongly nonlinear collision and friction forces lead to sharp deformations of the string, within time scales possibly shorter than the time step k, and therefore to the generation of high frequency components. At audio sample rates, aliasing may be an issue, where these high partials are reflected at the upper frequency limit, and pollute the audible spectrum with unwanted artefacts.

The issue of aliasing has not been tackled in this work. In recent modal-based modelling of string-fingerboard collisions [56], it was found that very high sample rates, in the order of the MHz (well above audio standards), were necessary to ensure convergence of the numerical solution, indicating that aliasing may have significant bearing on the results presented in this manuscript. In particular, given the strong nonlinearity of the bow friction coefficient, the effect of higher sampling rates on bowed string playability may be an interesting problem to consider.

6.3 Perspectives and further work

A natural extension of the physical modelling work presented in this thesis is the coupling of string motion, in two polarisations, to a model of the bridge and body of the instrument. Multiple strings could then also be coupled with each other, through this flexible system, reflecting the design of a full instrument, and giving rise to sympathetic string vibration. Bridge motion is primarily rotational, pivoting about the treble foot, under which the rigid soundpost is placed in many bowed string instruments. The two polarisations of transverse vibration of a string stretched across the top of the bridge are thus mutually coupled through the bridge's rotational motion. The dual polarisation model proposed here is ready for adaptation to such a setting.

At high audio sample rates, the resolution of the discrete spatial grid becomes high enough such that the pointwise bow and finger models constitute a lesser approximation to the physical world. Instead, in this situation, the contact areas between the string and the bow and fingertip cover a number of grid points, and may be treated as distributed. In particular, the finite width of the bow hair has been investigated experimentally and implemented in simulations [83, 84, 92, 72]; it was found to have significant influence on bowed string behaviour, as partial slipping of the string under sections of the bow hair was observed.

The transverse dynamics of the bow hair were approximated, in this work, with a 1-degree of freedom model. Previous work has concerned modelling of both transverse and longitudinal vibration of the bow hair (see, e.g., [73]), as well as dynamics of the bow stick [42]. A full bow model could constitute a worthwhile extension of this work, perhaps enhancing gestural control and playability.

Evidently, further refinements to the physical model would certainly come with increased computational costs. A different avenue of investigation should be taken if the aim is to bring the bowed string algorithm closer to real-time execution, for sound synthesis applications. In this context, two important aspects must be considered, namely algorithmic efficiency and user control interface.

At each time step, two non-sparse nonlinear systems (one in each polarisation) must be solved in order to update the state variables. The requirement to use iterative methods in order to solve these systems is a clear bottleneck in the execution of the algorithm, and constitutes the primary obstacle towards improving computational efficiency. The use of simplified, piecewise-linearised functions for impact and friction forces could provide a cursory path to real-time implementation. In any case, perhaps without resorting to such extremes, an extensive evaluation of the sensitivity of simulated output to incremental simplifications of the physical model could certainly be valuable; if realistic sound synthesis is the primary concern, listening tests could constitute part of such an evaluation.

With regards to user control, the exploratory parameter sweep presented in Section 5.2 could be the starting point for further playability studies. Due to the nature of the bowing control parameters, the same simulation data can be used for transient analysis, simply focusing the analysis window at different times during the initial transient. Furthermore, the waveform identification problem seems particularly well-suited to a machine learning classification algorithm, which could potentially provide a robust tool if systematic characterisation of the playable space of any given string is sought after.

The issue of user interface is a vastly different topic than those treated in this thesis, yet a crucial one for any real world applications of the work presented here. At this time, the synthesis of complex bowed string gestures can only be achieved with manual offline input of breakpoint functions for each control parameter, with no direct feedback before the sound output has been computed. If simulation is achievable in real time, in a realistic manner, mapping control parameters to a hardware controller would, without a doubt, reveal the full potential of the synthesis algorithm for gesture reproduction.

Appendix A

Maximum bow force and pitch flattening: relation with Friedlander's analysis

In Section 4.3.6.ii, a condition was found on the bow normal force, such that the solution of the discrete equation for the bow relative velocity was unique. It is shown here that this constraint is not a numerical one (like the stability condition is), but is rather related to the nature of the bowed string model.

Consider the simplified system of an ideal string, coupled to a pointwise bow at constant position $x_{\mathcal{B}}$, with constant velocity $v_{\mathcal{B}}$, pushing down onto the string with a constant force $f_{\mathcal{B}}$. Using the same notations as established in Section 4.2.3.ii, the transverse displacement $y(x,t)$ of the string obeys:

$$\rho S \partial_t^2 y = T \partial_x^2 y - J_{\mathcal{B}} f_{\mathcal{B}} \varphi_{\mathcal{B}} \left(v_{\text{rel},\mathcal{B}} \right) \tag{A.1}$$

where $J_{\mathcal{B}} \triangleq \delta \left(x - x_{\mathcal{B}} \right)$ is a Dirac delta function, and $v_{\text{rel},\mathcal{B}}$ is defined as:

$$v_{\text{rel},\mathcal{B}} \triangleq \dot{y} \left(x_{\mathcal{B}}, t \right) - v_{\mathcal{B}}(t) \tag{A.2}$$

Equation (A.1) may be discretised as:

$$\rho S \delta_{tt} \mathbf{y}^n = T \mathbf{D}_{xx} \mathbf{y}^n - \mathbf{j}_{\mathcal{B}} f_{\mathcal{B}} \varphi_{\mathcal{B}} \left(v_{\text{rel},\mathcal{B}}^n \right) \tag{A.3a}$$

$$v_{\text{rel},\mathcal{B}}^n \triangleq h \mathbf{j}_{\mathcal{B}}^{\mathsf{T}} \delta_{t\cdot} \mathbf{y}^n - v_{\mathcal{B}}^n \tag{A.3b}$$

The stability condition for this scheme is the same as that for the 1D wave equation:

$$\frac{h}{h_{\text{min}}} \geqslant 1 \tag{A.4a}$$

$$h_{\text{min}} \triangleq \sqrt{\frac{T}{\rho S}} k \triangleq ck \tag{A.4b}$$

Equation (A.3a) can be rearranged to derive an update equation for $\mathbf{y}^{n+1}$:

$$\mathbf{y}^{n+1} = \left(2\mathbf{I} + \frac{Tk^2}{\rho S}\mathbf{D}_{xx}\right)\mathbf{y}^n - \mathbf{y}^{n-1} - \frac{k^2}{\rho S}\mathbf{j}_{\mathcal{B}} f_{\mathcal{B}} \varphi_{\mathcal{B}} \tag{A.5}$$

Rewriting Equation (A.5) in terms of $v^n_{\text{rel},\mathcal{B}}$ yields the following nonlinear equation:

$$v^n_{\text{rel},\mathcal{B}} + \sigma_{\mathcal{B}} f_{\mathcal{B}} \varphi_{\mathcal{B}} + \zeta^n_{\mathcal{B}} = 0 \tag{A.6}$$

where $\sigma_{\mathcal{B}}$, $\zeta^n_{\mathcal{B}}$ are constants, defined as:

$$\sigma_{\mathcal{B}} \triangleq \frac{k}{2\rho S} h \mathbf{j}^{\mathsf{T}}_{\mathcal{B}} \mathbf{j}_{\mathcal{B}} \tag{A.7a}$$

$$\zeta^n_{\mathcal{B}} \triangleq v^n_{\mathcal{B}} - \frac{h}{2k}\mathbf{j}^{\mathsf{T}}_{\mathcal{B}}\left(\left(2\mathbf{I} + \frac{Tk^2}{\rho S}\mathbf{D}_{xx}\right)\mathbf{y}^n - 2\mathbf{y}^{n-1}\right) \tag{A.7b}$$

Friedlander's construction, detailed in Section 4.3.6.ii, yields a condition on $\sigma_{\mathcal{B}}$ so that the solution of Equation (A.6) is unique:

$$-\frac{1}{\sigma_{\mathcal{B}} f_{\mathcal{B}}} \leqslant \min\left(\varphi'_{\mathcal{B}}\right) \qquad \Rightarrow \qquad f_{\mathcal{B}} \leqslant -\frac{2\rho S}{kh\mathbf{j}^{\mathsf{T}}_{\mathcal{B}}\mathbf{j}_{\mathcal{B}} \min\left(\varphi'_{\mathcal{B}}\right)} \tag{A.8}$$

With the friction curve defined by (4.18), $-\min\left(\varphi'_{\mathcal{B}}\right) = 44.5$. The minimum bow force beyond which pitch flattening occurs therefore only depends on the string's physical parameters, the time step k, the grid spacing h, and the magnitude of the discrete distribution vector $\mathbf{j}^{\mathsf{T}}_{\mathcal{B}}$.

Without the bow force term, Scheme (A.3a) can be proved to provide the exact solution for the 1D wave equation, when the grid spacing and time step are set at the stability limit, that is $h = ck$ [8, pp. 133—136]. Furthermore, it was seen in Section 4.3.1 that $h\left|\mathbf{j}_{\mathcal{B}}\right| \leqslant 1$, and is indeed equal to 1 under the restriction that $x_{\mathcal{B}}$ lies exactly on a grid point.

In these limits, the bound on the bow force $f_{\mathcal{B}}$ such that the solution of (A.6) is unique is given by:

$$f_{\mathcal{B}} \leqslant -\frac{2c\rho S}{\min\left(\varphi'_{\mathcal{B}}\right)} \tag{A.9}$$

This is indeed the same bound as that found analytically by Friedlander [39], in the continuous domain. The bound does not vanish, even when the time step and grid spacing are made very small (keeping $\frac{h}{h_{\min}}$ constant).

Bibliography

[1] J.-M. Adrien, "The missing link: modal synthesis," in *Representations of Musical Signals*, G. De Poli, A. Piccialli, and C. Roads, Eds. Cambridge, MA, USA: MIT Press, 1991, pp. 269–298.

[2] A. Askenfelt, "Measurement of bow motion and bow force in violin playing," *Journal of the Acoustical Society of America*, vol. 80, no. 4, pp. 1007–1015, 1986.

[3] ——, "Measurement of the bowing parameters in violin playing. II: Bow-bridge distance, dynamic range, and limits of bow force," *Journal of the Acoustical Society of America*, vol. 86, no. 2, pp. 503–516, 1989.

[4] R. A. Bacon and J. M. Bowsher, "A discrete model of a struck string," *Acustica*, vol. 41, no. 1, pp. 21–27, 1978.

[5] G. Batchelor, *An Introduction to Fluid Dynamics.* London, UK: Cambridge University Press, 1967.

[6] E. Bavu, J. Smith, and J. Wolfe, "Torsional waves in a bowed string," *Acta Acustica united with Acustica*, vol. 91, no. 2, pp. 241–246, 2005.

[7] J. Bensa, S. Bilbao, R. Kronland-Martinet, and J. O. Smith III, "The simulation of piano string vibration: From physical models to finite difference schemes and digital waveguides," *Journal of the Acoustical Society of America*, vol. 114, no. 2, pp. 1095–1107, 2003.

[8] S. Bilbao, *Numerical sound synthesis.* Chichester, UK: John Wiley & Sons, 2009.

[9] S. Bilbao and R. Harrison, "Passive time-domain numerical models of viscothermal wave propagation in acoustic tubes of variable cross section," *Journal of the Acoustical Society of America*, vol. 140, no. 1, pp. 728–740, 2016.

[10] S. Bilbao and A. Torin, "Numerical simulation of string/barrier collisions: the fretboard," in *Proceedings of the International Conference on Digital Audio Effects (DAFx)*, Erlangen, Germany, September 2014.

[11] S. Bilbao, A. Torin, and V. Chatziioannou, "Numerical modeling of collisions in musical instruments," *Acta Acustica united with Acustica*, vol. 101, no. 1, pp. 155–173, 2015.

[12] X. Boutillon, “Model for piano hammers: Experimental determination and digital simulation,” *Journal of the Acoustical Society of America*, vol. 83, no. 2, pp. 746–754, 1988.

[13] J. Bridges and M. Van Walstijn, “Modal based tanpura simulation: combining tension modulation and distributed bridge interaction,” in *Proceedings of the International Conference on Digital Audio Effects (DAFx)*, Edinburgh, UK, September 2017.

[14] O. Brune, “Synthesis of a finite two-terminal network whose driving-point impedance is a prescribed function of frequency,” *MIT Journal of Mathematics and Physics*, vol. 10, no. 1–4, pp. 191–236, 1931.

[15] W. Cauer, “Die Verwirklichung der Wechselstromwiderstände vorgeschriebener Frequenzabhängigkeit,” *Archiv für Elektrotechnik*, vol. 17, pp. 355–388, 1926.

[16] J. Chabassier, A. Chaigne, and P. Joly, “Time domain simulation of a piano. Part 1: model description.” *ESAIM: Mathematical Modelling and Numerical Analysis*, vol. 48, no. 5, pp. 1241–1278, 2013.

[17] J. Chabassier, M. Duruflé, and P. Joly, “Time domain simulation of a piano. Part 2: numerical aspects,” *ESAIM: Mathematical Modelling and Numerical Analysis*, vol. 50, no. 1, pp. 93–133, 2016.

[18] A. Chaigne and A. Askenfelt, “Numerical simulations of piano strings. I. A physical model for a struck string using finite difference methods,” *Journal of the Acoustical Society of America*, vol. 95, no. 2, pp. 1112–1118, 1994.

[19] A. Chaigne, P. Joly, and L. Rhaouti, “Numerical Modeling of the Timpani,” in *European Congress on Computational Methods in Applied Sciences and Engineering*, Barcelona, Spain, September 2000.

[20] A. Chaigne and C. Lambourg, “Time-domain simulation of damped impacted plates. i. theory and experiments,” *Journal of the Acoustical Society of America*, vol. 109, no. 4, pp. 1422–1432, 2001.

[21] V. Chatziioannou and M. Van Walstijn, “Energy conserving schemes for the simulation of musical instrument contact dynamics,” *Journal of Sound and Vibration*, vol. 339, pp. 262–279, 2015.

[22] R. Courant, K. Friedrichs, and H. Lewy, “On the partial difference equations of mathematical physics (English translation: Phyllis Fox, 1956),” *Mathematische Annalen*, vol. 100, pp. 32–74, 1928.

[23] C. Cuesta and C. Valette, “Evolution temporelle de la vibration des cordes de clavecin,” *Acustica*, vol. 66, no. 1, pp. 37–45, 1988.

[24] V. Debut, J. Antunes, and O. Inácio, “Linear modal stability analysis of bowed-strings,” *Journal of the Acoustical Society of America*, vol. 141, no. 3, pp. 2107–2120, 2017.

[25] M. Demoucron, “On the control of virtual violins—Physical modelling and control of bowed string instruments,” Ph.D. dissertation, Université Pierre et Marie Curie-Paris VI, 2008.

[26] M. Demoucron, A. Askenfelt, and R. Caussé, “Measuring bow force in bowed string performance: theory and implementation of a bow force sensor,” *Acta Acustica united with Acustica*, vol. 95, no. 4, pp. 718–732, 2009.

[27] C. Desvages and S. Bilbao, “Physical modeling of nonlinear player-string interactions in bowed string sound synthesis using finite difference methods,” in *Proceedings of the International Symposium on Musical Acoustics (ISMA)*, Le Mans, France, July 2014.

[28] ——, “Two-polarisation finite difference model of bowed strings with nonlinear contact and friction forces,” in *Proceedings of the International Conference on Digital Audio Effects (DAFx)*, Trondheim, Norway, December 2015.

[29] ——, “Two-polarisation physical model of bowed strings with nonlinear contact and friction forces, and application to gesture-based sound synthesis,” *Applied Sciences*, vol. 6, no. 5, p. 135, 2016.

[30] C. Desvages, S. Bilbao, and M. Ducceschi, “Improved frequency-dependent damping for time domain modelling of linear string vibration,” in *Proceedings of the International Congress on Acoustics*, Buenos Aires, Argentina, September 2016.

[31] C. Desvages and M. Newton, “Bow control and playability of a two-polarisation time domain physical model of a bowed string,” in *Proceedings of the International Symposium on Musical and Room Acoustics*, La Plata, Argentina, September 2016.

[32] M. Ducceschi and S. Bilbao, “Modelling collisions of nonlinear strings against rigid barriers: conservative finite difference schemes with application to sound synthesis,” in *Proceedings of the International Congress on Acoustics*, Buenos Aires, Argentina, September 2016.

[33] ——, “Linear stiff string vibrations in musical acoustics : Assessment and comparison of models,” *Journal of the Acoustical Society of America*, vol. 140, no. 4, pp. 2445–2454, 2016.

[34] A. Falaize and T. Hélie, “Passive Guaranteed Simulation of Analog Audio Circuits: A Port-Hamiltonian Approach,” *Applied Sciences*, vol. 6, no. 10, p. 273, 2016.

[35] ——, “Passive simulation of the nonlinear port-Hamiltonian modeling of a Rhodes Piano,” *Journal of Sound and Vibration*, vol. 390, pp. 289–309, 2017.

[36] A. Falaize, N. Lopes, T. Hélie, D. Matignon, and B. Maschke, “Energy-balanced models for acoustic and audio systems: a port-Hamiltonian approach,” in *Unfold Mechanics for Sounds and Music*, Paris, France, September 2014.

[37] H. Fletcher, “Normal vibration frequencies of a stiff piano string,” *Journal of the Acoustical Society of America*, vol. 36, no. 1, pp. 203–209, 1964.

[38] R. M. Foster, “A Reactance Theorem,” *Bell System Technical Journal*, vol. 3, no. 2, pp. 259–267, 1924.

[39] F. G. Friedlander, “On the oscillations of a bowed string,” *Mathematical Proceedings of the Cambridge Philosophical Society*, vol. 49, no. 3, pp. 516–530, 1953.

[40] P. M. Galluzzo, “On the playability of stringed instruments,” Ph.D. dissertation, Trinity College, Dublin, 2004.

[41] P. M. Galluzzo, J. Woodhouse, and H. Mansour, “Assessing friction laws for simulating bowed-string motion,” *Acta Acustica united with Acustica*, vol. 103, no. 6, pp. 1080–1099, 2017.

[42] C. E. Gough, “Violin bow vibrations,” *Journal of the Acoustical Society of America*, vol. 131, no. 5, pp. 4152–4163, 2012.

[43] A. Granato and K. Lücke, “Theory of Mechanical Damping Due to Dislocations,” *Journal of Applied Physics*, vol. 27, no. 6, pp. 583–593, 1956.

[44] K. Guettler, “Some typical properties of bowed strings,” Tech. Rep.

[45] ——, “On the creation of the Helmholtz motion in bowed strings,” *Acta Acustica united with Acustica*, vol. 88, pp. 970–985, 2002.

[46] ——, “A Closer Look at the String Player’s Bowing Gestures,” *Catgut Acoustical Society Journal*, vol. 4, no. 7, pp. 12–16, 2003.

[47] K. Guettler and A. Askenfelt, “Acceptance limits for the duration of pre-Helmholtz transients,” *Journal of the Acoustical Society of America*, vol. 101, no. 5, pp. 2903–2913, 1997.

[48] E. A. Guillemin, “A Summary of Modern Methods of Network Synthesis,” in *Advances in Electronics and Electron Physics*, L. Marton, Ed. Academic Press, 1951, pp. 261–303.

[49] H. Haddar, T. Hélie, and D. Matignon, “A Webster-Lokshin model for waves with viscothermal losses and impedance boundary conditions: strong solutions,” in *Mathematical and Numerical Aspects of Wave Propagation (WAVES 2003)*, Jyväskylä, Finland, June 2003, pp. 66–71.

[50] S. M. Han, H. Benaroya, and T. Wei, “Dynamics of transversely vibrating beams using four engineering theories,” *Journal of Sound and Vibration*, vol. 225, no. 5, pp. 935–988, 1999.

[51] T. Hélie and D. Matignon, “Diffusive representations for the analysis and simulation of flared acoustic pipes with visco-thermal losses,” *Mathematical Models and Methods in Applied Sciences*, vol. 16, no. 4, pp. 503–536, 2006.

[52] L. Hiller and P. Ruiz, “Synthesizing musical sounds by solving the wave equation for vibrating objects: Part I,” *Journal of the Audio Engineering Society*, vol. 19, no. 6, pp. 462–470, 1971.

[53] ——, “Synthesizing musical sounds by solving the wave equation for vibrating objects: Part II,” *Journal of the Audio Engineering Society*, vol. 19, no. 7, pp. 542–551, 1971.

[54] J. Hollmon, R. Maurer, F. Seitz, and W. Shockley, *Imperfections in Nearly Perfect Crystals: Symposium held at Pocono Manor.* New York, USA: John Wiley & Sons, 1952.

[55] K. H. Hunt and F. R. E. Crossley, “Coefficient of restitution interpreted as damping in vibroimpact,” *Journal of Applied Mechanics*, vol. 42, no. 2, pp. 440–445, 1975.

[56] C. Issanchou, S. Bilbao, J.-L. Le Carrou, C. Touzé, and O. Doaré, “A modal-based approach to the nonlinear vibration of strings against a unilateral obstacle : Simulations and experiments in the pointwise case,” *Journal of Sound and Vibration*, vol. 393, pp. 229–251, 2017.

[57] D. Jaffe and J. O. Smith III, “Extensions of the Karplus-Strong plucked-string algorithm,” *Computer Music Journal*, vol. 7, no. 2, pp. 56–69, 1983.

[58] M. Karjalainen, V. Välimäki, and T. Tolonen, “Plucked-string models: from the Karplus-Strong algorithm to digital waveguides and beyond,” *Computer Music Journal*, vol. 22, no. 3, pp. 17–32, 1998.

[59] K. Karplus and A. Strong, “Digital synthesis of plucked-string and drum timbres,” *Computer Music Journal*, vol. 7, no. 2, pp. 43–55, 1983.

[60] T. W. B. Kibble and F. H. Berkshire, *Classical Mechanics*, 5th ed. London, UK: Imperial College Press, 2004.

[61] J. Kleimola, “Nonlinear abstract sound synthesis algorithms,” Ph.D. dissertation, Aalto University, 2013.

[62] F. F. Kuo, *Network analysis and synthesis*, 2nd ed. John Wiley & Sons, Ltd, 1966.

[63] Y. A. Kuznetsov, *Elements of Applied Bifurcation Theory*, 2nd ed. Springer, 1995.

[64] R. Lakes, *Viscoelastic Materials.* Cambridge: Cambridge University Press, 2009.

[65] C. Lambourg, A. Chaigne, and D. Matignon, “Time-domain simulation of damped impacted plates. II. Numerical model and results,” *Journal of the Acoustical Society of America*, vol. 109, no. 4, pp. 1433–1447, 2001.

[66] B. Lawergren, “On the motion of bowed violin strings,” *Journal of the Acoustical Society of America*, vol. 44, no. 3, pp. 194–206, 1980.

[67] J. le Rond D'Alembert, "Recherches sur la courbe que forme une corde tendue mise en vibrations," *Histoire de l'Académie Royale des Sciences et Belles Lettres*, no. 3, pp. 214–249, 1747.

[68] A. M. Lyapunov, "The general problem of the stability of motion (English translation: A. T. Fuller)," *International Journal of Control*, vol. 55, no. 3, pp. 531–773, 1992.

[69] E. Maestre, "Modeling instrumental gesture: an analysis/synthesis framework for violin bowing," Ph.D. dissertation, Univ. Pompeu Fabra, Barcelona, 2009.

[70] ——, "Analysis/synthesis of bowing control applied to violin sound rendering via physical models," in *Proceedings of Meetings on Acoustics*, vol. 19, Montreal, Canada, June 2013, p. 035016.

[71] E. Maestre, G. Scavone, and Smith III, Julius O., "Digital modeling of bridge driving-point admittances from measurements on violin-family instruments," in *Proceedings of the Stockholm Music Acoustics Conference (SMAC)*, August 2013.

[72] E. Maestre, C. Spa, and J. O. Smith III, "A bowed string physical model including finite-width thermal friction and hair dynamics," in *Proceedings of the International Computer Music Conference (ICMC)*, Athens, Greece, July 2014.

[73] H. Mansour, J. Woodhouse, and G. P. Scavone, "Enhanced wave-based modelling of musical strings. Part 2: Bowed strings," *Acta Acustica united with Acustica*, vol. 102, no. 6, pp. 1082–1093, 2016.

[74] M. E. McIntyre, R. T. Schumacher, and J. Woodhouse, "On the oscillations of musical instruments," *Journal of the Acoustical Society of America*, vol. 74, no. 5, pp. 1325–1345, 1983.

[75] M. E. McIntyre and J. Woodhouse, "On the fundamentals of bowed-string dynamics," *Acustica*, vol. 43, no. 2, pp. 93–108, 1979.

[76] G. Müller and W. Lauterborn, "The bowed string as a nonlinear dynamical system," *Acta Acustica united with Acustica*, vol. 82, no. 4, pp. 657–664, 1996.

[77] R. Nabben, "Two-sided bounds on the inverses of diagonally dominant tridiagonal matrices," *Linear Algebra and its Applications*, vol. 287, no. 1, pp. 289–305, 1999.

[78] F. Pantelić, C. Desvages, J. Prezelj, and D. Šumarac Pavlović, "Influence of bow-bridge distance on string timbre," in *Proceedings of the 7th Congress of the Alps Adria Acoustics Association (AAAA 2016)*, Ljubljana, Slovenia, September 2016.

[79] A. Parret-Fréaud, B. Cotté, and A. Chaigne, "Time-domain damping models in structural acoustics using digital filtering," *Mechanical Systems and Signal Processing*, vol. 68, pp. 587–607, 2016.

[80] A. Paté, J.-L. Le Carrou, and B. Fabre, “Predicting the decay time of solid body electric guitar tones,” *Journal of the Acoustical Society of America*, vol. 135, no. 5, pp. 3045–3055, 2014.

[81] G. K. Percival, “Physical modelling meets machine learning: performing music with a virtual string ensemble,” Ph.D. dissertation, University of Glasgow, 2013.

[82] N. C. Pickering, “Physical properties of violin strings,” *Catgut Acoustical Society Journal*, vol. 44, pp. 6–8, 1985.

[83] R. Pitteroff and J. Woodhouse, “Influence of a bow of finite width on bowed string motion: Numerical modelling and experimental evidence,” *Journal de Physique*, vol. 4, no. C5, pp. 605–608, 1994.

[84] ——, “Mechanics of the contact area between a violin bow and a string. Part I: Reflection and transmission behaviour,” *Acta Acustica united with Acustica*, vol. 84, pp. 543–562, 1998.

[85] C. Poepel, “Synthesized strings for string players,” in *Proceedings of the Conference on New Interfaces for Musical Expression (NIME)*, Hamamatsu, Japan, June 2004, pp. 150–153.

[86] C. Raman, “On the mechanical theory of the vibrations of bowed strings and of musical instruments of the violin family, with experimental verification of the results,” *Bulletin of the Indian Association for the Cultivation of Science*, vol. 15, pp. 1–158, 1918.

[87] J. Renton, “A check on the accuracy of Timoshenko’s beam theory,” *Journal of Sound and Vibration*, vol. 245, no. 3, pp. 559–561, 2001.

[88] L. Rhaouti, A. Chaigne, and P. Joly, “Time-domain modeling and numerical simulation of a kettledrum,” *Journal of the Acoustical Society of America*, vol. 105, no. 6, pp. 3545–3562, 1999.

[89] P. M. Ruiz, “A technique for simulating the vibration of strings with a digital computer,” Ph.D. dissertation, University of Illinois at Urbana-Champaign, 1970.

[90] J. C. Schelleng, “The bowed string and the player,” *Journal of the Acoustical Society of America*, vol. 53, no. 1, pp. 26–41, 1973.

[91] E. Schoonderwaldt, “The violinist’s sound palette: spectral centroid , pitch flattening and anomalous low frequencies,” *Acta Acustica united with Acustica*, vol. 95, pp. 901–914, 2009.

[92] E. Schoonderwaldt, K. Guettler, and A. Askenfelt, “Effect of the width of the bow hair on the violin string spectrum,” in *Proceedings of the Stockholm Music Acoustics Conference (SMAC)*, Stockholm, Sweden, August 2003, pp. 91–94.

[93] ——, "An empirical investigation of bow-force limits in the Schelleng diagram," *Acta Acustica united with Acustica*, vol. 94, no. 4, pp. 604–622, 2008.

[94] R. T. Schumacher and J. Woodhouse, "The transient behaviour of models of bowed-string motion." *Chaos*, vol. 5, no. 3, pp. 509–523, 1995.

[95] S. Serafin and J. O. Smith III, "Influence of attack parameters on the playability of a virtual bowed string instrument," in *Proceedings of the International Computer Music Conference (ICMC)*, Berlin, Germany, August 2000, pp. 473–476.

[96] S. Serafin, J. O. Smith III, and J. Woodhouse, "An investigation of the impact of torsion waves and friction characteristics on the playability of virtual bowed strings," in *Proceedings of the IEEE Workshop on Applications of Signal Processing to Audio and Acoustics*, New Paltz, New York, October 1999.

[97] S. Serafin and D. Young, "Recent advances in real-time bowed string synthesis: Evaluation of the models," in *Proceedings of the International Congress on Acoustics*, Madrid, Spain, September 2007.

[98] H. M. Simpson and A. Sosin, "Contribution of defect dragging to dislocation damping. I. Theory," *Physical Review B*, vol. 5, no. 4, pp. 1382–1393, 1972.

[99] H. M. Simpson, A. Sosin, and D. F. Johnson, "Contribution of defect dragging to dislocation damping. II. Experimental," *Physical Review B*, vol. 5, no. 4, pp. 1393–1401, 1972.

[100] J. H. Smith and J. Woodhouse, "The tribology of rosin," *Journal of the Mechanics and Physics of Solids*, vol. 48, pp. 1633–1681, 2000.

[101] J. O. Smith III, "A new approach to digital reverberation using closed waveguide networks," in *Proceedings of the International Computer Music Conference (ICMC)*, Burnaby, Canada, August 1985, pp. 47–53.

[102] ——, "Efficient simulation of the reed-bore and bow-string mechanisms," in *Proceedings of the International Computer Music Conference (ICMC)*, The Hague, Netherlands, October 1986, pp. 275–280.

[103] ——, "Physical modeling using digital waveguides," *Computer Music Journal*, vol. 16, no. 4, pp. 74–91, 1992.

[104] ——, "Efficient synthesis of stringed musical instruments," in *Proceedings of the International Computer Music Conference (ICMC)*, Tokyo, Japan, September 1993, pp. 64–71.

[105] M. Sterling, "Empirical physical modeling methods for bowed-string and wind instruments," Ph.D. dissertation, University of Rochester, New York, 2010.

[106] G. G. Stokes, "On the effect of the internal friction of fluids on the motion of pendulums," *Transactions of the Cambridge Philosophical Society*, vol. IX, 1850.

[107] J. C. Strikwerda, *Finite difference schemes and partial differential equations.* Siam, 2004.

[108] A. Stulov, “Dynamic behavior and mechanical features of wool felt,” *Acta Mechanica*, vol. 169, no. 1–4, pp. 13–21, 2004.

[109] V. Thomée, “From finite differences to finite elements: a short history of numerical analysis of partial differential equations,” *Journal of Computational and Applied Mathematics*, vol. 128, pp. 1–54, 2001.

[110] S. C. Thompson, T. B. Gabrielson, and D. M. Warren, “Analog model for thermoviscous propagation in a cylindrical tube,” *Journal of the Acoustical Society of America*, vol. 135, no. 2, pp. 585–590, 2014.

[111] S. P. Timoshenko, “On the transverse vibrations of bars of uniform cross-section,” *Philosophical Magazine*, vol. 43, no. 253, pp. 125–131, 1922.

[112] A. Torin, B. Hamilton, and S. Bilbao, “An energy conserving finite difference scheme for the simulation of collisions in snare drums,” in *Proceedings of the International Conference on Digital Audio Effects (DAFx)*, Erlangen, Germany, September 2014.

[113] C. Valette and C. Cuesta, *Mécanique de la corde vibrante.* Paris, France: Hermès, 1993.

[114] A. J. van der Schaft, “Port-Hamiltonian systems: an introductory survey,” in *Proceedings of the International Congress of Mathematicians*, Madrid, Spain, August 2006, pp. 1339–1365.

[115] H. von Helmholtz, *On the sensations of tone as a physiological basis for the theory of music (English translation A.J. Ellis, 1885, 1954); third edition.* Cambridge, UK: Cambridge University Press, 1877.

[116] J. Woodhouse, “Bowed string simulation using a thermal friction model,” *Acta Acustica united with Acustica*, vol. 89, no. 2, pp. 355–368, 2003.

[117] ——, “Playability of bowed-string instruments,” in *Proceedings of the Stockholm Music Acoustics Conference (SMAC)*, Stockholm, Sweden, August 2013.

[118] ——, “The acoustics of the violin: a review.” *Reports on Progress in Physics*, vol. 77, no. 11, p. 115901, 2014.

[119] J. Woodhouse and P. M. Galluzzo, “The bowed string as we know it today,” *Acta Acustica united with Acustica*, vol. 90, no. 4, pp. 579–589, 2004.